Investigating the rate-limiting step of mitochondrial complex I catalysis

Man Nok Choy

Downing College
September 2023

This thesis is submitted for the degree of Doctor of Philosophy

Declaration

This thesis is the result of my own work and includes nothing which is the outcome of work done in collaboration except as declared in the preface and specified in the text.

It is not substantially the same as any work that has already been submitted before for any degree or other qualification except as declared in the preface and specified in the text.

It does not exceed the prescribed word limit for the relevant Degree Committee.

Man N. Choy

September 2023

Abstract

Respiratory complex I (NADH:ubiquinone oxidoreductase) is a key enzyme in metabolism and is the least understood protein in the mitochondrial electron transfer chain (ETC). It couples the energy released from NADH oxidation and ubiquinone (Q) reduction to the translocation of four protons across the inner mitochondrial membrane, contributing to the proton motive force (PMF) used to synthesise ATP. Although structural knowledge of complex I is now extensive, the mechanism by which it couples the redox energy for proton translocation remains unclear.

First, the rate-limiting step of catalysis in complex I was investigated from the point of view of the proton. Using the proteoliposomes system, the pH and solvent isotope dependence of kinetic parameters of purified bovine and *Yarrowia lipolytica* complex I mutants were measured under a range of conditions. I find complex I robustly displays a solvent kinetic isotope effect (KIE), signifying that the rate-limiting step involves a proton transfer. This isotopic sensitive step is dependent on Q-chain length, Q binding-site mutations, and Q-concentration, but not dependent on Δp, suggesting that this step is Q-reduction. Proton inventory experiments suggest that a single proton is transferred in the rate-limiting step, and that complex I is rate-limited by a combination of a proton transfer step and an isotopically insensitive step, which was assigned as the product release of ubiquinol.

Next, the role of conserved charged residues in the central axis were investigated using the *Paracoccus denitrificans* model system. Mutants of residues involved in the energy propagation pathway and subunit hydration channel gating were evaluated using solvent isotope effect and proton pumping experiments. These mutations all exhibited a greater isotope dependence than WT, showing that proton pumping steps have become robustly rate-limiting. Then, experimental results were evaluated against computational and mechanistic proposals, to identify the role of these residues.

Finally, the role of a putative re-protonation channel in NUCM was investigated using the *Yarrowia lipolytica* model system. Point mutations, made up of conserved buried charged residues connecting the Q-binding site to the matrix were generated. Characterisation of mutants revealed that residues with strong ionic interactions (arginine and glutamate) did not express complex I, and that mutation effects were inconsistent with the abrogation of a protonation channel. I conclude that these residues likely play no role in re-protonation, but instead may be important for structural stabilisation.

Acknowledgements

First and foremost, I would like to thank Professor Judy Hirst for the opportunity to pursue research in complex I mechanism as part of her group. The PhD has not been easy, and her continued guidance, support and trust in my ability allowed me to persevere, improve my scientific understanding, and develop confidence in my abilities.

No less important are the sources of day-to-day support that have come from the strong team of scientists, past and present in the Hirst lab, that has made this such a collaborative and engaging environment. I would like to thank Justin Fedor for his immediate help at the start of my PhD, and John Wright for his continuous mentorship and help throughout my PhD. I'd also like to thank Hannah Bridges and Danial Grba for their help regarding structural analysis, Oliver Biner for proteoliposome preparation and Owen Jarman for his help in my work involving *Paracoccus denitrificans*. In addition, I'd like to thank other members of the Hirst lab: Noor, Zhan, Injae, Bo, Billy, Jessica, Robbie, Valentine, and Chris for their helpful advice and continuous friendship. I will miss our coffee breaks, corridor chats, and pub meetups. In addition, I have also learned tremendously from the other members of the MBU and enjoyed with them the unit's non-working hours and subsequent outings.

Outside of my PhD, I am grateful to the friends I have met in Cambridge. I would also like to thank my close friends Alex, Dominic, Jack, and Mikhail who have given me tremendous support over the years, and whom I rely on for my continuous sanity. I also owe my thanks to my inspirational teachers from Caterham School for inspiring me to pursue biochemistry and to Dr. David Leys, and Dr. Karl Fisher at the Manchester Institute for Biotechnology for guiding me on my academic path.

A huge thanks goes towards Cambridge MMA for keeping me physically healthy, and to its members for their friendship and inspiration.

Above all, I would like to thank my parents and family for their unconditional love and support, without which I could not have persevered through this journey. They have provided continuous encouragement and picked me up during my lowest times, for which I could not be more grateful. Lastly, I would like to dedicate this thesis to my dear brother Charles Siu, and I will always treasure our memories.

Man N. Choy

Abbreviations

ACMA	9-amino-6-chloro-2-methoxyacridine
ADP	Adenosine diphosphate
AOX	Alternative oxidase
Ap5A	Diadenosine pentaphosphate
$APAD^+$	3-acetylpyridine adenine dinucleotide
ATP	Adenosine triphosphate
BCA	Bicinchoninic acid
BN-PAGE	Blue native-polyacrylamide gel electrophoresis
Bovine	*Bos taurus*
BSA	Bovine serum albumin
CHAPS	3-[(3-cholamidopropyl) dimethylammonio]-1-propanesulphonate
CDL	Cardiolipin
Cryo-EM	Cryogenic electron microscopy
Cyt c	Cytochrome c
DDM	n-dodecyl β-D-maltoside
D. vulgaris	*Desulfovibrio vulgaris*
DMSO	Dimethyl sulfoxide
DNA	Deoxyribonucleic acid
dNADH	Reduced nicotinamide hypoxanthine dinucleotide
DOPC	1,2-dioleoyl-sn-glycero-3-phosphocholine
DOPE	1,2-dioleoyl-sn-glycero-3-phosphoethanolamine
DOPG	1,2-dioleoyl-sn-glycero-3-phospho-(1'-rac-glycerol)
DQ	Decylubiquinone
EDTA	Ethylenediaminetetraacetic acid
EPR	Electron paramagnetic resonance
ETC	Electron transfer chain
FAD	Flavin adenine dinucleotide
FET	Forward electron transfer
FES	Iron-sulfur
FMN	Flavin mononucleotide
H_2O_2	Hydrogen peroxide
HEPES	(4-(2-hydroxyethyl)-1-piperazineethanesulphonic acid)
IBM	Inner boundary membrane
Kan^R	Kanamycin resistance

KIE	Kinetic isotope effect
IMM	Inner mitochondrial membrane
IMS	Intermembrane space
MES	2-(N-morpholino)ethanesulphonic acid
MM	Mitochondrial matrix
MOPS	3-(N-morpholino)propanesulphonic acid
mtDNA	Mitochondrial DNA
NAD^+	Nicotinamide adenine dinucleotide
NADH	Reduced nicotinamide adenine dinucleotide
$NADP^+$	Nicotinamide adenine dinucleotide phosphate
NADPH	Reduced nicotinamide adenine dinucleotide phosphate
NanoDSF	Nano differential scanning fluorimetry
NBT	Nitroblue tetrazolium
NDH-2	Alternative NADH dehydrogenase
OD600	Optical density at 600 nm
OG	Octyl-glucoside
OMM	Outer mitochondrial membrane
OXPHOS	Oxidative phosphorylation
PAGE	Poly-acrylamide gel electrophoresis
PCR	Polymerase chain reaction
Pi	Inorganic phosphate
PL	Proteoliposome
PMSF	Phenylmethanesulphonylfluoride
Q	Ubiquinone
Q_1	Isoprenylubiquinone
Q_{10}	Coenzyme Q-decaisoprenylubiquinone
QH_2	Ubiquinol
RET	Reverse electron transfer
ROS	Reactive oxygen species
RPM	Rotations per minute
SBP	Sub-bacterial particles
SDS	Sodium dodecyl sulphate
SMP	Sub-mitochondrial particle
SOC	Super optimal broth with catabolite repression
TCA cycle	Tricarboxylic acid cycle
T. thermophilus	*Thermus thermophilus*

Tris	Tris(hydroxymethyl)aminomethane
Y. lipolytica	*Yarrowia lipolytica*
Δp	Proton motive force
ΔpH	Proton potential difference
ΔΨ	Charge potential difference

Table of Contents

1 Introduction

1.1 Bioenergetics

All life is supported by the constant regeneration of its own cellular components, performed by intricately organised chemical reactions involving small molecules and chemical elements obtained from the environment. The second law of thermodynamics states that for a reaction to be spontaneous, the total entropy of the system and its surroundings must increase. All life exists in an open system, and fundamental cellular reactions, such as metabolism, DNA replication, signalling, protein synthesis, and component transport, decrease entropy and are not spontaneous reactions. Life processes can only be maintained by the constant consumption of energy, observing the second law of thermodynamics. The energy comes in two forms: either light energy or redox-driven reactions that generate chemical disequilibria. The processes by which cells generate and harness this potential energy are the basis of bioenergetics.

Bioenergetic processes, releasing energy from light or chemical bonds, involve a series of redox reactions along a series of donors and acceptors of increasingly high potential, releasing energy from the flux of electrons. This energy is transduced into ion-pumps that pump protons across a membrane. These include the inner mitochondrial membrane, the thylakoid membrane in chloroplasts and cyanobacteria, and the plasma membrane in prokaryotes. These energy-transducing membranes must be impermeable to ions, thus maintaining an electro-chemical gradient. In the cell, these bioenergetic processes are accomplished by the enzymes that form the respiratory chain, or electron transport chain (ETC), in the process known as oxidative phosphorylation. The electrochemical gradient, $\Delta\mu_{H^+}$ is made of two components: one due to the difference in concentration of protons in the bulk phases on each side of the membrane (ΔpH), and one due to the differences in electrochemical potential between the two phases separated by the membrane (Δψ). The term $\Delta\mu_{H^+}$ is defined under thermodynamic terms as:

$$\Delta\mu_{H^+} = -F\Delta\psi + 2.3RT\Delta\mathrm{pH} \tag{1.1}$$

Where F is the Faraday constant (96485 $Jmol^{-1}$), *R* is the molar gas constant (8.31 $JK^{-1}mol^{-1}$), and *T* is the absolute temperature in Kelvin. The term $\Delta\mu_{H^+}$ has units of $Jmol^{-1}$ and is commonly converted into proton motive force (PMF or Δp) by dividing the term with the Faraday constant, F. Δp is then defined in units of electrical potential (millivolts).

The Δp generated by redox reactions in oxidative phosphorylation can be used to synthesize ATP, the energy currency in the cell, from ADP and inorganic phosphate (P_i). This is the basis of the chemiosmotic theory developed by Peter Mitchell (Peter Mitchell, 1961). ATP molecules do not inherently generate energy, but it is the chemical disequilibrium between [ATP]/ [ADP] that contain the potential energy used in coupled reactions in energetically unfavourable processes, allowing life to exist.

1.2 Mitochondria

In a non-photosynthetic eukaryotic cell, the chemiosmotic coupling between respiratory redox reactions (oxidation) and ATP synthesis (phosphorylation) occurs in the mitochondria.

1.2.1 Structure of mitochondria

Mitochondria are organelles that possess two membranes separating their matrix from the cytoplasm (Frey and Mannella, 2000) (Figure 1.1). The first is the outer mitochondrial membrane (OMM), which is porous to ions and metabolites under 10 kDa through pore-forming membrane proteins, such as the voltage-dependent anion channel (VDAC) (Mannella, 1992). The inner mitochondria membrane (IMM) is highly impermeable to ions and metabolites, and metabolites can only cross using specific membrane transport proteins (Mannella, Lederer and Jafri, 2013).

The outer and inner membranes define three compartments within mitochondria. The innermost compartment, enclosed by the IMM, is the mitochondrial matrix. The mitochondrial matrix is the site of mitochondrial DNA (mtDNA) replication, transcription, protein synthesis and, crucially, the numerous enzymatic reactions in the tricarboxylic acid (TCA) cycle, in fatty acid β-oxidation, and pyruvate oxidation (Figure 1.2).

The space between the inner and outer mitochondrial membrane is known as the intermembrane space (IMS) and is equivalent to the periplasm of prokaryotes. The

location in which the IMM and OMM are in close contact is called the inner boundary membrane (IBM) (Kühlbrandt, 2015) and is where metabolites and ions are exchanged between the matrix and cytoplasm through selective mitochondrial transporters and channels. In particular, the adenine nucleotide translocase (ANT) is crucial for oxidative phosphorylation, as it exchanges ADP in the cytosol for ATP in the mitochondrial matrix (Ruprecht and Kunji, 2020).

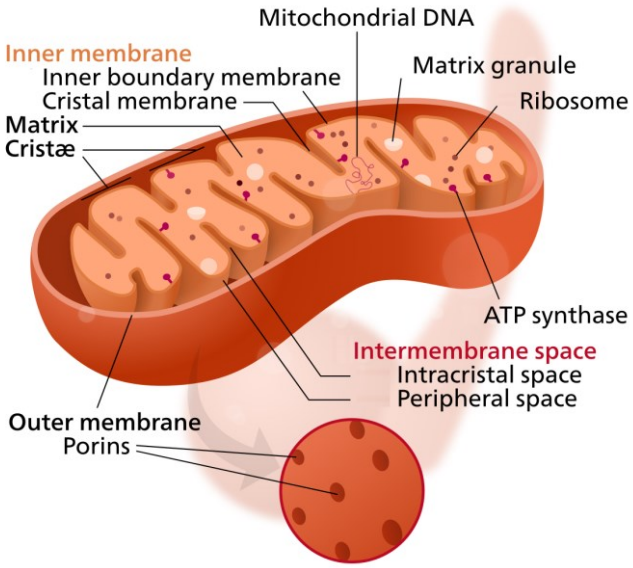

Figure 1.1. The structure of the mitochondria. A schematic of the mitochondrion showing the key features of the organelle. The outer mitochondrial membrane (OMM) contains pore-forming membrane proteins called porins. The inner membrane (OMM) is divided into the inner boundary membrane (IBM) and the cristae membrane (CM). The CM contains most, if not all the respiratory enzyme complex in oxidative phosphorylation. The space between the IMM and OMM is called the intermembrane space (IMS). Figure is adapted from (Frey and Mannella, 2000).

The IMM adopts a highly invaginated morphology, with folds of membrane protruding into the matrix called cristae (Mannella, 2006). The cristae define a third mitochondrial compartment, the cristae lumen (Figure 1.1). The crista membrane contains most, if not all the fully assembled complexes of the electron transport chain (ETC) and ATP synthase (Kühlbrandt, 2015). The invaginations and crista lumen likely prevent the rapid escape of protons pumped into the inter-membrane space and serve to increase the local concentration of protons. This makes for more effective ATP synthesis and is thus the main site of energy conversion in the mitochondria (Kühlbrandt, 2015).

1.2.2 Functions of mitochondria

The central role of mitochondria is metabolism, converting chemical energy from nutrient molecules into an energy supply for the cell. Pathways linked to the mitochondria include the tricarboxylic acid cycle (TCA), fatty acid β-oxidation, and pyruvate oxidation (Figure 1.2). In the cytoplasm, carbohydrates are broken down into pyruvate during glycolysis. This process releases two molecules of reduced nicotinamide adenine dinucleotide (NADH) per molecule of glucose. Pyruvate is then transported into the mitochondrial matrix by the mitochondrial pyruvate carrier (MPC) (Herzig *et al.*, 2012), where it is converted to acetyl-coenzyme A (CoA) through oxidative decarboxylation by pyruvate dehydrogenase, forming NADH in the process. Acetyl-CoA is an input in the TCA cycle and delivers the acetyl group for the conversion of oxaloacetate to citrate. A primary role of the TCA cycle is to reduce NAD^+ to NADH and succinate to fumarate, which are important electron donors in proton pumping. In addition to carbohydrate metabolism, mitochondria also release energy from the oxidation of lipids and amino acids. Fatty acid degradation generates acyl-CoA, which enters the mitochondrial matrix using the carnitine shuttle and undergoes fatty acid β-oxidation for the cyclical breakdown of the carbon chain two carbon atoms per cycle, producing flavin adenine dinucleotide ($FADH_2$), NADH, and acetyl-CoA. Amino acids are catabolised using a number of different pathways to generate intermediates for the TCA cycle.

In addition to the NADH generated in the TCA cycle in the mitochondrial matrix, the two molecules of NADH generated in glycolysis in the cytosol are directed back into the mitochondrial matrix by the malate-aspartate shuttle (Nicholls, 2013). Shuttles move reducing equivalents across the membrane, moving only charge but not the molecule itself. In this case, cytosolic malate dehydrogenase reduces oxaloacetate to malate by oxidising NADH. Malate is then imported into the mitochondria using the malate-oxoglutarate antiporter, which exports oxoglutarate from the matrix when malate is imported. Mitochondrial matrix malate dehydrogenase then oxidizes the malate back to oxaloacetate, regenerating the NADH. In totality, the NADH and $FADH_2$ are produced in the TCA and glycolysis are fed into the ETC for oxidative phosphorylation (OXPHOS) to form ATP.

In addition to their central role in metabolism, mitochondria also play a role in calcium homeostasis, localised signalling, apoptosis, iron-sulphur cluster biosynthesis and haem biosynthesis (Nicholls, 2013).

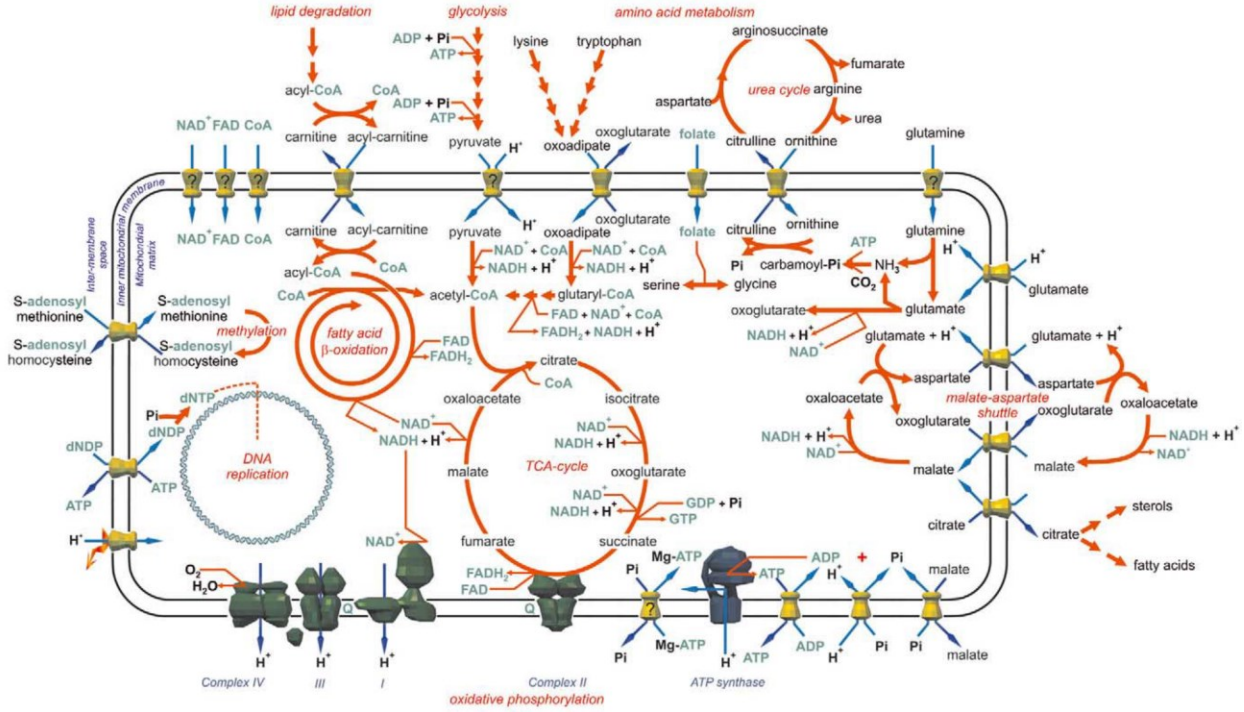

Figure 1.2. A schematic representation of the metabolic process and transport events that occur in a mammalian mitochondrion. The OMM is not shown. Red arrows indicate metabolic pathways and blue arrows indicate the directionality of metabolite transport carried out by membrane proteins. Green indicates co-factors and high-energy intermediates. Figure is adapted from (Kunji, 2004).

1.2.3 Mitochondrial origins

A distinct feature of mitochondria as an organelle is they contain their own DNA. In humans, mitochondrial DNA (mtDNA) encodes 13 proteins, 22 transfer RNAs, and two ribosomal RNAs in a small, circularised chromosome much like prokaryotic cells (Taanman, 1999). All encoded proteins in mtDNA are hydrophobic and membrane-bound subunits of the respiratory chain complex enzymes, or ATP synthase. Endosymbiotic theory suggests that mtDNA is most likely to be an evolutionary leftover when mitochondria were created in an endosymbiotic event that led to the formation of eukaryotic cells. Margulis proposed that the origin of eukaryotes was related to survival in the new oxygen-containing atmosphere, where an aerobic microbe, the protomitochondrion, was ingested into the cytoplasm of a heterotrophic

anaerobe, and the resultant endosymbiosis became obligate (Margulis, 1970). Over a billion years of evolution, many functions of the assimilated aerobic prokaryotic cell were lost to the host-cell, leading to a progressive loss of independence. The ingested prokaryote has been proposed to be purple nonsulfur bacteria, as the 31 most conserved mitochondrial gene groups are more closely aligned with *Rhodospirillum rubrum* than any heterotroph (Esser *et al.*, 2004; Cavalier-Smith, 2006). Evidence of such an endosymbiotic event can be observed in the presence of cardiolipin and porins in the IMM and OMM, respectively, which can only be found in bacterial cell membranes (Mileykovskaya and Dowhan, 2009; Zeth and Thein, 2010).

1.3 The mitochondrial electron transport chain

Oxidative phosphorylation is catalysed by five membrane-bound, multi-subunit enzyme complexes, four of which form the electron transport chain (ETC) (Figure 1.3). Electrons can enter the electron transport chain through the oxidation of NADH at NADH: ubiquinone oxidoreductase (complex I; CI) and the oxidation of succinate at succinate: ubiquinone oxidoreductase (complex II; CII). Both complexes catalyse the two-electron reduction of ubiquinone (Q), a hydrophobic molecule constrained to the lipid phase, to the reduced form ubiquinol. Ubiquinol is subsequently oxidised by ubiquinol: cytochrome c oxidoreductase (complex III; CIII) and reduces cytochrome c molecules with a stoichiometry of 1:2. Cytochrome c, found in the IMS, transfers electrons to the terminal complex, cytochrome c oxidase (complex IV: CIV). Complex IV oxidises cytochrome c to reduce oxygen to water, with a stoichiometry of four reduced cytochrome c required to reduce one molecule of oxygen. The electron transfer from NADH or succinate to oxygen is energetically favourable, with a redox potential difference (ΔE) of -1.14 and -0.8 V respectively. This redox potential energy is transduced by the electron transport chain to pump protons across the IMM from the mitochondrial matrix to establish Δp. Complexes I, III, and IV pump 4, 2 and 4 protons respectively. Per NADH oxidised, 10 protons contribute to Δp, whereas 6 contribute to Δp when succinate is oxidised. The established Δp is consumed by ATP synthase (Complex V; CV) to synthesise ATP, completing oxidative phosphorylation. In mitochondrial ATP synthase, 8 protons are consumed per 3 ATP molecules synthesised, thus having a stoichiometry of 2.67 protons per ATP.

This thesis focuses on the study of the mechanism of complex I, and an overview of the other respiratory complexes will be presented in more detail in the subsections below.

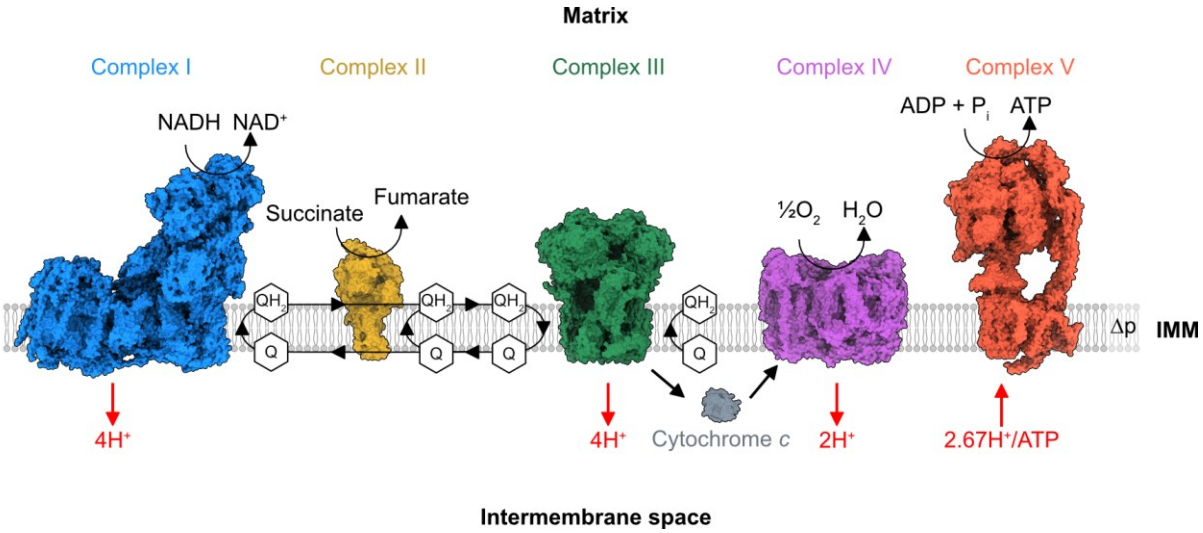

Figure 1.3. The five major complexes involved in oxidative phosphorylation in the inner mitochondrial membrane. Complex I and II reduce the ubiquinone pool through the oxidation of NADH and succinate respectively. Complex I-III are coupled through the Q-pool and complex III and IV are coupled through the membrane-associated electron carrier cytochrome c. A total of 10 protons are pumped with the oxidation of each molecule of NADH, and ATP synthase consumes this Δp to synthesise ATP with a stoichiometry of 2.67 protons per ATP. Figure adapted from (Jarman, 2022).

1.3.1 Succinate dehydrogenase (complex II)

Succinate: ubiquinone oxidoreductase (complex II) couples the oxidation of succinate to fumarate and the reduction of ubiquinone, creating a direct link between the TCA cycle and the ETC (Cecchini, 2003). The structure of the mammalian mitochondrial complex II from the porcine heart is shown in Figure 1.4. The complex consists of four subunits: SdhA and SdhB form the hydrophilic domain and contain the redox cofactors flavin adenine dinucleotide (FAD) coordinated to SdhA, and the three iron-sulphur clusters coordinated to SdhB that facilitate electron transfer. SdhC and SdhD form the membrane domain, which contains the ubiquinone binding site and a low potential cytochrome b haem cofactor (-185 mV) with no known catalytic role (Kim *et al.*, 2012). Mutants lacking the haem were not catalytically affected (Oyedotun, Sit and Lemire, 2007). All four subunits are nuclear-encoded; thus, complex II is the only ETC complex without any mitochondrially-encoded subunits.

During turnover, succinate is oxidised to fumarate by the FAD cofactor in the SdhA subunit using a hydride transfer mechanism, and the two electrons are singly passed from FADH2 down a chain of three FeS clusters in SdhB ([2Fe-2S], [4Fe-4S], and [3Fe-4S]) towards the Q-binding site in the membrane domain where bound ubiquinone is reduced to ubiquinol (Iverson, 2013). All electron transfer centres are within ~14 Å of each other, allowing fast electron transfer by tunnelling (Moser *et al.*, 2006). Due to the small differences in redox potential between succinate and ubiquinone (~0.03 V), insufficient energy is released in this redox couple for complex II to pump protons and therefore does not contribute directly to Δp across the IMM. Like most ETC complexes, complex II catalysis is reversible.

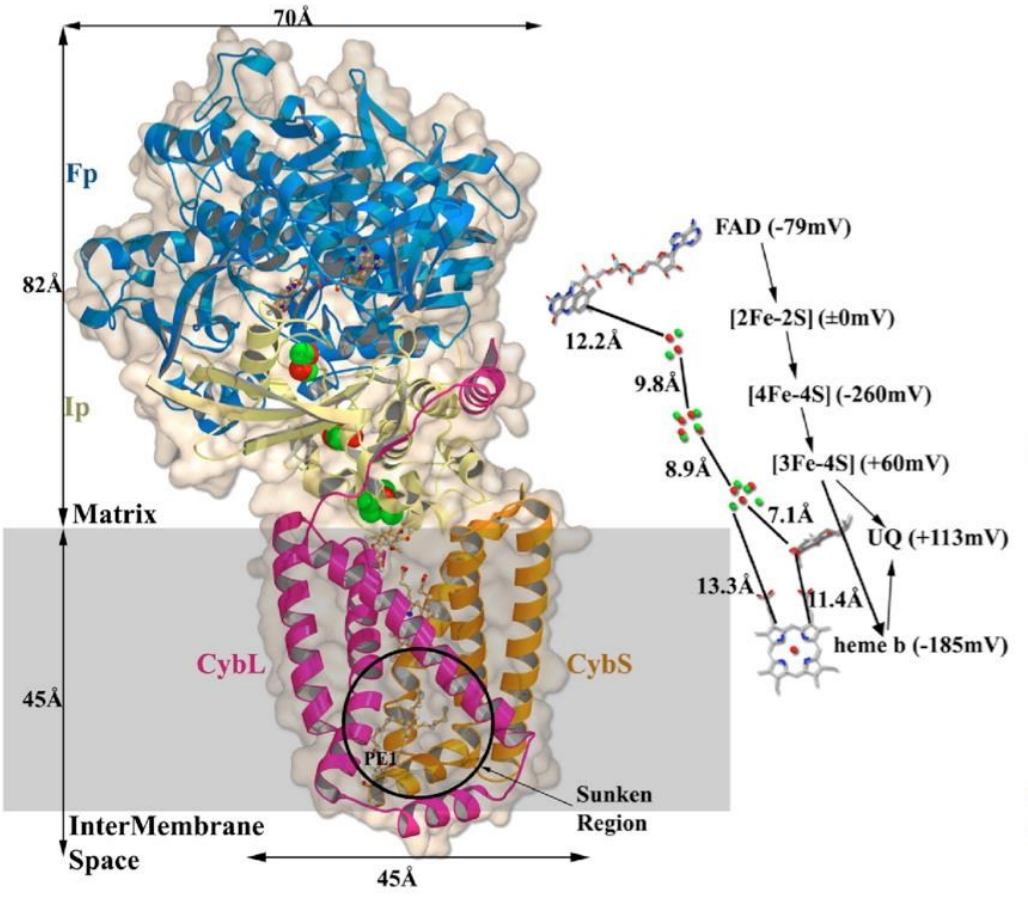

Figure 1.4. Structure of succinate dehydrogenase from porcine heart mitochondria. The Left shows the crystal structure is shown in cartoon showing the four subunits of complex II. Fp (FAD-binding protein SdhA), Ip (iron-sulphur protein, SdhB), CybL (large cytochrome *b* binding protein, SdhC) and CybS (small cytochrome b binding protein, SdhD). The right shows the cofactors constituting the electron transfer pathway and their respective redox potentials and distances. Figure adapted from (Sun *et al.*, 2005).

1.3.2 Ubiquinol: cytochrome c oxidoreductase (complex III)

Ubiquinol: cytochrome c oxidoreductase (complex III, cytochrome bc_1 complex) catalyses the two-electron oxidation of ubiquinol to reduce cytochrome c in two single-electron steps while transporting a total of four protons across the IMM in each Q-cycle (Crofts, 2004). Complex III is an oligomeric membrane protein complex and is a functional homodimer (Figure 1.5) (Guo *et al.*, 2017). The mammalian enzyme is 240 kDa and each monomer is comprised of 11 subunits (Iwata *et al.*, 1998), and three subunits contain redox cofactors: cyt b containing two b-type haems, one low ($E_{M,7}$ = -30 mV) and high ($E_{M,7}$ = +100 mV) potential haems named b_H and b_L respectively; cyt c_1 containing a c-type haem ($E_{M,7}$ = +230 mV); and the Rieske protein (Iron-sulphur protein, ISP), containing a high potential 2Fe-2S cluster, named the Rieske cluster, which is coordinated using two His and two Cys residues (Xia *et al.*, 2013). Complex III also contain two-distinct Q-binding sites, Q_o and Q_i, which face the IMS and the matrix respectively. Q_o catalyses the oxidation of QH_2 to Q, while Q_i catalyses the reduction of Q to QH_2 (Figure 1.5).

Complex III functions through a Q-cycle mechanism (Figure 1.5) (Sarewicz *et al.*, 2021). Ubiquinol binds at the Q_o site and is oxidised in a bifurcated reaction, in which the two electrons from ubiquinol are passed to different chains. The initial electron accept is the “high potential chain” comprised of the Rieske protein, cyt c_1 and cyt c. The 2Fe-2S cluster accepts the single electron, and the Rieske protein undergoes a large conformational change that positions it within electron transfer distance to the haem of cyt c1 (Yu *et al.*, 2008), which accepts the electron and transfers the electron to the mobile electron carrier protein cytochrome c. The second electron from the Q_o site is then transferred down the “low potential chain” comprised of haems b_L and b_H, reducing bound ubiquinone in Q_i on the matrix side, forming a semi-quinone intermediate. The cycle fully repeats for a second time, oxidising a second ubiquinol molecule at Q_o, reducing a second molecule of cytochrome c, and further reducing the semi-quinone intermediate at Q_i to ubiquinol. In total, two ubiquinol molecules are oxidised, and two cytochrome c and one ubiquinone molecule are reduced, transferring four protons across the IMM directly (Sarewicz *et al.*, 2021). Complex III catalysis is thermodynamically reversible.

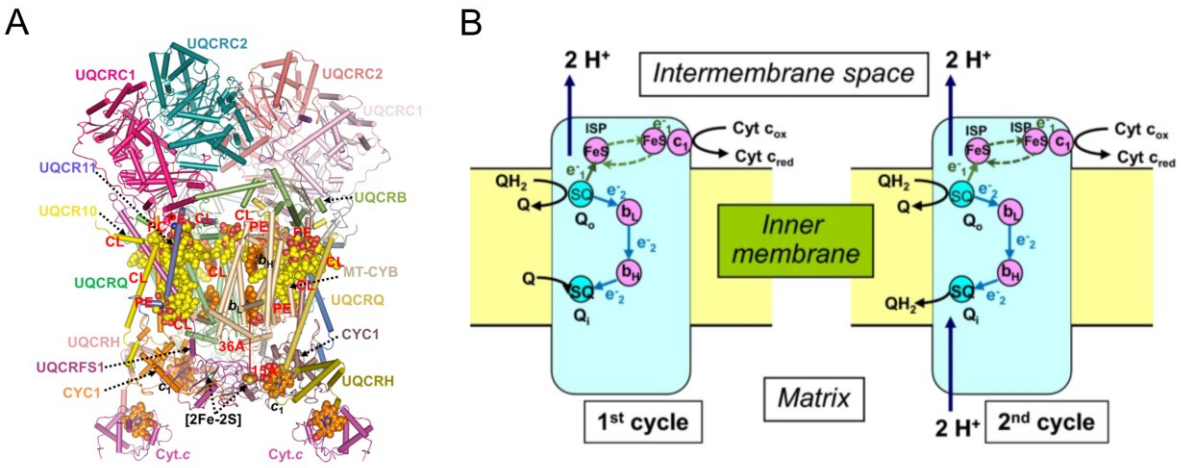

Figure 1.5. The structure of complex III from human mitochondria and the Q-cycle mechanism of QH_2 oxidation. (A) Cartoon representation of human complex III. Phospholipids and haems are shown in yellow and orange spheres, respectively. Figure taken from (Guo *et al.*, 2017). (B) The Q-cycle mechanism of complex III. The first cycle involves the oxidation of ubiquinol at Q_o, the single electron reduction of cytochrome c via the Rieske protein (ISP), and ubiquinone to semiquinone at Q_i. The second cycle oxidises a second molecule of ubiquinol to fully reduce the semiquinone at Q_i and reduces a second molecule of cytochrome C. In total four protons are translocated across the IMM. Figure taken from (Mazat, Devin and Ransac, 2020).

1.3.3 Cytochrome c oxidase (complex IV)

Cytochrome c oxidase (complex IV) is the terminal electron acceptor of the mammalian electron transport chain and catalyses the oxidation of four cytochrome c and the reduction of molecular oxygen (O_2) to two molecules of water while pumping four protons across the IMM. The mammalian complex IV has a molecular mass of approximately 200 kDa and consists of 13 subunits, three of which form the core subunits of the complex that are mitochondrially encoded. Complex IV also contains four cofactors: haem *a*, haem a_3, copper A (Cu_A), and copper B (Cu_B) (Figure 1.6A).

Complex IV reduces molecular oxygen to water through four single electron transfer steps (Figure 1.6C). During catalysis, cytochrome c binds to complex IV and Is oxidised by the binuclear copper site Cu_A. From there, the electron proceeds to haem a and then to another binuclear cluster, the active site consisting of haem a_3 and Cu_B, which reduces oxygen to water. Upon binding of molecular oxygen to the binuclear centre, oxygen undergoes a four-electron reduction that breaks the O-O bond: two electrons come from the haem a_3, one from Cu_B, and the fourth from a

conserved tyrosine residue, forming a neutral tyrosyl radical. One oxygen atom binds to the haem, forming a ferryl-species, and the other to Cu_B forming a hydroxyl group. Oxidation of cytochrome c delivers an electron to the tyrosyl radical from haem a, and a proton is taken up from the matrix to re-protonate the tyrosine. Further delivery of an electron from haem a to haem a_3 reduces the cofactor from a (+4) state to a (+3) state, and the bound oxygen is converted to a hydroxyl by uptaking a proton from the matrix. Two further electrons and protons from the matrix fully reduce the hydroxyl groups bound on haem a_3 and Cu_B to water molecules, which dissociate from the complex, reforming the enzyme in the initially reduced haem a_3 (+2) oxidation state, allowing another oxygen molecule to bind. In total, four molecules of cytochrome c are reduced, four protons are removed from the mitochondrial matrix, and a further four protons are pumped across the IMM to the IMS, contributing to Δp (Wikström and Verkhovsky, 2006; Nicholls, 2013).

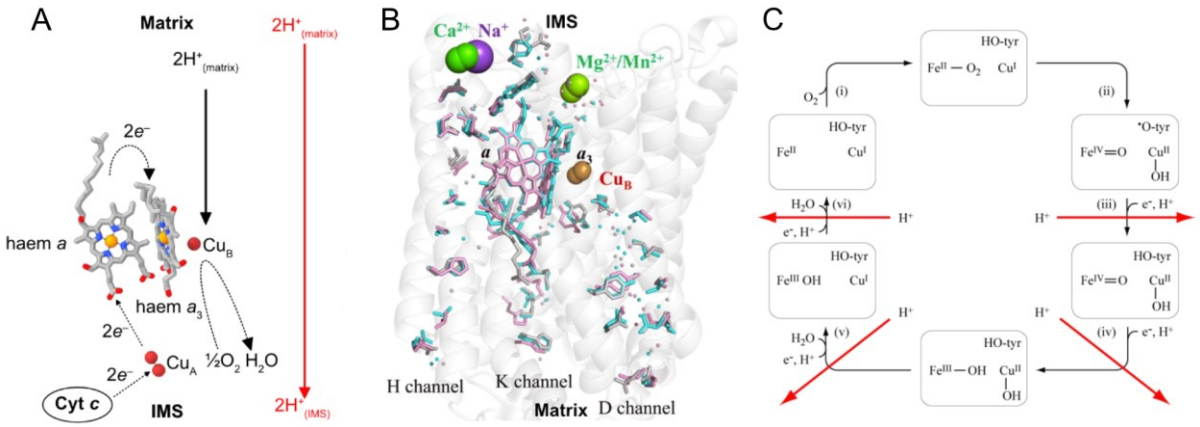

Figure 1.6. Schematic of the functional elements of complex IV and the catalytic mechanism of oxygen reduction. (A) Overview of the cofactors in complex IV and its reaction scheme. Stoichiometry is given per molecule of water released. The figure is taken from (Jarman, 2022). (B) Proposed proton channels in complex IV. H-, K-, and D- channels are highlighted in superimposed structures from the bovine heart, *P. dentifricans*, and *R. sphaeroides*. The figure is taken from (Rich and Maréchal, 2013). (C) The simplified catalytic cycle of complex IV. Proton pumping is indicated by red arrows. The complete cycle oxidises four molecules of cytochrome c and reduces one molecule of oxygen to two water molecules. Figure taken from (Martin S King, 2010).

The proton pumping pathways and the pathways by which chemical protons reduce oxygen to water are not fully understood. Currently, there are three proposed channels, the H-, K- and D-channels (Rich and Maréchal, 2013) (Figure 1.6B). The

K-channel Is proposed to be important for proton import (Iwata *et al.*, 1995). The D-pathway is proposed for both proton pumping and chemical protons based on mutagenesis data of bacterial complex IV (Konstantinov *et al.*, 1997). The third pathway, the H-pathway, is located near haem *a*, forms a connection between the matrix and the IMS, and is proposed as the proton pumping channel in vertebrates (Kamiya *et al.*, 2007). A number of "uncoupling" mutations have been made to the D-pathway in bacteria and the H-pathway in mammalian complex IV, which supposedly result in normal oxygen reduction and electron transfer but abolished proton pumping (Pfitzner *et al.*, 2000; Shimokata *et al.*, 2007; Zhu *et al.*, 2010). Such mutagenesis studies serve as a tool to understand the still unclear proton pathways.

1.3.4 F_1F_0 ATP synthase (complex V)

F_1F_0 ATP synthase (complex V) uses the potential energy with in the Δp created across the IMM to synthesise ATP from ADP and P_i. All F_1F_0 ATP synthases contain two functional domains: the hydrophilic F_1 domain and the membrane-bound F_0 domain (Figure 1.7). The F_1 domain is an assembly of three α- and three β-subunits arranged in a circular structure and is connected to the F_0 domain by a central stalk made up of the γ, δ, and ε subunits. The F_0 domain consists of the a-subunit and ring of c-subunits, which vary in oligomericity between species: in mammalian mitochondrial ATP synthase, the c-ring contains 8 subunits (Watt *et al.*, 2010), but the yeast enzyme contains 10 subunits (Symersky *et al.*, 2012), and the bacterial enzyme varies between individual species containing between 9-17 subunits (Kühlbrandt, 2019). The F_1 and F_0 subunits are also connected by another stalk, the peripheral stalk, which acts as a stator and prevents the rotation of the F_1 subunit upon the rotation of the central stalk (Dickson *et al.*, 2006). During catalysis, the c-ring and the central stalk act as the rotor, while the other subunits do not rotate.

To synthesize ATP, Δp is consumed to drive a rotary mechanism. The a-subunit in the F_0 domain contains two proton half-channels (Figure 1.7), one facing the IMS and the other facing the matrix. Protons enter the half-channel which protonate the conserved acidic aspartate or glutamate residues on the c-ring, leading to rotation as the neutralised charges move towards the more hydrophobic environment of the lipid belt. This rotational step brings another negatively charged c-subunit to be protonated by the half-channel consuming another proton, generating another rotational sub-step. These protons are carried on the exterior of the c-ring until each

c-subunit reaches the second half channel which deprotonates the aspartate or glutamate residues on each c-subunit, regenerating the enzyme. ATP synthase can rotate bi-directionally, and unidirectional rotation is sustained by the direction of Δp and its magnitude. The rotation of the c-ring drives the rotation of the central stalk, and the γ subunit interfaces with the F_1 subunit. Since the F1 subunit is held immobile by the peripheral stalk, each full rotation of the γ subunit around its axis leads to conformational changes that facilitate the binding of ADP + P_i, the phosphorylation of ADP, and the release of product ATP (Abrahams *et al.*, 1994; Cross, 2000). Catalytic and non-catalytic nucleotide binding sites are located in the β and α subunits respectively. The binding site in the β subunit undergoes three states, known as "β_{TP}" for ATP-bound, "β_{DP}" for ADP-bound, and "β_E" for empty. During ATP synthesis, clockwise rotation (when viewed from the matrix) of the γ subunit cycles the binding sites from the empty state, which allows ADP and P_i to bind, to the ADP bound state where phosphorylation occurs, to the ATP bound state where ATP is released. The non-catalytic nucleotide binding sites in the α subunit have unclear functionality, but it is suggested that the binding of nucleotides at these sites regulates ATP synthesis activity (Milgrom and Cross, 1993; Jault *et al.*, 1995). As there are three catalytic sites in the F_1 domain, for every full 360˚rotation of the c-ring, three ATP molecules are synthesised. Therefore, the stoichiometry of H^+/ATP differs between species as the c-ring oligomericity changes. E.g., In bovine mitochondria, ATP synthase has an H^+/ATP stoichiometry of 2.67, whereas in yeast, the stoichiometry is 3.3 H^+/ATP (Watt *et al.*, 2010; Symersky *et al.*, 2012). The reason for these species-specific stoichiometries is unknown but is hypothesized to be an evolutionary adaptation to different physiological environments (Kühlbrandt, 2019).

Mitochondrial ATP synthase is fully reversible and can hydrolyse ATP to pump protons across the IMM to generate a Δp. This occurs when Δp is depleted during anoxia, for example, and the enzyme works to re-established this proton gradient at the cost of ATP hydrolysis. This is not always beneficial, so organisms have evolved mechanisms to regulate ATPase activity. In mammalian mitochondria, an inhibitory protein IF_1 inserts itself at the αβγ interface to prevent anticlockwise rotation (Gledhill *et al.*, 2007). Subunits ε and ζ are proposed to act as endogenous regulators in bacterial ATPase for *E. coli* and *P. dentifricans* respectively (Kato-Yamada *et al.*,

1999; Morales-Rios *et al.*, 2015).

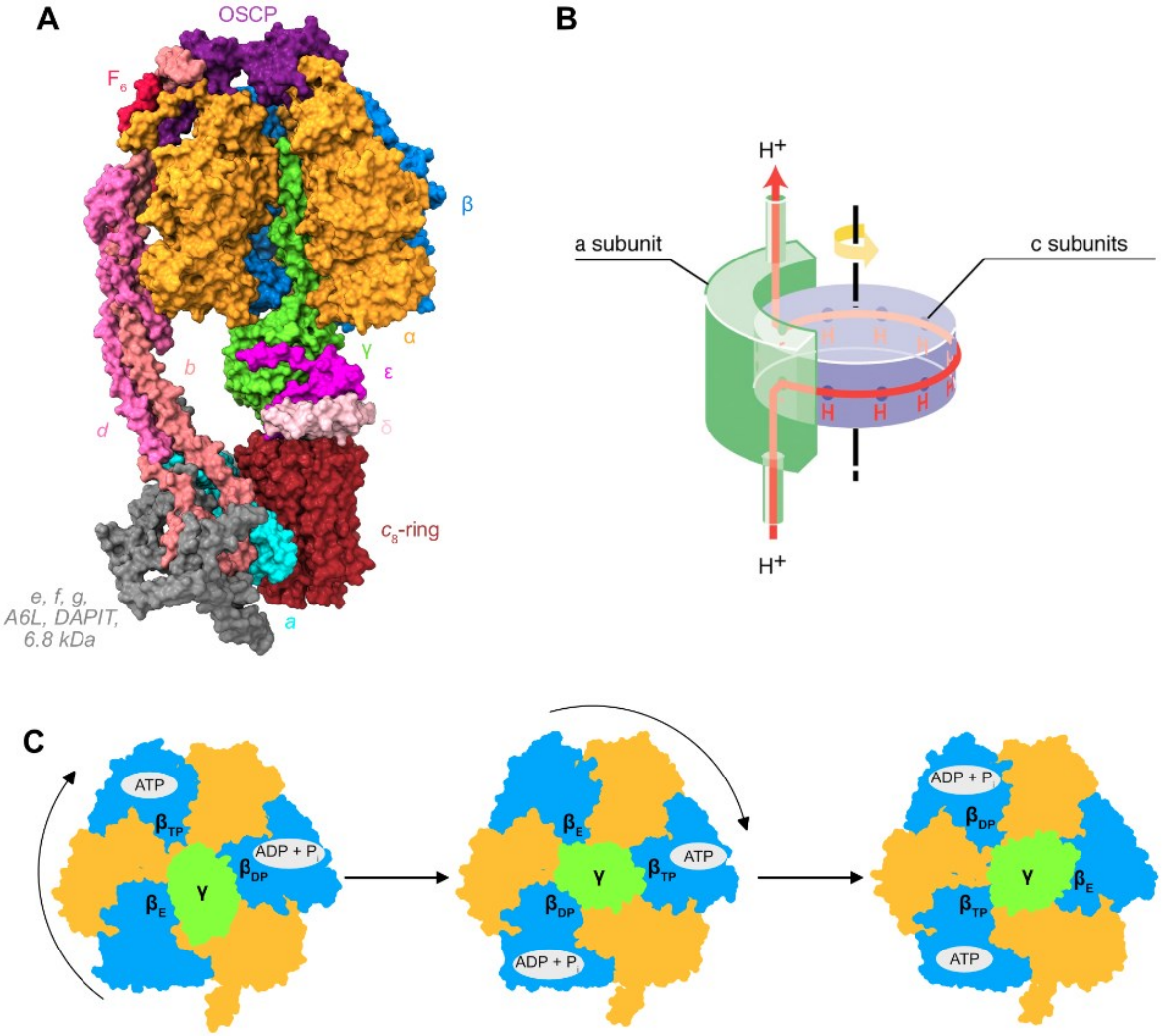

Figure 1.7. Structure and mechanism of ATP synthase. (A) Cryo-EM structure of ATP synthase monomer from bovine mitochondria. The front β subunit is removed to make visible the central stalk. Subunits are coloured and labelled. (PDB: 6ZPO) (Spikes, Montgomery and Walker, 2020). (B) Schematic of proton motive force induced c-ring rotation in the F_0 domain. The number of protons required to make a full 360˚rotation turn depends on the oligomericity of the c-ring. Figure is taken from (Walker, 2013). (C) The rotary mechanism for ATP synthesis in the F_1 domain from the perspective of the matrix. Rotation of the γ subunit induces conformational changes in the αβ subunit interface. The catalytic nucleotide binding site in the β subunits undergoes three different states: β_{TP}, β_{DP}, and β_E for the ATP bound, ADP and P_i bound, and Empty state respectively. Figure is taken from (Jarman, 2022).

1.4 NADH: ubiquinone oxidoreductase (Complex I)

Respiratory complex I (NADH: ubiquinone oxidoreductase) serves as the main entry point for electrons into the ETC. It catalyses the oxidation of NADH and the reduction of Q to QH_2 in the IMM, supplying the rest of the ETC with electrons for the eventual reduction of molecular oxygen to water. This redox energy is captured via an unknown mechanism and transduced for the vectoral pumping of four protons to build Δp across the IMM to support ATP synthesis. As the source of NADH oxidised by complex I is primarily produced by the TCA cycle and fatty acid β-oxidation, it serves a crucial metabolic function in the regeneration of the NAD^+ pool in the mitochondrial matrix (Hirst, 2013). Complex I is also an important source of reactive oxygen species (ROS) production in mitochondria (Kussmaul and Hirst, 2006; Pryde and Hirst, 2011), which contributes to retrograde redox signalling from the mitochondria to the cytosol and nucleus (Holmström and Finkel, 2014), and is the origin for a range of neuromuscular and metabolic disorders (Fassone and Rahman, 2012; Fiedorczuk and Sazanov, 2018). Complex I dysfunction has been associated with ~30% of all mitochondria-linked diseases (Mimaki *et al.*, 2012) and is targeted by anti-hyperglycaemic biguanide drugs such as metformin, phenformin and buformin (Bridges *et al.*, 2014, 2023). Although much is known about the NADH oxidation and electron transfer reaction in complex I, the mechanism by which redox energy is captured for proton pumping and the proton pumping mechanism itself is not well understood. Understanding the mechanism of complex I is important to understanding its dysfunction and may allow the development of drugs targeting complex I specifically. A detailed review of the structure and current literature of the proposed mechanism is presented here.

1.4.1 Architecture of complex I

Complex I is found in all major domains of life, in most eukaryotes (except *Saccharomyces cerevisiae* and *Schizosaccharomyces pombe*), bacteria, and archaea (Weiss *et al.*, 1991; Yagi *et al.*, 1998). In the past decade, vast progress has been made in the structural knowledge of complex I, first initiated by crystal structures of the bacterial (*Thermus thermophilus, Escherichia coli*) and yeast (*Y. lipolytica*) complexes, then later by Cryo-EM which led to a proliferation of structures for mammalian (*Bos taurus, Mus musculus, Ovis aries, Sus scrofa, Homo sapiens*), plant (*Brassica oleracea, Vigna radiata, Arabidopsis thaliana*), yeasts (*Y. lipolytica*),

ciliate (*Tetrahymena thermophilia*), and bacterial (*Escherichia. coli*) enzymes both in their isolated forms and supercomplex assemblies (Sazanov and Hinchliffe, 2006; Efremov and Sazanov, 2011; Zickermann *et al.*, 2015; Guo *et al.*, 2017; Blaza, Vinothkumar and Hirst, 2018; Fiedorczuk and Sazanov, 2018; Agip *et al.*, 2019; Soufari *et al.*, 2020; Grba and Hirst, 2020; Maldonado *et al.*, 2020; Parey *et al.*, 2021; Klusch *et al.*, 2021; Kolata and Efremov, 2021; Zhou *et al.*, 2022; Gu *et al.*, 2022).

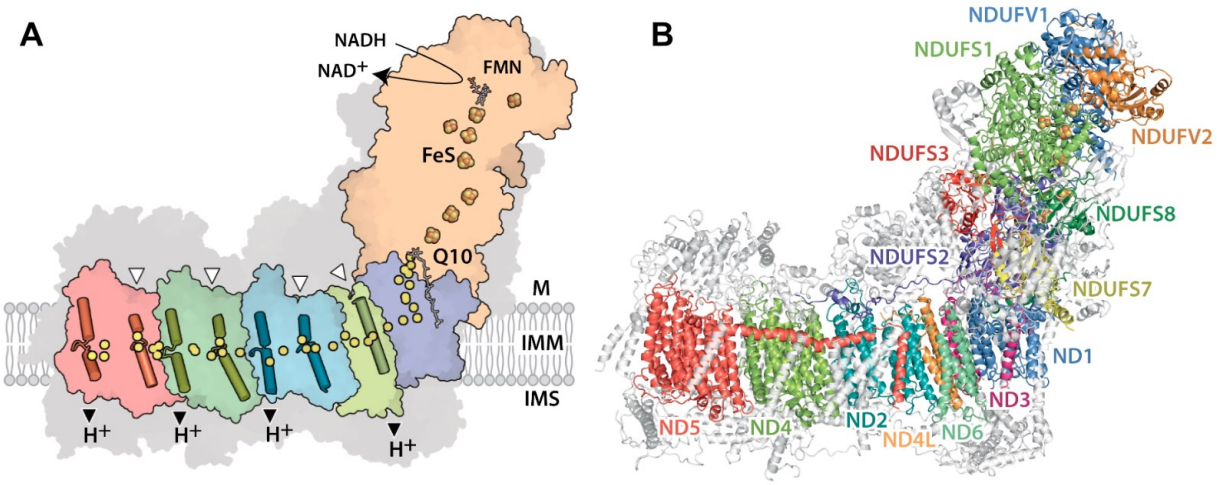

Figure 1.7. The overall architecture of complex I. (A) Schematic diagram of mitochondrial complex I with key features highlighted. Supernumerary subunits are coloured in grey; the core subunits are coloured. The hydrophilic domain is coloured in orange, the membrane arm is coloured in purple (ND1), blue (ND2), light green (ND3, ND6, ND4L), dark green (ND4), and red (ND5). NADH is oxidised at the FMN site, and electrons are passed along a chain of seven FeS clusters that connect the FMN site to the ubiquinone binding site. A fourth FeS cluster (to the right of FMN) is considered not to participate in electron transfer (Barker, Reda and Hirst, 2007). A series of charged residues lead the Q-binding site to a central hydrophilic axis along the membrane domain and are depicted as yellow circles. Conserved broken helices in the antiporter subunits are shown as cylinders. Proposed proton uptake pathways from the matrix are depicted with white arrows, and the efflux pathways to the IMS are depicted with black arrows. (B) Cartoon representation of mammalian complex I from mouse heart mitochondria (PDB: 6G2J). The 14 core subunits are highlighted with their respective labels, and the 31 supernumerary subunits are coloured in grey. Figure taken from (Agip *et al.*, 2019).

All forms of complex I form a distinctive “L” shape with two major domains: the hydrophilic peripheral arm, containing the FMN site, FeS clusters, and part of the Q-binding site, and the membrane arm imbedded in the IMM, which forms the

remainder of the Q-binding site and the proton pumping modules (**Figure 1.8**). Complex I have 14 core subunits (in *E. coli*, two subunits are fused making this number 13) that constitute the “minimal” enzyme sufficient for energy transduction. Seven of these subunits form the hydrophilic arm, encoded by nuclear DNA, and the remaining seven form the membrane arm, encoded by mtDNA (Chomyn *et al.*, 1986; Hirst *et al.*, 2003). Mitochondrial complex I in higher-order organisms contain additional supernumerary subunits: *Y. lipolytica* and *B. taurus* containing 42 and 45 subunits respectively (Hirst et al., 2003; Abdrakhmanova et al., 2004; Angerer et al., 2012), which are not considered catalytically important but may play other roles such as enzyme stabilisation, complex assembly, enzyme regulation (Hirst, 2011; Padavannil *et al.*, 2021). The large number of supernumerary subunits in mitochondrial complex I makes it the largest of the respiratory complexes, at around 1 MDa in size.

Mitochondrial respiratory chain enzymes are known to form respiratory supercomplexes, where complexes I, III, and IV are associated together. The mitochondrial “respirasome” is generally considered to have a stoichiometry of CI_1:$CIII_2$: CIV_1, but other stoichiometries that do not contain complex I or form even larger “megacomplexes” with a stoichiometry of CI_2:$CIII_2$:CIV_2 also exist (Letts, Fiedorczuk and Sazanov, 2016; Guo *et al.*, 2017; Milenkovic *et al.*, 2017). Supercomplexes may serve to channel ubiquinone and cytochrome c between the complexes, increasing local concentration and thereby offering a kinetic advantage (Bianchi *et al.*, 2004; Berndtsson *et al.*, 2020). However, other studies have suggested the contrary, based on the observation that the quinone pool accessed by complex I is accessible by other enzymes, such as alternative oxidase (Blaza *et al.*, 2014; Fedor and Hirst, 2018). Other proposals for the purpose of supercomplexes include stabilisation of assembly, decreased ROS production, regulatory roles, or prevention of protein aggregation (Blaza *et al.*, 2014; Milenkovic *et al.*, 2017).

The nomenclature for complex I subunits differ between organisms. Table 1.1 shows the standard nomenclature for the most commonly studied complex I and the species discussed in this thesis: *B. taurus, H. sapiens, Y. lipolytica, E. coli, and P. denitrificans*. Throughout this thesis, the nomenclature used will be that of the species referred.

Domain	*Bos taurus*	*H. sapiens*	*Yarrowia lipolytica*	*P. denitrificans*	*E. coli*
Hydrophilic arm	75 kDa	NDUFS1	NUAM	Nqo3	NuoG
	51 kDa	NDUFV1	NUBM	Nqo1	NuoF
	49 kDa	NDUFS2	NUCM	Nqo4	NuoD
	30 kDa	NDUFS3	NUGM	Nqo5	NuoC
	24 kDa	NDUFV2	NUHM	Nqo2	NuoE
	PSST	NDUFS7	NUKM	Nqo6	NuoB
	TYKY	NDUFS8	NUIM	Nqo9	NuoI
Hydrophobic arm	ND1	ND1	NU1M	Nqo8	NuoH
	ND2	ND2	NU2M	Nqo14	NuoN
	ND3	ND3	NU3M	Nqo7	NuoA
	ND4	ND4	NU4M	Nqo13	NuoM
	ND4L	ND4L	NULM	Nqo11	NuoK
	ND5	ND5	NU5M	Nqo12	NuoL
	ND6	ND6	NU6M	Nqo10	NuoJ
Supernumerary subunits	10 kDa	NDUFV3			
	13 kDa	NDUFS6	NUMM	PdNUMM	
	15 kDa	NDUFS5	NIPM		
	18 kDa	NDUFS4	NUYM	PdNUYM	
	39 kDa	NDUFA9	NUEM		
	42 kDa	NDUFA10			
	ACP	NDUFAB1α	ACPM		
	ACP	NDUFAB1β			
	AGGG	NDUFB2			
	ASHI	NDUFB8	NIAM		
	B8	NDUFA2	NI8M		
	B9	NDUFA3	NI9M		
	B12	NDUFB3	NB2M		
	B13	NDUFA5	NUFM		
	B14	NDUFA6	NB4M		
	B14.5a	NDUFA7	NUZM		
	B14.5b	NDUFC2	NEBM		
	B14.7	NDUFA11	NUJM		
	B15	NDUFB4	NB5M		
	B16.6	NDUFA13	NB6M		
	B17	NDUFB6	NUUM		
	B17.2	NDUFA12	N7BM	PdN7BM	
	B18	NDUFB7	NB8M		
	B22	NDUFB9	NI2M		
	ESSS	NDUFB11	NESM		
	KFYI	NDUFCI			
	MNLL	NDUFB11			
	MWFE	NDUFA1	NIMM		
	PGIV	NDUFA8	NUPM		
	PDSW	NDUFB10	NIDM		
	SGDH	NDUFB5	NUNM		
			NUXM		
			ST1		

Table 1.1. Complex I nomenclature from mammals (*B. taurus, H. Sapiens*), yeast (*Y. lipolytica*), and bacteria (*P. denitrificans, E. coli*). Table is taken from (Jarman, 2022).

1.4.2 Flavin site reaction and FeS clusters

By far, the most well-understood mechanism aspects of complex I catalysis are the oxidation of NADH and intramolecular electron transfer in the hydrophilic domain. At the tip of the hydrophilic arm, subunit FDUFV1 contains the FMN cofactor (Figure 1.8). NADH first coordinates to this site, positioned such that hydride transfer occurs between the C4 of the nicotinamide ring to position N5 of the flavin, oxidising the NADH (Berrisford and Sazanov, 2009). NADH oxidation is reversible as the redox potential of NAD+ is comparable to that of the bound FMN at pH 7.5 at -340 mV and -380 mV respectively. Bound FMN has a lower redox potential than free flavin, as oxidised FMN is bound more strongly than the reduced form (Hirst, 2013). The rate of NADH oxidation is extremely fast, and in bovine complex I is >15,000s^{-1}, which is at least an order of magnitude greater than the overall NADH:ubiquinone oxidoreduction reaction, which occurs at <1000s^{-1} (Birrell, Yakovlev and Hirst, 2009). In E. coli complex I, ultrafast freeze-quench experiments suggest that the oxidation of NADH and the dissociation of NAD^+ occur within 1 ms (Verkhovskaya *et al.*, 2008).

After the two-electron reduction of FMN, electrons are then sequentially cascaded down a chain of seven FeS clusters in the hydrophilic arm: one [2Fe-2S] and six [4Fe-4S] clusters (Hirst, 2013). A [2Fe-2S] cluster, N1a, is positioned “upstream” of FMN that does not participate in electron transfer and is proposed to be a structural anchor or an evolutionary relic in the mitochondrial enzyme (Barker, Reda and Hirst, 2007; Hirst, 2013). Instead, in the *E. coli* enzyme, this cluster has a high redox potential and is proposed to have a role in the sequestering of electron radicals from the flavin to prevent the formation of radical oxygen species (Verkhovskaya *et al.*, 2008). The FeS clusters in the hydrophilic domain are positioned within 14 Å of each other and exhibit a pattern of alternating high and low redox potentials (Baradaran *et al.*, 2013; Hirst and Roessler, 2016). The reduction potential for each FeS cluster is shown in (Figure 1.8), as determined by electron paramagnetic resonance (EPR) spectroscopy of the bovine enzyme or from estimated values where measurements are unavailable. This alternating profile may be the result of electrostatic interactions between adjacent clusters, in which the reduction of one cluster strongly disfavours the reduction of an adjacent cluster (Bridges, Bill and Hirst, 2012). It is also a common feature among biological redox chains to allow for faster electron transfer

compared to transfers between two adjacent low-potential clusters (Page *et al.*, 1999).

The terminal cluster, N2, is positioned approximately 20 Å above the membrane surface and donates electrons to ubiquinone bound in the Q-binding site. Because NADH oxidation is at least an order of magnitude faster than the NADH:ubiquinone oxidoreduction reaction and intramolecular electron transfer between the FeS chain is expected to occur within 100 µs, close to the rate of electron tunnelling (Verkhovskaya *et al.*, 2008; De Vries *et al.*, 2015), the N2 cluster can be considered "pre-loaded" with single electrons for the reduction of ubiquinone upon binding (Verkhovskaya *et al.*, 2008; De Vries *et al.*, 2015). Figure 1.8 illustrates a proposed scheme for the two-electron reduction of ubiquinone. Upon ubiquinone binding, electrons on the FeS chain reduce ubiquinone to ubiquinol. The high redox potential of the N2 cluster drags the electrons "upstream" of the chain "downstream" to reduce it, acting as an electron sink. The FeS chain then refills its electrons from the FMN, which in turn strips electrons from NADH. NAD^+ is exchanged for a new molecule of NADH, and the redox chain is poised again for the reduction of ubiquinone as ubiquinol exits from the Q-binding site.

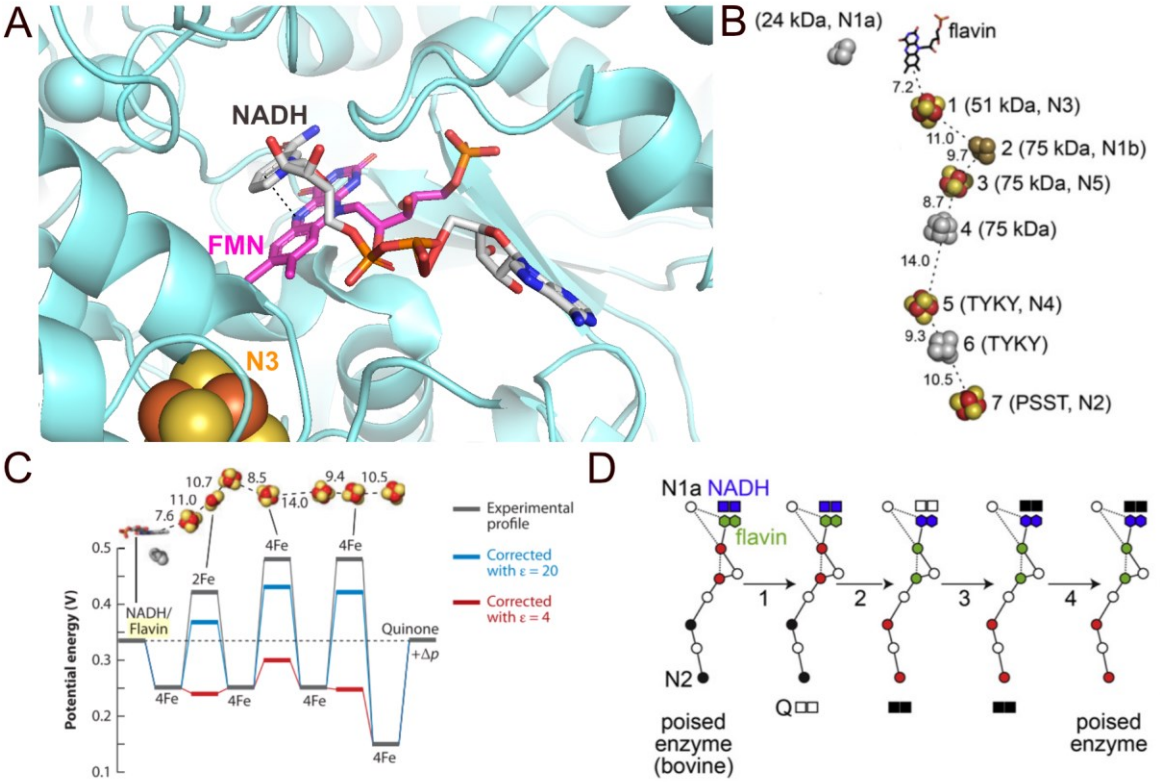

Figure 1.8. NADH binding and intramolecular electron transfer in complex I. (A) NADH (grey) binding to the FMN cofactor (magenta) in ovine complex I (PDB: 6ZKG) (Kampjut and Sazanov, 2020a). NADH forms a π-stacking interaction with the FMN via its adenine ring. Hydride transfer occurs between the C4 of the nicotinamide ring of NADH and N5 of the flavin (dashed line). (B) Chain of FeS in bovine complex I (PDB: 4UQ8). Distances between the clusters and the subunit of origin are labelled. The clusters are coloured if they are reduced by NADH (cluster 2 is partially reduced) and grey if not. Figure adapted from (Hirst and Roessler, 2016). (C) Potential energy profiles for the FeS cluster chain in complex I and simulations for electron transfer along the chain. Distances between clusters are labelled and are from the *T. thermophilus* structure (PDB: 4HEA). The experimental profiles (grey) are comprised of measured and estimated redox potentials and do not consider electrostatic effects. Large electrostatic effects (ε = 4) flatten the profile dramatically and increase the rate of electron transfer. The simulated effect of large and small electrostatic effects on the profile are shown in (red) and (blue) respectively. Figure taken from (Hirst, 2013). (D) Scheme for the two-electron reduction of ubiquinone (Q) by NADH in the bovine enzyme. Colours represent the occupation of electrons in the redox chain. A poised enzyme is ready for the binding and reduction of Q. Figure taken from (Hirst and Roessler, 2016).

1.4.3 Quinone reduction

Complex I typically use ubiquinone as an electron acceptor. Ubiquinone is a 1,4 benzoquinone and contains two methoxy groups in the 5 and 6 positions and a methyl group in the 2 position. The 3 position holds the isoprenoid tail made of repeating isoprenyl chemical subunits. In mammalian complex I, the quinone species is ubiquinone-10 (Q_{10}), but different organisms use different isoprenoid length ubiquinone as native electron acceptors in the membrane. Human, bovine, and *P. denitrificans* complex I use Q_{10}, whereas mouse complex I and *Y. lipolytica* use Q_9 (John and Whatley 1977, Lass et al. 1997; Olgun et al. 2003). *E. coli* complex I use Q_8 under aerobic conditions but can switch to menaquinone-8 under anaerobic conditions (Castro et al. 2016, Olgun et al. 2003).

The quinone-binding site (Q-site) is approximately 35 Å in length and is accessed through a narrow channel in the membrane (Tocilescu *et al.*, 2010; Baradaran *et al.*, 2013; Vinothkumar, Zhu and Hirst, 2014) (Figure 1.9). Despite the hydrophobicity of ubiquinone, the entire binding tunnel is long enough to accommodate the isoprenoid tail of ubiquinone and extends ~20 Å above the membrane surface. The quinone headgroup itself is bound at a site within 12 Å of the N2 terminal iron-sulfur cluster for efficient electron transfer (Baradaran *et al.*, 2013). NDUFS2 forms the upper section of the binding site and interacts with the headgroup and the first 3 isoprenoids of quinone, NDUFS7 forms the middle section of the binding site and interacts with the isoprenoid units of the substrate, and ND1 forms the lower cavity of the quinone binding site. There is a notable kink halfway down the Q-channel that resembles a bottleneck in the cavity and this is purported to be functionally important as it influences the reactivity of different substrates and regulates access to inhibitors (Zhu, Vinothkumar and Hirst, 2016; Fedor *et al.*, 2017; Chung *et al.*, 2021). This site is also proposed to be a secondary Q-head group binding site for native ubiquinone, as well as a key second site for the binding of rotenone and piericidin A (Warnau *et al.*, 2018; Hoias Teixeira and Menegon Arantes, 2019; Bridges *et al.*, 2020).

Interestingly, the Q-binding channel is hydrophobic at both ends and hydrophilic in the kink region, populated by charged and polar residues (Figure 1.9). These residues form the start of the E-channel that connects the ubiquinone channel to the proton-pumping machinery and is suggested to be involved in the transmission of energy released upon the reduction of quinone to proton pumping (Baradaran *et al.*,

2013; Zickermann *et al.*, 2015; Zhu, Vinothkumar and Hirst, 2016; Agip *et al.*, 2019; Di Luca and Kaila, 2021; Kaila, 2021). Short-chain ubiquinone analogues elicit the same proton-pumping stoichiometry as long-chain ubiquinone; thus, energy transduction is likely linked with the movement/ reactivity of the redox head-group (Galkin, Grivennikova and Vinogradov, 1999; Jones *et al.*, 2017).

Ubiquinone is reduced by the N2 cluster in two sequential one-electron reduction steps, forming a semi-quinone intermediate during turnover. Whether this semiquinone is long-lived and stable enough to play a role in the energy coupling mechanism is unclear. EPR spectroscopic signals have been attributed to a semiquinone species in complex I turnover samples in sub-mitochondrial particles (SMPs) (Magnitsky *et al.*, 2002; Yano *et al.*, 2005) and in proteoliposomes (Narayanan *et al.*, 2015), however the assignment has so far been ambiguous, with spectroscopic signals potentially convoluted between semiquinone formation in complex I, and in other respiratory enzymes (Wright *et al.*, 2020). The absence of UV-visible absorbance signals of the semiquinone suggests that the semiquinone present is unlikely to be a long-lived intermediate (Verkhovsky, Bloch and Verkhovskaya, 2012; Hirst and Roessler, 2016).

The complete reduction of the ubiquinone also requires two protonation events. Crystal structures and computational simulations suggest that the residues H59 and Y108 in NDUFS2 (mammalian numbering) form hydrogen bonding with the quinone headgroup carbonyls in the fully-bound state and are the most likely proton donors and are supported by mutagenesis studies (Tocilescu, Fendel, *et al.*, 2010; Tocilescu, Zickermann, *et al.*, 2010; Sharma *et al.*, 2015; Gamiz-Hernandez *et al.*, 2017; Warnau *et al.*, 2018; Gutiérrez-Fernández *et al.*, 2020; Kampjut and Sazanov, 2020b; Parey *et al.*, 2021). Various proton channels for the re-protonation of these residues have been proposed based on the presence of water molecules and Grotthuss-capable residues shown in high-resolution structures and mutagenesis studies. A chain of waters and charged residues in the NDUFS2 subunit from Y. lipolytica complex I observed in high-resolution Cryo-EM structures are conserved with the structurally homologous subunit from NiFe hydrogenase in *Desulfovibrio vulgaris*, and is suggested to be a potential re-protonation channel taking protons from the matrix side (Grba and Hirst, 2020). This channel is further investigated in chapter 5 of this thesis. Other re-protonation pathways have also been suggested originating

from the ND4L subunit (Kampjut and Sazanov, 2020a) and from a supernumerary subunit NDUFA6 in *Y. lipolytica* (Yoga *et al.*, 2020), connecting the matrix face with the ubiquinone binding site. As of yet, there is little consensus on the re-protonation mechanism of complex I.

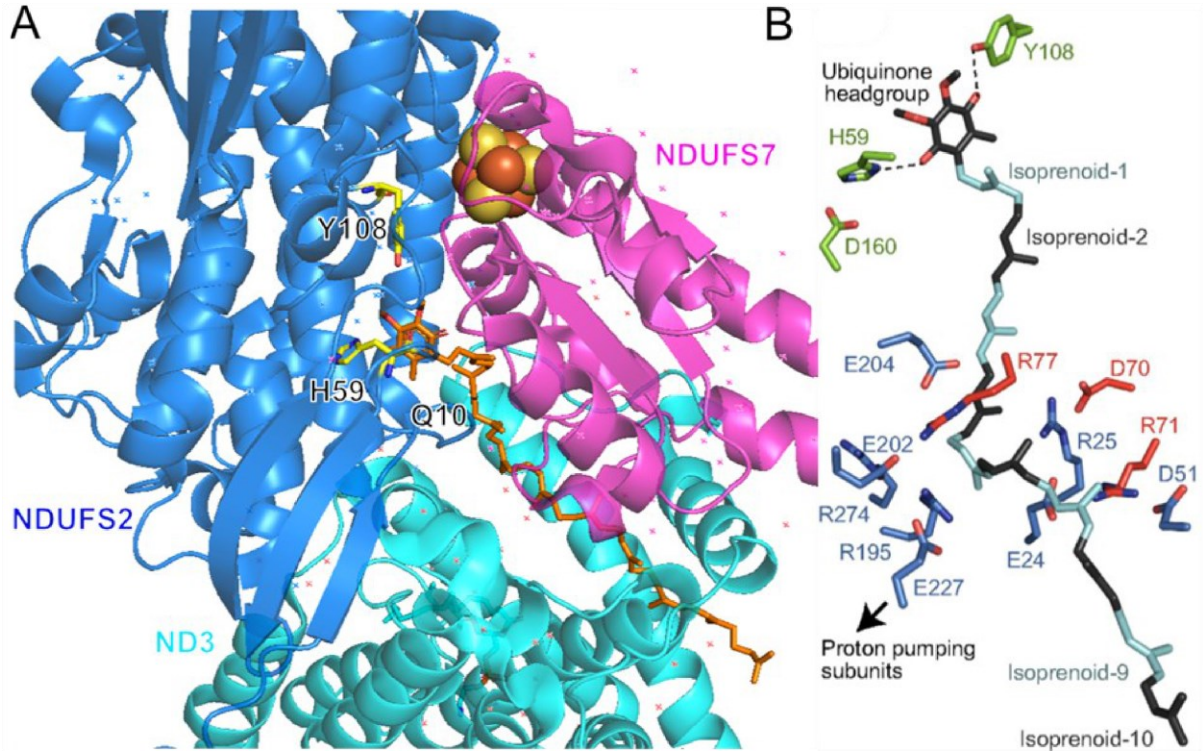

Figure 1.9. The Q-binding site in complex I. (A) Ubiquinone-10 bound Q-binding site in the active state of bovine complex I reconstituted in phospholipid nanodiscs (PDB: 7QSK) (Chung, Wright, *et al.*, 2022). (B) Q_{10} docked in bovine complex I. Charged residues within 5 Å of the Q10 are highlighted. The “kink” region is positioned approximately half-way down the channel and surrounded by charged residues coloured in blue and red. Figure adapted from (Fedor *et al.*, 2017).

1.4.4 Proton pumping

The pumping of four protons across the IMM by complex I occur in the membrane domain that contains the four putative proton translocation modules. The exact pathways and channels involved in proton pumping are not clear but are currently hypothesized based on structural and simulation studies. Three protons are expected to be pumped by the three core homologous antiporter-like subunits (ALS) in the membrane domain, ND2, ND4, and ND5, which are related to other membrane-bound antiporters such as NiFe hydrogenase (MBH), membrane-bound

sulphur reductases (MBS) and multiple resistance and pH (Mrp)-type Na^+/H^+ antiporter complexes (Fearnley and Walker, 1992; Yu *et al.*, 2018, 2020; Steiner and Sazanov, 2020). The fourth putative module is less defined and is predicted to be comprised of subunits ND1, ND3, ND4L, and ND6, based on structural analysis and hydration simulations performed on the *Thermus thermophilus* complex I structure (Baradaran *et al.*, 2013; Di Luca, Gamiz-Hernandez and Kaila, 2017; Jones *et al.*, 2017).

Each of these antiporter-like subunits possesses two half-channels related by pseudo symmetry with two discontinuous transmembrane helices (TMH 7 and TMH 12) (Figure 1.10). Hydration simulations proposed that matrix water enters at broken helix positions TMH7b, at conserved leucine and phenylalanine residues hypothesised to gate subunit hydration (Di Luca, Gamiz-Hernandez and Kaila, 2017; Di Luca *et al.*, 2018; Röpke *et al.*, 2020; Parey *et al.*, 2021). The proton exit sites on the IMS side for these antiporter-like subunits are less clear, with even extensively hydrated Cryo-EM structures showing that only ND5 clearly demonstrate a well-hydrated cavity exposed to the IMS that is proposed to be the proton-ejection site (Grba and Hirst, 2020; Kampjut and Sazanov, 2020a; Parey *et al.*, 2021; Gu *et al.*, 2022; Kravchuk *et al.*, 2022) (Figure 1.10). Thus, it is possible that all four protons are ejected at the distal end of ND5 despite the importation of such protons being from different channels. Yet this has yet to be sufficiently substantiated and has been challenged by functional data (Dröse, Galkin and Brandt, 2005).

Connecting the Q-binding site to the proton pumping modules is the E-channel, made up of conserved charged glutamate, arginine residues and water molecules proposed to be important in coupling the energy from electron transfer to proton pumping. The E-channel connects to a hydrophilic axis spanning the entire ~200 Å length of the membrane domain. The “central axis” is made up of conserved water molecules and hydrophilic residues that connect all four putative proton pumping modules (Figure 1.10). First identified in early bacterial structures and later in hydrated cryo-EM structures of complex I, these charged titratable residues are conserved and contain a glutamate-lysine pair at each subunit interface, a “central” lysine, and a “terminal” lysine or glutamate residue that are bridged by histidine (Efremov and Sazanov, 2011; Baradaran *et al.*, 2013; Di Luca, Gamiz-Hernandez

and Kaila, 2017; Di Luca *et al.*, 2018). These residues are considered to be crucial in energy and charge propagation between the proton pumping modules, and waters buried within the membrane domain support a Grotthuss-type proton transfer mechanism (Kaila, 2021). The role of these residues is further explored in Chapter 4 of this thesis.

Another feature of the membrane domain is the transverse α-helix of the terminal ND5 subunit, which spans the three antiporter subunits. Previous hypotheses have suggested that this helix acts as a piston to drive proton translocation and synchronise the pumps with each other like a locomotive (Efremov and Sazanov, 2011). However, mutation and crosslinking studies have argued against this proposal, showing that the helix may serve a structural role in clamping the membrane domain together for stability rather than a mechanistic role important for controlling proton pumping stoichiometry (Belevich *et al.*, 2011; Steimle *et al.*, 2012; Zhu and Vik, 2015; Jarman and Hirst, 2022).

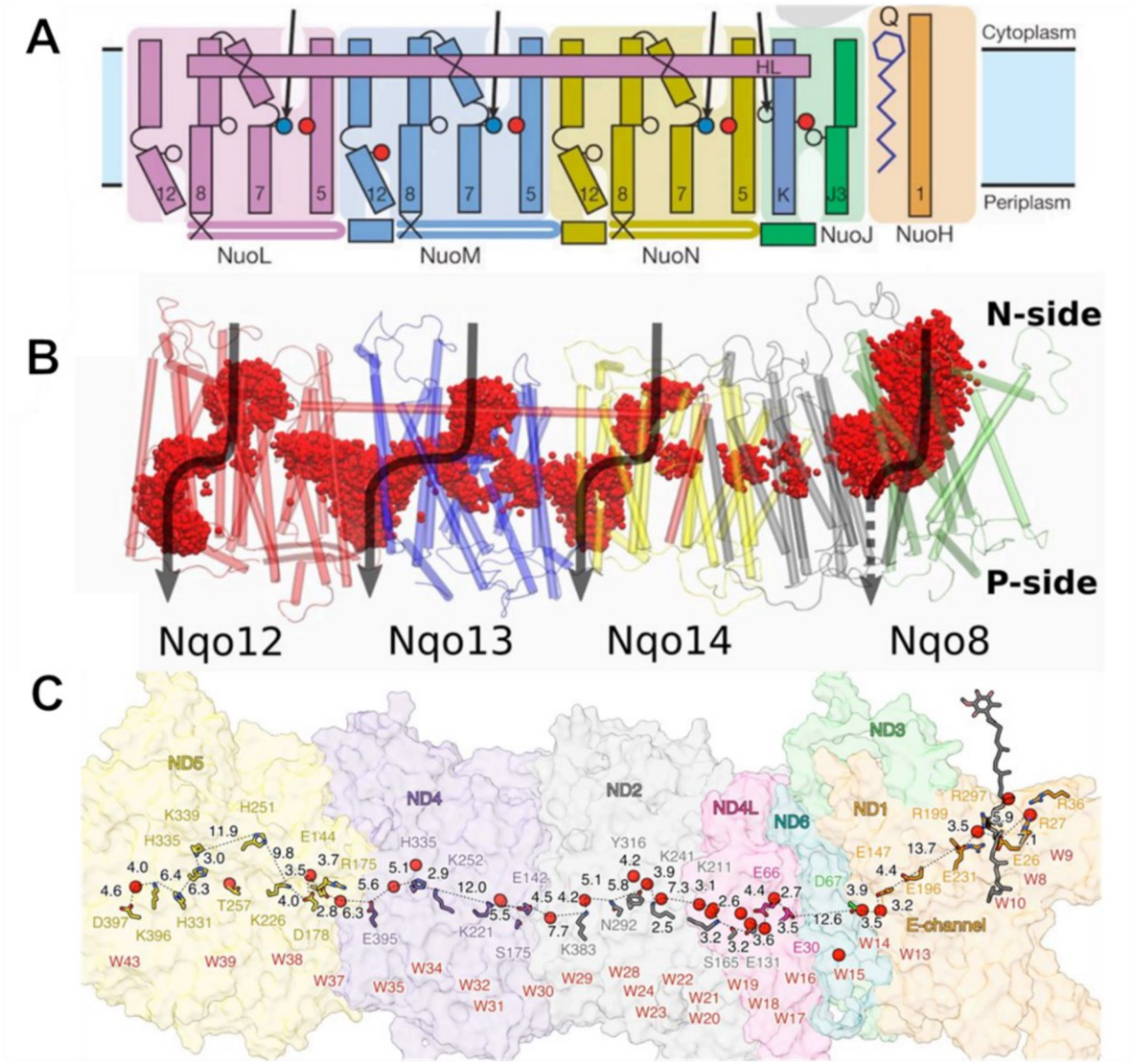

Figure 1.10. Membrane domain of complex I. (A) Schematic of the membrane domain of complex I. Key helices and residues are depicted as bars and circles, respectively. The antiporter subunits ND2, ND4, and ND5 are shown alongside a fourth putative channel comprised of ND1, ND6, and ND4L. Figure adapted from (Efremov and Sazanov, 2011). (B) Simulated water channels in the membrane domain of *T. thermophilus* complex I. The four putative proton channels are indicated by black arrows. Figure adapted from (Di Luca, Gamiz-Hernandez and Kaila, 2017). (C) Key conserved residues of the E-channel and hydrophilic axis of the membrane domain are shown as sticks in the membrane domain of *Y. lipolytica* complex I. Waters resolved by Cryo-EM are shown in spheres. The residues in the central axis and E-channel connect the putative proton pumping modules to the Q-binding site. Figure is taken from (Grba and Hirst, 2020).

1.4.5 Reverse electron transfer in complex I

Mitochondrial complex I is a thermodynamically reversible enzyme that can catalyse the forward (NADH:Q_{10} oxidoreduction) and the reverse (Δp-driven $Q_{10}H_2$:NAD^+ oxidoreduction) reactions. The forward reaction is known as forward electron transfer (FET) and pumps four protons across the IMM to the IMS. In the reverse reaction, reverse electron transfer (RET) consumes the Δp, and four protons move in reverse from the IMS to the matrix side. The reverse reaction is made possible because complex I operate close to the thermodynamic equilibrium, and so the direction of electron transfer can be reversed when the Δp is high and/or the Q-pool is reduced and/or the NADH pool Is oxidised. RET can then occur favourably when the proton transfer free energy (4 Δp) is greater than the redox potential free energy of the two-electron NADH oxidation/ ubiquinone reduction (2 ΔE_h). In other words, complex I use the potential energy across the IMM, Δp, to drive electrons from QH_2 (+80 mV) to reduce NAD+ (-320 mV) up the redox chain. FET and RET switch at the point of balance when the two energies are equal, establishing complex I as thermodynamically efficient and that minimal energy is lost in the coupling of electron transfer to proton pumping (Pryde and Hirst, 2011; Hirst, 2013; Robb *et al.*, 2018).

During RET, a significant production of mitochondrial reactive oxygen species (ROS) is observed. This is the result of the electrons on the reduced flavin being picked up by molecular oxygen, forming superoxide $O_2^{\bullet-}$ (Kussmaul and Hirst, 2006; Pryde and Hirst, 2011). This does not ordinarily occur under FET, as the FMN site is blocked by NADH coordination and thus is not exposed to oxygen. ROS has a physiological role acting as signalling molecules in the stimulation of muscle differentiation and oxygen sensing (Lee *et al.*, 2011; Fernández-Agüera *et al.*, 2015). Importantly, complex I RET play an important role in ischaemia-reperfusion (IR) injury (Pryde and Hirst, 2011; Hirst, 2013; Chouchani *et al.*, 2014, 2016; Galkin, 2019). Ischaemia occurs when the blood supply to an organ is reduced or blocked, for example, during a heart attack or stroke, depriving the cells of the oxygen required for respiration. In such an instance, the terminal reduction step of complex IV cannot occur; thus, the Q-pool becomes predominantly reduced. Concurrently, due to the reduced Q-pool, succinate accumulates (Chouchani *et al.*, 2014). ATP is also hydrolysed by complex V to maintain the electrochemical gradient, restricting Δp dissipation (Grover *et al.*, 2004). Following reperfusion, when the oxygen supply is re-established, QH_2 is

oxidised by complex III, and electrons are transferred to reduce molecular oxygen to water at complex IV, allowing the pumping of protons to re-establish the Δp across the IMM. Accumulated succinate is then rapidly oxidised to fumarate, and thus continually reducing the Q-pool during reperfusion, favouring RET by complex I and resulting in a burst of ROS mainly in the form of superoxide, which can damage the surrounding tissue (Pryde and Hirst, 2011; Chouchani *et al.*, 2016). The development of therapeutics to inhibit the RET reaction or slow the reactivation of complex I (the deactive form of which is incapable of performing RET) may serve to prevent ischemia-reperfusion injury (Niatsetskaya *et al.*, 2012; Galkin and Moncada, 2017).

1.4.6 Active/ deactive transition of mammalian complex I

Mammalian complex I have been observed to rest in two distinct states termed the "active" and "deactive" states, first identified biochemically by Vinogradov and co-workers (Kotlyar and Vinogradov, 1990; Vinogradov, 1998) and later replicated in high-resolution cryo-EM samples (Blaza, Vinothkumar and Hirst, 2018; Agip *et al.*, 2019). Mammalian complex I can transition between the two states in a process known as the active/deactive (A/D) transition. In the absence of substrates, mammalian complex I adopts a "ready-to-catalyse" active resting state that gradually converts to the deactive state in physiological temperatures. The deactive state is reactivated to the active state by the oxidation of NADH and the binding of ubiquinone (Kotlyar and Vinogradov, 1990; Vinogradov, 1998). A feature of the deactive transition is a characteristic "lag phase" observed in NADH oxidation traces of SMPs and membranes, a process which is slowed by the addition of divalent cations and elevated pH (Blaza, Vinothkumar and Hirst, 2018). The deactive state can be differentiated biochemically by sensitivity to N-ethylmaleimide (NEM). NEM covalently modifies solvent-exposed cysteine residues in proteins and derivatizes $Cys39^{ND3}$ on the ND3 TMH1-2 loop, which is only exposed during the deactive state. The active state is therefore insensitive to NEM, whereas the deactive state is locked and prevented from reactivation by NEM derivatisation (Galkin *et al.*, 2008).

As the deactive state is unable to catalyse the RET reaction unless it has been first reactivated by NADH (Kotlyar and Vinogradov, 1990), the A/D transition may be a physiologically relevant mechanism in the prevention of ischemia-reperfusion injury (Chouchani *et al.*, 2014, 2016; Dröse, Stepanova and Galkin, 2016; Galkin and

Moncada, 2017). The deactive state forms spontaneously upon ischemia (when the lack of oxygen prevents oxidative phosphorylation and the Q-pool is reduced) and subsequently protects against IR injury by minimising complex I mediated ROS production by RET, as it is unable to catalyse RET until it is reactivated when ubiquinone and NADH levels are replenished during reperfusion. Consistently, a single point mutation in the ND6 subunit of mouse complex I, ND6-P25L, has been shown to rapidly transition to the deactive state and is incapable of performing RET even after pre-activation by NADH (Yin *et al.*, 2021; Wright *et al.*, 2022). This mutation has been shown to be protective against IR injury *in vivo* without affecting the FET reaction (Yin *et al.*, 2021).

Structurally, the active and deactive state of mammalian complex I have been identified by cryo-EM (Zhu, Vinothkumar and Hirst, 2016; Blaza, Vinothkumar and Hirst, 2018; Agip *et al.*, 2019). The two states are differentiated structurally by global and other key markers. Globally, a twisting motion between the hydrophilic and hydrophobic arms leads to a more obtuse inter-arm angle for the deactive state. Generally, the deactive state can be recognised by disordered loops in the Q-site. The established features of the deactive state include a restricted NDUFA5/ NDUFA10 interface, a π-bulge in ND6-TMH3, a straight ND1-TMH4, disordered loops in the Q-binding site (ND3-TMH1-2 which contain Cys39, ND1-TMH5-6, and NDUFS2-β1-β2), and an Arg77^{NDUFS7}-containing loop that points towards NDUFS2, with a neighbouring stretch of peptides in a β-strand conformation (Figure 1.11). The active state, in contrast, has an extensive NDUFA5/ NDUFA10 interface, an α-helical ND6-TMH3, a bent ND1-TMH4, well-ordered loops in the Q-binding site (ND3-TMH1-2, ND1-TMH5-6, and NDUFS2-β1-β2), and an Arg77^{NDUFS7}-containing loop that points away from NDUFS2, with a neighbouring stretch of peptides in a loop conformation (Figure 1.11) (Zhu, Vinothkumar and Hirst, 2016; Blaza, Vinothkumar and Hirst, 2018; Agip *et al.*, 2019; Grba and Hirst, 2020; Yin *et al.*, 2021).

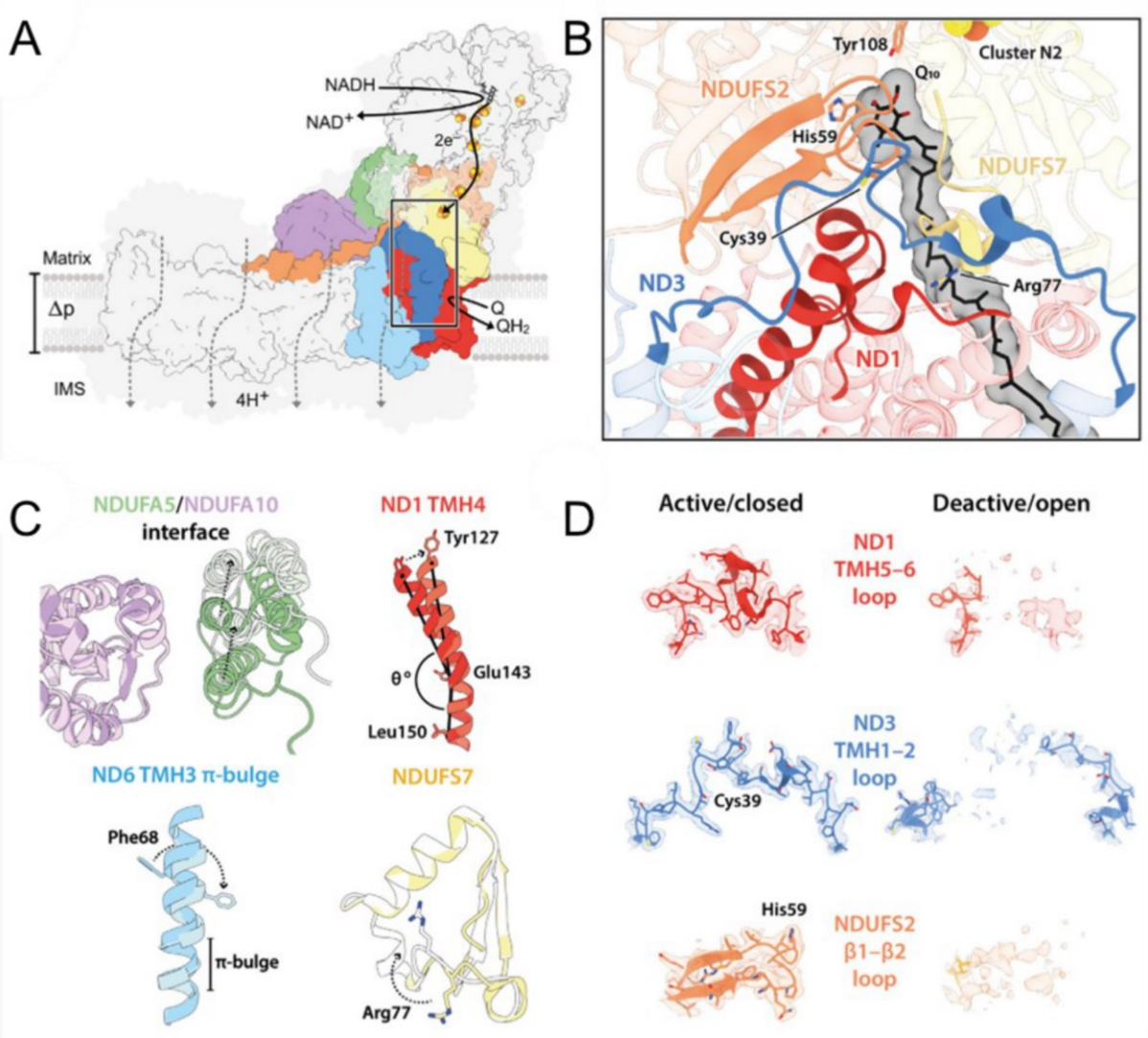

Figure 1.11. Key features of the active/deactive transition. (A) A schematic of mammalian complex I. Subunits involved in the A/D transition are coloured, and supernumerary subunits are coloured in grey. The Q-binding channel is outlined with a box, and ubiquinone binding and NADH oxidation mediate reactivation from the deactive to the active state. The dashed arrows represent proton pumping; solid arrow represents electron transfer. (B) A cartoon representation of the ubiquinone-binding channel in the active/ closed state [PDB: 7QSL (protein), 7QSK (Q_{10})]. Key loops in the active/deactive transition of the Q-site are highlighted: ND1-TMH4, ND1-TMH5-6, ND3-TMH1-2, NDUFS2-β1-β2, and NDUFS7-Arg77 loops. (C-D) Key features of the active/deactive transition modelled in cartoon (PDB: 7QSN), with the deactive state shown in lighter shades. Key residues are annotated. Figure is taken from (Chung, Grba, *et al.*, 2022).

Of considerable debate currently in the field of complex I is whether the deactive/ closed states identified by cryo-EM are off-pathway resting states or are on-cycle catalytic intermediates (Figure 1.12) (Zhu, Vinothkumar and Hirst, 2016; Blaza,

Vinothkumar and Hirst, 2018; Agip *et al.*, 2019; Kampjut and Sazanov, 2020b; Chung, Grba, *et al.*, 2022; Kravchuk *et al.*, 2022). Consequently, there is ambiguity in the nomenclature used to describe the conformational states of mammalian complex I identified by cryo-EM: “active/deactive” vs. “closed/ open”. Classified by the global angle between the hydrophilic and hydrophilic arms, the “closed” state exhibits the smallest angle and is equivalent to the “active” state, whereas the “open” state has a more obtuse angle and is equivalent to the “deactive” state.

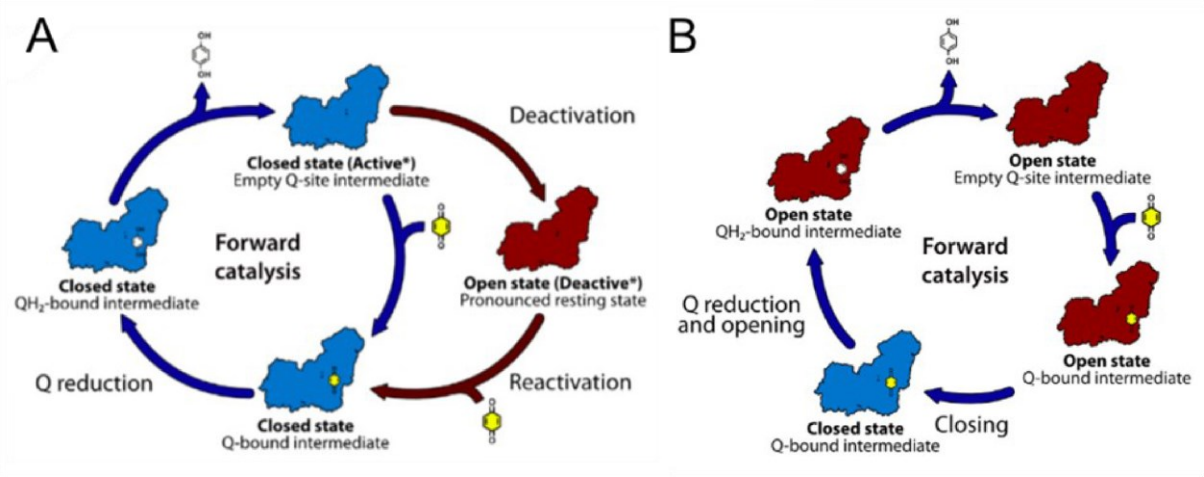

Figure 1.12. Two interpretations for the presence of open and closed states in resting preparations of mammalian complex I. (A) “Off-pathway” resting state interpretation. The active and deactive states defined initially by cryo-EM are labelled with an asterisk, which are both oxidised forms of the enzyme. (B) The “on cycle catalytic intermediates” interpretation. To avoid confusion, the off-cycle deactivation state is not depicted in b, which was described by Kampjut and Sazanov and observed only following in-vitro treatment of the purified enzyme (Kampjut and Sazanov, 2020a). Figure adapted from (Chung, Grba, *et al.*, 2022).

In the off-pathway state resting interpretation of the deactive state, built upon biochemical assays on the A/D transition (NEM labelling experiments, lag phase/ reactivation), the catalytic cycle exists only with intermediates that exhibit a globally closed/ active state. When catalysis stops due to a lack of substrate, the “resting” substrate-free enzyme gradually deactivates under physiological temperature to the deactive/ open state, which is an off-pathway state that is catalytically inactive with a partially unstructured Q-binding channel. Reactivation of the deactive state into the catalytic cycle occurs upon the addition of substrates, thus exhibiting the “lag phase” behaviour in the “on cycle” catalytic intermediates interpretation; catalysis proceeds

by a series of open and closed states. The open state is responsible for the binding/ release of ubiquinone/ ubiquinol, and the closed state is responsible for the reduction of ubiquinone. This interpretation is built upon cryo-EM studies of supposedly "turnover" complex I samples that exhibit both open and closed states. However, this interpretation is incompatible with the observation that deactive complex I and ND6-P25L cannot catalyse RET (and protect against IR injury *in-vivo*), considering the on-cycle catalytic steps must be fully reversible. This interpretation also does not explain why only mammalian complex I display a "lag phase" in SMPs and membranes if the open state is a catalytic intermediate, of which transition to the closed state must take place within the timescale of catalytic turnover of complex I.

1.4.7 Proposed coupling mechanisms for complex I catalysis

The energy-coupling mechanism between redox catalysis and proton transfer is the least understood aspect of respiratory complex I. Over the last decade, various energy-coupling mechanisms have been proposed based on detailed structural information and comparisons between enzyme states observed in "as-prepared" and apparent catalytic intermediates observed in "turnover" samples. Connecting the hydrophilic and hydrophobic domains is the "E-channel", a chain of conserved charged residues that serve as a link between the Q-binding channel "kink" region and the charged central axis of the membrane domain. All the proposed mechanisms involve the use of the E-channel as a means of signal-propagation, but the exact protonation steps and how it contributes as a coupling mechanism are unclear. Presented below are four different mechanisms recently proposed (Kampjut and Sazanov, 2020a; Kaila, 2021; Parey *et al.*, 2021; Gu *et al.*, 2022; Kravchuk *et al.*, 2022).

Long-range two-stroke electrostatic pulse mechanism

Based on molecular dynamics simulations, Kaila and coworkers describe a long-range pumping mechanism involving a forward and backward electrostatic pulse through the membrane domain (Di Luca, Gamiz-Hernandez and Kaila, 2017; Mühlbauer *et al.*, 2020; Kaila, 2021) (Figure 1.13a). Upon Q-reduction, movement of ubiquinol down the Q-channel to the second binding site provides the thermodynamic driving force for proton uptake and conformational changes at ND1, propagating charge into the membrane domain via the E-channel (Warnau *et al.*,

2018). During the forward pulse, the conserved Glu-Lys ion pairs in the antiporter-like subunits (ND2, ND4, ND5) open sequentially, favouring hydration of the half channels within each subunit, allowing the uptake of a proton from the matrix. After reaching the terminal ND5 subunit, a proton in the ND5 subunit is pumped to the IMS by ND5, and a proton is up taken from the mitochondrial matrix; the reverse wave propagates laterally towards the Q-site. This closes the ion pairs sequentially, leading to dehydration of the half channels and subsequent pumping by each antiporter subunit (ND2, ND4) and at the ND1/ND3/ND4L/ND6 interface where the fourth putative proton pumping module resides. A total of four protons are pumped across the membrane, with each proton pumping module up taking and ejecting one proton each. Ubiquinol in the second binding site is subsequently released and exchanged for ubiquinone in the membrane. The proton donors, likely Tyr-108^{NDUFS2} and His-59^{NDUFS2}, are re-protonated for the next cycle. A more detailed description of the protonation steps in the central axis and evaluation of this mechanism is discussed in chapter 4.

<u>“Domino effect” coupling mechanism</u>

Based on high-resolution structures of the mammalian (ovine) and bacterial (*E. coli*) enzymes under apparent turnover conditions, the “domino effect” mechanism is proposed by Sazanov and coworkers (Figure 1.13b). First, the binding of ubiquinone “closes” the “open” state of the enzyme (see section 1.4.6), which establishes a water wire at the E-channel linking the Q-binding channel to the central hydrophilic axis of the membrane arm. This allows the re-protonation of Tyr108^{NDUFS2} and His95^{NDUFS2} by the two E-channel residues Glu34^{ND4L} and Glu70^{ND4L} via aspartate and glutamate residues in the ND1 subunit, leaving a negative charge in the on the ND4L subunit. This triggers proton transfer from TMH8 of ND2 to offset the negative charge in the E-channel, triggering a series of protonation and re-protonation events along the chain of charged residues in the central axis. The movement of ubiquinol to the second binding site triggers the “opening” of the Q-binding site to release ubiquinol to the membrane. As a result, the two glutamate residues of ND4L are fully accessible and re-protonated from the central axis, which is blocked off from the Q-site by the π-bulge in ND6-TMH3, which formed during the “closed” to “open” transition. A total of six protons are taken up from the matrix side. Five of these enter the central axis via ND4 and ND5 subunits and are subsequently redistributed along

the central axis and E-channel on conserved lysine and glutamate residues. A sixth proton enters via the open Q cavity to re-protonate ND1. In this fully protonated state, the “dominoes fall” and protons are ejected using electrostatic “pressure” from the central axis which leads to a large decrease in pKa of TMH12 residues, forcing them to lose their protons. This redistribution means that four protons are eventually ejected to the IMS in three back-and-forth “waves”, releasing protons first stored on ND5, then ND4/ ND2, all at a terminal lysine of $TMH12^{ND5}$ and resetting the system. This mechanism proposes that all protons are released through ND5 and are imported from ND4 and ND2 based on the observation that only the ND5 subunit is hydrated in cryo-EM studies (Kampjut and Sazanov, 2020a; Kravchuk *et al.*, 2022; Sazanov, 2023). A more detailed description of the protonation steps in the central axis and evaluation of this mechanism is discussed in Chapter 4.

Two-state stabilisation-change mechanism

Based on high-resolution cryo-EM structures of *Y. lipolytica* complex I, a different mechanistic proposal that supposes all four protons are ejected at ND5 is described by Zickermann and coworkers (Parey *et al.*, 2021) (Figure 1.13c). This mechanism requires two separate electron/proton transfer events to ubiquinone, reliant on the negative charge of the semi-quinone for proton uptake and propulsion. A key proton channel identified in the ND1 subunit was proposed to connect the N-side of the protein surface to the acidic cluster at the entrance of the E-channel, a site named the proton-loading site (PLS). First, ubiquinone binds to the primary binding site and is reduced to an anionic semi-quinone by the N2 cluster, which is linked to conformational changes in ND1 (specifically the TMH4 and TMH5-6 loop). The negative charge on anionic semi-quinone drives the uptake of a proton from the N-side to the proton loading site; the positive charge state on the PLS is neutralised by the negative charge on the anionic semi-quinone. A substrate proton then neutralises the anionic semiquinone intermediate, which triggers the release of the proton from the PLS into the E-channel. This set of events would repeat for a second time, forming ubiquinol and importing a total of two protons into the E-channel. These two protons then travel across the hydrophilic axis, and two more protons are taken from the N-side and fed into the hydrophilic axis by the three antiporter-like subunits, making a pumping stoichiometry of $4H^+/2e^-$. Protons are pushed along by electrostatic pressure from successive injections of protons into the E-channel in

subsequent catalysis until they are ejected from ND5. This model implies functional asymmetry in ND2, ND4, and ND5 during the two-electron/ proton transfer events, and the matrix side proton pathways of the antiporter-like subunits are silent in one of the two cycles. However, this mechanistic model lacks specific clarity on which antiporter-like subunit imports protons and how the protons are translocated across the central axis and eventually ejected.

Two-Q mechanism

Based on high-resolution cryo-EM structures of *Sus scrofa* complex I, a mechanism named the “two-Q” model is proposed by Yang and coworkers (Gu *et al.*, 2022) (Figure 1.13d). This model posits that an invariably bound Q_{10} molecule shuttles up and down the Q-channel, collecting electrons from N2 and then transferring them to a secondary Q_{10} bound at a site outside the channel in the mitochondrial membrane to trigger proton pumping. First, ubiquinone bound at the primary binding site close to N2 is reduced fully by two-electron transfers and proton transfers by $Tyr108^{NDUFS2}$ and $His59^{NDUFS2}$ to ubiquinol. Deprotonated $His59^{NDUFS2}$ then abstracts a proton from $Asp160^{NDUFS2}$, and ubiquinol diffuses to the secondary binding site at the channel entrance, accompanied by the importation of four protons into half channels of the membrane arm. At the secondary binding site, QH_2 transfers its electrons to the second Q_{10} bound at a site outside the channel. The two protons released by this electron transfer are taken by the E-channel, triggering an electrostatic signal that propagates across the central axis, triggering proton pumping. $Tyr108^{NDUFS2}$ and $His59^{NDUFS2}$ and the secondary Q_{10} are subsequently re-protonated by protons from the mitochondrial matrix, and the bound Q_{10} moves back up to the primary binding site. This mechanism is further discussed in Chapter 3.

All of these mechanisms are speculative and conceptually different, but all lack robust biochemical and biophysical support. As such this highlights the need for novel functional approaches to investigate the mechanism.

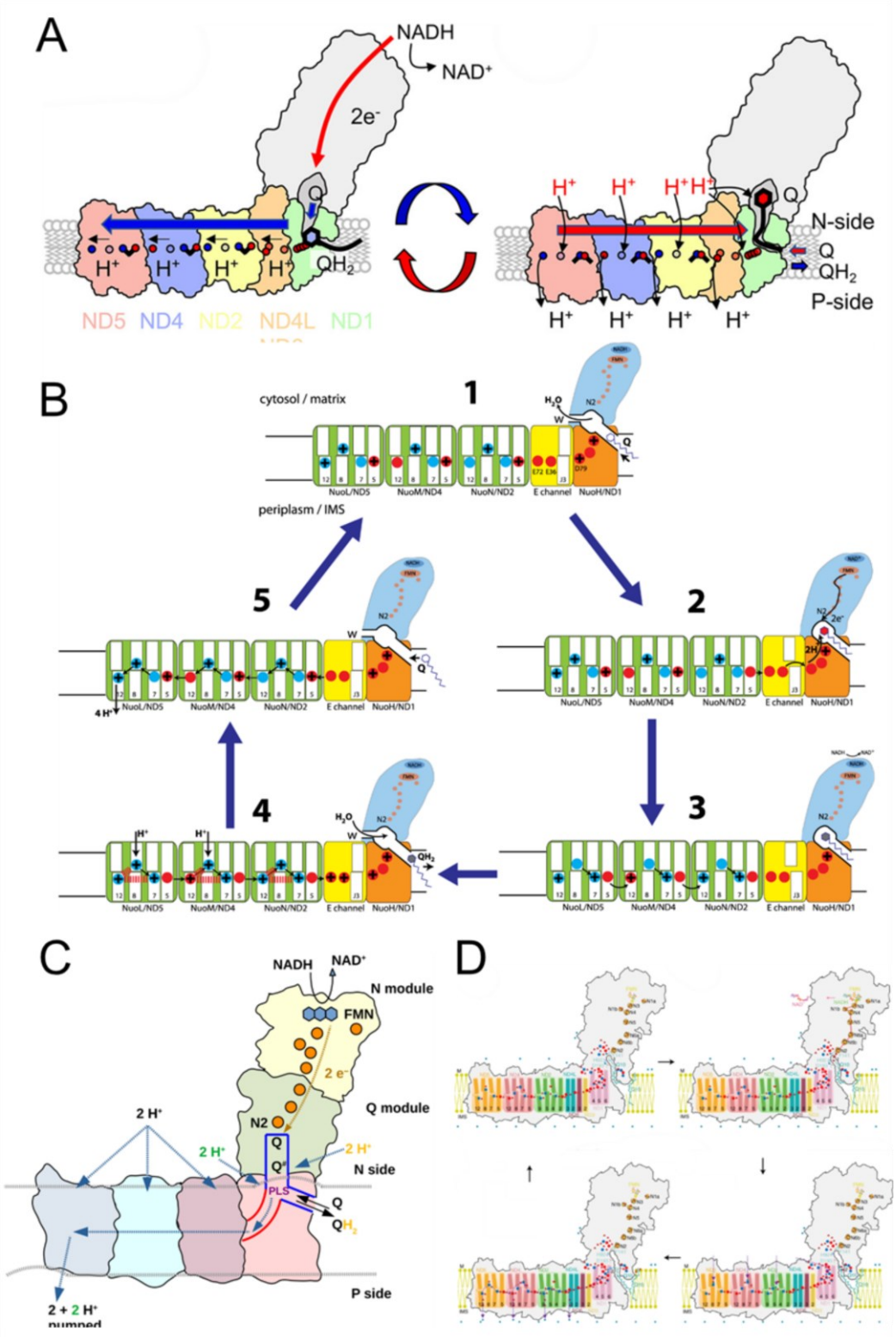

Figure 1.13. Proposed coupling mechanisms of complex I. (A) A long-range two-stroke forward and backward electrostatic pulse mechanism. (B) "Domino effect" coupling mechanism. (C) A two-state stabilisation change mechanism. (D) A two-Q mechanism. Figures panels adapted from (Kaila, 2021; Parey *et al.*, 2021; Gu *et al.*, 2022; Sazanov, 2023).

1.5 Models for respiratory complex I

Studying the mechanism of complex I requires a model system that combines structural, biochemical, and biophysical characterisation. In particular, the ability to create mutations in complex I is of great importance, as it allows the study of the underlying mechanisms of pathogenetic mutations in phenotypes and the evaluation of structurally led proposals of function. This section outlines the various model organisms used to study complex I and the main benefits and drawbacks of each.

1.5.1 Mammalian models

The mammalian enzymes from bovine (*Bos taurus*) and ovine (*Ovis aries*) mitochondria have been staples for both structural and biochemical studies of complex I, owing to the ease of obtaining a high yield of mitochondrial membranes from heart tissue. Biochemically, bovine material has been studied extensively in the form of mammalian membranes and SMPs. Mitochondrial membranes are generally prepared as fragments of the isolated mitochondrial inner membrane and do not have any coupling, as there is no distinction between an internal and external phase. Sub-mitochondrial particles (SMPs) however are outward-facing vesicle systems that are prepared by “pinching” off the cristae of isolated mitochondria by sonication. Hence they contain the entire respiratory chain of the inner membrane and are also well coupled with distinct phase separation between inside and outside the vesicle. The ETC active sites are exposed to the external phase, thus allowing specific assays of each enzyme’s activities through measuring e.g., substrate oxidation. That SMPs can sustain a Δp allows for investigation of ROS production during RET and assessment of pumping stoichiometry (Pryde and Hirst, 2011; Jones *et al.*, 2017). In addition, key studies that have used mitochondrial SMPs include the study of complex I reversibility (Pryde and Hirst, 2011), evaluation of the active/ deactive transition (Kotlyar and Vinogradov, 1990), inhibitor binding (Ino, Nishioka and Miyoshi, 2003; Chung *et al.*, 2021), and substrate channelling (Fedor and Hirst, 2018).

Aside from membranes and SMPs, the purified bovine enzyme can also be reconstituted into liposomes containing Q_{10} or other insoluble quinone analogues to be studied in a defined lipid membrane system without the complications of other proteins present in the sample. Like SMPs this system is well coupled and can retain a Δp. This system has been used to assess quinone kinetics (Fedor *et al.*, 2017; Uno

et al., 2020), complex I lipid requirements (Biner *et al.*, 2020), modes of inhibition from inhibitors and small molecules (Bridges *et al.*, 2020; Chung *et al.*, 2021), as well as RET in complex I (Wright *et al.*, 2022). Details of the SMP and proteoliposome assay system are further described in Chapter 3.

The major drawback of using a mammalian model system is the difficulty of performing mutagenesis, which is a typical and powerful way to reveal mechanistic information. Mouse models allow for some extent of genetic manipulation in nuclear genes, yet there are ethical, time, and cost concerns in generating and screening for mutations in mice, especially if they are pathogenic. In addition, the amount of purified material gained from mouse hearts is not adequate for much more than structural studies and basic characterisations of the purified enzyme, and one cannot prepare a usable amount of SMPs, limiting the scope of biochemical-based studies.

1.5.2 Yeast models

A common fungal model for studying mitochondrial complex I is from the yeast *Yarrowia lipolytica*. *Y. lipolytica* is an obligate aerobic yeast that preferentially grows using respiration and contains an electron transport chain more similar to mammals than to fermentative yeasts such as *S. cerevisiae*, which prefers ethanolic fermentation even in the presence of oxygen. Unlike the mammalian ETC*,* the electron transport chain of *Y. lipolytica* includes complex I use Q_9 instead (Djafarzadeh *et al.*, 2000). *Y. lipolytica* contains a branched respiratory chain that includes complex I, II, III, IV, and two enzymes absent in mammals, an alternative oxidase AOX and an alternative NADH dehydrogenase (NDH2). NDH2 is a single subunit NADH:ubiquinone oxidoreductase and carries out the same redox reaction as complex I but does not pump protons (Kerscher, 2000). AOX can directly oxidize ubiquinol to water bypassing both complex III and IV, thus dissipating energy.

The advantage of using *Y. lipolytica* over the mammalian model is the ability to generate mutations in the nuclear-encoded hydrophilic domain of the enzyme (but not the mitochondrially encoded ones). Knock-out strains are available for the 7-core nuclear-encoded subunits in complex I (NUAM, NUBM, NUCM, NUGM, NUHM, NUIM, and NUKM) and these subunits can be expressed using plasmids to perform site-directed mutagenesis on complex I. To generate pathogenic mutations, NDH-2 is redirected from the IMS face to the mitochondrial matrix face of the IMM, allowing

for complex I to be non-essential (Kerscher *et al.*, 2002). Chapters 3 and 5 show studies using mutation in the hydrophilic domain created using this system.

While *Y. lipolytica* complex I in the form of membranes, isolated enzymes, and reconstituted proteoliposomes have been used in biochemical studies, it has proven difficult to generate SMPs using these cells because of the tough cell wall creating sub-optimal yields. *Y. lipolytica* SMPs have also not demonstrated a capability to retain Δp, limiting the determination of complex I proton pumping stoichiometry (Lin, Puhar and Steuber, 2008). Thus, proton pumping in *Y. lipolytica* complex I is studied using proteoliposomes using semi-quantitative pH/Ψ sensitive dyes (Dröse *et al.*, 2011; Cabrera-Orefice *et al.*, 2018). Moreover, since *Y. lipolytica* complex I readily fall into the deactive state, it cannot catalyze RET (Wright *et al.*, 2022). *Y. lipolytica* is also not ideal as a disease model, as mutations that have been shown to be pathogenic in humans are not pathogenic (or expressed) in *Y. lipolytica* (Varghese *et al.*, 2015).

1.5.3 Bacterial models

Bacterial systems offer the only alternative in which mutations can be made in any complex I subunit, as all the subunits are encoded by genomic DNA. This opens the possibility of generating mutations in the core hydrophobic subunits associated with proton pumping and the E-channel associated with many proposed coupling mechanisms (see section 1.4.7). To date, most mutational studies have been carried out in the *E. coli* enzyme, where every key residue in each hydrophobic core subunit has been investigated (Kao *et al.*, 2005; Torres-Bacete *et al.*, 2007; Nakamaru-Ogiso *et al.*, 2010; Sato *et al.*, 2013). However, these studies pre-date the availability of high-resolution structures of the enzyme, limiting interpretation. Since then, high-resolution structure of the *E. coli* enzyme has been solved (Efremov and Sazanov, 2011; Kolata and Efremov, 2021; Kravchuk *et al.*, 2022; Schimpf *et al.*, 2022) and mutagenesis studies linking computational simulations, structural data, and biochemical assays have been performed (Mühlbauer *et al.*, 2020; Nuber *et al.*, 2021). However, the *E. coli* enzyme may not be a suitable model system because it uses menaquinone or ubiquinone-8 as an electron acceptor rather than ubiquinone-10 in mammals, and it has a lower sequence homology with the human enzyme than other species such as *B. taurus*, *Y. lipolytica*, and *P. denitrificans* (Kerscher *et al.*, 2002; Yip *et al.*, 2011). The redox potential difference between NADH and

menaquinone and ubiquinone (when bound in the Q-site) is 240 mV and 420 mV, respectively, which suggests that the proton pumping stoichiometry may not be identical between the two. Since *E. coli* complex I have been studied in proteoliposomes and not in inverted membrane vesicles (that result in poorly coupled vesicles), studies of RET and proton pumping stoichiometry have not been carried out (Jones *et al.*, 2017). Further, *E. coli* lacks complex III and an aa_3-type complex IV and thus cannot form respiratory supercomplexes (Anraku and Gennis, 1987).

Another bacterial model, the α-proteobacterium *P. denitrificans* emerges as a great alternative, eliminating many of the limitations of the *E. coli* system. *P. denitrificans* is a gram-negative, soil bacterium that is well adapted for aerobic and anaerobic growth on a variety of carbon sources (Baker *et al.*, 1998). To adapt to an ever-changing environment, *P. denitrificans* possesses three different aerobic routes in its ETC for passing electrons to oxygen (Van Spanning *et al.*, 1995). The first route mirrors the complexes in the ETC, whereas alternative routes include the expression of alternative ba_3 and cbb_3-type oxidases in addition to complex IV (aa_3-type oxidases) depending on the oxygen concentration in the environment (de Gier *et al.*, 1994). In addition to aerobic respiration, *P. denitrificans* can use hydrogen as an electron donor or nitrate as a terminal electron acceptor instead of oxygen (Baker *et al.*, 1998).

P. denitrificans serves as a great model system as the ETC is similar to the mammalian counterpart, containing all central components and using ubiquinone-10 as the electron acceptor. Importantly, complex I from *P. denitrificans* is more similar to human complex I when compared to *E. coli* or *T. thermophilus* (Yip *et al.*, 2011), particularly in the hydrophilic domain. Further, it also possesses a subset of supernumerary subunits, which are present in the mammalian enzyme and as part of the respiratory supercomplex (Stroh *et al.*, 2004; Yip *et al.*, 2011). Importantly, well-coupled sub-bacterial particles (SBPs) can be generated from *P. denitrificans* cells by osmolysis of the bacterial cytoplasmic membrane (Burnell, John and Whatley, 1975), allowing measurement of proton pumping stoichiometry ($4H^+/2e^-$) and RET (Kotlyar, Albracht and van Spanning, 1998). Additionally, strains of *P. denitrificans* (*Pd*-Nqo5^{His6}) containing the *E. coli* ndh2 gene have been created (Jarman *et al.*, 2021), allowing complex I to be non-essential and pathogenic mutations to be

created. Chapter 4 studies mutations in the membrane domain created with this system.

1.6 Aims

Currently, proposed mechanisms of complex I coupling lack functional substantiation and rely on purely computational or structural approaches. The main focus of this thesis is to investigate the rate limiting step of complex I catalysis through the point of view of the proton, to gain insight into its mechanism.

Chapter 3 aims to identify the rate-limiting step in the catalysis of complex I by measuring the solvent isotope, and pH effects on kinetic parameters of complex I catalysis under different conditions. These experiments aim to identify whether proton transfer steps are rate-limiting in complex I and how this rate limiting proton transfer changes with Q-binding site mutations, Q-concentration, Q-chain length, and Δp.

Chapter 4 aims to investigate the role of conserved charged residues in the central axis of subunit ND4 of the hydrophobic domain by using the *P. denitrificans* model system. Thus far, specific mechanistic information regarding proton transfers is only computationally generated. This study aims to elucidate the effect of central axis mutations on proton transfer steps during proton pumping.

Chapter 5 aims to investigate the function of a network of conserved buried charged residues proposed to form a re-protonation channel for the Q-binding site. Mutations based on this pathway are identified, generated, and characterised using the *Y. lipolytica* model system by using structural and computational led approaches.

2 Materials and Methods

2.1 Strains, plasmids, and growth media

2.1.1 Yeast and bacterial strains used

Strain	Species	Details	References/Source
NEB® 5-α	*E. coli*	*fhu*A2, Δ(*arg*F-*lac*Z)U169, *pho*A, *gln*V44, Φ80Δ(*lac*Z)M15, *gyr*A96, *rec*A1, *rel*A1, *end*A1, *thi*-1, *hsd*R17	New England BioLabs
BL21 (DE3)	*E. coli*	F^-, *ompT*, *gal*, *dcm*, hsdSB (rB^-, mB^-), (DE3)	New England BioLabs
GB10	*Y. lipolytica*	*30Htg2, MatB, ndh2i, ura3-302, leu2-270, lys-1*	Prof. Ulrich Brandt
Δnucm L1	*Y. lipolytica*	nucm::URA3, MatA, 30Htg2, ndh2i, lys11–23, ura3–302, leu2–270, xpr2–322	(Grgic *et al.*, 2004)
Δnukm L1	*Y. lipolytica*	nucm::URA3, MatA, 30Htg2, ndh2i, lys11–23, ura3–302, leu2–270, xpr2–322	(Grgic *et al.*, 2004)
nucm mutants	*Y. lipolytica*	Δnucm + nucm/ pUB26 carrying a point mutation	Andrew Jones, this work
nukm mutants	*Y. lipolytica*	Δnukm + nukm/ pUB26 carrying a point mutation	Andrew Jones
Pd1222	*P. denitrificans*	rif^R, spc^R, enhanced conjugation frequencies, m^+	(de Vries *et al.*, 1989)
***Pd*-Nqo13^{E141Q}**	*P. denitrificans*	*Pd*-Nqo5^{His6}, *nqo13*^{E141Q}	Owen Jarman
***Pd*-Nqo13^{K263Q}**	*P. denitrificans*	*Pd*-Nqo5^{His6}, *nqo13*^{K263Q}	Owen Jarman
***Pd*-Nqo13^{H320L}**	*P. denitrificans*	*Pd*-Nqo5^{His6}, *nqo13*^{H320L}	Owen Jarman
***Pd*-Nqo13^{H346Q}**	*P. denitrificans*	*Pd*-Nqo5^{His6}, *nqo13*^{H346Q}	Owen Jarman
***Pd*-Nqo13^{L242A}**	*P. denitrificans*	*Pd*-Nqo5^{His6}, *nqo13*^{L242A}	Owen Jarman

Table 2.1. All yeast and bacterial strains used in this work.

2.1.2 Plasmids used

Plasmids	Details	Reference/Source
nucm/pUB26	pBR322 *ori*V, *amp*^{R}, *hyg*^{R}	(Grgic *et al.*, 2004)
nukm/pUB26	pBR322 *ori*V, *amp*^{R}, *hyg*^{R}	(Grgic *et al.*, 2004)
pET15b	*Amp*^{R}, *lacI*, *lacO*, ColE1 *ori*, rop, N-terminal fusion for twin-strep-tag, *AOX*$^{\Delta 1\text{-}24}$	(Fedor *et al.*, 2017)

Table 2.2. All plasmids used in this work.

2.1.3 Growth Media used

Media	Composition	Quantity / L^{-1}	Reference
LB	Tryptone Yeast extract NaCl NaOH	10 g 5 g 10 g to pH 7.2	(Luria et al., 1960)
SOC	Tryptone Yeast extract NaCl KCl MgCl2 Glucose NaOH	20 g 5 g 10 mmol 2.5 mmol 10 mmol 20 mmol to pH 7.0	(Hanahan, 1983)
2x YPD	Yeast extract Peptone Glucose NaOH	20 g 40 g 40 g to pH 5.5	(Bridges *et al.*, 2009)
K broth	Tryptone Yeast extract Casamino acids KH_2PO_4 K_2PO_4 Na_3-citrate.$2H_2O$ $(NH_4)_2SO_4$	10 g 5.0 g 5.0 g 10.4 g 3.0 g 0.74 g 2.5 g	(Nihei *et al.*, 2003)

Table 2.3. All growth media used in this work.

2.2 Molecular biology

2.2.1 Mutagenesis of *Y. lipolytica* complex I

The *Y. lipolytica* deletion strain of GB10 nucm (*Δnucm*) and the pUB26 plasmid were supplied by Professor Ulrich Brandt (Kerscher *et al.*, 2002). The NUCM gene was inserted into the pUB26 plasmid by digesting both the PCR amplified gene and the pUB26 plasmid with the NheI restriction enzyme and then ligating the two fragments

together (Grgic *et al.*, 2004). The mutagenesis method here was taken from Dr Febin Varghese's work (Varghese *et al.*, 2015), which uses non-overlapping primers containing the point mutation in the forward primer and a reverse primer that is complementary to the template DNA.

KOD Xtreme™ Hot Start DNA Polymerase (Novagen) was used to perform the PCR to amplify the required DNA. PCR products were analysed on 0.7% (w/v) agarose gels with 1 µg mL^{-1} ethidium bromide. The required DNA fragment was extracted using the Monarch® gel extraction kit (New England Biolabs), and the concentration of DNA was measured using a NanoDrop™ ND-1000 Spectrophotometer (Typical DNA concentration of 5 to 10 ng μL^{-1}). The blunt-ended DNA was 5'- terminally phosphorylated and ligated using T4 DNA ligase (New England BioLabs). 50 µL of NEB® 10-β Competent *E. coli* cells (New England BioLabs) were used to transform the circularised plasmid (see section 2.2.3). The transformants were initially plated on LB-agar plates containing 100 µg mL^{-1} ampicillin (Sigma) and incubated at 37 ºC overnight. Single colonies of transformants were inoculated into 10 mL of LB medium containing 100 µg ml^{-1} ampicillin and cultured overnight at 37 ºC. The plasmid was isolated using a QIAprep Spin Miniprep Kit (Qiagen) by following the manufacturer's instructions and submitted for sanger sequencing (Genewiz).

2.2.2 Transformation of *Y. lipolytica*

Prior to transformation, the *Δnucm* strain was grown in 50 ml of 2xYPD media overnight at 27 ºC and 225 rpm. Cells were inoculated to start at an OD_{600} of 0.1 and harvested at an OD_{600} of 1.3-1.5. 2 mL of culture was centrifuged, and the pellet resuspended in 120 µL of buffer (45% (w/v) poly(ethylene glycol) 4000, 0.1 M lithium acetate at pH 6.0, 0.1 M dithiothreitol (DTT)) and incubated for 15 minutes at 30 ºC. Then, 2 ml of water was added and centrifuged. The resulting pellet was washed with water again and then 1 M sorbitol, then finally resuspended in 120 µL of 1 M sorbitol. Then, 40 µL of cells were added to an electroporation cuvette (Bio-Rad) along with 0.1 µg of DNA. The cells were pulsed with a Gene Pulser® (Bio-Rad) with the following settings: 2 mm gap – 40 µl, 1500 V, 25 µG, 200 Ω, 7500 kV/cm, 5 ms pulse length. Then 1 mL of cold 1 M sorbitol was added to the cuvette and resuspended cells were plated onto 1xYPD plates with 50 µg mL^{-1} Hygromycin B (Invitrogen) and incubated for three days. Single transformant colonies were grown in 50 mL of 2xYPD media containing 50 µg mL^{-1} Hygromycin B. Then cells were

pelleted from 3 ml of yeast culture by centrifuge and resuspended in 500 µL of TE buffer containing 40 µl of 5000 unit/ mL of lyticase (Sigma, L4025) at 30 ºC for 1 hour on a water bath to digest the cell wall. After lyticase digestion, plasmid extraction was performed using the QIAprep Spin Miniprep Kit (QIAGEN) following the manufacturer's instructions. Extracted plasmids were sent for Sanger sequencing to confirm the mutation (Genewiz).

2.2.3 Transformation of *E. coli*

NEB® 5-α Competent *E. coli* cells (New England BioLabs) were used for *E. coli* transformations. The cells were transformed by incubating 1 – 100 ng of plasmid DNA with the cell mixture, placing the mixture on ice for 30 minutes and heat-shocking the cells at exactly 42 ºC for 30 seconds in a water bath. Immediately after, the cells were placed back on ice for 5 minutes. 950 µl of SOC media was added to the mixture and then incubated at 37 ºC for 60 minutes with vigorous shaking at 250 rpm. Several serial dilutions of this mixture were done with SOC media and at each dilution, 50 to 100 µL of the mixture was spread on LB agar plates with 100 µg mL^{-1} ampicillin. The plates were incubated at 37 ºC overnight and single colonies were selected as positive transformants.

2.3 Purification of complex I from *Y. lipolytica*

2.3.1 Preparation of Y. lipolytica mitochondrial membranes

Y. lipolytica cells from frozen glycerol stocks were inoculated into 250 mL conical flasks containing 50 mL of 2xYPD media (containing 50 µg mL^{-1} of Hygromycin B) and grown overnight at 27 ºC with shaking at 225 rpm. The cells were then inoculated into a 2.5 L non-baffled conical flask containing 0.5 L media (20% capacity to support aerobic growth) at 27 ºC with shaking at 225 rpm. The cells were inoculated at an OD_{600} of 0.05 and grown until an OD_{600} of ~40 (approximately 3 days).

Large scale

The cells were harvested by centrifugation at 4500 x *g* for 15 minutes at 4 ºC and washed twice with deionised water. All subsequent steps were carried out at 4 ºC. Cells were resuspended at 500 g L^{-1} in buffer containing 20 mM Na-MOPS (pH 7.2), 400 mM sorbitol, 0.2% (w/v) bovine serum albumin (BSA), 5 mM EDTA, 2 mM benzamidine and 5 mM ε-caproic acid. Prior to cell disruption, 1 mM

phenylmethylsulphonyl (PMSF) was added to the cell suspension. Cells were disrupted by two passes through a CF2 continuous flow cell disruptor (Constant Systems) operating at 35 kpsi. The temperature of the disruption chamber was maintained at below 10 ºC using a HAAKE TC 500 temperature control unit (Thermo Scientific). The disrupted cell suspension was centrifuged at 5,000 x *g* for 15 minutes to remove unbroken cells, cell walls and cell debris. Then, the mitochondrial membranes were collected by ultracentrifugation of the supernatant at 140,000 x *g* for 45 minutes. The membranes were resuspended in buffer containing 20 mM Na-MOPS (pH 7.2), 300 mM Sorbitol, 2 mM benzamidine and 5 mM ε-caproic acid, and recentrifuged (140,000 x *g* for 45 minutes); this step was repeated twice to wash the membranes. After the final centrifugation step, the membranes were resuspended in a minimum amount of resuspension buffer (20 mM NaH_2PO_4, 150 mM NaCl, pH 7.45) and stored as 50 mL aliquots at -80 ºC.

Small scale

For high-throughput preparations of *Y. lipolytica* mitochondrial membranes, harvested cells were resuspended at 2000 g L^{-1} in buffer containing 20 mM Na-MOPS (pH 7.2), 400 mM sorbitol, 0.2% (w/v) bovine serum albumin (BSA), 5 mM EDTA, 2 mM benzamidine, 5 mM ε-caproic acid and 1 mM phenylmethylsulphonyl (PMSF). Samples were added to 2 mL reinforced homogenizer tubes (Bertin Instruments) filled 1/3rd volume with 0.5 mm glass beads. Care was taken to fill the sample to the top of the tube to remove as much air as possible. Then the samples were pre-chilled on ice for 20 minutes prior to cell disruption in a Precellys 24 Tissue homogenizer (Bertin Instruments). Samples were homogenized at 6000 rpm for 30 seconds and immediately chilled on a cooling block for 2 minutes. This step is repeated 20 times until the homogenisation time is a total of 10 minutes. Then cell lysate was extracted from the homogenizer tubes using a syringe, transferred to 2 ml Eppendorf tubes and centrifuged at 16,000 x *g* for 40 minutes at 4 ºC in a microcentrifuge. The membranes were resuspended in 20 mM Na-MOPS (pH 7.2), 2 mM benzamidine and 5 mM ε-caproic acid and centrifuged at 16,000 x *g* for 40 minutes at 4 ºC. This step is repeated twice to wash the membranes. After the final centrifugation step, the membranes were resuspended in a minimum amount of resuspension buffer (20 mM NaH_2PO_4, 150 mM NaCl, pH 7.45) and stored as 20 µL aliquots at -80 ºC.

2.3.2 Purification of *Y. lipolytica* complex I from mitochondrial membranes

The purification protocol was adapted from (Cabrera-Orefice *et al.*, 2018) and produces purified complex I free of NDH-2 contamination. A 50 mL frozen aliquot of *Y. lipolytica* mitochondrial membranes (~25-30 mg mL^{-1}) was defrosted at 4 ºC and diluted to 20 mg mL^{-1} in the same resuspension buffer. One crushed cOmplete™ EDTA-free protease inhibitor cocktail tablet (Roche) was added per 50 mL of membranes. All subsequent steps were carried out at 4 ºC. The membranes were solubilised for 30 minutes by dropwise addition of dodecyl-*β*-D-maltoside (DDM, Glycon Biochemicals) from a 10% (w/v) stock solution to a ratio of 1:1 DDM:protein. After stirring on ice for 30 minutes, the solubilised membranes were centrifuged at 120,000x *g* for 45 minutes and solid NaCl and 1 M imidazole, pH 7.5, were added to the supernatant to a final concentration of 400 mM and 50 mM, respectively. The solution was then filtered through a 0.22 µm (Millipore) syringe filter before loading onto a 10 mL nickel-Sepharose 6 Fast Flow column (GE Healthcare), pre-equilibrated with buffer A (20 mM NaH_2PO_4, pH 7.2, 400 mM NaCl, 52 mM imidazole, 0.025% (w/v) DDM). The column was washed at 2 mL min^{-1} until the absorbance at 280 nm returned to baseline and was unchanged (~100 mL), after which complex I was eluted in a single peak with 100% buffer B (20 mM NaH_2PO_4, pH 7.2, 400 mM NaCl, 140 mM imidazole, 0.025% (w/v) DDM). Complex I containing fractions were pooled and concentrated to 500 µL using an Amicon® Ultra-15 Centrifugal Filter (Millipore) with molecular weight cut-off 50K by centrifugation at 5000 x *g* for 30 minutes. The concentrated samples were injected through a 500 µL injecting loop onto a Superose 6 size-exclusion column, pre-equilibrated with buffer C (20 mM Na-MOPS, pH 7.45, 150 mM NaCl, 10% (v/v) glycerol and 0.025% DDM). The column was run at 0.25 mL min^{-1} and complex I eluted as a single peak at ~13 mL. The central 2 mL of the peak were pooled and concentrated to 250 µL as described above, and aliquots flash-frozen on dry ice and stored at -80 ºC.

2.4 Purification of complex I containing materials from bovine heart mitochondria

2.4.1 Isolation of bovine heart mitochondria

The following protocol was adapted from (Smith, 1967). All steps were carried out at 4 ºC. Hearts from freshly slain cows were transported, on ice, to a cold room. The muscle tissue was dissected from the fat and connective tissue before being

mechanically minced. 1 kg batches of the minced heart were mixed with 1.4 L of bovine mitochondria buffer (250 mM sucrose, 10 mM tris-SO_4, pH 7.8 at RT) and strained through muslin. The strained batches were mixed with 1.6 L of bovine mitochondria buffer + 0.2 mM EDTA and blended in a Waring blender on “high” for 30 seconds. The resulting homogenate was centrifuged at 2,600 x *g* for 15 minutes in an RC12-BP centrifuge. The supernatant was strained through muslin and centrifuged again at 20,400 x *g* for 27 minutes in an SLA 3000 motor (Sorvall). The pellets were resuspended in 600 mL of bovine mitochondria buffer and centrifuged again at 20,400 x *g* for 42 minutes in SLA 3000 tubes. The supernatant was discarded, and the pellets were stored in the final SLA 3000 tubes at -80 ºC. Two bovine hearts yield one ~50 g (wet weight) pellet.

2.4.2 Preparation of bovine mitochondrial membranes

The following mitochondrial membrane preparation is based on the method of Walker and co-workers (Walker, Skehel and Buchanan, 1995). All steps were carried out at 4 ºC. A ~50 g (wet weight) pellet of bovine mitochondria was thawed in the cold room overnight. Once thawed, the mitochondria were resuspended into 2 L of double distilled water (ddH_2O) and homogenised in a Waring blender on “medium” for 2 minutes. Solid KCl was added to 150 mM and the mixture homogenised again on medium for a further 3 minutes. The resulting membranes were pelleted at 13,700 x *g* for 30 minutes and subsequently resuspended in 250 mL of buffer (1 mM EDTA, 10% glycerol and 20 mM tris-HCl, pH 7.55 at 4 ºC). The membrane suspension typically had a concentration of 10 mg mL^{-1} and was stored at -80 ºC.

2.4.3 Preparation of submitochondrial particles from bovine heart mitochondria.

The following protocol was based on the protocol developed by Dr Kenneth Pryde (Pryde and Hirst, 2011). All steps were carried out at 4 ºC, and SMP preparation buffer (250 mM sucrose and 10 mM tris-SO_4, pH 7.5 at 4 ºC) was used throughout.

A ~10 g (wet weight) pellet of bovine heart mitochondria was resuspended in 40 mL of SMP buffer. The suspension was centrifuged for 12 minutes at 11,300 x *g*. Following centrifugation, the supernatants were discarded, and the pellets were homogenised in 30 mL of buffer. The pH of this suspension was raised to pH 9 for 10 minutes using 2 M Tris (not pH corrected) to cause dissociation of the endogenous

IF_1 ATPase inhibitor from ATPase (Beltrán and Franco, 2019), allowing ATP hydrolysis in later experiments. The suspension was then centrifuged for 14 minutes at 37,900 x *g*, then twice for 12 minutes each at 11,300 x *g*; the supernatant was discarded each time.

The resulting pellet was resuspended to 40 mL in SMP buffer, and solid $MgSO_4$ was added to 15 mM, and the mixture was sonicated using a large sonication horn attached to a Q700 sonicator (QSonica) for ten 15-second bursts at ~150 W with 1-minute intervals. The mixture was then centrifuged for 30 minutes at 74,700 x *g*, and the pellets were rinsed with buffer and resuspended to ~10 mg mL^{-1} for storage at -80 ºC.

2.4.4 Purification of bovine complex I from bovine mitochondrial membranes

The following purification is based on the method described by (Blaza, Vinothkumar and Hirst, 2018). All steps were carried out at 4 ºC. 30 mL of bovine mitochondrial membranes was thawed and phenylmethylsulphonyl (PMSF) was added to 0.005% prior to solubilisation. The membranes were then solubilised by dropwise addition of dodecyl-*β*-D-maltoside (DDM, Glycon Biochemicals) from a 10% (w/v) stock solution to a final concentration of 1%. After stirring on ice for 20 minutes, the mixture was clarified by centrifugation at 47,800 x *g* for 30 minutes. The solution was then filtered through a 0.22 µm (Millipore) syringe filter before loading onto a Q-Sepharose column (GE Healthcare), pre-equilibrated with buffer A (20 mM Tris-Cl, pH 7.55, 2 mM EDTA, 10% ethylene glycol, 0.2% (w/v) DDM, 0.02% azolectin (Avanti Polar Lipids, and 0.02% CHAPS (Santa Cruz Biotechnology)). The column was washed at 27.5% buffer B (buffer A with 1 M NaCl added) until the absorbance at 420 nm reached 0.025, after which complex I was eluted with 36% buffer B. Complex I containing fractions were pooled and concentrated to 500 µl using an Amicon® Ultra-15 Centrifugal Filter (Millipore) with molecular weight cut-off 50K by centrifugation at 5000 x *g* for 30 minutes. The concentrated samples were injected through a 500 µl injecting loop onto a Superose 6 size-exclusion column, pre-equilibrated with buffer C (20 mM Tris-Cl, pH 7.55, 150 mM NaCl, and 0.1% DDM). The column was run at 0.25 ml min^{-1} and complex I eluted as a single peak at ~13 mL^{-1}. The central 2 mL of the peak were pooled and concentrated to 250 µL as described above, and aliquots flash-frozen on dry ice and stored at -80 ºC.

2.5 Preparation of recombinant trypanosomal alternative oxidase (AOX)

2.5.1 Expression of AOX in *E. coli* FN102

The following protocol was adapted from (Nihei *et al.*, 2003; Jones *et al.*, 2016; Fedor *et al.*, 2017). AOX was overexpressed in a *hemA* deficient derivative of *E. coli* BL21(DE3)(FN102) from the plasmid pET15b-aox. Frozen glycerol stocks of FN102 cells were plated onto LB agar supplemented with 100 μg mL^{-1} ampicillin (Sigma-Aldrich), 50 mg L^{-1} kanamycin (Merck & Co. Inc) and 100 mg L^{-1} of 5-aminolevulinic acid (Sigma-Aldrich) and incubated for 18 hours at 37 ºC. Large colonies were used to inoculate two 50 mL aliquots in “K broth” supplemented with ampicillin (Melford Laboratories Ltd.), kanamycin, and 5-aminolevulinic acid as above.

The cultures were grown aerobically at 37 ˚C for ~3 hours (until OD_{600} reached 0.6-0.8), and the cells were collected by centrifugation. The medium was then exchanged for “K broth” supplemented with 100 mg L^{-1} ampicillin, 50 mg L^{-1} $MgSO_4$, 25 mgL^{-1} $FeSO_4$, 25 mgL^{-1} $FeCl_3$, and 0.2% (w/v) glucose; following a single wash step all the cells were resuspended into a common 5 mL aliquot. The cells were then used to inoculate eight 1 L cultures of the same supplemented medium; the cultures were incubated aerobically at 30 ˚C shaking at 190 rpm for ~6 hours (until OD_{600} reached ~0.6), 100 μM isopropyl β-D-1-thiogalactopyranoside (IPTG) was added to induce AOX expression, and the cultures were incubated aerobically at 30 ˚C with shaking at 190 rpm overnight.

2.5.2 Preparation of AOX-containing membranes

The cells were harvested by centrifugation in 2 L batches at 7000 x *g* for 15 minutes in an RC12-BP centrifuge (Sorvall). All steps from hereon were carried out at 4 ˚C. The cell pellet was resuspended to 10 g mL^{-1} in buffer (50 mM Tris-HCl (pH 7.5) and protease inhibitor cocktail tablets (Roche, 4 tablets per 200 mL), ~2.5 U mL^{-1} of benzonase and 1 mM $MgSO_4$ were added. Then, the cells were disrupted with one pass at 15 kpsi and two at 30 kpsi through a pre-cooled CF2 cell disruptor (Constant Systems). The lysate was centrifuged for 15 minutes at 8300 x *g*), with the pelleted cell debris and unbroken cells discarded. The membrane fragments were collected by centrifuging at 160,000 x *g* for 80 minutes. The membrane fraction was

resuspended to 12 mg mL^{-1} in ~20 mL in the same buffer and snap-frozen in liquid nitrogen for storage at -80 ˚C.

2.5.3 Purification of AOX

The following steps were carried out at 4 ˚C. A 20 mL membrane aliquot was thawed on ice for ~1 hour before being solubilised at ~6 mg mL^{-1} in solubilisation buffer (25 mM Tris-Cl, pH 8.0, 200 mM $MgSO_4$, 20% glycerol, 1.4% (w/v) n-octyl-glucopyranoside (Anatrace)) for 1 hour by adding the membranes dropwise to a stirring volume of solubilisation buffer. The sample was then centrifuged for 30 minutes at 165,000 x *g*.

The supernatant was filtered through a 0.22 µm (Millipore) syringe filter before loading onto an 8 mL Strep-Tactin Superflow high-capacity resin column (IBA GmbH), pre-equilibrated with strep buffer (20 mM Tris-Cl, pH 8.0 at 4 °C, 50 mM $MgSO_4$, 160 mM NaCl, and 20% (v/v) glycerol. The column was washed at 2.5 mL min^{-1} in the same buffer until A_{280} reached the baseline. AOX was eluted using strep buffer supplemented with 2.5 mM desthiobiotin (Sigma-Aldrich) and 0.042% n-dodecyl-β-D-maltopyranoside (DDM) (Anagrade, Anatrace). AOX-containing fractions were pooled, concentrated ten-fold to ~1.3 mg mL^{-1} using a 30 KDa molecular weight cut-off centrifugal filter (Amicon), and dialysed against 2 L of strep buffer supplemented with 0.0432% DDM. The final product was aliquoted and snap-frozen in liquid nitrogen for storage at -80 °C.

2.6 Preparation of co-reconstituted complex I:AOX proteoliposomes

The following preparation was adapted from (Biner *et al.*, 2020; Wright *et al.*, 2022). The same buffer (10 mM MOPS, pH 7.5, 50 mM KCl) was used throughout. A total of 10 mg of lipids was required for 1 mL of preparation. 1,2-dioleoyl-sn-glycero-3-phospho-choline (DOPC), 1,2-dioleoyl-sn-glycero-3-phospho-ethanolamine (DOPE), and 18:1 cardiolipin (CDL) in chloroform were combined in a ratio of 8:1:1. Then Q_{10} at 10 nmol mg $lipid^{-1}$ was added from a chloroform stock to the lipid mixture, and the solvent was evaporated with a continuous flow of N_2 before drying under a vacuum for >1 h.

The lipids were re-hydrated in 1 mL of proteoliposome buffer for 30 min with frequent vortexing and then sonicated on ice using a Q700 probe sonicator (QSonica)

equipped with a 1.6 mm microtip with the following settings: 60% amplitude, 2.5 min total run time (15 seconds on/ 30seconds off). The resulting liposomes have a lipid concentration of 10 mg mL^{-1} and were reconstituted by partially solubilizing the lipids with sodium cholate added to a final concentration of 0.5% for 10 minutes on ice. Complex I (50:1 (w/w) lipid to protein), alongside AOX (1:1 (w/w) complex I:AOX), was then added and the lipid mixture was incubated on ice for a further 10 min. The detergent was removed using a pre-chilled PD10 desalting column (Cytiva) pre-equilibrated with proteoliposome buffer. The sample was centrifuged at 150,000 x *g* for 1 h at 4 °C followed by resuspension in a minimal amount of proteoliposome buffer (~typically 100 µL total volume). Proteoliposomes were kept on ice or at 4 °C before use and stored at -80 °C.

To quantify complex I in proteoliposomes, the NADH:$APAD^+$ assay (section 2.9.1) was used with and without the addition of 15 µg mL^{-1} alamethicin to determine the outward facing ratio and compared to NADH:$APAD^+$ rate of 1 µg mL^{-1} of complex I quantified previously using a BCA assay (section 2.8.1).

2.7 Preparation of sub bacterial particles from *P. denitrificans*

The following protocol was adapted from (Jarman and Hirst, 2022). P. denitrificans was grown aerobically to the mid-exponential phase in 500 mL of LB media (OD_{600} ~2.5-3.0) at 30 °C with shaking at 225 rpm in 2 L flasks. For mutant variants, taurine was added to a final concentration of 10 mM to induce NDH-2 expression. Cells were then harvested by centrifugation for 10 minutes and resuspended in ~400 mL of wash buffer (10 mM Tris-SO_4, pH 7.5 at 4 ˚C, 150 mM NaCl). The resuspended material was centrifuged for a further 10 min, and pellets were resuspended in digestion buffer (10 mM Tris-SO_4, pH 7.5 at 4 ˚C, 500 mM sucrose) to an OD_{600} of 7.5. Then to digest the cell walls, lysozyme was added to a final concentration of 250 µg mL^{-1} and incubated at 4 ˚C for 1 hour (without stirring). Digested cells were pelleted after being centrifuged for 15 min and resuspended in 50 mL lysis buffer (10mM Tris-SO_4, pH 7.5 at 4 ˚C) before topping up to 450 mL with the same buffer to induce osmolysis. After 15 min, $MgSO_4$ was added to a final concentration of 5 mM along with a few flakes of bovine pancreatic DNase to reduce the viscosity of the solution. The solution was then centrifuged twice for 15 min and the pellet was discarded each time. The final supernatant was centrifuged for 1 hour, and the pellet was collected and resuspended in a small volume of kinetics buffer (10 mM Tris, pH

7.5 at 32 ˚C, 250 mM sucrose). The SBPs were aliquoted, flash-frozen in liquid nitrogen and stored at −80 ˚C.

2.8 Analytical methods

2.8.1 Protein quantification

All protein concentrations were determined by bicinchoninic acid (BCA) assay using Pierce™ BCA assay kits following the manufacturer's instructions. The assay works by measuring the absorbance increase at 562 nm that occurs when Cu^{2+} is reduced by peptide bonds to Cu^{+}, which is then chelated by BCA (Smith *et al.*, 1985). The reaction was incubated at 37 ˚C for 30 min, and the absorbance samples were quantified in a 96-well plate format and compared to BSA protein standards in the range 0-1 mg mL^{-1}. A range of dilutions for the unknown samples were prepared to fit within the range of the BSA standards.

2.8.2 SDS-PAGE analysis

This technique is based on the work of (Laemmli, 1970). NuPAGE Bis-tris mini gels (Life Technologies) were used and run at 200 V for 35 minutes in MES buffer (1 mM EDTA, 3.5 mM EDTA, 50 mM Tris, and 50 mM MES) as per the manufacturer's instructions. Loaded samples were diluted 1:1 with 2× loading buffer (0.125 M Tris-HCl, pH 6.8, 20% (v/v) glycerol, 4% (w/v) SDS, 0.005% (w/v) bromophenol blue and 0.1 M DTT) and incubated for 10 min at room temperature. Unless otherwise stated, 10 µg protein was typically loaded onto each well alongside Precision Plus Protein™ Kaleidoscope™ pre-stained protein standards. When the running time had elapsed, gels were stained with colloidal Coomassie stain (0.2% Coomassie blue, 7% acetic acid, and 50% methanol) for 15 minutes. Excess Coomassie stain was destained using a destaining solution (7% acetic acid and 20% methanol) overnight. The gel was then imaged using a Chemi-doc imager (Bio-Rad).

2.8.3 Blue Native PAGE

To visualise mitochondrial membrane complexes in *P. denitrificans* SBP samples, Blue native polyacrylamide gel electrophoresis (BN-PAGE) was performed as described by (Schägger and von Jagow, 1991). In BN-PAGE, Coomassie G250 binds to proteins conferring a negative charge without denaturing the protein, and proteins are separated by the matrix of the PAGE gel. All subsequent steps were carried out at 4 ˚C.

Typically, SBPs were solubilised at 5 mg mL^{-1} in detergent in a 2:1 ratio of DDM to protein (w/w) and incubated in a Thermomixer comfort (Eppendorf) for 30 min with continuous mixing at 700 rpm. Then, insoluble material was removed by centrifugation at 30,000 × *g* for 30 min. The solubilised protein was then diluted in 1 × NativePAGE™ sample buffer also containing Coomassie G250 at a quarter the concentration of the final detergent concentration in the diluted sample and loaded onto a NativePAGE™ Novex™ 3-12% Bis-Tris Protein Gel (Invitrogen). Typically, 40 µg of *Y. lipolytica* membranes were loaded into each well.

The outer chamber contained running buffer (50 mM Bis-Tris, pH 6.8, 50 mM Tricine), and the inner chamber contained a mixture made of 1 × running buffer and 1× cathode buffer (0.4% (w/v) Coomassie G-250). The gel was run at 80 V for 30 minutes before replacing the inner chamber buffer with a mixture of 1× running buffer and 0.1× cathode buffer and running the gel at 180 V for a further 90 hours. To visualise the protein bands, gels were stained with 0.2% (w/v) Coomassie blue, 7% (v/v) acetic acid, and 50% methanol for 15 minutes, and destained with destaining solution (7% acetic acid and 20% methanol) overnight.

In-gel complex I activity assays

In-gel NADH oxidation by complex I was detected on BN-PAGE gels following a protocol from (Varghese *et al.*, 2015). Complex I is reduced by NADH and catalyses the reduction of nitroblue tetrazolium (NBT, Sigma) into a purple precipitate. Following the separation of complex I from membrane complexes by BN-PAGE, the gel was thoroughly destained in Milli-Q water to rinse off excess Coomassie Blue G-250. Then the gel was incubated in 10 mM Tris-Cl, pH 7.5, 0.5 mg mL^{-1} NBT and 150 µM of NADH. Once the purple colour had developed on complex I bands, the gel was washed in Milli-Q water to stop the reaction.

2.8.4 DNA gel electrophoresis

DNA fragments from a PCR reaction were identified and purified using DNA gel electrophoresis. Agarose gels (BioGene Ltd) were prepared at 1% (w/v) in 1 x TBE buffer (100 mM Tris, pH 8, 100 mM boric acid, 2 mM EDTA) with a 1/25,000 dilution of SYBR™ Safe DNA gel stain (Invitrogen). DNA samples were mixed with gel loading dye (New England BioLabs) and loaded onto agarose gel wells alongside a MassRuler Express Forward DNA ladder (Thermo Scientific) to estimate the DNA

length of the fragment. Agarose gels were run at 100 V for 40 minutes and the gel was imaged on a ChemiDoc imager (Bio-Rad). When required, DNA bands were purified using a Monarch® DNA gel extraction kit (New England BioLabs) according to the manufacturer's instructions.

DNA was quantified using a NanoDrop™ ND-1000 spectrophotometer (ThermoFisher Scientific) by measuring the absorbance at 260 nm. Purity was assessed by comparing the absorbance at 260 nm to the absorbance at 280 nm. Pure DNA samples typically had a ratio of > 1.8 of 260/280.

2.8.5 Proteoliposome Q_{10} quantification

The quantification protocol was adapted from (Fedor *et al.*, 2017). To quantify the quinone present, 90 µL of HPLC-grade ethanol (Sigma-Aldrich) was added to 10 µL of proteoliposomes, and the sample was sonicated for 1 minute. The sample was then centrifuged at 16,300 × g for 10 minutes, retaining the supernatant. A total of 50 µL of supernatant was injected onto a Nucleosil 100–5C18 (Hichrom) column and run at 30 °C at 800 µL min^{-1} on an Agilent 1100 series HPLC equilibrated with 70% ethanol, 30% methanol, 0.07% $HClO_4$, and 50 mM $NaClO_4$. Concentrations were determined by comparison with known standards.

2.8.6 Proteoliposome phospholipid quantification

This protocol was adapted from (Jones *et al.*, 2016). First, 100 µl of sample or standard was pipetted into boiling tubes and mixed with 50 µl of methanol and 30 390 mM $Mg(NO_3)_2$ in ethanol. The tubes were heated over a roaring blue flame in a fume hood without boiling or bumping the samples until no further brown fumes were formed and the residue in the tubes had turned white. The tubes were left to cool for 5 minutes, and then 0.3 mL of 500 mM HCl was added to each tube. The tubes were then heated at 99 ˚C for 15 min in a heat block and marbles were placed on top of the tubes to lightly stopper them. The tubes were cooled once more and 0.7 mL of 114 mM ascorbic acid, 2.72 mM $(NH_4)_6Mo_7O_{24}$ and 400 mM H_2SO_4 were added to each tube. Then the tubes were again incubated at 37 ˚C for 1 hour with marble stoppers. 200 µL aliquots were transferred into the wells of a quartz 96-well plate, the absorbance (from reduced phosphomolybdate) was measured at 820 nm, and the phospholipid contents of the samples were determined by reference to known standards.

2.9 Kinetic measurements and spectroscopic assays

2.9.1 Complex I catalytic activity measurements

Most assays carried out in this work used a Spectramax 348 plus 96-well plate reader (Molecular devices). When kinetic measurements were required to be carried out in an anaerobic environment, an SX20 stopped-flow spectrometer (Applied Photophysics) was used as it was housed within an anaerobic glove box. Changes in absorbance of a range of spectrally active compounds were used to monitor reactions. Generally, linear regression of the raw absorbance trace (with the maximum slope used to report the rate) was used to calculate the rate of substrate consumption/ production in an assay. To measure complex I specific activity, 5 μM Piericidin A was added to inhibit complex I and measure the background rate. Typically, 5-10 μg mL^{-1} of membranes, 10-50 μg mL^{-1} of SBPs, and 0.5-1 μg mL^{-1} of outward-facing complex I proteoliposomes were added to assays. All kinetic assays were carried out at 32 ºC unless otherwise stated. Data is analysed using SoftMax Pro 7 (Molecular Devices) and GraphPad Prism 9.

NADH:O_2 oxidoreduction

Turnover of complex I was initiated by the addition of NADH, and the change in absorbance of NADH as it is oxidised to NAD^+ was monitored at 340nm, subtracted by the absorbance at 380nm (ε = 4.81 $mM^{-1}cm^{-1}$). In mitochondrial membrane assays, typically, 8 μM cytochrome C was added to maximise the rate of ubiquinol reoxidation. Alternatively, AOX can be added to reoxidise ubiquinol, usually with the concomitant inhibition of complex III and IV using Antimycin and KCN respectively.

NADH:DQ oxidoreduction

Purified complex I activity was assessed using the soluble quinone analogues decyl ubiquinone (DQ) or isoprenyl-ubiquinone (Q_1). Standard assays contained 0.5 μg mL^{-1} complex I, 200 μM NADH, 200 μM DQ/Q1, 0.15% (w/v) azolectin and 0.15% (w/v) CHAPS to provide a lipid phase for complex I. Non-complex background rates were assessed by the addition of 5 μM piericidin A.

NADH:$APAD^+$ oxidoreduction

NADH:APAD+ oxidoreduction was measured to quantify complex I in various assay systems. The change of absorbance of $APAD^+$ at 400 subtracted by absorbance at

450 nm (ε = 3.16 mM^{-1} cm^{-1}) was monitored as $APAD^+$ is reduced in the assay by the transhydrogenase reaction catalysed by complex I. NADH:$APAD^+$ oxidoreduction assays were initiated by the addition of 100 µM NADH (or dNADH) and 500 µM $APAD^+$. In all samples, 1 µM piericidin A was added to prevent Q-reductase activity and allow the transfer of electrons from the flavin site to the Q-site.

Succinate:NAD^+ oxidoreduction (RET)

Complex I RET was measured in bovine SMPs as described by (Fedor and Hirst, 2018). To drive complex I RET, the quinone pool was reduced via succinate oxidation at complex II, and a ∆p was generated by ATP hydrolysis by ATP synthase. SBPs (50 µg mL^{-1}) were added to a reaction mixture containing 10 mM succinate, 1 mM NAD^+, and 1 mM MgATP. NAD^+ reduction was monitored at 340–380 nm (ε = 4.81 mM^{-1} cm^{-1}). As AOX was added to the SMPs, the reaction was carried out in an anaerobic glove box and the reaction was monitored using an SX20 stopped-flow spectrometer (Applied Photophysics) stored inside the glove box.

2.9.2 ATP synthesis measurements

ATP production is monitored using the real-time/ continuous method. For SBPs, 12 µg mL^{-1} SBPs were assayed at room temperature in the presence of 50 µM ADP in the assay buffer contained 20 mM Tris-PO_4, pH 7.5, 5 mM $MgCl_2$, 100 µM ap5A and a 1:50 dilution of luciferase reagent (ATP Bioluminescence Assay Kit CLS-KII, Roche). The baseline luminescence (560 nm) was recorded for 30 seconds before the addition of 1 µM ATP, which was used to calibrate the luminescence. The reaction was initiated by the addition of NADH and ATP synthesis was monitored continuously by a Clariostar plus plate reader (BMG LABTECH) using a 200 µL reaction volume. ATP synthesis measurements were carried out using the initial slope.

2.9.3 ACMA fluorescence quenching

9-Amino-6-chloro-2-methoxyacridine (ACMA) fluorescence quenching can be used as a qualitative measure for membrane energisation and coupling in vesicles (Dröse, Galkin and Brandt, 2005). Upon formation of a pH gradient across the membrane, the protonated form of ACMA accumulates in the lumen, which quenches its fluorescence signal (Huang, Kopacz and Lee, 1983). The quench depth and slope are semi-quantitative and relative to the amount of membrane coupling/energisation, but also the size of the lumen. ACMA quenches in SBPs or proteoliposomes were

initiated by addition of 500 µM NADH to 50 µg mL^{-1} SBPs or 1 µg mL^{-1} of outward-facing CI in proteoliposomes stirring in a 3 ml quartz cuvette containing proteoliposome buffer (10 mM MOPS, pH 7.5 at 32 ˚C, 50 mM KCl) supplemented with 0.5 µM ACMA and 100 µM valinomycin. The ionophore valinomycin was added to convert $\Delta\Psi$ to ΔpH by moving K^+ ions in the opposite direction to pumped protons. To uncouple membranes and dissipate the ΔpH, 20 µg mL^{-1} of alamethicin was added. The ACMA fluorescence was followed in a Shimadzu RF-5301PC spectrofluorometer at 419 nm excitation wavelength and 484 nm emission wavelength with an excitation and emission bandwidth of 5 nm and 10 nm, respectively.

3 Investigating the rate-limiting step in catalysis by mitochondrial complex I

3.1 Introduction

3.1.1 Previous works examining the rate-limiting steps of complex I

A rate-limiting step is the slowest step of a chemical reaction that determines the rate at which the overall reaction proceeds, i.e., the bottleneck of the overall reaction. The identification of the rate-limiting step in complex I allows the proposal of experimentally backed catalytic mechanisms, as well as the evaluation of previously proposed mechanisms. In a chemical reaction that involves multiple steps, the rate-limiting step has the greatest activation energy. This present work investigates the rate-limiting step of complex I catalysis by looking through the point of view of the proton by conducting a combination of solvent isotope effects, pH effects, and mutation experiments. Previous work has demonstrated that the rate of NADH oxidation approaches the value for diffusion control (Birrell, Yakovlev, and Hirst, 2009), so possible rate-limiting steps include electron transfer (from flavin to N2), reduction of quinone, quinone binding/ quinol release, or proton pumping steps. An analysis of each of those steps is discussed below.

Electron transfer from FMN to N_2

Electrons transfer from reduced FMN to a chain of seven FeS clusters to deliver electrons to the ubiquinone. Electron transfer along this chain of FeS is generally considered fast and not rate-limiting (Page *et al.*, 1999). However, EPR spectroscopy assigns alternating strongly high and low potentials for these clusters (Figure 1.8), and the rate constant calculated by the Moser-Dutton equation using experimentally determined potential profiles shows that electron transfer occurs at ~15 ms, far too slow when compared to observed values. The discrepancy most likely originates from electrostatic interactions increasing the amplitude of the alternations in redox titrations and slowing the predicted rate. Corrections for these redox effects for relative permittivity using the dielectric constant ε, ε = 20 and ε = 4 places the times required to 3.9 ms and 0.4 ms, respectively (Hirst, 2013). These rates are consistent with the overall electron transfer rate, but electron transfer is rate-limiting in the ε = 20 scenario. Thus, from a simulation point of view, electron transfer cannot be ruled out of being rate-limiting. Experimentally, freeze quench

EPR studies place the rate of electron transfer between FMN to N2 within 100 μs (Verkhovskaya *et al.*, 2008; De Vries *et al.*, 2015), thus strictly not rate-limiting. The present chapter further investigates this.

Ubiquinone binding and ubiquinol release

To investigate the kinetics of ubiquinone binding and ubiquinol release, Fedor et al. measured the k_{cat} and k_{cat}/ K_M for complex I with different chain length substrates (Q_1 to Q_{10}). It was found that K_M and k_{cat}/ K_M varied with chain length, suggesting that ubiquinone binding is rate-limiting in shorter chain lengths. k_{cat} did not change after a chain length equal to or longer than Q_4. Thus, product release, also expected to be chain length-dependent, is not likely to be rate-limiting except for short-chain ubiquinones (Fedor *et al.*, 2017).

Ubiquinone reduction

The exact quinone reduction mechanism is unknown. Differential redox spectra experiments suggest the formation of anionic semiquinone is disfavoured by 100-150 mV (2-3 kcal mol^{-1}) because the semiquinone has a redox potential of less than -300 mV (Verkhovskaya and Wikström, 2014). Moreover, QM/ MM experiments proposed that the bound ubiquinone has a redox potential of -260 mV, and both electron transfer steps taking ubiquinone to ubiquinol are iso-energetic with the N2 cluster, implying that these steps do not provide the main driving force for the proton-pumping processes, nor have a barrier height sufficient to make these steps rate-limiting (Gamiz-Hernandez *et al.*, 2017). Continuum Poisson-Boltzmann electrostatic calculations suggest that both of these electron transfers occur in the picoseconds timescale, and the second electron transfer is coupled to the deprotonation of $His59^{NDUFS2}$ (Gamiz-Hernandez *et al.*, 2017), so the formation of QH^- is not expected to be rate-limiting. However, it is worth nothing that computational simulations are heavily dependent on the quality of input parameters and cannot be treated as empirical results.

Proton pumping

The redox potential of Q at the binding site near N2 is approximately -260 mV but +90 mV in the membranes. This means that the main energy transduction step occurs when QH_2 moves towards the membrane. Detailed proposals for proton

pumping steps have been made by Kaila et al. (Kaila, 2021) (Figure 1.13A). The free-energy barrier of opening the Lys/ Glu ion pair as part of the proton pumping mechanism has been approximated to be 4 kcal mol^{-1} based on free-energy simulations (Di Luca, Gamiz-Hernandez and Kaila, 2017), and subsequent proton transfer steps have a $\Delta G^{\ddagger}$ of < 10 kcal mol^{-1} based on model calculations. Proton release is assumed to have a free-energy barrier of 8-10 kcal mol^{-1} (Kaila, 2021). This suggests that these steps are not rate-limiting as the turnover of mitochondrial complex I occurs in the milliseconds timescale, and so a barrier of between 14-15 kcal mol^{-1} is expected based on transition state theory (see section 3.1.2).

3.1.2 Theoretical basis of kinetic isotope effects

Kinetic isotope effects have been used as a general methodology to investigate the rate-limiting steps in catalysis for enzymes and used to specifically probe the properties of the chemical proton transfer step. Many enzymes, including complex I (Birrell and Hirst, 2013) have previously been examined using this technique, including ribonuclease (Yoon and Harris, 2021), HIV proteases (Hyland, Tomaszek and Meek, 1991), lipoxygenases (Hu *et al.*, 2019), cholinesterases (Quinn, 1987), and nitrate-ester reductases (Pudney *et al.*, 2013) among many others.

To identify a rate-limiting step, measuring the kinetic isotope effect (KIE) allows the direct observation of an isotopically sensitive step in the catalytic mechanism and, therefore, creates a means to differentiate between isotopically sensitive steps, containing proton transfers such as quinone reduction and non-isotopically sensitive steps, such as quinone binding and quinol dissociation. A KIE is a phenomenon whereby isotopically substituted molecules exhibit different reaction rates. The most common isotope used for light-atom isotope effect studies is hydrogen (^{1}H) typically replaced by its isotope deuterium (^{2}H). Carbon (^{12}C, ^{13}C), nitrogen (^{14}N, ^{15}N), and oxygen (^{16}O, ^{18}O) are also commonly used and are referred to as heavy-atom isotope effects. A primary isotope effect occurs when the isotopically substituted bond is broken during the rate-limiting transition state and it typically results in relatively large kinetic effects. When the isotopic substitution changes the force field between the reactant and transition state, but the substituted bond itself remains unbroken, a secondary isotope effect arises, and the effects are typically small. The observed KIE for the whole turnover reaction is not always equal to the intrinsic KIE of a single isotopically sensitive step as it may be wholly or partially obscured by

slower or comparable non-isotopically sensitive steps preceding or succeeding that step. Even if the mechanism contains a known isotopically sensitive proton transfer step, that step must be at least partially rate-limiting in the catalytic mechanism for a KIE to be observed.

Consider the reaction below (Figure 3.1), which is a hypothetical proton transfer reaction between R_1 and R_2. The transition state $[R_1\text{-H-}R_2]^{\ddagger}$ is in a quasi-equilibrium denoted by $K^{\ddagger}$ with the reactants and is broken down into products with the rate constant $k^{\ddagger}$. The relationship between the overall rate, free energy barriers, and isotopic substitution are explained in Derivation 3.1 (Laidler and King, 1983). KIEs are the direct result of differences in the zero-point energy with isotopic substitution and are independent of barrier height. Zero-point vibrational energy (ZPE) denotes the lowest possible energy of a system and equates to ground-state energy. ZPE is dependent on the mass of the molecule, and lighter atoms have a greater vibrational frequency. Deuterium is heavier than hydrogen and therefore have a lower ZPE.

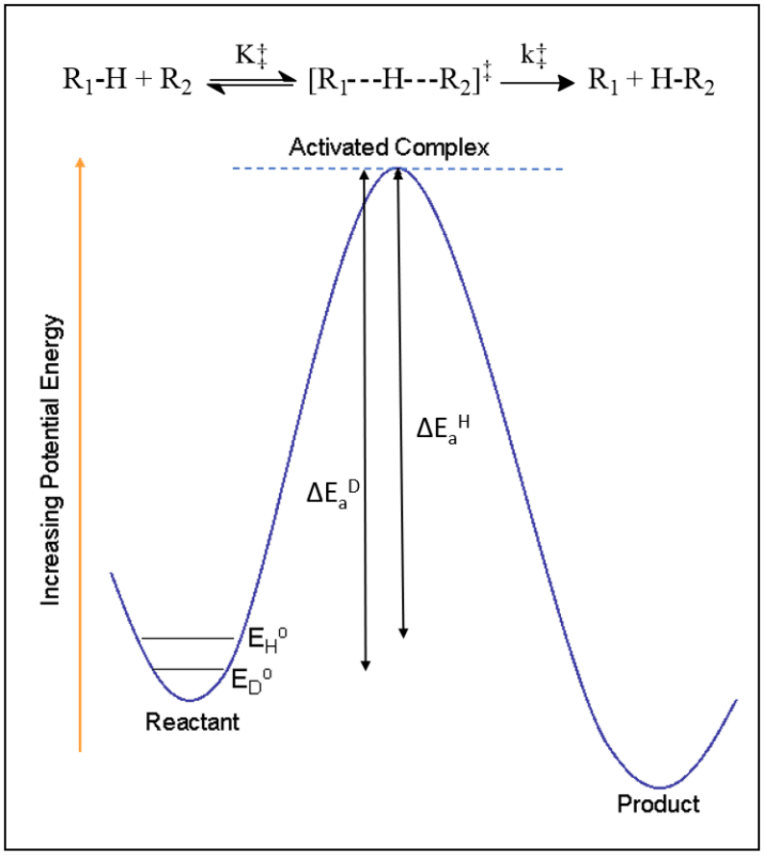

Figure 3.1. Morse potential curve of a hypothetical proton transfer reaction. $E_H{}^0$ and $E_D{}^0$ represent the zero-point vibrational energy of the two isotopic molecules R-H and R-D, and $\Delta E_a{}^H$ and $\Delta E_a{}^D$ represent their respective activation energies.

Derivation 3.1: Transition state theory and kinetic isotope effect

The equilibrium constant between the transition state and reactants.

$$K^{\ddagger} = \frac{[R_1 - H - R_2]^{\ddagger}}{[R_1 - H][R_2]} \quad (1)$$

Thus, the rate equation for product formation is:

$$\frac{d[P]}{dt} = k^{\ddagger}[R_1 - H - R_2]^{\ddagger} = k^{\ddagger}K^{\ddagger}[R_1 - H][R_2] \quad (2)$$

And the rate constant *k* is equal to:

$$k = k^{\ddagger}K^{\ddagger} \quad (3)$$

$k^{\ddagger}$ is defined by the vibrational frequency of the transition state and the transmission coefficient, a measure of the effectiveness of barrier crossing.

$$k^{\ddagger} = \kappa\nu \quad (4)$$

Equilibrium constant $K^{\ddagger}$ is defined by the temperature *T*, Boltzmann constant k_B, Planck's constant *h*, and the activation energy E_a.

$$K^{\ddagger} = \frac{k_B T}{h\nu} e^{\frac{-{E_a}^H}{RT}} \quad (5)$$

Combining 3, 4, and 5:

$$k = k^{\ddagger}K^{\ddagger} = \kappa\frac{k_B T}{h} e^{\frac{-E_a}{RT}} \quad (6)$$

Dividing 6 with its equivalent in deuterium, the isotope is defined as:

$$KIE = \frac{k_H}{k_D} = \frac{\kappa_H}{\kappa_D} e^{\frac{({E_a}^D - {E_a}^H)}{RT}} \quad (7)$$

The tunnelling contribution to the kinetic isotope effect is therefore:

$$KIE_{tunn} = \frac{\kappa_H}{\kappa_D} \quad (8)$$

In this thesis, solvent isotope effect experiments are conducted, which involve proton-stable transition states (Quinn and Sutton, 1991). So, tunnelling isotope effects are not considered. Therefore, the transmission coefficient κ is usually set to one in both for both proton and deuteron as is generally accepted (Kaila, 2021).

In solvent isotope effect experiments, all the H_2O molecules in the solvent are replaced with D_2O to probe proton transfer isotope effects. Because all solvent-exchangeable protons are replaced by deuterons, the effects of solvent substitution on diffusion, enzyme conformation, and pH profiles must be considered. The pH profile is also informative to characterise whether the proton donor is solvent titratable during the rate-determining transition in mutational experiments (see section 3.1.3). Unlike substrate substitution isotope effect experiments, solvent isotope effects must consider isotope effects occurring at multiple sites, and the exact catalytic elements that produce the isotope effects are not uniquely revealed. Nonetheless, reasonable mechanistic proposals can be constructed by the use of solvent isotope effects, should careful considerations be made of its limitations.

3.1.3 Mutations in the ubiquinone binding site of complex I

Mutations in NUCM and NUKM were generated in *Y. lipolytica* complex I to explore in depth the role of these residues in the catalytic mechanism of complex I. Here, mutations are made to the quinone binding site residues in the NUCM and NUKM subunits of *Y. lipolytica* complex I. The sequence of NUCM and NUKM is 63% and 70% conserved with human complex I, and the mutations chosen are in regions of high sequence conservation (Figure 3.2). The high degree of sequence similarity means *Y. lipolytica* complex I serves as a good model for studying mammalian complex I. Figure 3.3 shows the structural positions of mutations chosen for this study, all of which are conserved across humans and *Y. lipolytica*. Point mutations were made for an earlier separate study by Dr Andrew Jones (see Materials and Methods section 2.2.1), using knock-out strains of NUCM and NUKM (*Δnucm, Δnukm*) derived from the parental GB10 *Y. lipolytica* made by Brandt et al. (Grgic *et al.*, 2004) and adopted for this study. This strain contains an internally directed NDH2 (Kerscher *et al.*, 2002) which allows complex I to be non-essential, as well as a His-tag on the NDUFS3 subunit, to allow for purification of complex I (Kashani-Poor *et al.*, 2001).

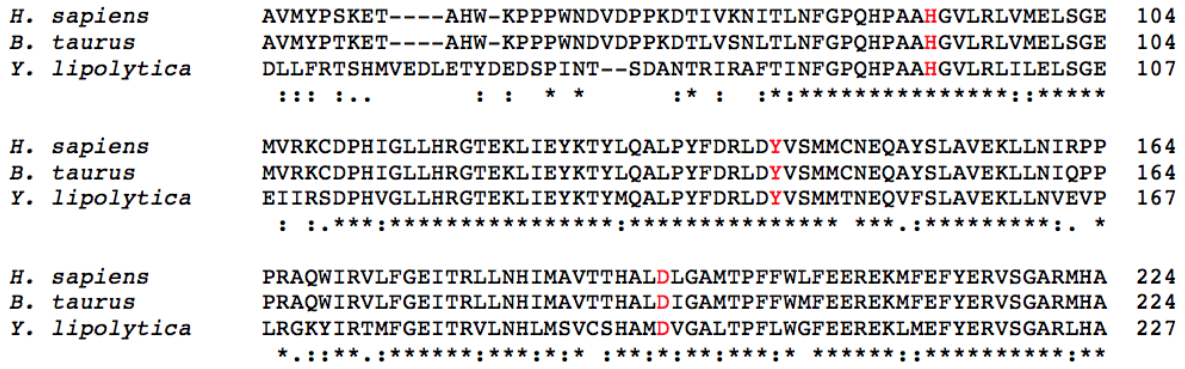

Figure 3.2. Alignment of NDUFS2 sequences from human, bovine and *Y. lipolytica* complex I. Mutations carried out in this chapter are highlighted in red. * denotes a fully conserved residue, : denotes a strongly conserved residue, . denotes a weakly conserved residue and a gap denotes no conservation. Figure adapted from (Marino, 2018).

The choice of residues was informed by previous experimental work as well as simulations. The role of these residues has well-defined proposals. Y144 and H95 are proposed by computational studies to interact directly with the quinone headgroup and are proposed to donate protons to reduce quinone (Sharma *et al.*, 2015; Gamiz-Hernandez *et al.*, 2017; Warnau *et al.*, 2018). Mutation of these residues in the “first coordination sphere” likely affects substrate binding and quinone reduction. D196 forms a hydrogen bond with H95 and the protonation state of this residue likely determines the pKa of H95 and affects the dynamics of quinone binding (Chung, Wright, *et al.*, 2022). It is also proposed to donate protons to H59 upon its deprotonation and proton pumping (Sharma *et al.*, 2015; Warnau *et al.*, 2018; Gu *et al.*, 2022), which triggers protonation and conformational changes in the E-channel that localizes a negative charge in ND4L in a proposed complex I coupling mechanism (Kampjut and Sazanov, 2020b). Mutation of this residue in the “second coordination sphere” is also likely to result in changes in substrate binding and catalysis but to a lesser degree than mutations in the “first coordination sphere” and may instead affect signal propagation for coupling (Sharma *et al.*, 2015). Finally, M91 forms hydrophobic interactions with the first isoprenoid subunit of quinone and is proposed to support substrate binding (Angerer *et al.*, 2012; Haapanen, Djurabekova and Sharma, 2019; Parey *et al.*, 2021). This is expected to be a mild mutation that affects only substrate binding but not catalysis.

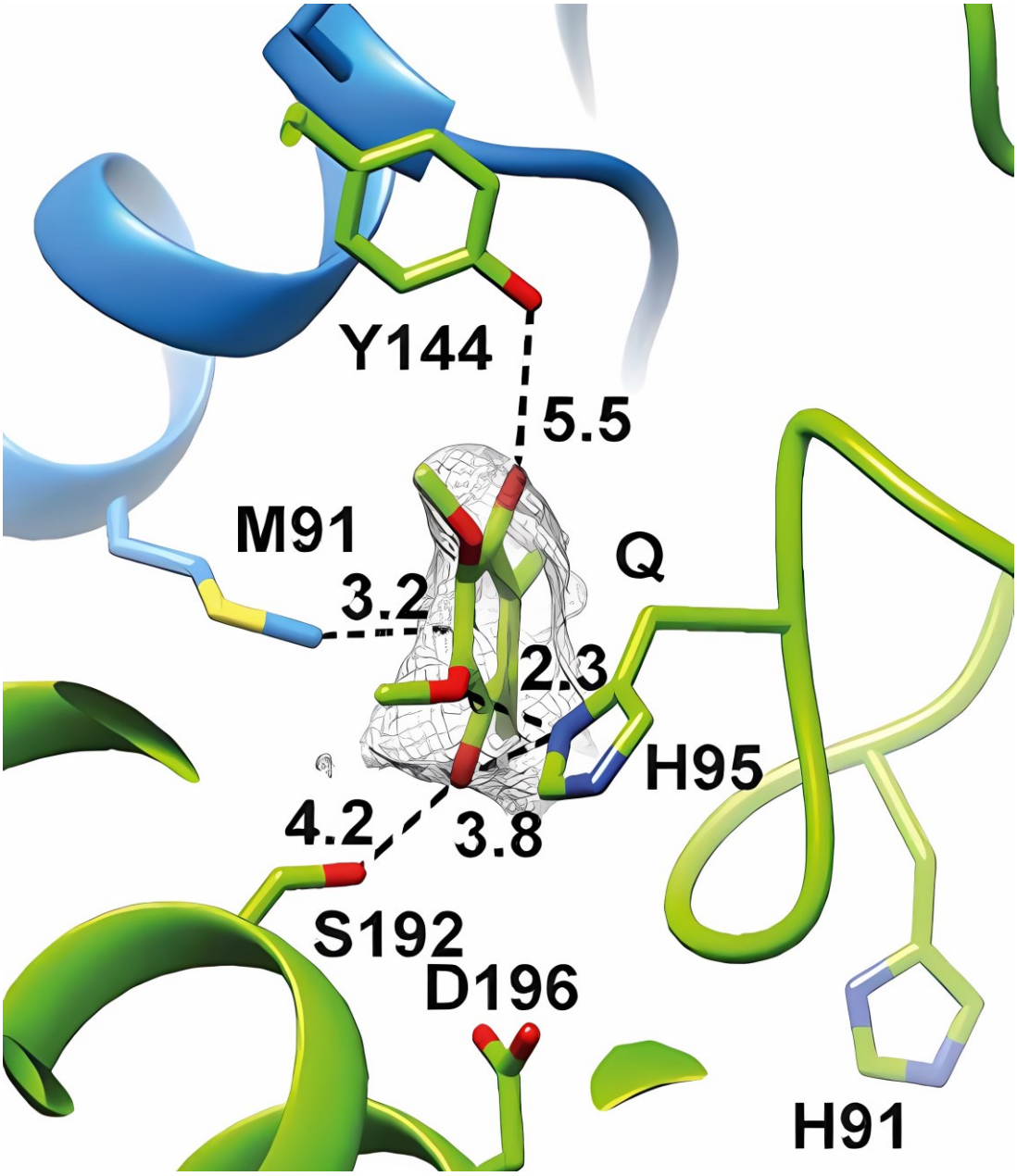

Figure 3.3. The proposed ubiquinone binding site in complex I in *Yarrowia lipolytica* under turnover conditions. Decyl-ubiquinone is modelled in the binding site, with interacting residues shown in sticks. Figure adapted from (Parey *et al.*, 2021).

Here, complex I variants in the ubiquinone binding site are used to investigate their effects on ubiquinone binding, reduction, and ubiquinol release in complex I. This is achieved by using the proteoliposome system, which allows the measurement of kinetic parameters using native long-chain Q_{10}. Further, I also measure the pH dependence of k_{cat}, K_{sp}, as well as its kinetic isotope effect and proton inventory of these mutants, which probes and characterizes specifically the rate-limiting proton transfer step in these mutations.

3.1.4 Previous mutagenesis studies in the chosen mutations.

Tyrosine-144 in NUCM

Brandt et al. have explored the effect of six different mutations (F, W, I, H, S, and R) on Y144 (Tocilescu, Fendel, *et al.*, 2010) by measuring NADH:O_2 oxidoreduction rates in mitochondrial membranes using DQ, Q_1, and Q_2 as substrates. All measured rates using DQ were <20% as compared to WT. No rate can be determined reliably (<5%) using the native substrate Q_9 for any mutant. However, activity can be rescued by the use of the soluble short-chain quinone Q_1 as a substrate, with rates in Y144F/ W/ H having an activity of 72%, 93% and 48%, respectively. This demonstrates that using short-chain quinones can rescue activity, potentially through an alternate binding mode. Previous EPR results on mitochondrial membranes showed that mutation of these residues led to loss of signal in the N2 cluster in Y144W/ I/ H/ S/ R, but no effect was found for Y144F. Y144F reconstituted in proteoliposomes can still pump protons when using Q_1 as a substrate, suggesting that despite a potentially different reaction geometry, coupling between NADH:Q oxidoreduction and proton pumping is not affected (Tocilescu, Fendel, *et al.*, 2010). The k_{cat} and K_M of the Y144F mutant using Q_{10} and Q_1 as substrates were determined in proteoliposomes (Marino, 2018). It was found that the k_{cat} of Y144F using Q_{10} was ~10% that of WT, with activity increasing to a range between 35% to 100% of WT using Q_1, demonstrating that measurable kinetic data of long-chain quinone catalysis can be obtained using the proteoliposomes system. The K_M of Y144F has increased to 4.3 mM (compared to 3.8 mM in WT) using Q_{10}, and an apparent K_M of > 50 mM (30.6 mM in WT) was measured using Q_1 as a substrate. The piericidin sensitivity of the Y144F mutant has also decreased, with IC50 increasing to 1.3 mM (0.24 mM in WT). The Hill coefficient has also decreased from 1.5 in WT to 0.6 mM in Y144F. The increased K_M and IC50 are consistent with the mutation affecting the primary binding site more than the secondary binding site of piericidin (Bridges *et al.*, 2020). In this present study, Y144 is mutated to phenylalanine to remove the protonatable group without other structural effects and or affecting the N2 cluster redox potential.

Histidine-95 in NUCM

Grgic et al. have previously studied this residue in mitochondrial membranes with mutation to A, M, and R (Grgic *et al.*, 2004). All measured rates with DQ were <5% and EPR measurements show that the mutation had no effects on the N2 cluster. Reconstituted purified H95M in proteoliposomes show that the measured activities were <5% using DQ, Q_1, and Q_{10} as substrates. However, these results were only measured at pH 7.5. If an alternative substrate reduction mechanism is used, the pKa of the reaction may shift and activity may be rescued at a different pH. H95 is mutated to the aliphatic methionine to remove the protonatable group and maintain a similar steric effect.

Aspartate-196 in NUCM

The equivalent residue, D329, has been mutated in *E. coli* to asparagine and the activity was lowered to ~25% of the WT enzyme (Sharma *et al.*, 2015). Despite the proposal by Sharma et al. that this residue is responsible for the initiation of proton pumping, no effect has been found on proton pumping in Oxonol VI quenching experiments. Instead, Sharma et al. suggest that the QH^- species is formed via a single protonation by Tyrosine (without Histidine donating a proton), and it is the movement of QH^- species that is responsible for activation of proton pumping. *Y. lipolytica* D196N complex I reconstituted into proteoliposomes shows that the k_{cat} has dropped to 17% of WT and K_M has increased from 3.8 mM in WT to 4.9 mM using Q_{10} as a substrate (Marino, 2018). Using Q_1 as a substrate, the activity was rescued to ~43% of WT and the apparent K_M has increased from 30.6 mM to 43.7 mM. The mutation has also decreased piericidin sensitivity, with the IC50 increasing from 0.24 mM to 2.2 mM. Similarly to Y144F, the hill coefficient has also dropped from 1.5 in WT to 0.8. These results suggest that substrate binding in the primary binding site has been affected by this mutation. In this present study, D196 is mutated to asparagine to remove a protonatable group and its ability to donate protons to H95. Fixing the protonation state in this residue this may change the pKa of H95 within the reaction cycle and affect substrate entry/ exit dynamics (Chung, Wright, *et al.*, 2022).

Methionine-91 in NUKM

Angerer et al. have previously studied this residue with mutations to A, E, C, and K in *Y. lipolytica* complex I and activities were determined using mitochondrial membranes (Angerer *et al.*, 2012). Mutations to K and E reduced the oxidoreduction rate to <10% of WT using DQ, Q_1, and Q_2 as substrates. This suggests that either the steric effects of a larger substituted residue or the polar nature of the residue inhibits substrate binding. Mutations to A and C resulted in k_{cat} of oxidoreduction rates of 118% and 160% using Q_1 and Q_2 respectively, with M91A and M91C not significantly different in rate. The activity using DQ was not determined. Apparent K_M cannot be determined for the E and K mutants. Using Q1, the apparent K_M has increased to 393 μM and 141 μM (as compared to 29 μM in WT) in the M91A and M91C mutants, respectively, and the same has increased to 26 μM and 17 μM (as compared to 12 μM in WT) using Q_2. These results suggest that this residue does not have a deleterious effect on catalysis but on substrate/ product entry/ exit dynamics. The much larger effect on K_M in Q_1 as compared to Q_2 is in support of the results found by Fedor et al. (Fedor *et al.*, 2017), that they have a different binding pose. Although more substrate is needed to saturate the binding site as indicated by a decrease in k_{cat}/ K_M, an increase in k_{cat} is consistent with looser product binding, increasing the rate of product release, with an unknown effect on the rate of the catalytic step. In this present study, M91 is mutated to isoleucine to retain the aliphatic nature of this residue but decrease its size to reduce its hydrophobic interaction with the isoprene tail.

3.2 Aims & strategy.

- Determine the rate-limiting step in mitochondrial complex I catalysis from the perspective of the proton by:
- Measuring the pH and isotopic dependence of kinetic parameters (k_{cat}, k_{cat}/ K_M) of complex I;
- Using Q-binding site mutations to probe their effects on the rate-limiting step;
- Kinetic modelling of the pH and isotopic dependence of complex I;
- Characterise the isotopically sensitive step using proton inventory experiment: by measuring the ratio of rates under fractional solute site deuteron occupancy.

3.3 Optimisation of bovine membrane assay system to determine the kinetic isotope effect of complex I

3.3.1 Correcting the effect of D_2O on acid ionisation behaviour in enzyme catalysis

When measuring a kinetic isotope effect, it is important to compare between equivalent protein ionisation states by correcting for solvent isotope effects on the pKa values of weak acids and bases. The use of equivalent buffers ensures that rates are measured at the equivalent positions in the pH and pD-rate profiles, meaning concentrations of all solutes are the same, including electrolytes and acid/ base pairs that provide buffering capacity.

When preparing D_2O-containing buffers, it is necessary to account for the solvent isotope effect on the glass electrode used to measure the pH values. The relationship pD = pH + 0.41 (Forcé and Carr, 1974) has been previously established for the glass electrode, where pD signifies the equivalent pH in D_2O buffer. So, when preparing buffers using the glass electrode, +0.4 must be added to the pH meter reading to obtain the correct pD for a buffer in D_2O.

Additionally, the pKa values of weak acids and weak bases also change in D_2O. This includes the enzyme active site residues as well as buffer components. This means that the bell-shaped curves determined for enzyme activities will typically shift on the pH (pD) axis due to the solvent isotope substitution (Barbara Schowen and Schowen, 1982). Schowen et al. have tabulated the solvent isotope effects for a large number of weak organic and inorganic acids (pKa 1 to 10). With few exceptions, the acids have a pKa shift of between 0.3 – 0.7 pH units upon isotopic substitution from H_2O to D_2O. 13 weak acids have pKa shifts in the range of 0.45 to 0.52, approximately similar to the shift seen in the response of the glass electrode. These include citric and boric acid, which are components of the buffer system used to measure pH and pD rate profiles in this chapter. In the present experiments, only the relationship of pD = pH + 0.41 is used to correct for equivalent ionization in the preparation of buffers solvated in D_2O, and activities are plotted using pH and pD values, without correcting for the shift in weak acid pK.

3.3.2 Single buffer system for measuring the pH dependence of complex I catalysis

To measure the pH dependence of complex I catalysis, a buffer system must be developed that is well tolerated by the enzyme, has a linear buffering capacity across the working pH range, and has minimal temperature dependence. This allows easy buffer preparation whilst avoiding the need to switch between buffering systems and create an uncontrolled variable.

I developed a three-component assay buffer for this purpose, which contains 20 mM citrate (pH range 2.5 to 7) , 30 mM HEPES (pH range 6.8 to 8.2), and 40 mM boric acid (pH range 8.5 to 10.2), which was found to be well tolerated by complex I and that buffers almost linearly across the entire pH range (Figure 3.4). Buffers were adjusted to the correct pH/ pD using sodium hydroxide made up in either H_2O or D_2O.

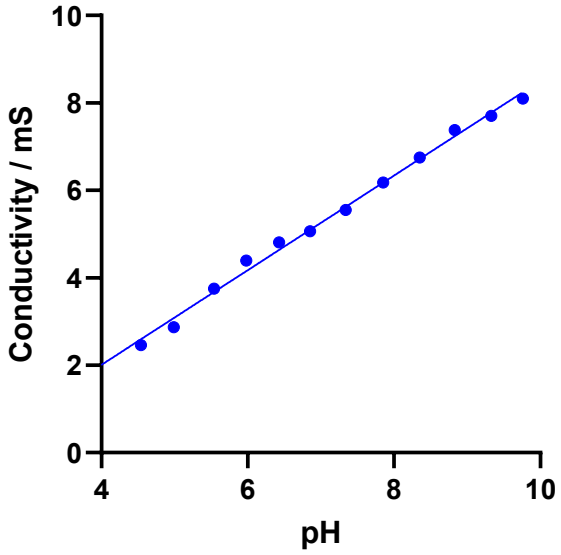

Figure 3.4 Conductivity measurements on the tri-component buffer system used for complex I catalytic assays. pH dependence across the pH range 4-10 is linear and, therefore, allows linear interpolation when preparing different pH buffers within this range. Conductivity measurements were carried out using the triple-buffered system containing 20 mM citrate, 30 mM HEPES, and 40 mM boric acid, under room temperature.

The temperature dependence of the buffer system is also excellent as citrate, HEPES, and boric acid have -0.0024, -0.014, and -0.008 dpKa/ dT, respectively (Good *et al.*, 1966). For comparison, the commonly used buffer Tris has a temperature dependence of -0.028 dpKa/ dT, double that of HEPES. As the

conductivity of the buffer system varies with pH, with pH 4 equivalent to 18 mM NaCl and pH 10 equivalent to 80 mM NaCl, I tested the [NaCl] dependence of the NADH:O_2 oxidoreductase activity of bovine complex I membranes (Appendix 7.1), to determine whether a correction for salt concentration / ionic strength was necessary. The titration of bovine membranes with [NaCl] did not yield any significant change in catalytic rate until 200 mM NaCl, well above the range used here. All assays described were measured using this buffer system.

3.3.3 Ensuring complex I catalysis is rate-limiting in assays

The rates of complex I turnover were measured using a NADH-coupled assay system comprised of mitochondrial membranes and an enzyme regenerating the complex I substrate quinone (Figure 3.5). The NADH oxidation reaction can be observed spectroscopically as a disappearance of the NADH absorbance, which is stoichiometrically proportional to the rate of Q reduction. To functionally isolate complex I in the NADH:O_2 oxidoreduction assay, such that the activity measured is not dependent on contributions from other enzymes, complex I must be rate-limiting.

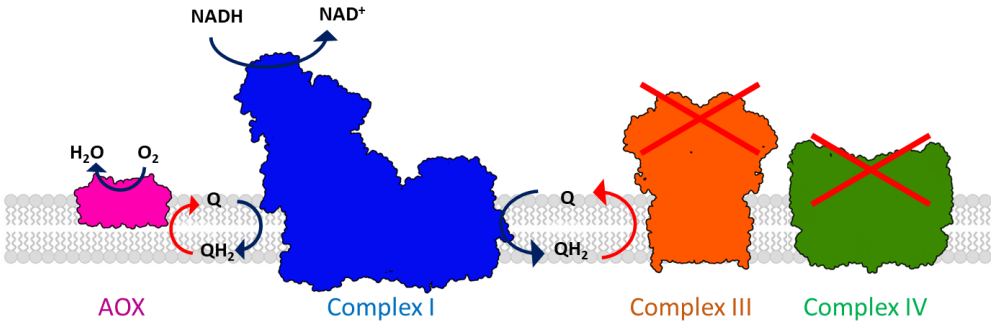

Figure 3.5: Illustration of the NADH:O_2 coupled oxidoreduction assay. The Q pool is reduced by complex I through NADH oxidation and is oxidised by AOX activity. AOX is, in turn, oxidised by oxygen. Cyanide addition removes the native quinone oxidase in the membranes by inhibiting complex IV activity, also silencing the activity of complex III.

First, the NADH concentration (200 uM) used is much higher than the K_M value of 79 ± 8 µM for NADH oxidation at the complex I flavin site to achieve saturation of the flavin reaction and maximise the rate of NADH oxidation (Fedor *et al.*, 2017). Second, to maximise the rate of turnover and ensure product inhibition does not contribute, quinone reoxidation by the partner enzymes must be sufficiently fast so that the quinone pool is as fully oxidised as possible. To achieve this, 400 µM of cyanide was added to inhibit complex IV, and Alternative Oxidase (AOX) from *Trypanosoma*

brucei was used to oxidise the quinone pool instead (AOX re-oxidises quinol by reducing O_2) (Jones *et al.*, 2016). AOX was titrated on a mg bovine membrane per mg AOX basis, and the resultant rate of NADH:O_2 oxidoreduction was measured. Figure 3.6 shows that 0.8-1 mg AOX per 1 mg bovine membranes is sufficient for maximal activity, with further addition decreasing NADH:O_2 activity, likely due to protein aggregation in the sample well (see section 4.3.2). The Q oxidation rate of AOX is ~240 μM Q_1 s^1umol^{-1} (Xu, 2021), which is approximately 60% of the Q reduction rate of complex I. But because the molecular mass difference between complex I and AOX is 30:1, and complex I represents only ~10 % of the mass of bovine SMPs (Pryde and Hirst, 2011), and is expected to represent a smaller percentage in membranes, 1 mg:mg represents a vast stoichiometric excess even if not all added AOX will be associated with the lipid membrane. The oxygen concentration in the buffer is approximately 250 μM and larger than the K_M value of 1-2 μM for AOX catalysis (Bendall and Bonner, 1971), so AOX activity is unlikely to be oxygen-limited. Because an excess of AOX does not increase the catalytic activity further, it is understood that complex I is rate-limiting, and the Q pool is almost entirely oxidised (Jones *et al.*, 2016; Fedor *et al.*, 2017).

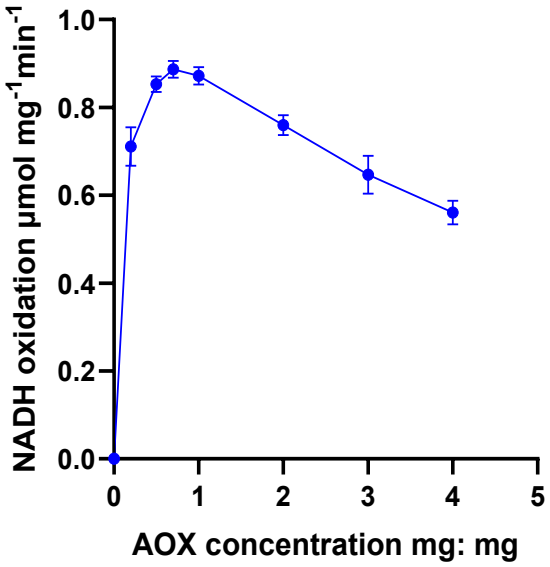

Figure 3.6 NADH:O_2 rates of bovine membranes with increasing AOX concentration. Bovine membranes were supplemented with 400 μM cyanide to inhibit complex IV. At 0 mg AOX, no activity was measured as expected, but full activity was measured with at a ratio of 1 mg:mg addition of AOX. Errors are calculated as standard error of the mean (n = 3).

3.3.4 Initial measurement of a Kinetic Isotope Effect for complex I

As a first test of whether complex I displays a solvent KIE, I measured the NADH:O_2 oxidoreduction rates of bovine membranes in pH 7.5 and pD 7.5 using 200 µM of NADH and 1 mg: mg AOX (Figure 3.7). A KIE of 1.31 ± 0.04 was observed.

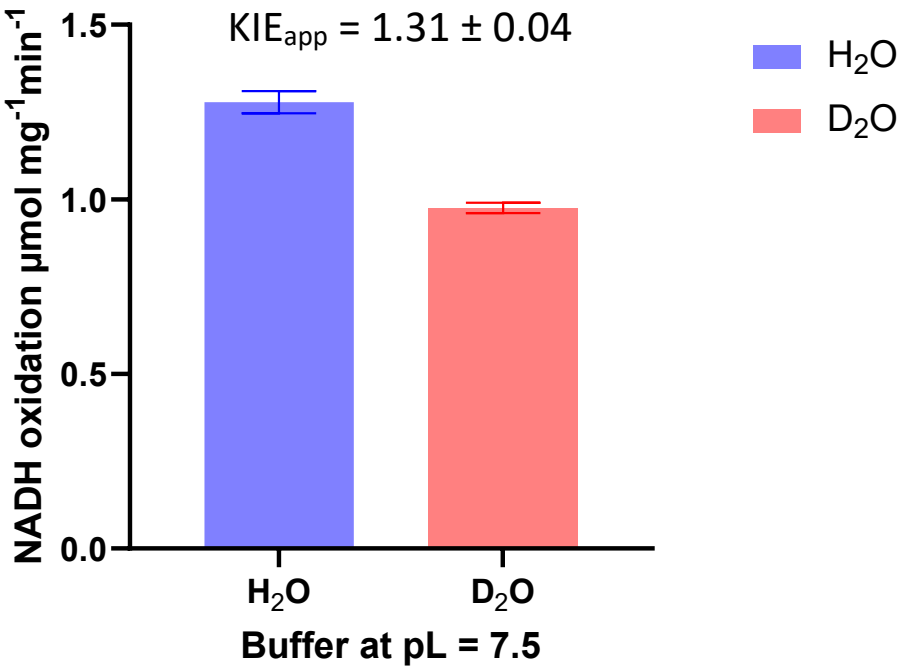

Figure 3.7 Solvent KIE of bovine mitochondrial membranes. The NADH:O_2 oxidoreduction rates of bovine membranes at pH 7.5 and pD 7.5 were measured using 200 µM NADH, 1 mg:mg AOX, and 400 µM cyanide. An apparent KIE of 1.31 ± 0.04 was measured. Errors are calculated as standard error of the mean (n = 3).

Because D_2O has a greater viscosity than H_2O, the measured solvent KIE may be attributable to slower substrate diffusion or protein conformational dynamics in greater viscosity rather than isotopic sensitivity within the complex I mechanism. D_2O has a viscosity of 1.25 Centipoise (cP, 1cm^{-1}gs^{-1}), compared to 1.005 cP for H_2O at room temperature (Hardy and Cottington, 1949). Thus, the viscosity of D_2O at room temperature is equivalent to approximately 15% glycerol in H_2O (Sheely, 1932). The NADH:O_2 oxidoreduction rates of bovine membranes supplemented with 1 mg:mg AOX and 400 µM cyanide were therefore measured under various concentrations of glycerol in pH 7.5 (H_2O) buffer.

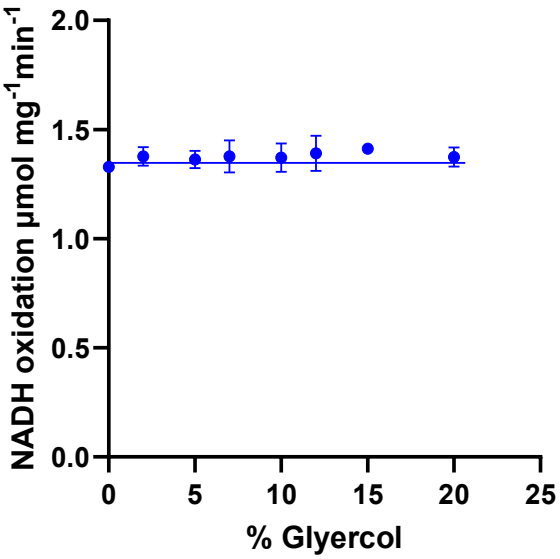

Figure 3.8 Complex I NADH:O_2 oxidoreduction rates measured under different concentrations of glycerol. The viscosity of 15% glycerol is equivalent to D_2O at room temperature. There is no change in the rate even with 20% glycerol added. Errors are calculated as standard error of the mean (n = 3).

Figure 3.8 shows that there is no dependence of the rate on glycerol concentration. This is unsurprising if (as is expected) complex I is limited by Q_{10} catalysis or proton pumping steps, which are located within the lipid membrane. The flavin site for NADH oxidation is solvent-exposed; however, the catalytic rate is extremely fast and close to diffusion-limited, with k_{cat}/ K_M at ~7.5 x 10^7 $M^{-1}s^{-1}$ (Birrell, Yakovlev and Hirst, 2009), which is more than an order of magnitude greater than the k_{cat} of the overall bovine complex I reaction. These results show that the difference in viscosity between H_2O and D_2O is not the cause of the observed solvent kinetic isotope effect, which can thus be attributed directly to complex I activity.

3.4 Measuring the pH dependence and kinetic isotope effect of complex I catalysis in bovine mitochondrial membranes

3.4.1 The pH-dependent stability of complex I in bovine mitochondrial membranes

To measure the pH dependence of the catalytic rate in complex I, it is important to differentiate between the catalytic rate loss due to enzyme denaturation and the titration of ionisation states at different pH levels. I tested the pH-dependent stability of bovine complex I by measuring the NADH:O_2 rates of bovine membranes.

Membranes were first pre-incubated for an hour in the tested pH buffer on ice and then diluted to assay concentration in either pH 7.5 buffer or assayed in the same incubation pH buffer. AOX was added at 1mg:mg after the incubation step to control for the loss of rate caused by the irreversible loss of complex III and IV in the bovine membranes. Figure 3.9 shows that complex I has a bell-shaped pH rate profile and that pre-incubation at high pH was fully reversible, whereas pre-incubation at a pH value lower than 6 caused substantially irreversible inactivation.

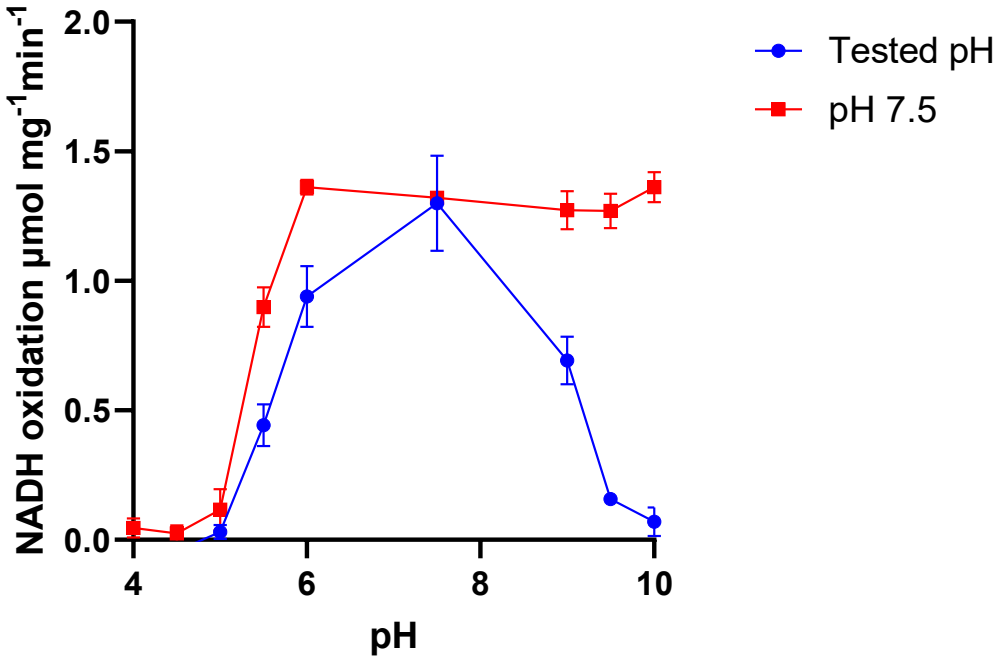

Figure 3.9 Reversibility of pH-inactivation of Complex I. Complex I activity was measured after a 1-hour incubation at each corresponding pH after dilution in either pH 7.5 buffer (Red) or in the same incubation buffer (Blue). Changes in activity at pH 6 to 10 are completely reversible, whereas below pH 6, substantial irreversible loss of rate occurs. Errors are calculated as standard error of the mean (n = 3).

3.4.2 Fitting pH rate profiles to delineate between pH and isotopic effects

Like a typical enzyme, complex I shows a bell-shaped pH-dependent activity. To analyze the pH and pD rate profiles, Equation 1 was therefore used to describe the shape of the bell-shaped curve, where pK_{a1} represents the proton dissociation constant of the group(s) that defines the ascending arm and pK_{a2} the group(s) that defines the descending arm (Quinn and Sutton, 1991). The measured rate is represented by *v*.

$$v = \frac{V_{opt}}{1 + 10^{pK_{a1} - pH} + 10^{pH - pK_{a2}}} \quad (3.1)$$

V_{opt} defines the pH-independent optimal rate of catalysis. In other words, it is the hypothetical rate of the optimally protonated complex I species. The bell shape results from the combination of two separate single pKa titration curves (Figure 3.10). The closer the pK_as, the lower the apparent peak height of the bell shape, which can be equal to, or lesser than, the underlying maximal value.

pKa values of weak acids/ bases shift in the range of 0.3 to 0.7 in D_2O (Barbara Schowen and Schowen, 1982). Solvent KIE of an enzyme is a ratio of rates in the same ionization state between isotopic solvents. Therefore, it is erroneous to directly compare the rates between isotopic solvents along the pH/ pD axis. Comparing V_{opt} ensures that the enzymic species compared are in the same state (e.g., in Figure 3.10). Another advantage of comparing V_{opt} values is that V_{opt} is a fitted value using data in the entire curve and is more robust than measuring the rate of a single pH value. Note pL (ligand) means the experiment is performed in pH and pD.

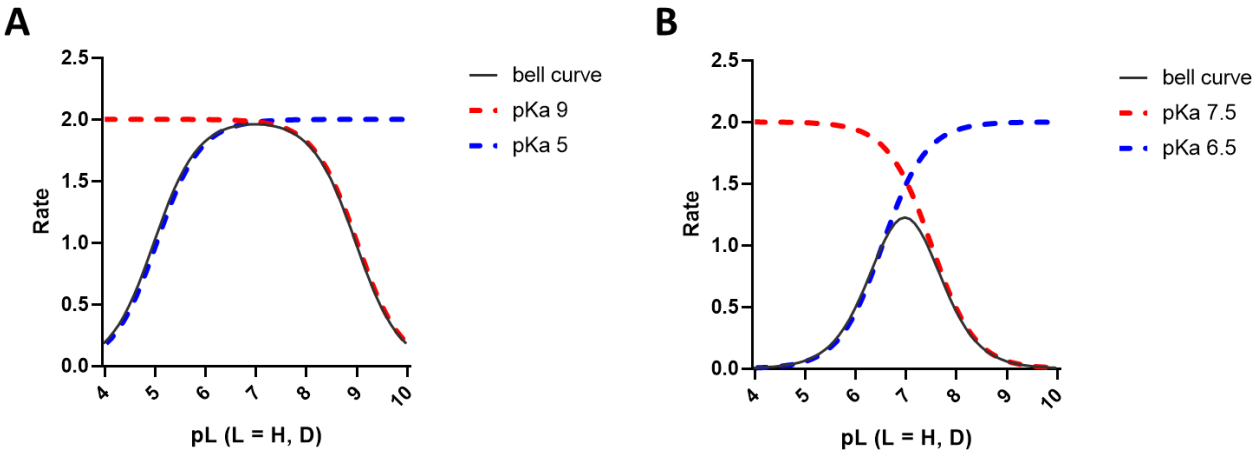

Figure 3.10 An illustration of equation 1 in graphical form. These plots are generated with a common V_{opt} of 2, with differing pK_a1 and pK_a2 values. (A) pK_a1 is 5, and pK_a2 is 9. The pK_as are well spaced, and the apparent peak height approximates V_{opt} or the pH-independent value of V_{max}. (B) pK_a1 is 6.5, and pK_a2 is 7.5. The pK_as are close together, and consequently, the apparent peak height Is much lower than the V_{opt} value of 2.

Of course, it is unknown whether there are only two titrating residues, and the likelihood is that far more than two residues are responsible for the catalytic

mechanism of complex I. The resultant fitted pKa values are thus the average of values of numerous residues, and we should be careful not to over-interpret the meaning of the resultant pK_a values from equation fitting.

3.4.3 Measuring the pH and pD rate profile of bovine complex I in membranes

To measure the pH rate profile of bovine membranes, the NADH:O_2 rate of bovine membranes supplemented with 1mg:mg AOX and 400 µM cyanide was determined across the accessible pH range 6- 9.5 (Figure 3.11). The shape of the curves shows a broad peak in activity between pH 7 and pH 8, which represents the optimal protonation state, with the decreasing activity at low pH representing an increased proportion of an inactive protonated state, and at high pH, an inactive deprotonated state.

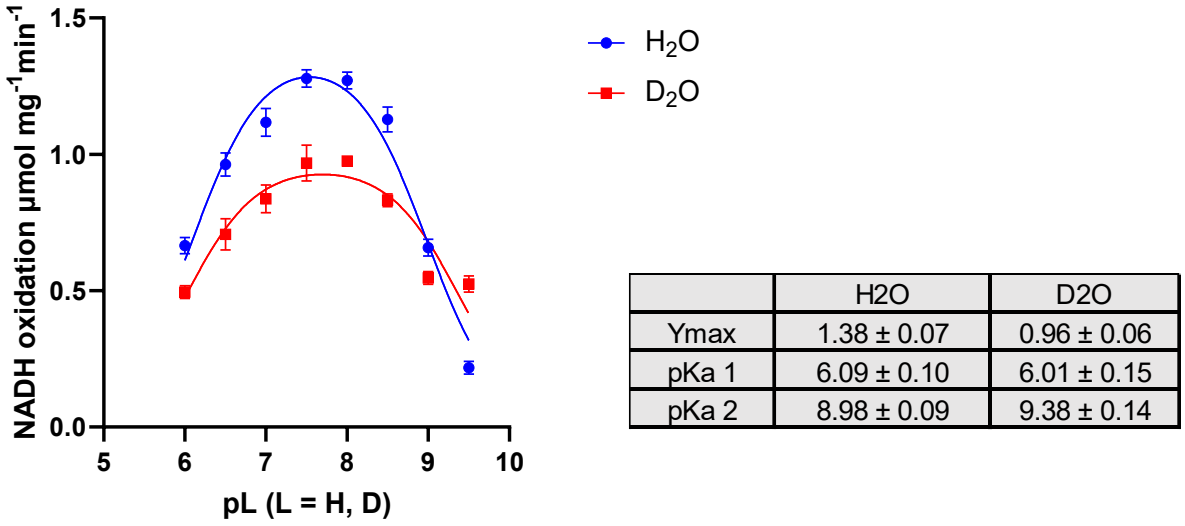

	H2O	D2O
Ymax	1.38 ± 0.07	0.96 ± 0.06
pKa 1	6.09 ± 0.10	6.01 ± 0.15
pKa 2	8.98 ± 0.09	9.38 ± 0.14

Figure 3.11 NADH:O_2 rates of bovine membranes supplemented with 1 mg:mg AOX measured in H_2O or D_2O solvated buffer. The fitted V_{opt} values represent a KIE of 1.43 ± 0.11. Errors are calculated as standard error of the mean (n = 3).

The calculated V_{opt} values of Figure 3.11 are 1.38 and 0.96 in H_2O and D_2O, respectively, and the fitted pKas are 6.10 and 8.97 in H_2O and 5.6 and 9.0 in D_2O. This represents an observed KIE of 1.43 ± 0.11, taking the ratio of V_{opt} fitted in H_2O and D_2O to minimise the effects of varying pH dependence. To further confirm that the observed KIE is the result of complex I activity and not AOX activity, the NADH:DQ (Figure 3.12) rates were also measured. 400 µM cyanide was added to the assay to inhibit complex III and IV activity and no AOX was added. A KIE of 1.52

± 0.06 was observed for bovine complex I using DQ as a substrate, which is not significantly different to the KIE observed for NADH:O_2 rates using endogenous Q_{10}. These results further confirm that complex I activity is the cause of the observed KIE.

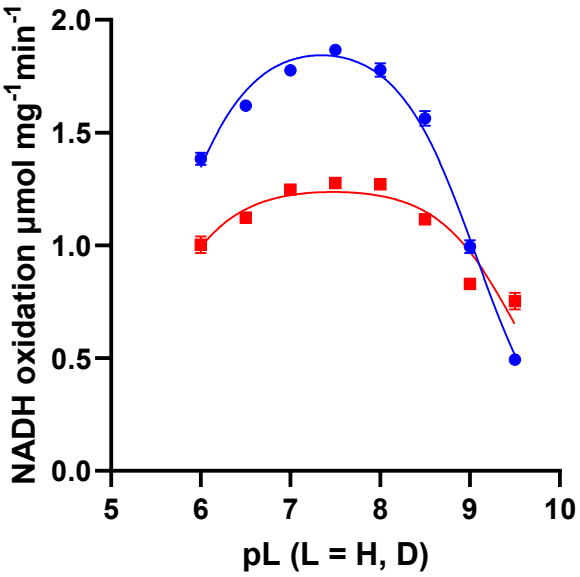

	H2O	D2O
Ymax	1.91 ± 0.04	1.26 ± 0.05
pKa 1	5.62 ± 0.07	5.43 ± 0.20
pKa 2	9.06 ± 0.04	9.53 ± 0.12

Figure 3.12 NADH:DQ rates of bovine complex I in membranes. Membranes were supplemented with 200 µM DQ and 0.15% Asolectin/Chaps The fitted V_{opt} values represent a KIE of 1.519 ± 0.06. Errors are calculated as standard error of the mean (n = 3).

3.5 Preparation and characterization of complex I-containing proteoliposomes for KIE studies

3.5.1 Characterisation of the bovine complex I proteoliposome system

Although there is strong evidence that complex I causes the observed kinetic isotope effect in bovine membranes, I decided to further confirm this by using the proteoliposome (PLs) assay system: lipid particles containing purified complex I, AOX and a titratable amount of quinone (Jones *et al.*, 2016), illustrated in Figure 3.13. The first advantage is all components in the system are known. Second is that quinone can be added at various concentrations to measure a K_M curve (Jones *et al.*, 2016; Fedor *et al.*, 2017). Third, this system allows the complete characterisation of all components: complex I concentration, AOX concentration, phospholipid content, and the membrane concentration of added quinone.

Briefly, the PL system is comprised of sealed lipid vesicles in an 8:1:1 ratio of phospholipids phosphatidylcholine (PC), phosphatidylethanolamine(PE), and

cardiolipin (CL). Complex I, when reconstituted into the lipid vesicles, will adopt one of two orientations: outward-facing or inward-facing. The outward-facing orientation is the active concentration and the matrix arm of complex I faces the outside of the PL and is accessible to solvent NADH, whereas the inward-facing arm is silent to activity. AOX, when reconstituted into PLs, does not become silent because of its orientation, as AOX acts upon a membrane-bound substrate (QH_2) and a membrane-permeable substrate (O_2).

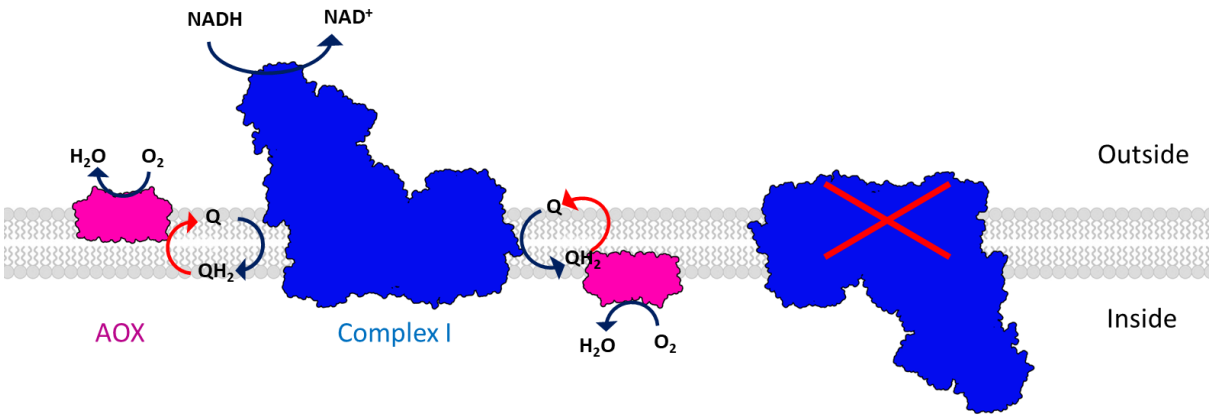

Figure 3.13 – Schematic representation of complex I proteoliposomes. Complex I, with the hydrophilic domain facing the outside of the proteoliposomes, is able to access NADH and reduce the membrane Q pool. Whereas inside facing complex I is silent. AOX acts on the membrane-soluble substrate ubiquinone and is not bound by orientation.

Here, purified complex I was co-reconstituted with AOX into proteoliposomes in a 1 mg:mg ratio to re-oxidise the substrate quinol to quinone, with an expected range of between 0 to 10 mM quinone in six separate preparations (A-F). Because the logP of Q10 is 19.4 (https://www.ncbi.nlm.nih.gov/pccompound), it is extremely hydrophobic and can be reasonably assumed to be completely partitioned within the PL lipid bilayer. Therefore, the membrane concentration of Q_{10} can be measured as the value obtained from HPLC analysis, divided by the phospholipid amount present in each PL sample, which can be measured in a phospholipid assay. The details of each assay can be found in the materials and methods section.

Complex I concentration in each proteoliposome sample was quantified using the NADH:$APAD^+$ rate relative to the rate from purified complex I. The artificial electron acceptor $APAD^+$ reacts at the flavin site with a ping-pong mechanism, reduced by the fully reduced flavin in the absence of a nucleotide (Birrell, Yakovlev and Hirst,

2009). Assays were performed with 2 μM Piericidin A added to prevent electrons from passing from the reduced flavin to quinone as a side reaction. The in/out proportion of complex I was measured by taking the ratio of rates with and without the addition of 15 μg mL^{-1} alamethicin, which permeabilises the lipid bilayer so that NADH can access both outer and inner facing complex I. The bicinchoninic acid assay (BCA) could not be used here because the BCA assay quantifies total protein concentration, which includes both the AOX and complex I, and can also be interfered with by lipid concentration in the sample (Kessler and Fanestil, 1986). Table 3.1 shows data for complex I quantification using the techniques highlighted above.

Bovine complex I: AOX proteoliposomes						
PL preparation	A - 10 mM	B - 6 mM	C - 3 mM	D - 1 mM	E - 0.5 mM	F - 0.1 mM
Phospholipid (mg/ml)	14.87 ± 0.14	18.53 ± 1.90	16.22 ± 1.01	15.93 ± 0.11	15.59 ± 0.03	17.14 ± 1.75
[Q_{10}] uM	206.38 ± 1.83	113.01 ± 3.33	49.57 ± 1.689	17.47 ± 2.07	12.85 ± 1.84	2.54 ± 0.006
[Q_{10}] (mM membrane)	13.87 ± 0.18	6.09 ± 0.65	3.05 ± 0.21	1.09 ± 0.13	0.82 ± 0.11	0.14 ± 0.01
NADH: APAD (uM/min/mg)	3.01 ± 0.09	3.51 ± 0.08	2.34 ± 0.03	2.83 ± 0.05	2.05 ± 0.04	2.69 ± 0.06
Complex I outward (ug/ml)	792.15 ± 31	921.08 ± 29	617.15 ± 15	746.42 ± 20	540.66 ± 15	708.69 ± 23
% outward facing	76%	75%	65%	77%	58%	62%

Table 3.1. Quantification of components from proteoliposomes for bovine complex I in 6 different Q concentrations. Phospholipid concentration and Q10 concentration were used to calculate the membrane concentration of Q_{10}. The concentration of complex I in each PL preparation is calculated as a ratio of measured APAD rates compared to the rate of 1ug/mL purified complex I. Errors are calculated as standard error of the mean (n = 3).

3.5.2 Complex I is rate-limiting within the proteoliposome system.

Although quantification of AOX is possible using the amido black assay to determine total protein concentration, the AOX quantification itself is unnecessary as long as AOX is at a sufficiently high concentration to allow complex I to be rate-limiting. However, because AOX could be lost during the reconstitution process at a proportion greater than complex I, it is unknown whether a saturating AOX concentration was retained. Therefore, to determine whether complex I is rate-limiting, colletochlorin B (an AOX inhibitor) was titrated into PLs, with the rates of NADH:O_2 oxidoreduction measured to determine whether the AOX concentration is saturating. Preparation A was used for this experiment as it contains the highest membrane Q_{10} concentration, and hence gives the highest NADH:O_2 oxidoreduction rate and has the greatest demand of Q pool oxidation of all prepared PL samples.

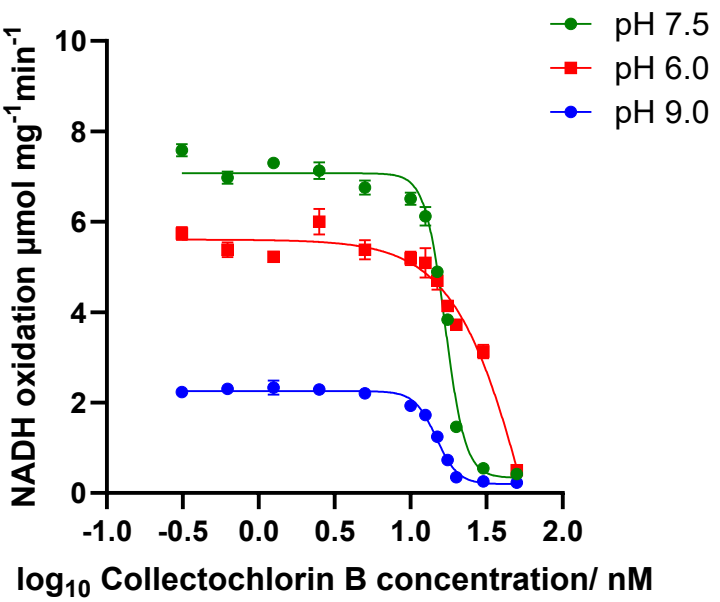

Figure 3.14 AOX is not rate-limiting within complex I proteoliposomes. Colletochlorin B, an AOX inhibitor, was titrated against NADH:O_2 oxidoreduction rate in bovine proteoliposomes with 10 mM Q_{10} and 1mg:mg AOX. IC50 values are 16.87 nM, 69.39 nM, and 14.72 nM ,respectively, at pH 7.5, 6.0, and 9.0 ,respectively. Errors are calculated as standard error of the mean (n = 3).

Figure 3.14 shows the titration curve of complex I: AOX PIs containing approximately 10 mM Q_{10}, with colletochlorin B in 3 different pH (pH 6, pH 7.5, and pH 9) as those pHs represent the experimental pH range used in subsequent analysis. At all pH, NADH:O_2 oxidoreduction rates were unaffected by colletochlorin B concentrations until approximately 10 nM addition, with IC50 values of between 14.72 nM at pH 9.0 to a high IC50 value of 69.39 at pH 6.0. Because there is a "flat" region in the IC50 assay, it shows that the amount of AOX added is in excess and saturating. In comparison, low AOX ratios show a marked decrease in IC50 (Figure 3.21). These results suggest that AOX concentration is saturating and complex I is rate-limiting within this system.

3.5.3 Measuring the isotope dependence of the kinetic parameters k_{cat}, K_M, K_{sp} for bovine complex I catalysis

To check whether complex I proteoliposomes have a catalytic behaviour consistent with previous experiments using bovine membranes, I first measured the pH-rate profile using the highest Q_{10} concentration preparation ([Q_{10}] = 13 mM) (Figure 3.15). A KIE of 1.46 ± 0.09 was found, and the fitted pKas are 5.6 and 8.4 in H_2O and 5.8

and 8.3 in D_2O. These results are consistent with previously found results in bovine membranes (Figure 3.11), confirming that the enzyme exhibiting a KIE and bell-shaped pH dependence is indeed complex I.

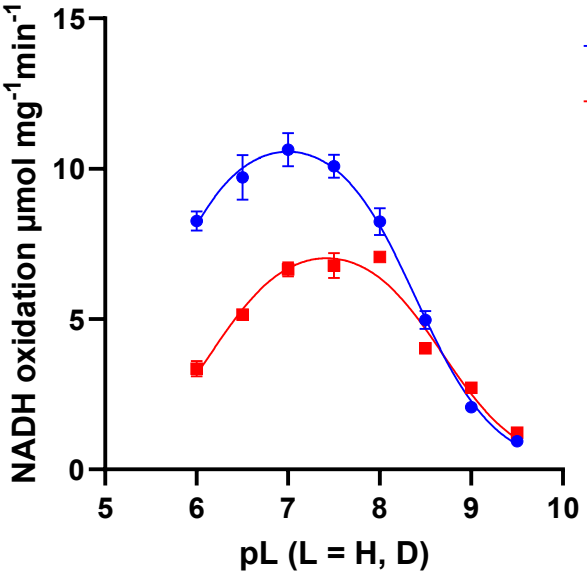

	H2O	D2O
Ymax	11.41 ± 0.18	7.802 ± 0.46
pKa 1	5.6 ± 0.05	6.16 ± 0.11
pKa 2	8.394 ± 0.03	8.675 ± 0.09

Figure 3.15 pL dependence of NADH:O_2 rates of bovine complex I in proteoliposomes reconstituted with 1 mg:mg AOX and 13 mM Q_{10}. A KIE of 1.46 ± 0.09 on V_{opt} was measured. The fitted pKas are 5.6 & 8.4 in H_2O, and 6.2 & 8.7 in D_2O. Errors are calculated as standard error of the mean (n = 3).

Furthermore, to gain additional insight into the rate-limiting step of complex I, it is informative to measure kinetic parameters and how they are affected by isotopic substitution. The activity of complex I is dependent on substrate Q_{10} and exhibits saturation kinetics, and at each pH value can be fitted well to the Michaelis-Menten equation (Equation 3.2). Figure 3.16 illustrates the parameters k_{cat}, K_{sp}, and K_M as fitted on a typical Michaelis Menten plot.

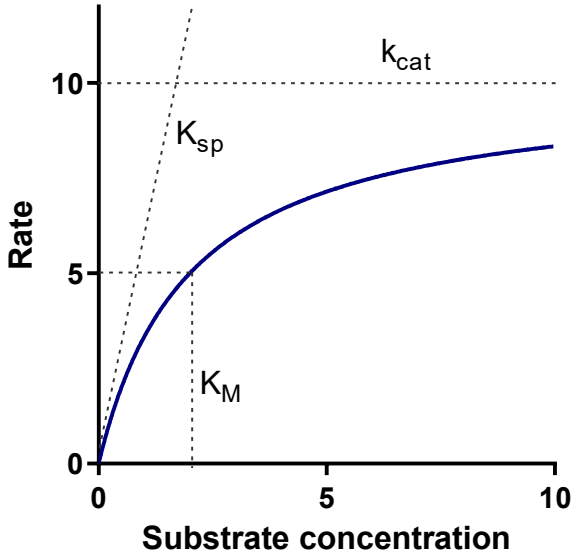

Figure 3.16 An illustrative Michaelis Menten plot wherein k_{cat} = 10, K_{sp} = 5, and K_M = 2. The rate of product formation is plotted against substrate concentration, resulting in a hyperbola due to saturating kinetics. k_{cat} represents the hypothetical rate achieved at infinite substrate concentration, wherein all enzyme binding sites are saturated with bound substrate. K_{sp} (slope) also known as the specificity constant, is the rate constant for the formation of productive enzyme-substrate complex or the net rate constant for substrate binding. K_M is the substrate concentration at which k_{cat} and K_{sp} are equal and is empirically seen as the substrate concentration at half k_{cat}.

The Michaelis-Menten equation has two main parameters, k_{cat} and K_M. A third derived parameter, commonly referred to as the specificity constant, is k_{cat}/ K_M or K_{sp} (Equation 3.3). Here, to avoid confusion, only the term K_{sp} is used. Equation 3.4 to 3.6 shows the rate constants k_{cat}, K_M, and K_{sp} as defined under Scheme 3.1, which contains an isotopically sensitive transition step converting [ES] to [EP].

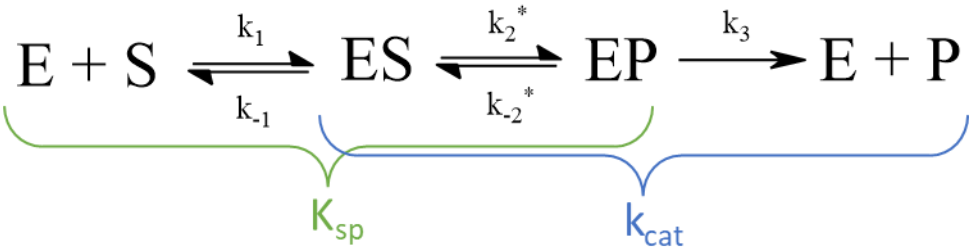

Scheme 3.1 – A reaction scheme representing substrate binding, a catalytic step, and a product release step. k_1 represents the rate of substrate encounter with the enzyme to form the enzyme-substrate complex, and k_{-1} represents the breakdown of the enzyme-substrate complex. k_2 represents the isotopically sensitive chemical step (asterisk). K_{sp} is informative for steps from substrate binding until the first irreversible step, whereas k_{cat} is informative for steps after substrate binding.

$$v = \frac{k_{cat}[S]}{K_M + [S]} \tag{3.2}$$

$$v = \frac{K_{sp}[S]}{1 + \frac{K_{sp}[S]}{k_{cat}}} \tag{3.3}$$

$$K_{sp} = k_1 \cdot \frac{k_2 k_3}{k_2 k_3 + k_{-1}(k_{-2} + k_3)} \tag{3.4}$$

$$k_{cat} = \frac{k_2 k_3}{k_2 + k_{-2} + k_3} \tag{3.5}$$

$$K_M = \frac{k_2 k_3 + k_{-1}(k_{-2} + k_3)}{k_1(k_2 + k_{-2} + k_3)} \tag{3.6}$$

k_{cat} is informative on mechanistic steps after the first substrate binding step, whereas K_{sp} is informative on mechanistic steps from the first substrate binding step until the first irreversible step (Northrop, 1998). k_{cat} is the turnover rate constant under infinite and completely saturating substrate concentration. It can be simply understood by varying [S] in the Michaelis Menten equation, where saturating [S] leads K_M to be insignificant in the rate equation, whereas at very low [S], k_{cat}/ K_M (K_{sp}) dominates the rate equation. Therefore, K_{sp} defines the rate constant for the formation of a "productive" enzyme-substrate complex: an ES complex transformed into the product rather than dissociated into the substrate and free enzyme. In other words, K_{sp} is the net second-order rate constant for substrate binding and has units of $mM^{-1}s^{-1}$.

K_M is not a primary parameter and is difficult to interpret. Empirically, K_M is equal to the substrate concentration at half maximal rate. A common mistake is to interpret K_M as the dissociation constant of substrate binding, which relies on the assumption that catalysis is extremely slow compared to the rapid equilibrium of the enzyme-substrate complex. This assumption was made by Michaelis-Menten, and therefore K_M approximates the binding constant of $K_d = [E][S]/ [ES]$ or $K_d = k_{-1}/ k_1$ However, K_M is defined by (Equation 3.6) under the steady state approximation as developed by Briggs-Haldane applied to scheme 1. In this case, only when non-binding steps rates (k_2, k_3, k_{-2}, k_{-3}) are insignificant compared to binding step rates (k_1, k_{-1}) would K_M approximate to k_{-1}/ k_1, or K_d (Beltrán and Franco, 2019). Not to mention that if k_2 is very fast, there is no such binding equilibria that occur as substrate is rapidly converted to product upon binding. Hence, rather than interpreting K_M as a static dissociation constant, it is interpreted as an "apparent dynamic dissociation constant under steady-state conditions as opposed to equilibrium conditions" (Cleland, 1959; Plesner, 1986), or in other words, K_M describes the [S] where time for substrate turnover is equal to the time for substrate binding (Northrop, 1998; Johnson, 2019); $K_M = V/(V/K) = k_{cat}/ K_{sp}$ where K_{sp} is the rate constant of formation of productive enzyme-substrate complexes, and k_{cat} is the release of product from said productive enzyme-substrate complexes. So, K_M represents the [S] that is the balance point between the net rate of substrate binding and the rate of turnover.

Substrate dependence of complex I at each pH/ pD

To obtain the kinetic parameters outlined above, the NADH:O_2 oxidoreduction rates of complex I: AOX proteoliposomes with different Q_{10} concentrations were measured between pH 6 and 9.5 in H_2O and D_2O. The resultant substrate dependence plots are shown in Figure 3.17. At all pH values, saturating kinetics were observed that could be fitted well to the Michaelis Menten equation.

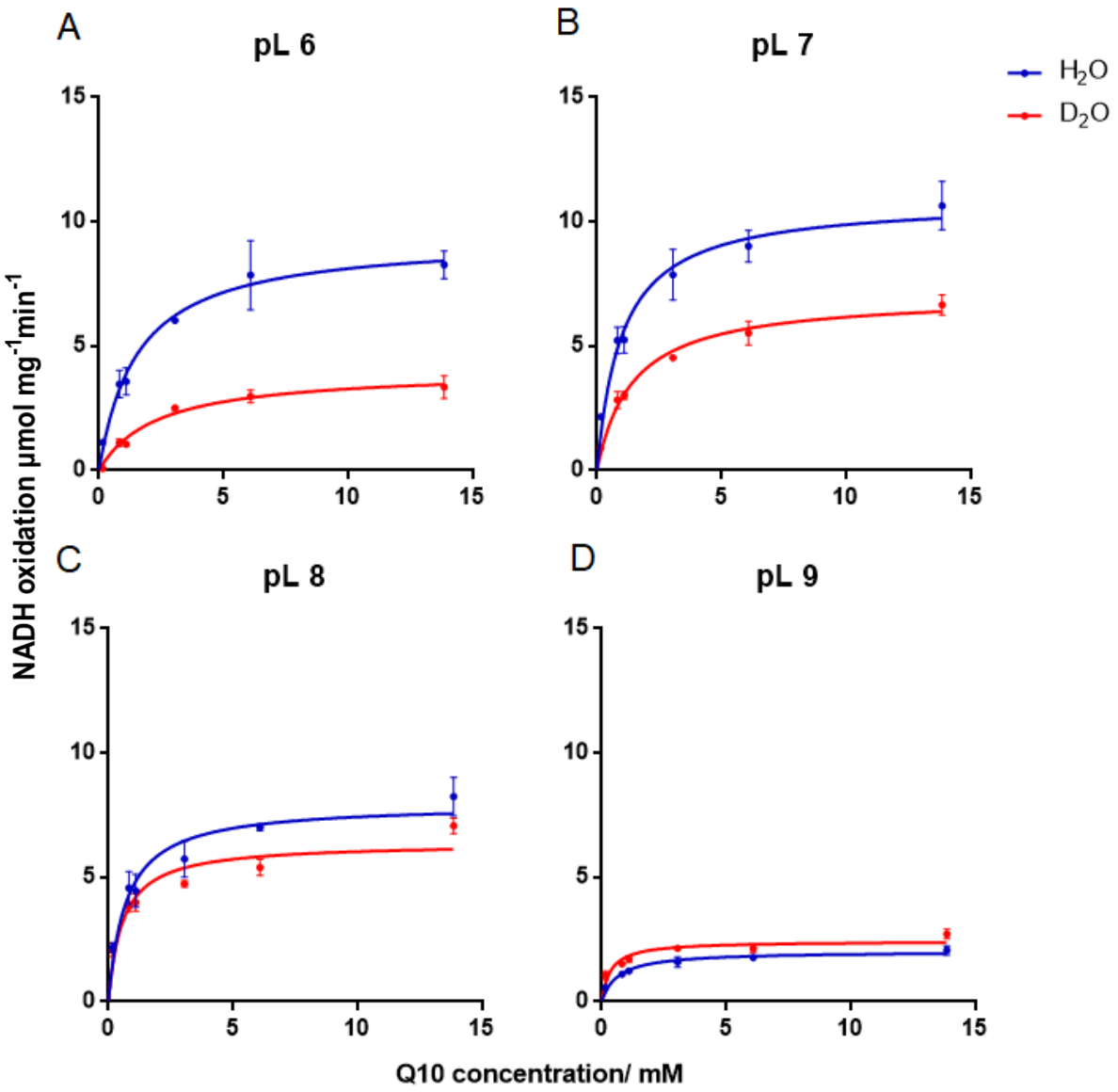

Figure 3.17. Substrate dependence plots of bovine complex I proteoliposomes. Various concentrations of Q_{10} as a substrate were measured under pH 6 – 9.5 and fitted using the Michaelis Menten equation. Only data in whole pH increments are shown. (A) pL 6. (B) pL 7. (C) pL 8. (D) pL 9. Errors are calculated as standard error of the mean (n = 3).

Fitting the pH/ pD independent variables of k_{cat} and K_{sp}

To determine the pH and pD dependence of k_{cat} and K_{sp} and determine the pH and pD independent optimal rate of each parameter, the fitted values derived from substrate dependence plots at each pH are fitted to equation 3.1. Figure 3.18 shows the pL (pL = pH or pD) dependence of k_{cat} and K_{sp}. These parameter values were generated using the curve fitting and graphing software Prism. Unlike k_{cat}, the pH-independent value of K_{sp} is not fitted to equation 3.1. This is because K_{sp} is dependent on pKa values of the parameters k_{cat} and K_M. Fitted pKa values have high experimental errors as they rely on every point on the pH curve, compounding the error of the entire dataset. Since V_{opt} of equation 3.1 depends on fitted pKa values, fitting K_{sp} compounds the pKa error of both k_{cat} and K_M datasets. Also, the pKa of K_{sp} is dependent on the pH-dependence of K_M, which has high relative errors especially at low rates (extremes of pH). To avoid drawing erroneous conclusions, throughout this work, the maximum K_{sp} is taken as the largest calculated value within the pH/ pD series and is not equation-fitted.

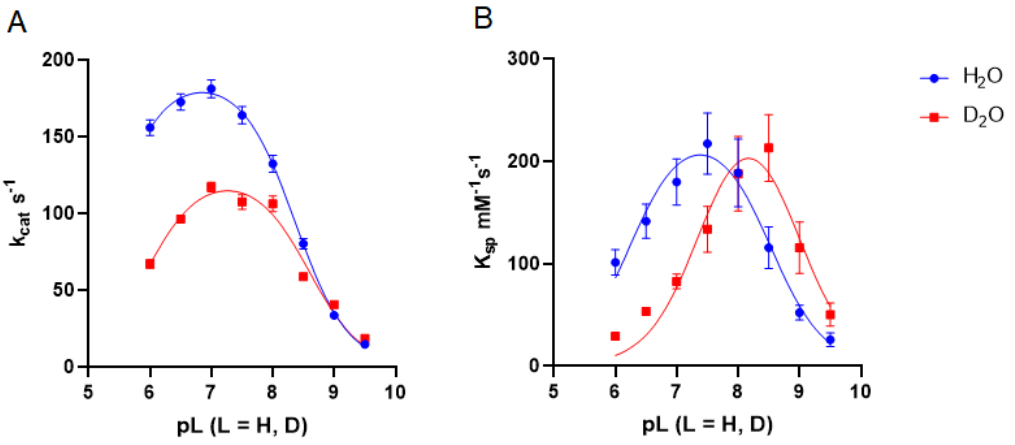

	H2O	D2O
Ymax	189.6 ± 2.1	125.6 ± 6.8
pKa 1	5.3 ± 0.05	5.9 ± 0.1
pKa 2	8.4 ± 0.02	8.6 ± 0.09

Figure 3.18 pL dependence of k_{cat} and K_{sp} of bovine proteoliposomes. (A) shows how fitted k_{cat} values of bovine complex I activity vary with pH and isotopic substitution. k_{cat} values were fitted using the Michaelis Menten equation, and the pH-independent value of k_{cat} was fitted using equation 1. The inset table shows the derived parameters from fitting to equation 3.1, where Y_{max} is the pH-independent value of k_{cat}. The fitted KIE on the pL-independent k_{cat} is 1.51 ± 0.08. (B) The maximum K_{sp} is not isotope dependent. Errors are standard error values calculated using Prism 9, and KIE is calculated using error compounding (n = 3).

It is immediately striking that the KIE of k_{cat} ($^{D}k_{cat}$) is 1.51 ± 0.08. However, the KIE on K_{sp} ($^{D}K_{sp}$) is one and not isotopically sensitive in bovine complex I with Q_{10}. Considering Scheme 3.1, This means that substrate binding is not the isotopically sensitive step because otherwise, a KIE will be measured in K_{sp} but not k_{cat} (Northrop, 1975).

Interpreting the relationship between $^{D}k_{cat}$ and $^{D}K_{sp}$.

The relationship between the KIE of k_{cat} and K_{sp} is informative on the magnitude of each catalytic step and, therefore, allows an estimation of the rate-limiting step. Under scheme 1, Equations 3.7 and 3.8 describe the observed isotope effect on K_{sp} and k_{cat}. The two equations, 3.7 and 3.8, are derived by dividing equation 3.4 and 3.5 in H_2O by itself in D_2O. Resulting in parameters $KIE_{Int,}$ the intrinsic KIE for microscopic rate constant k_2, and various ratios known as commitment factors. Where $C_f = k_2/ k_{-1}$, and $C_{vf} = k_2/ k_3$ are the forward commitment factors for K_{sp} and k_{cat} respectively, and $Cr = k_{-2}/ k_3$ is the reverse commitment factor. The equilibrium isotope effect term, $EIE = (k_2^H/ k_2^D)/ (k_{-2}^H/k_{-2}^D)$, is the ratio of KIE for the forward and reverse reaction for the isotope-sensitive step and is generally considered to be one and can be ignored, but is included here for completeness (Quinn and Sutton, 1991).

$$\frac{(K_{sp})_H}{(K_{sp})_D} = \frac{KIE_{Int} + C_f + C_r.EIE}{C_f + C_r + 1}; C_f = \frac{k_2}{k_{-1}}; C_r = \frac{k_{-2}}{k_3} \tag{3.7}$$

$$\frac{(k_{cat})_H}{(k_{cat})_D} = \frac{KIE_{Int} + C_{vf} + C_r.EIE}{C_{vf} + C_r + 1}; C_{vf} = \frac{k_2}{k_3}; C_r = \frac{k_{-2}}{k_3} \tag{3.8}$$

The lower the commitment factors, the closer the observed isotope effect on K_{sp} and k_{cat} is to the intrinsic isotope effect on k_2. C_r affects both k_{cat} and K_{sp}, and the two parameters differ by their dependence on C_{vf} and C_f respectively.

In the reaction of bovine complex I with the substrate Q_{10}, ^{D}Ksp is lower than $^{D}k_{cat}$. Since C_r is shared among the two parameters, the lower isotope effect on K_{sp}

suggests that C_f is high and is also comparatively higher than the corresponding forward commitment factor C_{vf} for k_{cat} ($C_f > C_{vf}$). In other words, the observed isotope effect on K_{sp} is more suppressed than that for k_{cat}, and that the rate of substrate release from the ES complex, k_{-1}, is lower than the rate of product release k_3.

Observed KIE on rate increases with Q_{10} concentration

At each [Q_{10}], the pH/ pD independent values of rate are fitted with equation 3.1. Figure 3.19A shows that the observed KIE increases with increasing Q_{10} concentration. The catalytic rate is defined by K_{sp} at very low substrate concentration and defined by k_{cat} at high [S]. So, the observed KIE at a low Q concentration of ~0.14 mM approximates unity and increases to the maximum KIE at a substrate concentration of approximately 1 mM Q_{10}. At any [S], the observed isotope effect on measured rates is the weighted average of the observed KIE on k_{cat} and K_{sp}, so as [S] increases the observed KIE on measured rate shifts from that observed in K_{sp} to that in k_{cat}. Substrate binding is second order and dependent on substrate concentration and becomes rate-limiting at very low [S]. Because the steady-state distribution of the enzyme form [E_T] approximates the free-enzyme [E_f], no isotope effect is observed at low [S] (Northrop, 1975).

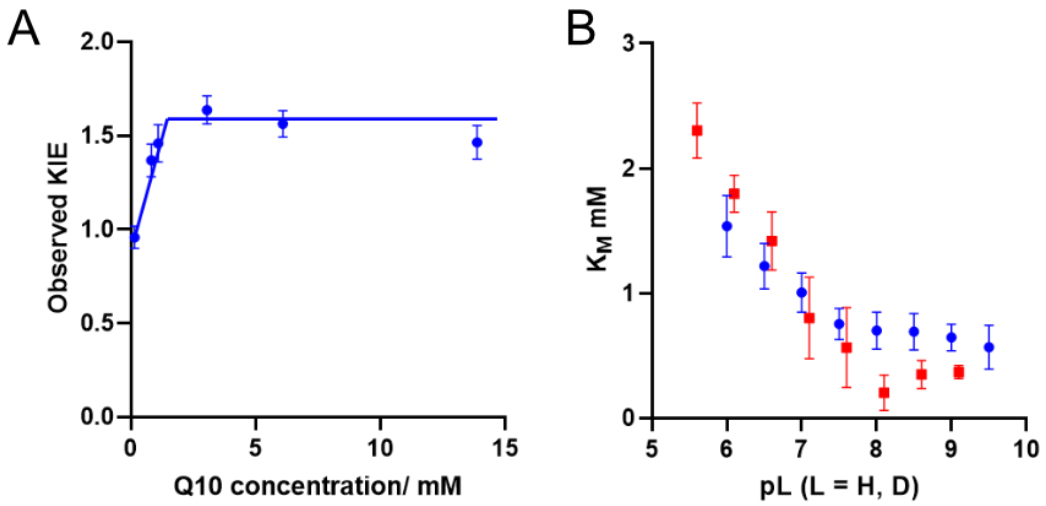

Figure 3.19 KIE of pL independent rate is substrate concentration-dependent, and K_M is pH-dependent. (A) At each substrate concentration, pH rate profiles are fitted with Equation 1, and the KIE on the fitted Vopt value of measured rates is plotted. At low (~0.1 mM) Q_{10}, observed KIE is approximately unity and increases to the maximum of ~1.5 at a substrate concentration of ~ 1 mM. (B) K_M at each pL is fitted using the Michaelis Menten equation and is pL dependent with lower pL increasing K_M. There is no clear isotope effect on K_M. Errors are standard error values calculated using Prism 9.

These results suggest that the isotopically sensitive step is linked to quinone reduction. However, these experiments do not give information on whether quinone reduction specifically is the most rate-limiting step, as the rate-limiting step may be an isotopically insensitive step. In this case, the observed isotope effect is different to the intrinsic isotope effect.

The pH dependence of K_M is uni-directional (Figure 3.19B), with increasing pH decreasing K_M. Uni-directionality suggests that it is the result of a titration of a single pKa that controls this behaviour. There is no clear isotope dependence on the magnitude of K_M, and values for the isotope effect on K_M have no diagnostic utility (Northrop, 1975), so it will not be discussed in this thesis. It is tempting to interpret this change in K_M as the increasing affinity of Q_{10} binding with increasing pH, but that need not be true if the rapid equilibrium assumption does not hold (see above). Because K_M is the apparent dynamic dissociation constant under a steady state (Cleland, 1959; Plesner, 1986), and $K_M = k_{cat}/ K_{sp}$, it is unclear whether it is substrate "capture" that is relatively slower or turnover is relatively higher at lower pH.

3.6 Effect of membrane potential on observed kinetic isotope effects

3.6.1 Optimization of bovine submitochondrial particles for KIE measurements

There are multiple potentially isotope-sensitive proton transfer steps in the catalytic mechanism of complex I, and therefore I attempted to differentiate proton pumping steps (vectoral protons) from quinone reduction steps (chemical protons). Although both sets of steps are likely to exhibit intrinsic isotope sensitivity, the relevant question to this topic is whether the step is sufficiently rate-limiting for its effects to be manifest in a KIE for the entire catalytic reaction.

Computational modelling has previously suggested that steps involved in proton pumping in the membrane domain have a pmf-dependent activation energy barrier (Kaila, 2021). Specifically, the release of protons from the antiporter subunits to the p side of the mitochondrial membrane, and subsequent re-charging of these domains against a 200 mV pmf (as opposed to 0 mV) is calculated to cost an extra 10 kcal mol^{-1} of free energy (Kaila, 2021). If the isotope-sensitive step has a pmf-dependent activation energy barrier, it is expected that lowering the rate constant in this step by

increasing the pmf will make this step more rate-limiting and change the observed KIE.

When this experiment was conducted, bovine complex I proteoliposomes prepared with the bio-beads method (Jones *et al.*, 2016; Fedor *et al.*, 2017) are unsuitable for studying the effects of pmf on catalytic activity, as they remain leaky to protons when reconstituted with bovine complex I. Therefore, bovine submitochondrial particles (SMPs) were prepared and used for the following experiments. Bovine SMPs are inverted sealed vesicles of the inner membrane (Fedor and Hirst, 2018) that can retain Δp. Bovine SMPs prepared for the following experiments have a respiratory control ratio of (RCR) of 2.33, measured without the addition of AOX or cyanide. The RCR is the factor by which NADH: O_2 rates increase upon the uncoupling of the membrane by the addition of an ionophore Gramicidin A and is often used as a test of membrane integrity.

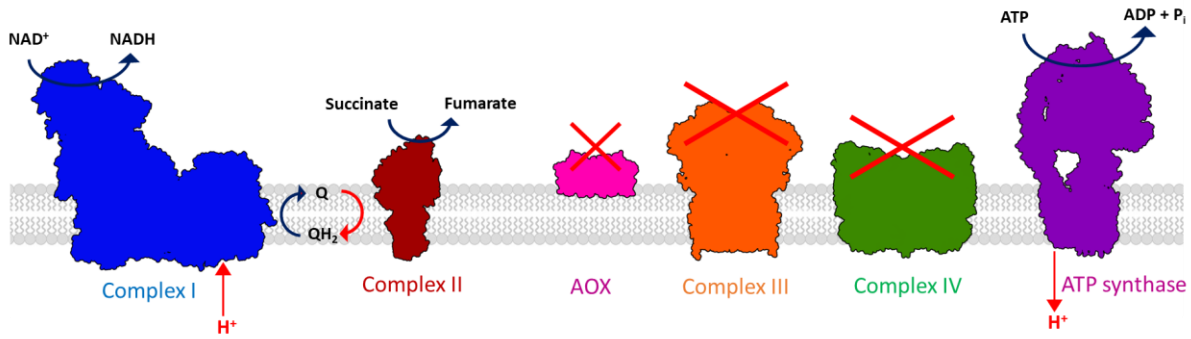

Figure 3.20 Reverse electron transfer (RET) in complex I. RET assays are conducted under anaerobic conditions to deprive AOX and complex IV of oxygen so that the Q pool remains reduced. The Q pool is reduced by succinate oxidation by complex II. Complex IV is further inhibited with cyanide to inhibit complex III and IV activity. Δp is created by the addition of ATP to drive ATP hydrolysis by ATP synthase. This Δp is consumed by complex I to drive QH_2 oxidation and the energetically unfavourable reaction to reduce NAD^+ to NADH.

AOX is required to functionally isolate complex I activity and ensure complex I is rate-limiting, but it is purified with associated detergent n-dodecyl β-D-maltoside (DDM), which disrupts membrane integrity (Fedor and Hirst, 2018). To check how much AOX can be added without disrupting membrane integrity, I measured reverse electron transfer (RET) activity with increasing AOX concentration. In RET (illustrated in Figure 3.20), NAD^+ is reduced by complex I, driven by high Δp created by the addition of ATP and its hydrolysis by ATP synthase, as well as a reduced Q

pool through succinate oxidation by complex II (Chance and Hollunger, 1960; Pryde and Hirst, 2011). To force the equilibrium towards RET, the assay must be performed in an anaerobic glove box to render AOX and complex III, IV inactive (as AOX inhibitors also inhibit RET in complex I by competitively inhibiting the Q-binding site).

Figure 3.21A shows how the rate of RET is affected by the addition of AOX and that the RET rate is maintained with the addition of 0.2:1 mass ratio of AOX to SMPs, whereas the addition of Gramicidin causes immediate rupture of the membrane and eliminates RET activity. This result agrees with previous data by Fedor et al. (Fedor and Hirst, 2018), showing that RET Is maintained until the addition of 0.25:1 mass ratio of AOX to SMP, beyond which a sharp decrease in RET activity is observed.

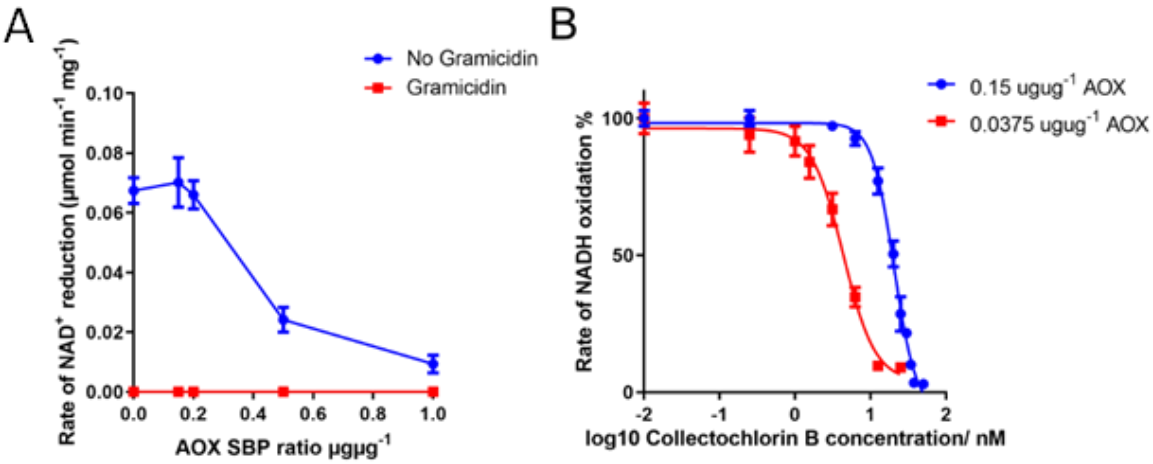

Figure 3.21 Bovine SMPs remain intact with a saturating amount of AOX addition. (A) Reverse electron transfer (RET) reaction by bovine SMPs as a function of AOX concentration. RET is maintained up until the addition of 0.2 µg µg^{-1} of AOX, but higher ratios lead to uncoupling of the membranes. (B) Normalised rates of NADH:O_2 reaction by bovine SMP with high AOX (0.15:1 mass ratio) and low AOX (0.0375 mass ratio) inhibited by Colletochlorin B, an AOX inhibitor. IC50 values are 20.54 nM and 4.36 nM for high and low AOX amounts, respectively. Errors are calculated as standard error of the mean (n = 3).

To provide a margin of safety from the uncoupling effects of AOX-associated DDM, I added a 0.15 mass ratio of AOX to SMPs. To test whether this concentration is sufficient to make complex I rate-limiting, I measured the IC50 values of NADH:O_2 oxidoreduction rates titrated with Colletochlorin B within the SMP system reconstituted with two concentrations of AOX (0.15 and 0.0375 mass ratio), with the

lower AOX concentration providing a form of negative control. Figure 3.21B shows that low concentrations of Colletochlorin B had no effect on NADH:O_2 oxidoreduction rates on 0.15 ug ug^{-1} AOX, and a significant reduction in rate only occurs after ~10 nM of Colletochlorin B addition. This shows that the AOX concentration in this sample is in excess and saturating. In contrast, the 0.0375 µg $µg^{-1}$ AOX sample had a significant reduction in rate upon only ~1 nM of Colletochlorin B addition. The IC50 of 0.15 µg $µg^{-1}$ and 0.0375 µg $µg^{-1}$ is 20.54 nM and 4.360 nM respectively, representing a ~5x difference. This demonstrates that with a 0.15 mass ratio of AOX added, complex I is rate-limiting within the SMP assay system. Therefore, I chose to supplement SMP with 0.15:1 µg $µg^{-1}$ of AOX as it is sufficiently high to make complex I rate-limiting but also sufficiently low to retain membrane integrity.

3.6.2 Delta P does not change observed KIE in bovine submitochondrial particles

NADH:O_2 oxidoreduction rates by bovine SMPs were measured between pH 6 and pH 9.5 in the presence or absence of Gramicidin A in either H_2O or D_2O (Figure 3.22), with KIE measured as the ratio of V_{opt}, as fitted with equation 1. There is no change in pH dependence with the addition of gramicidin, suggesting that the rate-limiting step has remained the same. The observed KIE is 1.24 ± 0.079 and 1.17 ± 0.105, with and without the addition of gramicidin respectively, and the difference is not statistically significant beyond 95% confidence. The magnitude of the KIE is smaller than that observed in bovine membranes or proteoliposomes for both samples, which suggests that there may be a degree of substrate limitation. However, this does not confound the interpretation of the results because it is not the absolute value of the KIE that is of interest but the relative change.

Using only the kinetic perspective, a few scenarios can be expected. First, if the presence of Δp changes the rate-limiting step to proton pumping, and that proton pumping steps have a distinct intrinsic KIE, then a change in the observed KIE and rate (RCR effect) is expected. Second, there is no change in rate-limiting step with Δp, but its activation barrier is Δp dependent. This would yield no change in KIE, but an RCR effect (KIE depends only on ΔZPE, not $\Delta G^{‡}$). Third, if proton pumping steps are not rate-limiting at all, and the rate-limiting step is not Δp dependent, then there will be no change in observed isotope effect, nor an RCR effect. Alternatively, using the thermodynamic perspective, addition of gramicidin modally changes the function

of complex I by eliminating the RET reaction, and alters the free-energy landscape of complex I. The presence of Δp make reverse steps more favourable by altering the thermodynamic equilibrium between FET and RET towards RET by reducing the forward driving energy ΔE/2 – Δp. In this regime, RCR is reflective not purely on a Δp dependent activation barrier, but instead on the overall thermodynamic equilibrium between FET and RET. Since it is expected that no equilibrium isotope effect (EIE) occurs, the isotope effect in the forward and reverse direction for each catalytic step is identical, thus no change in observed KIE can be expected unless a different step has become rate-limiting, and that step has a different intrinsic KIE. This is evidenced by the observation that RCR is AOX concentration dependent (Figure 3.22B).

No difference was observed in the KIE with the addition of a Δp, but an RCR effect of 1.35 was observed. This suggests that the identity of the rate-limiting step is unchanged, and that there is a thermodynamic effect when Δp is introduced. However, this experiment does not allow for identification of the rate-limiting step.

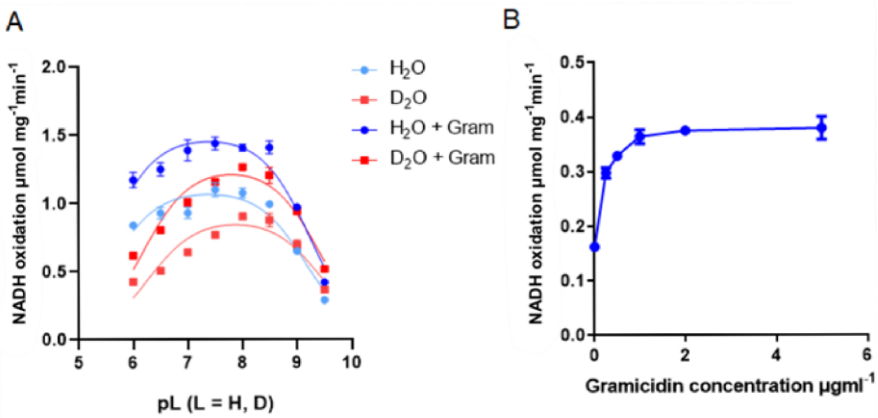

	H2O	D2O	H2O + Gram	D2O + Gram
Ymax	1.1 ± 0.05	0.9 ± 0.07	1.5 ± 0.06	1.3 ± 0.06
pKa 1	5.6 ± 0.2	6.3 ± 0.2	5.5 ± 0.2	6.2 ± 0.1
pKa 2	9.2 ± 0.1	9.5 ± 0.2	9.2 ± 0.1	9.4 ± 0.1

Figure 3.22 pL dependence of NADH:O_2 oxidoreduction rates in bovine SMPs with and without Gramicidin A. (A) pH dependence of NADH: O_2 oxidoreduction rate of bovine SMP supplemented with 0.15:1 mass ratio of AOX in H_2O and D_2O, with and without the addition of 2 µgmL^{-1} gramicidin A. Observed KIE on V_{opt} is 1.24 ± 0.079 and 1.17 ± 0.105, with and without the addition of gramicidin respectively. (B) Gramicidin was titrated into bovine SMPs without the addition of AOX or cyanide. 2 µgmL^{-1} was found to be sufficient to uncouple the membranes and give the highest RCR value of 2.3. Errors are calculated as standard error of the mean (n = 3).

3.6.3 Delta P does not change observed KIE in *Y. lipolytica* WT proteoliposomes

The above experiment was repeated in a purer system with a higher known observed isotope effect and a modifiable quinone concentration. *Y. lipolytica* complex I proteoliposomes remain fully coupled, retaining a Δp (Dröse, Galkin and Brandt, 2005; Wright *et al.*, 2022). The method used to prepare the proteoliposomes is described in (section 2.6) and is a more up-to-date method compared to that used for bovine proteoliposomes above (Biner *et al.*, 2020). *Y. lipolytica* complex I has a higher observed KIE (see section 3.7), which allows smaller changes to be observed compared to bovine complex I. Here, I reconstituted WT *Y. lipolytica* complex I into proteoliposomes with 13 mM Q_{10} concentration to make quinone binding and reduction steps as fast as possible so that proton pumping steps are as relatively rate-limiting as possible. The pL dependence of NADH:O_2 oxidoreduction rates was measured with and without the addition of 0.5 $\mu g ml^{-1}$ Gramicidin A to uncouple the membrane (Figure 3.23). 20:1 mass ratio of AOX was added to the solution assay, a concentration found to be saturating but does not uncouple membranes (Wright *et al.*, 2022). pL rate profiles were fitted to equation 3.1 and the pL independent rates were calculated using Prism 9.

As the membrane quinone concentration is at least five-fold higher than K_M across the pL range, measured rates approximate V_{max}. Consistent with that observed in bovine SMPs, *Y. lipolytica* complex I displays a KIE of 2.10 ± 0.16 and 2.13 ± 0.15 in samples with and without the addition of gramicidin A respectively, showing that the presence of Δp does not change the measured isotope effect. An RCR of 1.2 was measured, suggesting that membranes are intact. In totality, considering the same observation in bovine SMPs, as well as the quinone concentration dependence of the observed KIE, it is highly likely that quinone reduction but not proton pumping steps are the primary isotope-sensitive step in mitochondrial complex I. A system where proton pumping steps are rate-limiting is explored in Chapter 4.

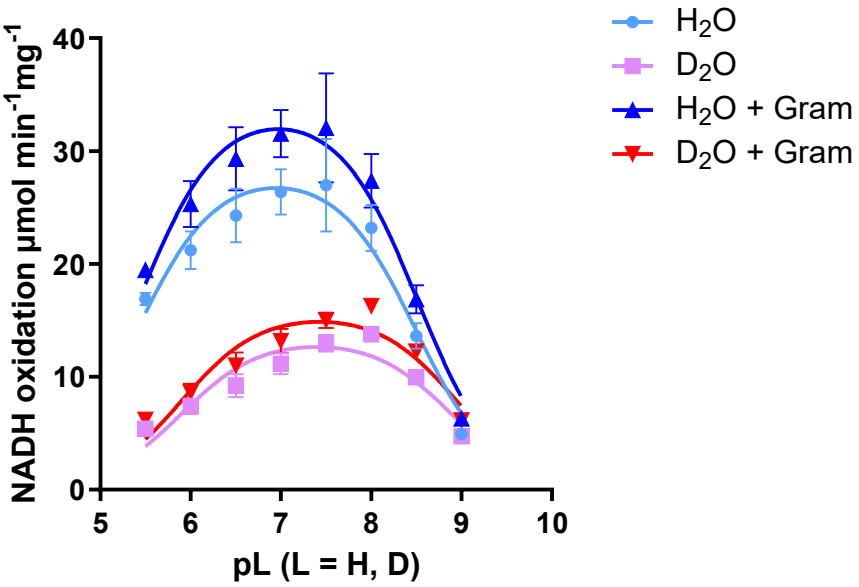

	H_2O	D_2O	H_2O + Gram	D_2O + Gram
Ymax	28.2 ± 1.5	13.4 ± 0.74	33.8 ± 1.7	15.8 ± 0.8
pKa 1	5.4 ± 0.13	5.9 ± 0.11	5.4 ± 0.12	5.9 ± 0.1
pKa 2	8.5 ± 0.11	8.9 ± 0.12	8.5 ± 0.1	8.9 ± 0.11
KIE	2.1 ± 0.16		2.13 ± 0.15	

Figure 3.23 The pL dependence of NADH:O_2 oxidoreduction rate of *Y. lipolytica* WT complex I proteoliposomes with and without the addition of 0.5 µgml^{-1} gramicidin. A 20:1 mass ratio of AOX was added to make complex I rate-limiting. PL rate profiles are fitted to equation 1. Observed KIE was 2.10 ± 0.16 and 2.13 ± 0.15 with and without the addition of gramicidin, the difference of which is not significant. An RCR of 1.2 was detected. Errors are calculated as standard error of the mean (n = 3).

3.7 Measuring kinetic isotope effect of *Y. lipolytica* complex I in mitochondrial membranes

3.7.1 *Y. lipolytica* complex I exhibits an isotope effect

As an initial test of whether *Y. lipolytica* complex I displays a solvent isotope effect (like bovine complex I), the dNADH:O_2 oxidoreduction rates were measured in pL 7.5 using 150 µM of dNADH and a saturating concentration of cytochrome C at 8 µM (Figure 3.24). Because the *Y. lipolytica* strains used in this study have an internally directed NDH-2, deamino NADH (dNADH), an analogue of NADH with the adenine moiety replaced with a hypoxanthine was used instead to specifically measure the activity of complex I, as NDH2 cannot oxidize dNADH (Matsushita, Ohnishi and

Kaback, 1987). A KIE of 1.36 ± 0.04 was observed, which is consistent with that observed in bovine complex I in membranes.

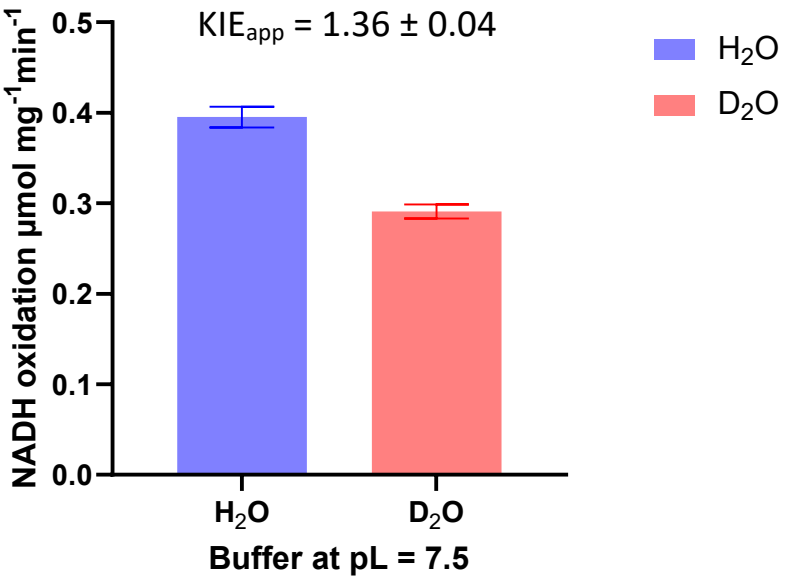

Figure 3.24 *Y. lipolytica* complex I displays a solvent isotope effect similar to bovine mitochondrial complex I. The dNADH:O_2 oxidoreduction rates of *Y. lipolytica* membranes at pH 7.5 and pD 7.5 were measured using. 150 µM dNADH and 8 µM cytochrome C. An apparent KIE of 1.36 ± 0.04 was measured. Errors are calculated as standard error of the mean (n = 3).

3.7.2 The reversibility of pH inactivation of *Y. lipolytica* complex I

To differentiate between pH effects on enzyme denaturation and ionization state changes, I measured the pH tolerance of *Y. lipolytica* WT complex I in the method described in section 3.4.1, with the exception that 150 µM of dNADH was added instead of NADH as the electron donor. Figure 3.25 shows that like bovine complex I, *Y. lipolytica* complex I, when pre-incubated at a high pH, retained its activity, but pre-incubation at a pH lower than 5.5 caused irreversible inactivation.

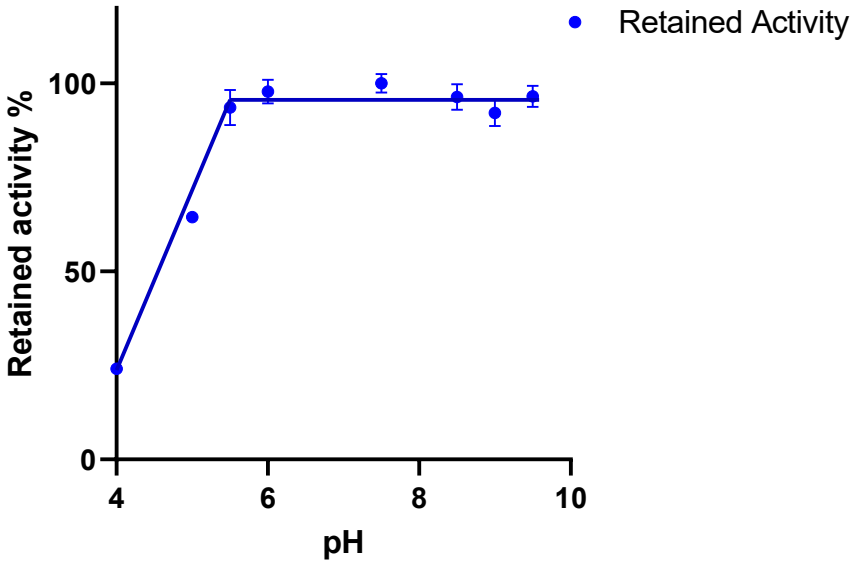

Figure 3.25 Reversibility of pH-inactivation of *Y. lipolytica* complex I in membranes. Complex I activity was measured after 1-hour incubation at each corresponding pH and measured after dilution in pH 7.5 buffer. the ratio of activity to the maximum at pH 7.5 is plotted as the retained activity. Errors are calculated as standard error of the mean (n = 3).

3.7.3 The effect of quinone binding site mutations on the expression of complex I in mitochondrial membranes

Mitochondrial membranes were prepared for each of the 5 variants (Y144F, D196N, M91I, H95M, and WT) using the large-scale preparation described in section 2.3.1. These mutants were previously generated by Dr. Andrew Jones, using the methods as described in section 2.2.1. dNADH:APAD$^+$ oxidoreduction activity, dependent on the flavin site, was measured to approximate complex I expression. It is expected that mutations in the quinone binding site do not affect the reaction kinetics at the flavin site, and so given the same amount of complex I, the dNADH:APAD$^+$ rates should be approximately identical. Figure 3.26 shows that all variants expressed close to normal amounts of complex I, from 73% to 89% of WT. Thus, all variants of complex I can express and assemble into stable complex I, and mutations did not affect the abundance considerably.

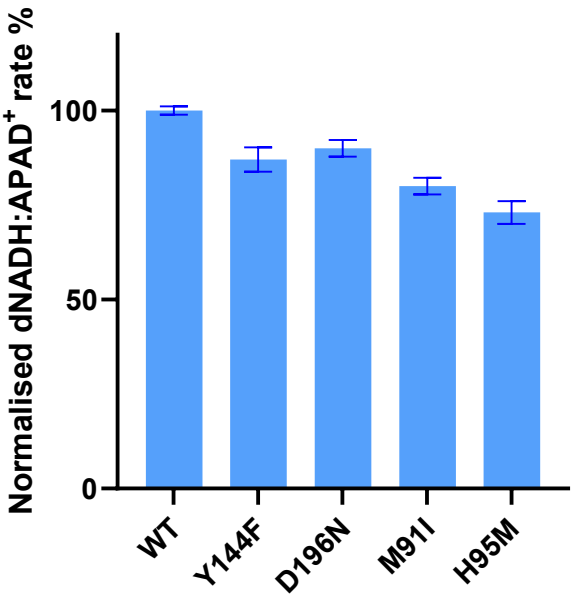

Figure 3.26 Normalised dNADH:APAD$^+$ rates of mitochondrial membranes prepared from each *Y. lipolytica* variant. 100 µM dNADH was added as the electron donor and 500 µM APAD$^+$ as the electron acceptor. 2 µM piericidin was added to inhibit quinone reduction by complex I. All variants expressed between 73% and 89% of WT. Errors are calculated as standard error of the mean (n = 8).

3.7.4 Short-chain quinones rescue the catalytic activity of complex I in membranes

The pH-dependent dNADH:O_2 oxidoreduction activity (Q_9) of each *Y. lipolytica* variant was determined between pL 5.5 and 9. Mitochondrial membranes were supplemented with 1 mg:mg AOX and 400 µM cyanide to measure the activity using the native quinone Q_9 as a substrate. Except for the *Y. lipolytica* WT variant, all variants displayed rates <5% and were not measurable, which is consistent with previously published results (Data not shown).

However, piericidin-sensitive activity in all variants except H95M can be measured when Q_1 was added as a substrate. Figure 3.27 shows the dNADH:Q_1 oxidoreduction activity of the *Y. lipolytica* variants across pL 5.5 to 9 in mitochondrial membranes supplemented with 200 µM Q_1. The measured rates were normalized to complex I content by adjusting the assay enzyme concentration using dNADH:APAD$^+$ activity.

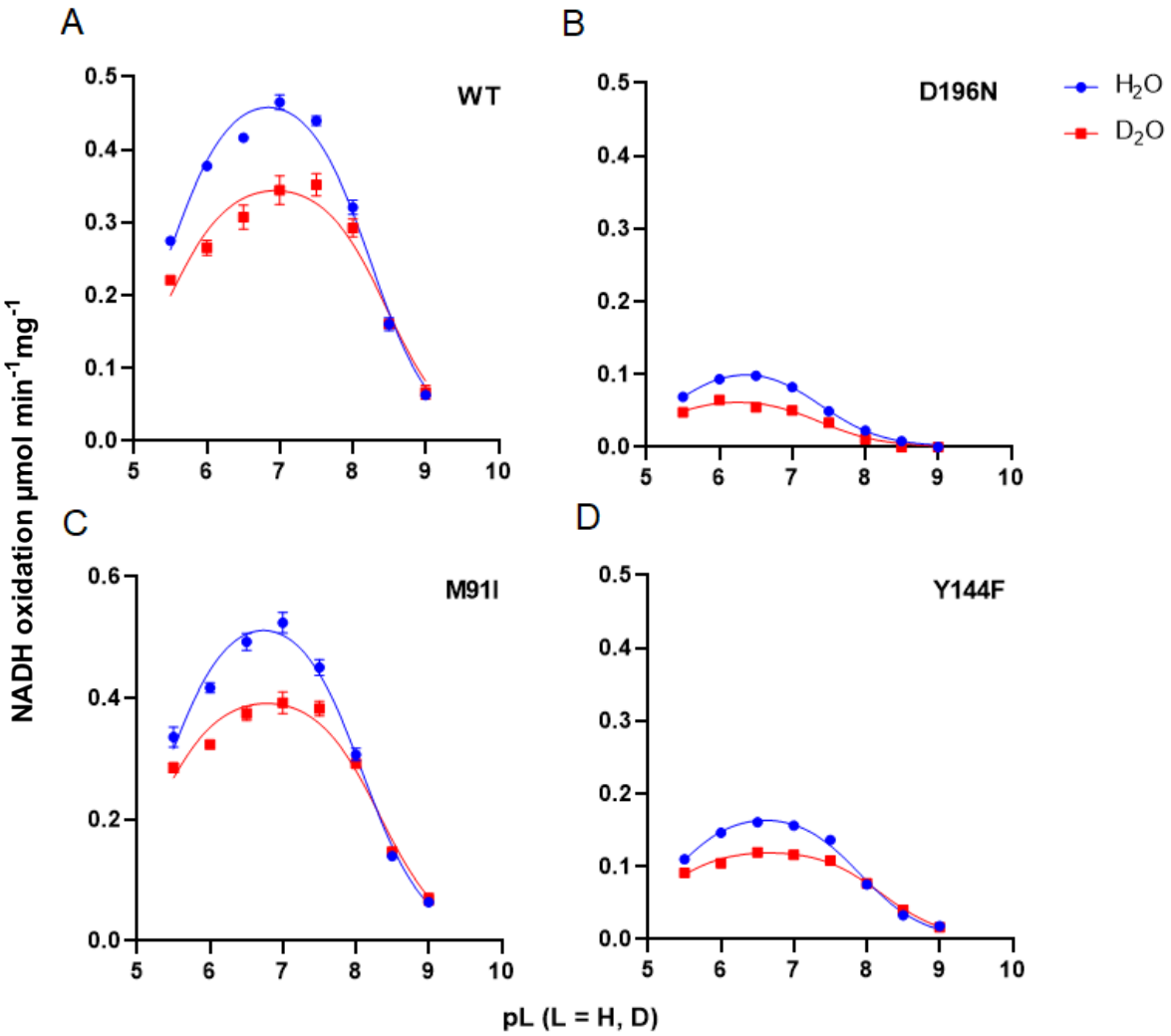

	Ymax H_2O	Ymax D_2O	pKa 1 in H_2O	pKa 1 in D_2O	pKa 2 in H_2O	pKa 2 in D_2O
WT	0.49 ± 0.02	0.36 ± 0.02	5.4 ± 0.07	5.4 ± 0.06	8.2 ± 0.10	8.5 ± 0.10
D196N	0.12 ± 0.001	0.07 ± 0.006	5.4 ± 0.07	5.1 ± 0.06	7.9 ± 0.09	7.9 ± 0.08
M91I	0.56 ± 0.02	0.41 ± 0.02	5.4 ± 0.07	5.2 ± 0.06	8.0 ± 0.09	8.3 ± 0.09
Y144F	0.18 ± 0.01	0.12 ± 0.002	5.3 ± 0.07	5.1 ± 0.06	7.9 ± 0.09	8.2 ± 0.10

Figure 3.27 pL dependence of dNADH:Q_1 oxidoreduction rates of Y. lipolytica mitochondrial membranes in 4 different variants. (A) WT variant. The observed KIE on V_{opt} is 1.36 ± 0.13. (B) D196N variant. The observed KIE on V_{opt} is 1.71 ± 0.16. (C) M91I variant. The observed KIE on V_{opt} is 1.36 ± 0.13. (D) Y144F variant. The observed KIE on V_{opt} is 1.5 ± 0.14. Errors are calculated as standard error of the mean (n = 3).

The pL profiles of *Y. lipolytica* variants in mitochondrial membranes are all bell-shaped curves with pKa values of approximately 5 and 8 and are less than 0.5 pH units apart from the WT enzyme. This is consistent with previous results seen in bovine complex I (membranes and proteoliposomes). The exception is pKa 2 in D196N, which is 0.6 pH units more acidic than WT. However, because this is not reproducible in other assay systems (see section 3.8), this is likely because of

measurement error due to the low rates of activity in that mutant, as fitted pKa values can be altered by a single inaccurate point on the curve.

The pH-independent maximum dNADH:Q_1 oxidoreduction activity of M91I and D196N are 114% and 24% of WT respectively, in line with previously published results. The rate of Y144F however is 36% of WT, which is lower than the 72% reported by Tocilescu et al. (Tocilescu, Fendel, *et al.*, 2010). Reported apparent K_M increases from 9 µM in WT to 54 µM in the Y144F variant, and the concentration of Q_1 is necessary to reach the maximum rate was not published. So, the Q_1 concentration (200 µM) used in this experiment may not be sufficient to allow Y144F to reach its maximum rate in membranes, accounting for the discrepancy. However, the addition of a higher concentration of Q_1 leads to precipitation of the soluble substrate, affecting the spectrometric measurement of the assay.

The observed isotope effects are 1.36 ± 0.13, 1.36 ± 0.13, 1.71 ± 0.16, and 1.5 ± 0.14 in the variants WT, M91I, D196N, and Y144F respectively. The magnitude of the KIE is similar to that observed in bovine mitochondrial membranes, which is approximately 1.4. Variant D196N exhibits a larger isotope effect of 1.71, which is statistically significant to that of the WT variant. This suggests that either the intrinsic isotope effect has increased, or the isotopic step has become more rate-limiting. However, this result must be corroborated with further measurements in proteoliposomes, which also allows measurement of other kinetic parameters.

3.8 Measuring kinetic isotope effect of *Y. lipolytica* complex I variants in proteoliposomes

Y. lipolytica complex I was purified using the same method as Brandt et al. (Cabrera-Orefice *et al.*, 2018) which yielded pure complex I with no NDH2 contamination. The background NADH oxidation rate when piericidin was added is similar to that observed for bovine proteoliposomes. Thus, NADH may be used as an electron donor in NADH:O_2 in oxidoreduction assays. Here *Y. lipolytica* complex I proteoliposomes of the variants WT, H95M, Y144F, and M91I were reconstituted with multiple Q_{10} concentrations (0.1, 0.5, 1, 3, 6, 10 mM). Although this is different to the native quinone Q_9, Q_{10} is also a long-chain quinone and the difference of 1 isoprenoid unit does not change the binding geometry (Fedor *et al.*, 2017), so it serves as a good approximation. AOX was not co-reconstituted with complex I to

avoid complications with differential loss of AOX between different samples, and instead, a 20:1 mg ratio of AOX was added into assays, which is a saturating amount (Wright *et al.*, 2022). The complex I concentration of each sample was determined using the NADH:APAD$^+$ assay.

The pL dependence of NADH:O_2 oxidoreduction rates of the four *Y. lipolytica* complex I variants were measured, and K_M curves are plotted in Figure 3.28. At all pL values, saturating kinetics were observed that could be fitted to the Michaelis Menten equation.

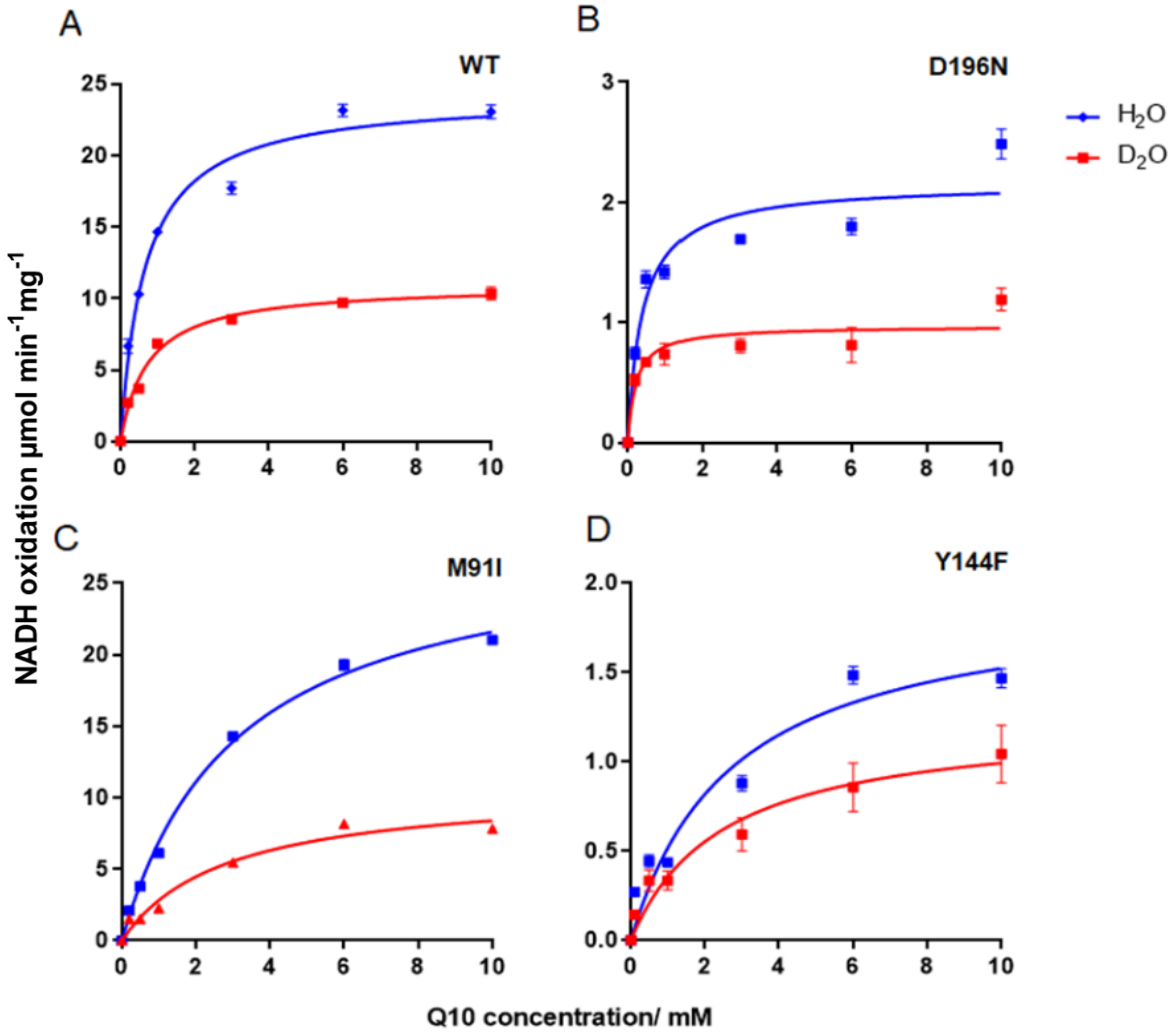

Figure 3.28 The K_M curve of four *Y. lipolytica* complex I variants at pL 7.5. NADH:O_2 rates of complex I reconstituted in proteoliposome using various concentrations of Q_{10} as a substrate were measured under pL 5.5 – 9, but only pL 7.5 is plotted to save space. All K_M curves displayed saturating kinetics and were fitted to the Michaelis-Menten equation. Errors are calculated as standard error of the mean (n = 3).

3.8.1 The isotope dependence of kinetic parameters k_{cat}, K_{sp}, K_M in *Y. lipolytica* complex I variants

Figure 3.29 shows the pL dependence of k_{cat} in each *Y. lipolytica* variant. k_{cat} parameter values were generated as seen in section 3.5.3. Briefly, each k_{cat} value is the V_{max} of K_M curves, with a conversion of the activity unit μM min^{-1} mg^{-1} to s^{-1} by adjusting for enzyme concentration. Although the rate of mutants Y144F and D196N could not be measured with the native Q_9 with the addition of AOX in mitochondrial membranes, measurable activity can be determined using Q_{10} within the proteoliposome system, owing to an increased Q_{10} concentration and higher specific complex I concentrations.

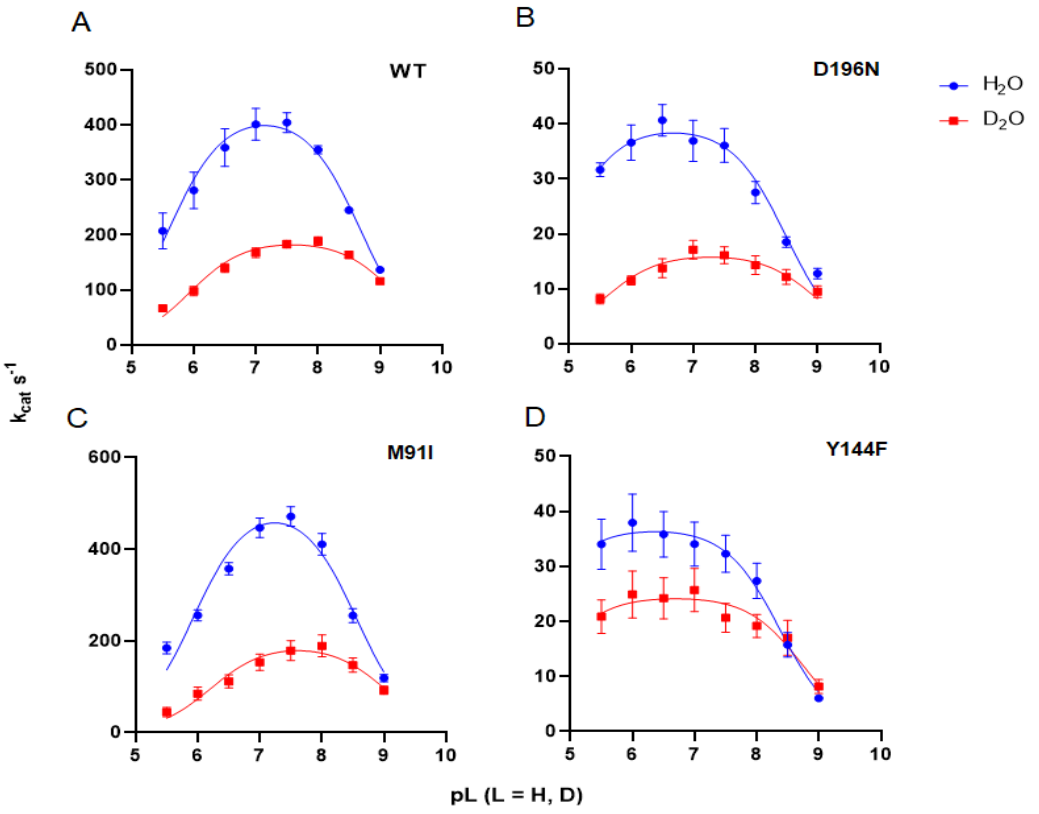

	Ymax H_2O	Ymax D_2O	pKa 1 H_2O	pKa 1 D_2O	pKa 2 H_2O	pKa 2 D_2O	KIE
WT	421 ± 12	190 ± 7.2	5.6 ± 0.06	5.9 ± 0.08	8.7 ± 0.06	9.2 ± 0.11	2.21 ± 0.10
D196N	39 ± 1.5	193 ± 12	4.9 ± 0.19	5 ± 0.11	8.5 ± 0.084	9 ± 0.11	2.43 ± 0.14
M91I	502 ± 29	193 ± 12	5.9 ± 0.1	6.2 ± 0.11	8.6 ± 0.1	9 ± 0.14	2.60 ± 0.22
Y144F	39 ± 0.9	24 ± 1.1	4.3 ± 0.33	4.6 ± 0.35	8.4 ± 0.05	8.7 ± 0.11	1.60 ± 0.08

Figure 3.29 pL dependence of k_{cat} of four *Y. lipolytica* complex I variants. k_{cat} values were fitted using the Michaelis Menten equation, and the pH-independent value of k_{cat} was fitted using equation 1. pKa values are reported in the associated table. (A) WT enzyme. The KIE is 2.21 ± 0.10. (B) D196N mutant. The KIE is 2.43 ± 0.14. (C) M91I mutant. The KIE is 2.60 ± 0.22. (D) Y144F mutant. The KIE is 1.60 ± 0.08. Errors bars are standard error values calculated using Prism 9, and the error of KIE is calculated using error compounding.

Bell-shaped pL dependence is observed with pK_a values of approximately 5 and 8. Y144F and D196N show a more acidic shift of > 0.5 pH unit in pK_a 1 as compared to WT; however, this change is not reproduced within mitochondrial membranes and is likely due to measurement error from low rates. The k_{cat} of Y144F and D196N are both ~9% of the WT enzyme representing a significant decrease in activity. This is consistent with the results measured by Dr. Polly Marino (Marino, 2018) with Y144F and D196N having a k_{cat} at pH 7.5 approximating 10% and 17% of the WT enzyme. M91I conversely increased the activity of complex I, with activity approximately 119% of WT and is consistent with previous results that the k_{cat} is approximately 20% greater than WT using Q_1 as a substrate (Angerer *et al.*, 2012). This suggests that oxidoreduction rates using Q_9 in mitochondrial membranes could not be measured because the membrane concentration of Q_9 is insufficient to promote measurable activity (K_M has increased) rather than intrinsic incompatibility of the substrate binding geometry (as in Y144F) with this mutation. However, care must be taken in comparing kinetic parameters between mutants. Because within each preparation of complex I, there is an unquantified amount of “broken” complex I, an inactive enzyme that is NADH:$APAD^+$ sensitive but cannot catalyse quinone reduction, thus complicating the interpretation of results.

The observed KIE in k_{cat} of *Y. lipolytica* complex I variants with the exception of Y144F, is > 2.2, which is significantly larger than that measured in bovine complex I or mitochondrial membranes. This increased KIE in the *Y. lipolytica* proteoliposome system is reproducible. The results in proteoliposomes are more robust than that measured in mitochondrial membranes and the reason for the discrepancy in measured KIE is likely due to impurity and substrate concentration limitation within mitochondrial membranes. The apparent KIE on k_{cat} of the four complex I variants are 2.21 ± 0.10, 2.43 ± 0.14, 2.60 ± 0.22, and 1.54 ± 0.08 for WT, D196N, M91I, and Y144F respectively. The changes in observed KIE measured between WT and Y144F are statistically significant beyond 95% confidence but are not statistically significant between WT, D196N, and M91I.

The magnitude of the intrinsic kinetic isotope effect of a particular bond-breaking step is related to the zero-point energy difference in the reactant state and transition state, which is dependent on each vibrational frequency and the tightness of the particular hydrogen bond broken. If in the Y144F mutation, a different proton is

transferred in the quinone reduction mechanism or the proton transfer transition state has a different geometry, this may change the ΔZPE in the reactant, transition state, or both. This would result in a difference in intrinsic KIE, which may explain the change in observed KIE on k_{cat} on Y144F (Tocilescu, Fendel, *et al.*, 2010; Chung, Wright, *et al.*, 2022)

However, a change in the observed KIE may not be caused entirely by a change in the intrinsic KIE. As effects on commitment to catalysis both in substrate binding and product release can also change the observed KIE with no effect on intrinsic KIE. Further experiments are required to delineate these effects.

Figure 3.30 shows the pL dependence of K_{sp} of each *Y. lipolytica* variant. Similar to what was observed in bovine complex I, the pL dependence of K_{sp} is bell-shaped for all mutants except D196N, which has large errors and a basic shift in K_{sp}. So, it is unclear whether it is a bell-shaped or linear dependence, with the profile able to fit both. The *Y. lipolytica* WT complex I has a 3.5-fold higher catalytic efficiency, K_{sp}, than bovine complex I. Despite similar k_{cat} between D196N and Y144F, there is a large difference in K_{sp} between the two enzymes, with each displaying a K_{sp} that is 21% and < 2% of the WT enzyme, respectively. This suggests that there is a much larger deleterious effect on substrate binding in the Y144F mutant, which is expected as it is proposed to directly hydrogen bond with the carbonyl group of quinone. M91I despite having a k_{cat} that is approximately 13-fold higher than D196N, has comparable specificity constant, consistent with the expectation that M91I negatively affects substrate binding.

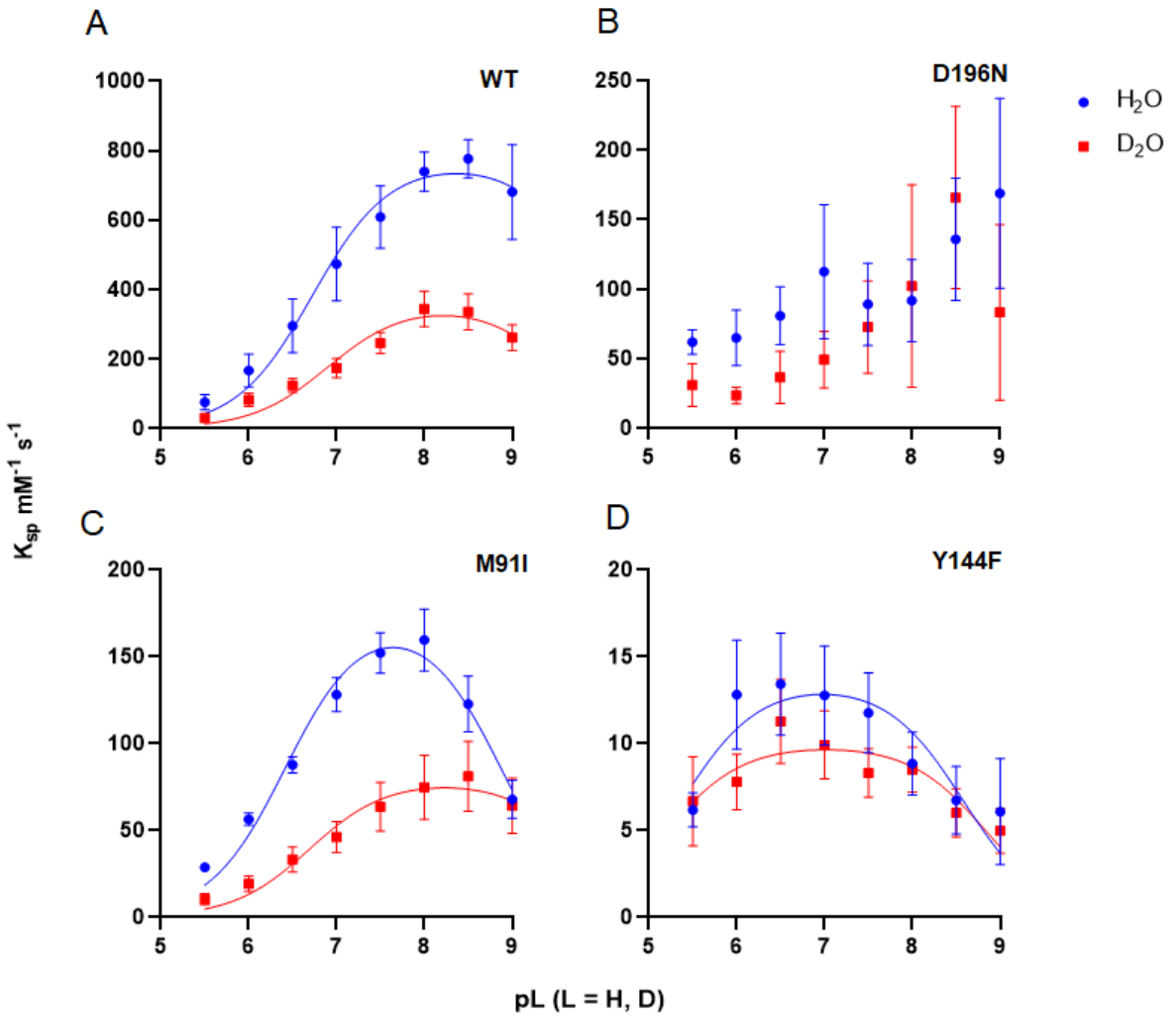

	Ksp max H2O	Ksp max D2O	KIE K_{sp}
WT	775.7 ± 55	344.3 ± 51	2.09 ± 0.32
M91I	159.5 ± 18	81.15 ± 20	1.96 ± 0.53
D196N	168.8 ± 68.3	165.7 ± 66	1.018 ± 0.577
Y144F	13.42 ± 2.9	9.57 ± 2.4	1.40 ± 0.47
Bovine	217.4 ± 30	213 ± 32	1.02 ± 0.21

Figure 3.30 pL dependent K_{sp} profiles of four *Y. lipolytica* complex I variants. K_{sp} values were fitted using equation 3 and the pH-independent value is taken as the highest measured value. (A) WT enzyme. (B) D196N mutant. (C) M91I mutant. (D) Y144F mutant. Errors bars are standard error values calculated using Prism 9.

Observed KIE on K_{sp} is lower than on k_{cat} for all variants, which is consistent with results seen in bovine complex I. However, in contrast to bovine complex I, the WT *Y. lipolytica* complex I exhibits a large observed KIE on K_{sp} of 2.09 ± 0.32 compared to 2.21 ± 0.10 on k_{cat}. Observed KIE on K_{sp} is obscured by $C_f = k_2/ k_{-1}$, and k_{cat} by $C_{vf} = k_2/ k_3$. So, this suggests that the forward commitment factor C_f is low and that the

denominators k_{-1} and k_3 have similar rates as both C_f and C_{vf} have similar values. D196N, similar to bovine complex I, does not show a clear isotope effect on K_{sp} with a KIE of 1.018 ± 0.577, which is low compared to its high KIE on k_{cat} of 2.43 ± 0.14, suggesting a high C_f relative to C_{vf}. So, the product release rate k_3 is much greater than the substrate release rate k_{-1} ($k_3 >> k_{-1}$). M91I, as expected, behaves much more similarly to WT *Y. lipolytica* complex I, with a large KIE on K_{sp} of 1.96 ± 0.53 compared to the KIE on k_{cat} of 2.60 ± 0.22, suggesting that k_3 is greater than k_{-1} (but less substantially than in D196N or bovine). Y144F also has a lower KIE on K_{sp} of 1.40 ± 0.47 compared to KIE on k_{cat} of 1.60 ± 0.08, but the two are within error, suggesting that k_3 is similar to k_{-1}.

Estimation of microscopic rate constants for the complex I-Q_{10} reaction.

With parameters k_{cat}, K_{sp}, and $^{D}k_{cat}$, $^{D}K_{sp}$ measured, a preliminary estimation of the microscopic rate constants in scheme 1 can be made using equations 4 to 8 (Table 3.2). The evolutionary non-linear algorithm was used as part of the Excel data solver suite. This algorithm uses a genetic algorithm approach to find the optimal solution from within the entire constrained range, avoiding the problem of local optima (Powell and Batt, 2008). A genetic algorithm iteratively selects the best fits through cycles of selection and mutation, until there is a convergence to the optimised values. By using mutations, a greater possibility space is searched, and allows the optimisation to escape a local minimum (by finding a better local minimum). The intrinsic isotope effect has yet to be determined experimentally, but it was constrained to 3.3 in this calculation as an approximation, as it is the upper limit expected for a proton catalytic bridge (transferring a proton among O, N, and S in the transition state) (Venkatasubban and Schowen, 1984). The parameters k_1, k_{-1}, k_2, and k_3 were constrained to positive values, and k_{-2} was constrained to 1 to avoid overfitting the model. Parameters k_{cat}, K_{sp}, and $^{D}k_{cat}$, $^{D}K_{sp}$ were constrained to the experimentally obtained pH/ pD-independent (V_{opt}) values. K_M was not constrained and calculated using calculated microscopic rate constants using Equation 3.6 as a sense check. The binding constant is determined by the ratio of on and off rates for substrate binding, $K_d = k_{-1}/ k_1$.

	WT Q_{10}	M91I Q_{10}	D196N Q_{10}	Y144F Q_{10}	Bovine Q_{10}
k_1 $mM^{-1}s^{-1}$	1369.29	266.09	176.69	16.49	190.66
k_{-1} s^{-1}	685.66	546.05	2.85	33.96	7.32
k_2 s^{-1}	760.33	761.88	62.73	147.05	834.81
k_{-2} s^{-1}	1.00	1.00	1.00	1.00	1.00
k_3 s^{-1}	845.15	1743.71	104.75	53.44	256.44
KIE_{Int}	3.30	3.30	3.30	3.30	3.30
Obs $^{D}K_{sp}$	2.09	1.96	1.10	1.43	1.02
Obs $^{D}k_{cat}$	2.21	2.60	2.43	1.61	1.54
C_f	1.11	1.40	21.99	4.33	114.00
C_r	0.00	0.00	0.01	0.02	0.00
C_{vf}	0.90	0.44	0.60	2.75	3.26
k_{cat} s^{-1}	421.00	502.00	39.00	39.00	196.00
K_{sp} $mM^{-1}s^{-1}$	775.00	159.00	169.00	13.40	189.00
K_d (μM)	500.74	2052.10	16.14	2058.83	38.41
K_M (mM)	0.56	3.42	0.23	2.92	1.04

Table 3.2. Scheme 1 kinetic parameters and commitment factors for each complex I variant. Parameters were solved using equations 3.4 to 3.8 using Excel solver and the evolutionary nonlinear algorithm. Parameters k_{cat}, K_{sp}, and their respective observed KIE were constrained to their pH-independent values. Parameters k_1, k_{-1}, k_2, and k_3 were constrained to positive values. K_M was calculated using calculated microscopic rate constants. The reverse rate constant k_{-2} was constrained to 1, and intrinsic KIE was constrained to 3.3.

Interestingly and perhaps expected, the catalytic rate k_2 is similar for *Y. lipolytica* WT, M91I, and bovine complex I at ~760 – 830 s^{-1}. Further supporting that M91I does not affect the catalysis step and that the increased k_{cat} is due to an increase in the product release rate k_3. WT *Y. lipolytica* complex I has the highest substrate binding rate at 1370 mM^{-1} s^{-1} which is at least 5-fold higher than the next highest variant M91I. This is somewhat expected as other *Y. lipolytica* variants contain a binding site mutation. However, it is unexpectedly much higher than bovine complex I. Even more surprising is the low substrate off rates for the complex I variant D196N, which instead is closer to bovine complex I than to WT *Y. lipolytica.* By comparing fitted K_d values, D196N in fact, has the highest binding affinity (despite low substrate k_{on} rates), followed by the bovine enzyme, with M91I and Y144F having an expectedly low affinity due to mutations that directly impact quinone binding residues. Clearly,

the impact of D196N on substrate binding is nuanced and perhaps involves changes to substrate steering dynamics rather than purely hydrogen bonding or hydrophobic interactions. For example, the presence of a local minimum in the binding channel may lower both k_{on} and k_{off} rates. Further to the point that K_M is not an analogue of K_d, the fitted K_M values are consistent with experimentally measured K_M at approximately pH 7.5 (see below) but can diverge from the fitted K_d value. K_M approximates K_d for variants *Y. lipolytica* WT, M91I, and Y144F but diverges by order of magnitude in bovine and D196N.

The estimation of microscopic rate constants is informative on the rate-limiting step. The first-order rate constants k_2 and k_3 can be directly compared, with k_1 being substrate concentration-dependent (second order). In the *Y. lipolytica* WT, D196N, and M91I variants, the catalytic step, k_2, is slower than product release step k_3; however, the two rates are closely matched with C_{vf} ($C_{vf} = k_2/ k_3$) at 0.9, 0.6 and 0.44 respectively. In the variants Y144F and bovine, product release is clearly rate-limiting with C_{vf} at 2.75 and 3.26 respectively ($k_2 > k_3$).

Table 3.3 summarises the turnover time of each complex I variant, as well as the proportion of time spent catalysing the chemical step and product release steps, represented by fraction a (F_a) and fraction b (F_b) respectively. On the whole, the catalytic step and product release rates are well matched with no step more than 80% rate-limiting, and substrate binding is rate-limiting depending on substrate concentration. This indicates that the enzyme is well-evolved to maximise catalytic efficiency.

Time	WT Q_{10}	M91I Q_{10}	D196N Q_{10}	Y144F Q_{10}	Bovine Q_{10}
k_{cat} ms	2.50	1.89	25.49	25.51	5.10
k_2 ms	1.32	1.31	15.94	6.80	1.20
k_3 ms	1.18	0.57	9.55	18.71	3.90
F_a	53%	70%	63%	27%	23%
F_b	47%	30%	37%	73%	77%

Table 3.3. The time taken for each kinetic step during catalysis in complex I variants. Calculated as the inverse of the k_{cat}, k_2, and k_3 microscopic rates, with F_a and F_b representing the proportion of total turnover time spent on the catalytic step and product release step respectively.

Observed KIE on rate increases with Q_{10} concentration for Q-binding site mutants but not WT

Figure 3.31 shows the substrate concentration dependence of observed KIE for each *Y. lipolytica* complex I variant. Briefly, the pL-independent optimal rate of each pL profile was collected at each quinone concentration and compared between H_2O and D_2O. Unlike the other *Y. lipolytica* complex I variants and bovine complex I, WT does not demonstrate a substrate concentration dependence on the observed KIE, which reaches the maximum of ~2.2 even with a low substrate concentration of 0.1 mM, consistent with *Y. lipolytica* WT complex I having a high substrate binding k_{on} rate. In contrast, the M91I variant, despite a sizable KIE on K_{sp}, has a clear substrate concentration dependence on observed KIE, with observed KIE approaching ~1.4 at very low substrate concentrations of 0.1 mM and increasing to its maximum of ~2.6 at 3 mM. Similar is observed in the mutants Y144F and D196N, where each variant has an observed KIE that approaches ~1.2 and ~1.4 at 0.1 mM substrate and approaches the maximum KIE of 1.6 and 2.4 at 6 mM substrate, respectively. Although it can be observed that this behaviour is dependent on a single point (at 0.2 mM Q_{10}), this result is reproducible when using Q_1 as substrate (see section 3.9.2) and consistent with the KIE on K_{sp} in all three variants is less than that on k_{cat}, supporting that substrate binding is rate-limiting at very low substrate concentrations. Overall, these results suggest that these mutations affect Q-binding dynamics.

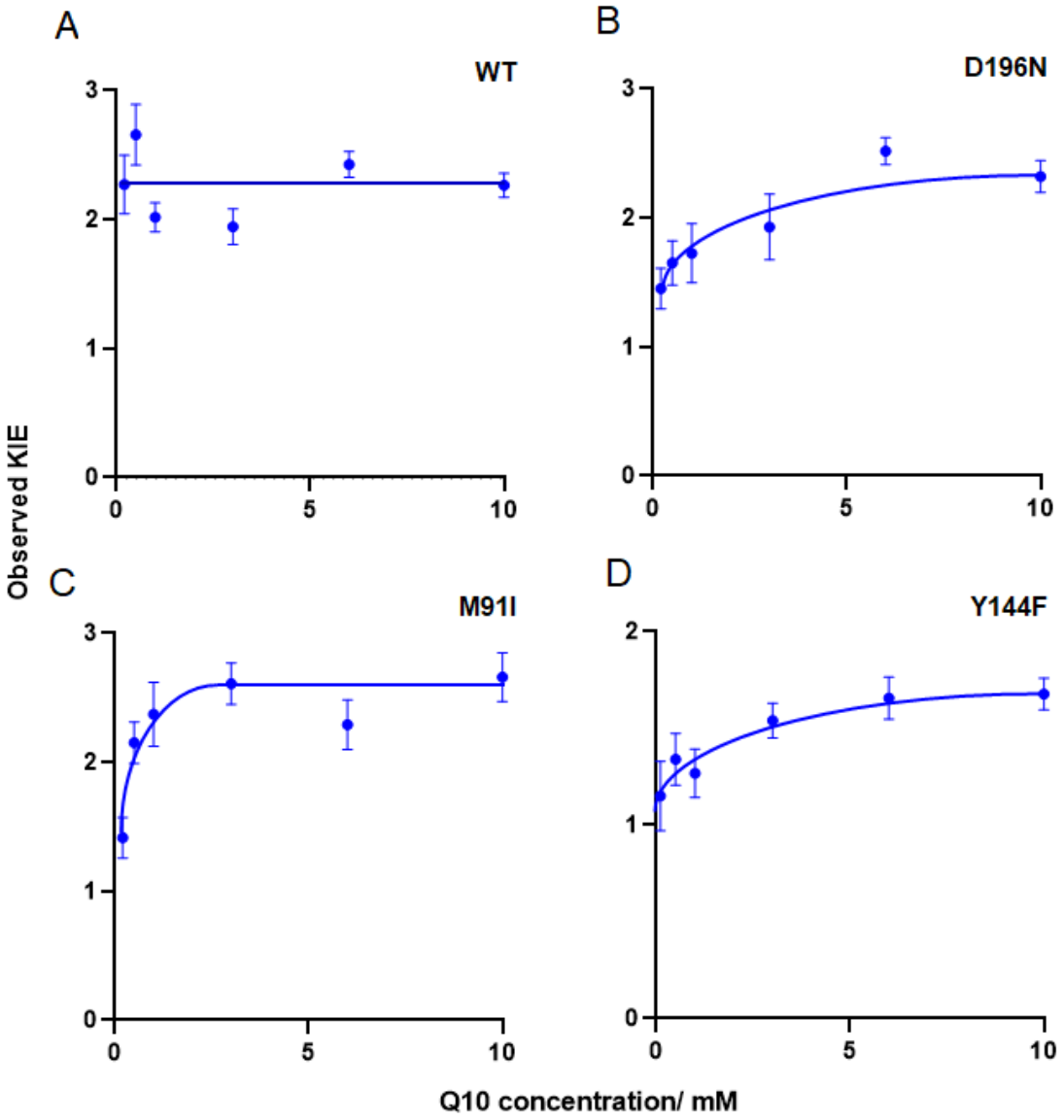

Figure 3.31 The substrate dependence on observed KIE for each *Y. lipolytica* complex I variant. At each substrate concentration, pH rate profiles are fitted with Equation 1, and the KIE on the fitted Vopt value is plotted. (A) WT enzyme. (B) D196N mutant. (C) M91I mutant. (D) Y144F mutant. Errors are standard error values calculated using Prism 9.

Figure 3.32 shows the pL dependence of K_M in each of the *Y. lipolytica* complex I variants. The WT, M91I, and D196N variants display a unidirectional pL dependence on K_M as seen in the bovine enzyme, which suggests that substrate binding is competitively inhibited by proton binding. The Y144F variant resembles a “flattened” unidirectional pL dependence. The WT and D196N variants hold comparable K_M at pL more basic than pH 7 but diverge at more acidic pL. At equivalent pL, both M91I and Y144F have higher K_M compared to the WT and D196N variants.

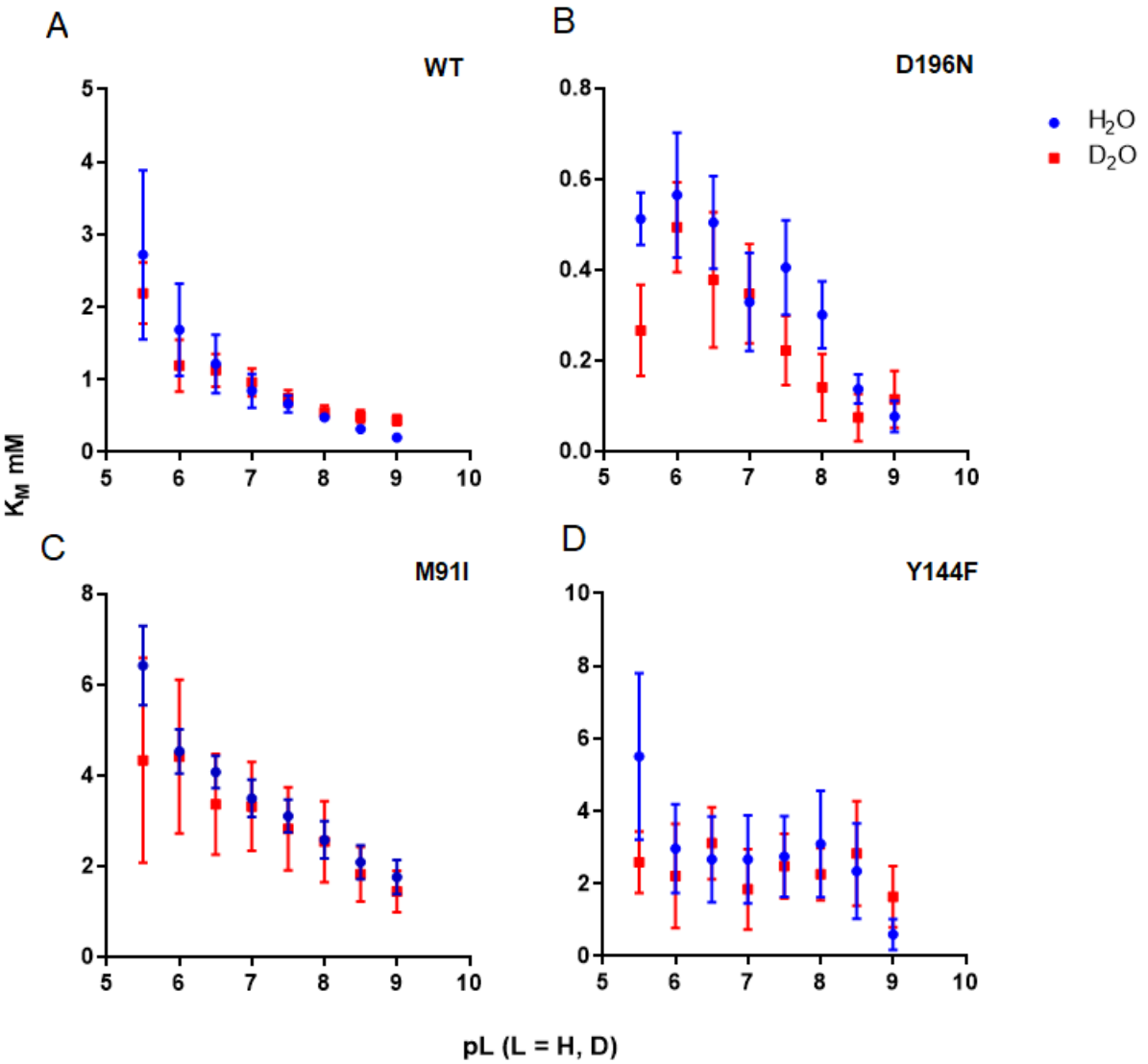

Figure 3.32 pL dependence of K_M in each *Y. lipolytica* complex I variant. K_M at each pL is fitted using the Michaelis Menten equation. (A) WT enzyme. (B) D196N mutant. (C) M91I mutant. (D) Y144F mutant. Errors are standard error values calculated using Prism 9.

3.8.2 Using NADPH as the electron donor changes the rate-limiting step

Although it is expected that the NADH oxidation is not rate-limiting because the k_{cat} is > 15000 s^{-1} and at least an order of magnitude greater than that of quinone reduction (Birrell, Yakovlev and Hirst, 2009), it is useful to use a negative control to rule out this possibility. To accomplish this, the flavin site reaction may be slowed by using a different electron donor. Although the complex I flavin site has a strong specificity for NADH, it can also catalyze the oxidation of NADPH, although this process is likely not physiologically relevant (Yakovlev and Hirst, 2007). NADPH differs from NADH by the presence of an additional phosphate group on the 2' position of the ribose ring that carries the adenine moiety. Previous experiments by Yakovlev et al. measured

the kinetic parameters k_{cat}, K_M, and K_{sp} derived from the Michaelis Menten model and the ping-pong mechanism model for a range of flavin site electron donors and acceptors. It is found that using NADPH, the K_M as compared to NADH for the trans hydrogenation reaction with $APAD^{+,}$ has increased at least 20-fold from 0.094 mM to between 2.0 and 4.6 mM. The k_{cat} has decreased from ~ 2700 s^{-1} to 13-22 s^{-1} and k_{cat}/ K_M from 2.9 $x10^7$ to 3.0-6.5 $x10^3$ $s^{-1}M^{-1}$, representing a more than 200-fold and 4000-fold decrease, which turns a reaction that is close to diffusion-limited with NADH, to a poor reaction with a high proportion of futile encounters using NADPH. The use of NADPH as an electron donor to reduce quinone means that the expected rate-limiting step is NADPH oxidation, which has a k_{cat} at least 20-fold slower than quinone reduction. In this experiment, the NADPH:O_2 oxidoreduction rates were measured with WT *Y. lipolytica* complex I proteoliposomes reconstituted with 13 mM Q_{10}, with 20:1 mass ratio of AOX added, and a concentration of 2 mM NADPH between pL 5.5 and 9 in H_2O or D_2O (Figure 3.33). Because of the high concentration of NADPH used in this assay, the change in absorbance was monitored at 360 nm to avoid saturation of the optical detector.

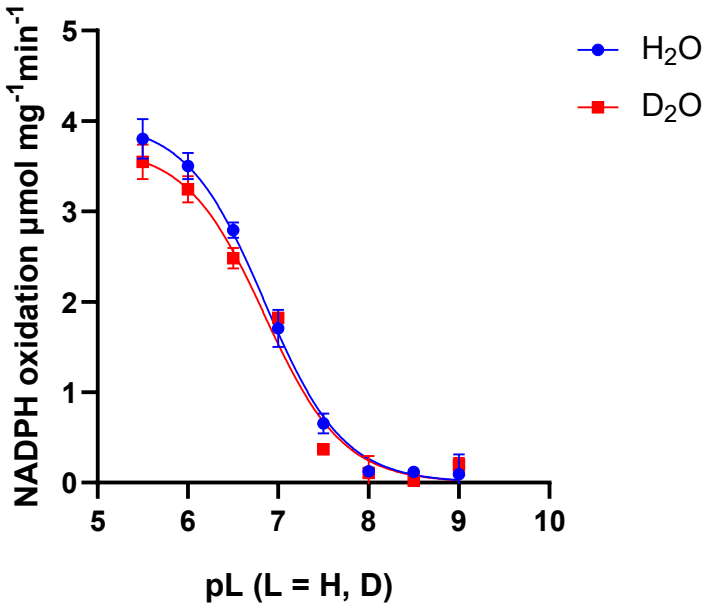

Figure 3.33 The pL dependence of NADPH:O_2 oxidoreduction rate of *Y. lipolytica* complex I proteoliposomes. A 20:1 mass ratio of AOX was added to make complex I rate-limiting. There is no observed KIE. Errors are calculated as standard error of the mean (n = 3).

The rate measured at pH 7.5 is ~0.7 μM mg^{-1} min^{-1}, which corresponds to an enzyme concentration independent rate of approximately 12 s^{-1} and is consistent with previously measured rates. The reaction is also unidirectionally pH-dependent, as opposed to bell-shaped, with the oxidoreduction rate increasing with decreasing pL. The fitted pKa is 6.8 using the Henderson-Hasselbalch equation and may reflect the favorability of NAPDH binding at low pH. This change in the shape of pH dependence is a strong indication that the rate-limiting step has changed. The KIE on measured rates has also disappeared from ~2.2 using NADH to 1 using NADPH. Because the substitution of D_2O in the assay buffer does not substitute the nicotinamide C4 hydride transferred to the N5 flavin, no isotope effect is expected for this step and is consistent with NADPH oxidation being rate-determining. This experiment adds further conviction that complex I is robustly rate-limited by a proton transfer-dependent step and is not NADH oxidation or a viscosity effect, which will also affect NADPH as a substrate.

3.9 Short chain quinones alter catalytic behavior of *Y. lipolytica* complex I

As previously shown in section 3.7.4 and by published results by Tocilescu et al. (Tocilescu, Fendel, *et al.*, 2010), the use of short-chain quinones Q_1 and Q_2 rescues catalytic activity in the Y144F mutant. This suggests that when complex I catalyzes the reduction of short-chain quinones, the headgroup may adopt a different binding or reaction geometry, distinct from that in Q_{10}, made possible by its increased mobility within the binding site (Fedor *et al.*, 2017). Here, I investigate this alternate reaction geometry by measuring the pL dependence of K_{sp}, k_{cat}, and K_M and their observed isotope effects, which is informative of the reaction mechanism and determining if the rate-limiting step changes with quinone chain lengths and can be diagnostic of whether the reaction mechanisms are different.

3.9.1 Using Q_2 as a substrate changes the rate-limiting step to product release

The data presented so far consistently suggests that there is an isotopically sensitive rate-determining step and that this step can be obscured by a non-isotopically sensitive step (E.g., with NADPH). This section demonstrates this principle, where the rate-limiting step has shifted to product release.

The pL dependence of NADH:Q_2 oxidoreduction activity of proteoliposomes reconstituted with WT *Y. lipolytica* complex I and the Y144F mutant were measured, and K_M curves are shown in Figure 3.34.

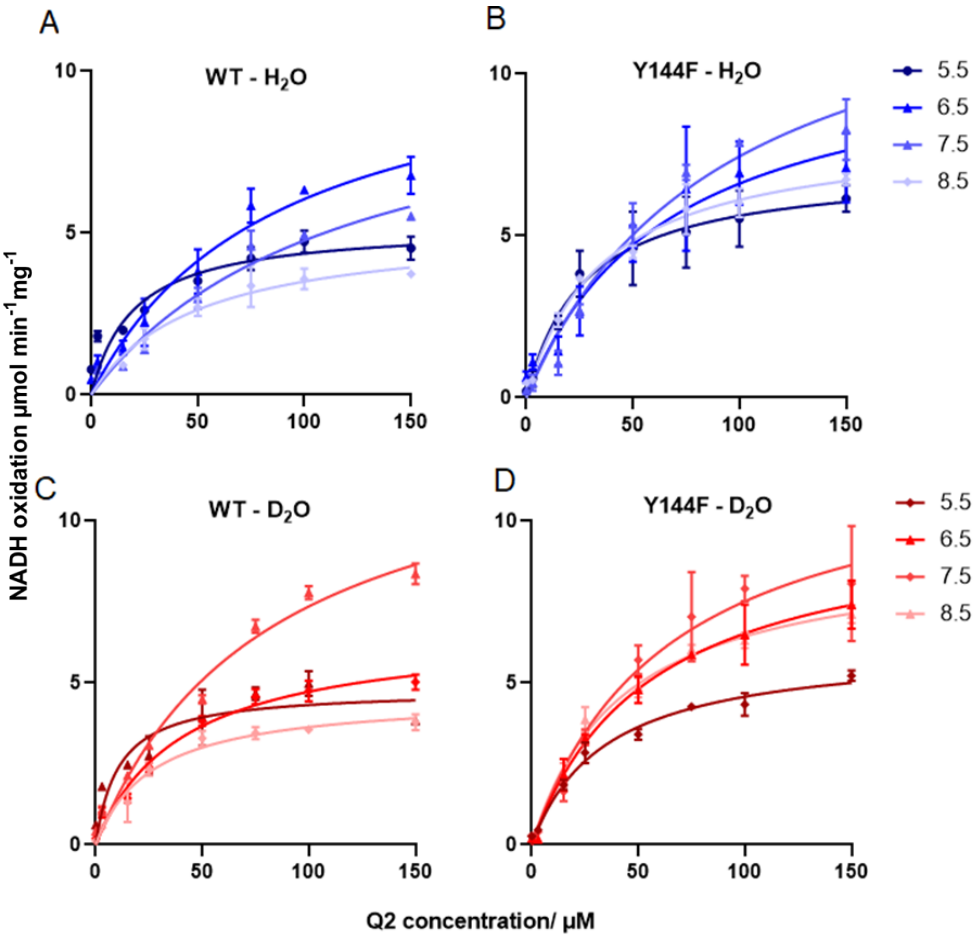

Figure 3.34: The K_M curves at a range of pL in H_2O or D_2O. NADH:Q_2 rates of complex I proteoliposomes were measured with increasing concentrations of Q_2 added from ethanol stocks at pL 5.5 – 9, but only the pH 5.5, 6.5, 7.5, and 8.5 are plotted. (A) *Y. lipolytica* WT assayed in H_2O. (A) *Y. lipolytica* Y144F assayed in H_2O. (C) *Y. lipolytica* WT assayed in D_2O. (D) *Y. lipolytica* Y144F assayed in D_2O. All K_M curves displayed saturating kinetics and fitted well to the Michaelis-Menten equation. Errors are calculated as standard error of the mean (n = 3).

These proteoliposomes do not contain co-reconstituted long-chain quinone and soluble quinone Q_2 is instead added during assays from ethanol stocks. Therefore, K_M and K_{sp} are given as apparent values. This doesn't change the interpretation of the results when apparent K_M and K_{sp} are compared between isotopic substitution and pL within the same proteoliposome sample. However, when comparing apparent K_M and K_{sp} between different proteoliposome samples care must be made in

interpretation. First, the effective membrane concentration is much higher than the apparent substrate concentration reflected in the total volume of the assay, as short-chain quinones are hydrophobic and have a preferential partition within the lipid membrane. Secondly, substrates may form micelles at higher concentrations, which limits substrate accessibility. Therefore, when comparing apparent K_M and K_{sp} between mutants, these values should be taken as crude estimates, and there is a high degree of error associated with these measurements.

At all pL values, results were fitted well with the Michaelis Menten equation, and the pL dependence of resultant fitted k_{cat} and apparent K_{sp} values are shown in Figure 3.35.

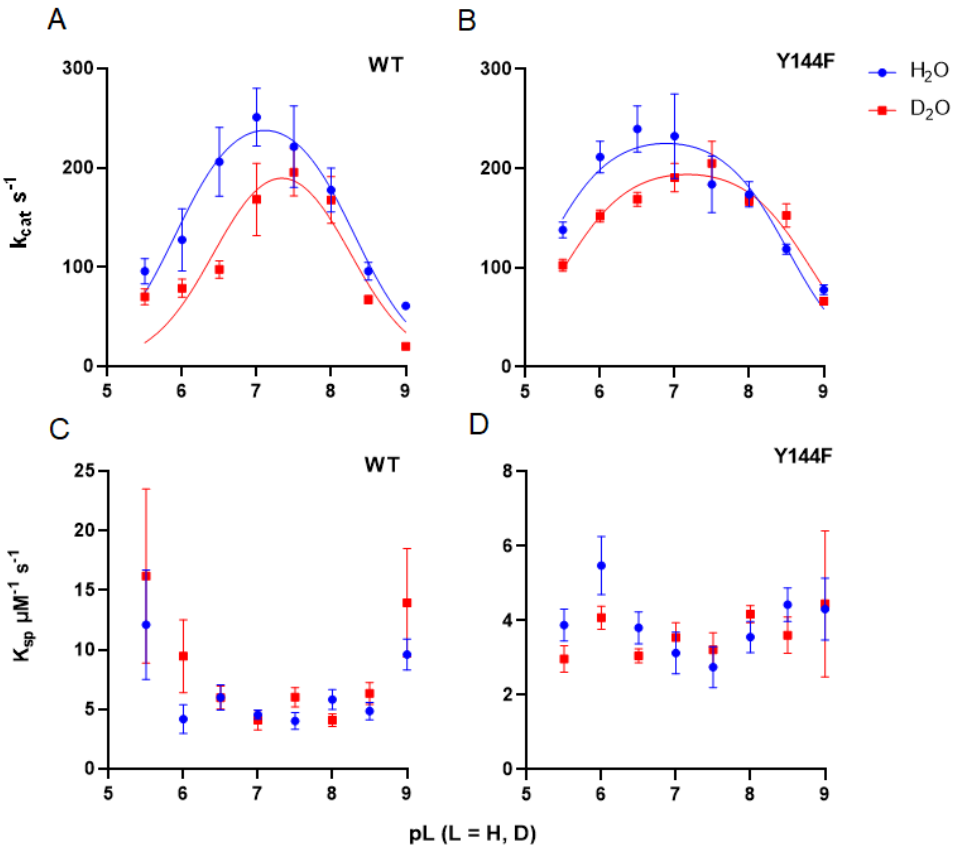

	WT H_2O	WT D_2O	Y144F H_2O	Y144F D_2O
k_{cat} s^{-1}	268 ± 17.6	238.9 ± 49.2	235.7 ± 14.4	202.6 ± 9.2
pKa 1	5.9 ± 0.11	6.5 ± 0.27	5.3 ± 0.18	5.5 ± 0.11
pKa 2	8.3 ± 0.11	8.2 ± 0.26	8.5 ± 0.13	8.8 ± 0.1
KIE	1.12 ± 0.24		1.16 ± 0.09	

Figure 3.35. pL dependence profiles of k_{cat} and K_{sp} of NADH:Q_2 oxidoreduction in proteoliposomes. (A) k_{cat} of the WT enzyme. The KIE is 1.12 ± 0.24 (B) k_{cat} of the Y144F variant. The KIE is 1.16 ± 0.09. (C) K_{sp} of the WT enzyme. (D) K_{sp} of the Y144F variant. Errors bars are standard error values calculated using Prism 9.

Although k_{cat} shows a bell-shaped dependence on pL, with pK_as consistent with that measured using Q_{10} as a substrate, the same is not observed with apparent K_{sp} which has a "flat" pL dependence, with the WT sample showing a "concave" pL dependence due to outliers at extremities of pL. The pL-independent k_{cat} value of the Y144F variant was 87% that of WT, consistent with previously observed results that Q_1 rescues quinone reduction activity in the Y144F mitochondrial membranes. More strikingly, the solvent isotope effect on k_{cat} is much smaller than previously observed using Q_{10} as a substrate at 1.12 ± 0.24 and 1.16 ± 0.09 for WT and Y144F, respectively. This suggests that a non-isotopically sensitive step is rate-limiting, likely product release, consistent with a high forward commitment factor, C_{vf} (k_2/ k_3), obscuring the observed KIE. This is consistent with k_{cat} dropping to 64% of the Q_{10} equivalent. The solvent isotope effect on K_{sp} is difficult to determine and is not indistinguishable from unity, which signifies that C_f (k_2/ k_{-1}) is high.

The pL dependence of apparent K_M has changed from unidirectional into a bell-shaped dependence using Q_2 as a substrate (Figure 3.36). Thus, in addition to a descending leg, which can be attributed to competitive inhibition by protons, there is also an ascending leg where increasing proton concentration increases the rate of substrate "capture" (see section 3.10.1). The K_i of the competitive inhibition by protons has likely shifted to reveal this bell-shaped dependence.

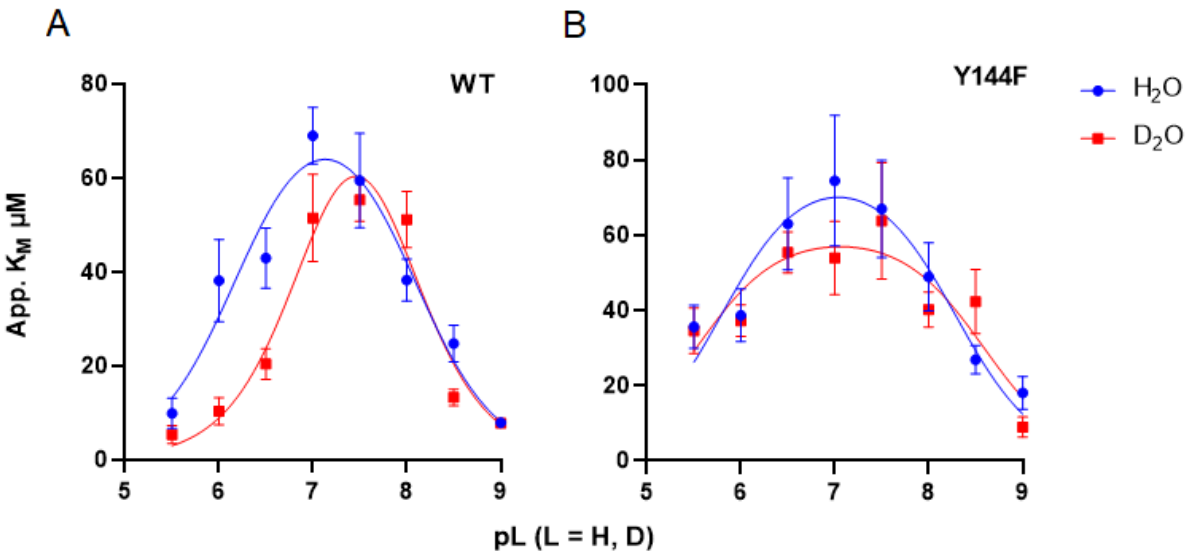

Figure 3.36 pL dependence profiles of K_M of NADH:Q_2 oxidoreduction in proteoliposomes. (A) K_M of the WT enzyme. (B) K_M of the Y144F variant. Errors bars are standard error values calculated using Prism 9.

The apparent K_M of the Y144F mutant is closely matched to the WT enzyme, with a peak value of 75 μM and 68 μM at pH 7 respectively, which is consistent with previously measured results by Tocilescu et al. (Tocilescu, Fendel, *et al.*, 2010). The closely matched apparent K_M and K_{sp} values between Y144F and WT suggest that when using Q_2 as a substrate specifically, the Y144F mutation is not deleterious, because both variants are severely rate-limited by product release.

Together, the lack of solvent KIE on k_{cat} and K_{sp} suggest that Q_2 has slow diffusion dynamics within the Q channel, with both substrate and product release rates (k_{-1}, k_3) slow, leading to high C_f and C_{vf} factors obscuring both $^Dk_{cat}$ and $^DK_{sp}$. Closely matched K_{sp} suggest that the rate of substrate binding is similar between the two complex I variants. This supports the conclusion by Fedor et al. that the rate-limiting step changes to a chain length-dependent step, most likely product release when using short-chained quinone as substrate (Fedor *et al.*, 2017). This is proposed to be due to increased conformational mobility of short-chained quinones Q_1, Q_2, and Q_4 within the binding site and may hinder dissociation by lack of directionality. The long chain hydrophobic tail is proposed to serve an anchoring effect to guide quinone/ quinol dissociation. Fedor et al. also suggest that additional molecules may enter the Q channel behind the short-chain quinone substrate, impeding dissociation. This is well supported by the observation that two piericidin A molecules, which resemble Q_3, may bind at the same time within the complex I Q channel (Bridges *et al.*, 2020).

This effectively "traps" Q_2 in the binding channel for longer and along with increased conformational mobility, raises the likelihood of the quinone headgroup adopting a favorable binding or reaction geometry in the mutant, bypassing the effect of the mutation. With long-chain quinone, the hydrophobic tail constrains the Q-headgroup into an unfavourable reaction geometry for the Y144F mutant, slowing catalysis.

3.9.2 WT and *Y. lipolytica* Y144F complex I do not share a common mechanism when catalyzing the reduction of Q_1

Although the apparent K_M for Q_2 in Y144F and WT are closely matched, the apparent K_M for Q_1 in Y144F (54 μM) was significantly larger than WT (9 μM) in previous results by Tocilescu et al. (Tocilescu, Fendel, *et al.*, 2010). This implies that when using Q_1, the Y144F mutation impairs substrate binding. To investigate this discrepancy, I measured the pL dependence of NADH:Q_1 oxidoreduction activity of

WT *Y. lipolytica* complex I and the Y144F mutant (Figure 3.37). As previously described, Q_1 was added from ethanol stocks during assays. Hence, K_M and K_{sp} are reported as apparent values. All K_M curves display saturating kinetics and could fit well into the Michaelis Menten equation as expected.

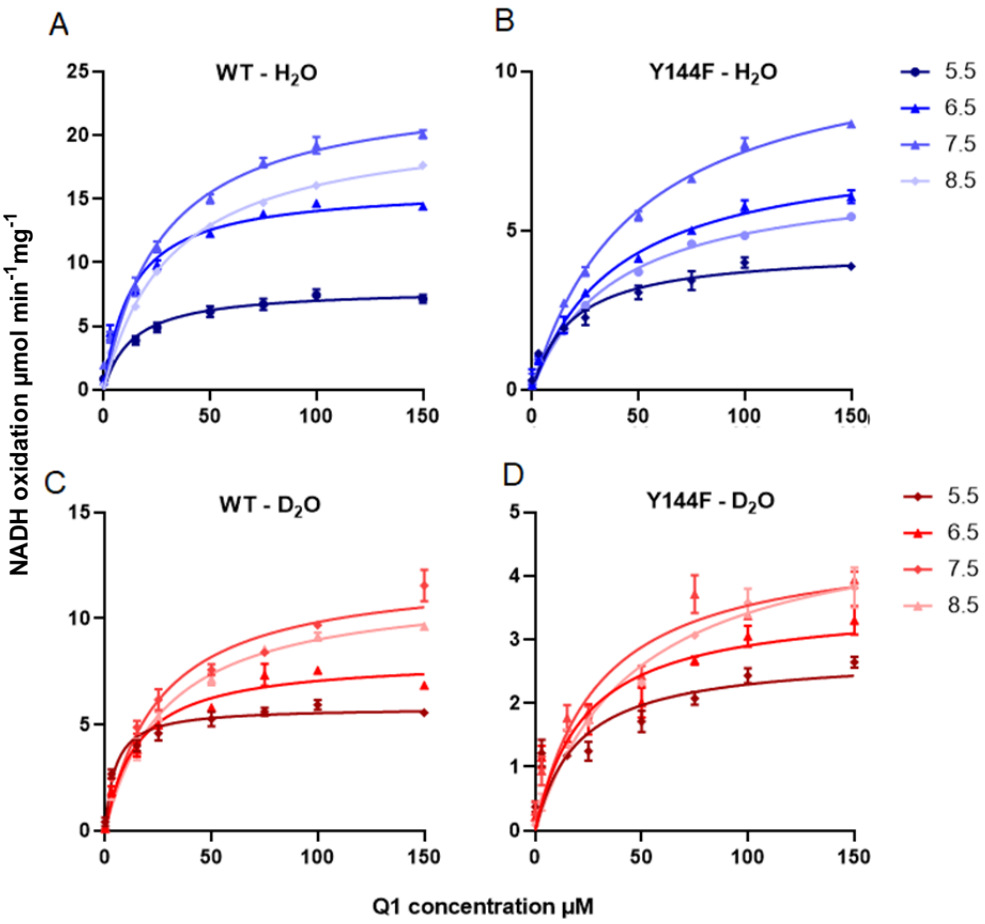

Figure 3.37: K_M curves of the NADH:Q1 oxidoreduction reaction at a range of pL in WT and Y144F proteoliposomes. NADH:Q_1 rates of complex I proteoliposomes were measured with increasing concentrations of Q_1 added from ethanol stocks at pL 5.5 – 9, but only the pH 5.5, 6.5, 7.5, and 8.5 are plotted. (A) *Y. lipolytica* WT assayed in H_2O. (A) *Y. lipolytica* Y144F assayed in H_2O. (C) *Y. lipolytica* WT assayed in D_2O. (D) *Y. lipolytica* Y144F assayed in D_2O. Errors are calculated as standard error of the mean (n = 3).

The pL dependence of fitted k_{cat} and apparent K_{sp} values are shown in Figure 3.38. The pL dependence of k_{cat} is bell-shaped and pKa values are consistent with that measured using other chain-length quinones as substrates. Apparent K_{sp} has a flat pL dependence like previously found using Q_2 as a substrate. The Y144F mutant appears to be far more deleterious when catalysing Q_1 than Q_2, with k_{cat} and K_{sp} representing 44% and 25% of WT. Despite catalysing the reduction of short-chain

quinones, the solvent isotope effect is large and comparable to that measured in Q_{10}. The observed KIE on k_{cat} and K_{sp} is 2.06 ± 0.26 and 1.84 ± 0.20 in the WT enzyme and 2.5 ± 0.24 and 1.82 ± 0.18 in the Y144F mutant.

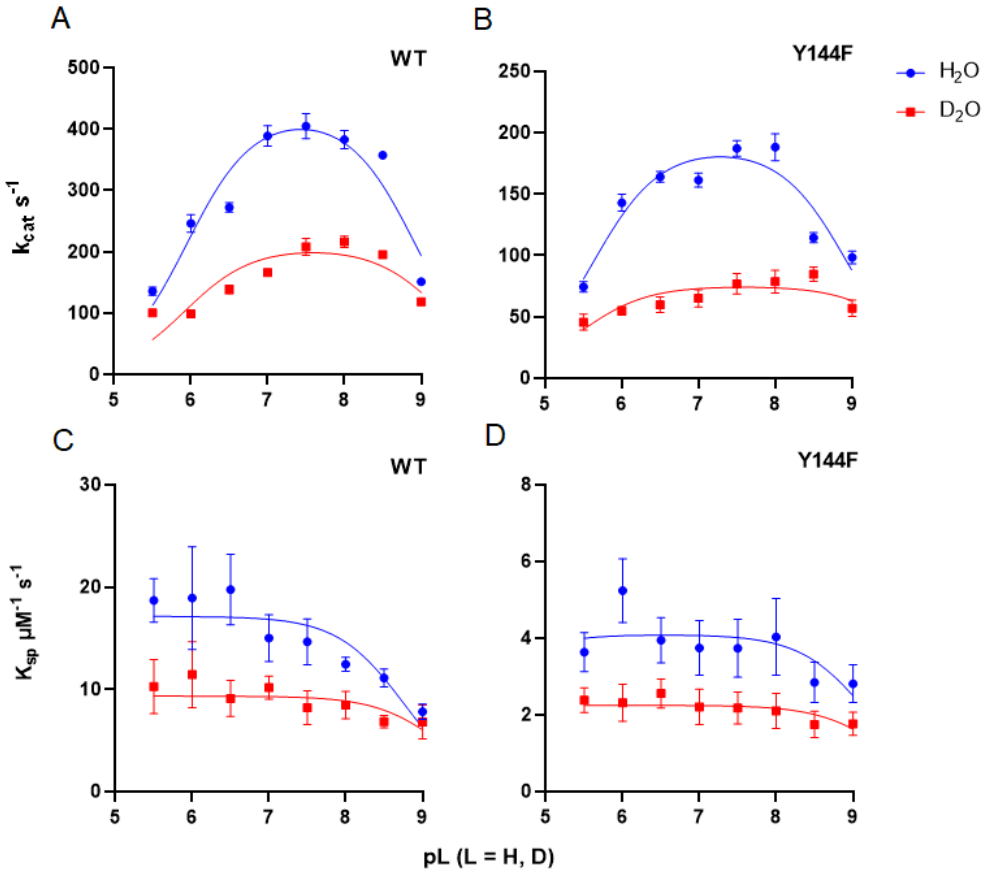

	WT H_2O	WT D_2O	Y144F H_2O	Y144F D_2O
k_{cat} s^{-1}	425.2 ± 32.5	206.6 ± 20.7	188.2 ± 12.09	75.08 ± 5.4
pKa 1	5.9 ± 0.15	5.9 ± 0.22	5.6 ± 0.15	5.5 ± 0.21
pKa 2	8.9 ± 0.17	9.3 ± 0.31	8.9 ± 0.16	9.7 ± 0.47
KIE	2.06 ± 0.26		2.5 ± 0.24	

Figure 3.38 pL dependence profiles of k_{cat} and K_{sp} of NADH:Q_1 oxidoreduction in proteoliposomes. (A) k_{cat} of the WT enzyme. The KIE is 2.06 ± 0.26 (B) k_{cat} of the Y144F variant. The KIE is 2.5 ± 0.24. (C) K_{sp} of the WT enzyme. The KIE is 1.84 ± 0.20 (D) K_{sp} of the Y144F variant. The KIE is 1.82 ± 0.18. Errors bars are standard error values calculated using Prism 9.

The large isotope effect on K_{sp} suggests that C_f (k_2/k_{-1}) is relatively small, and substrate release rates (k_{-1}) are relatively fast (compared to Q_2). A comparable observed KIE on k_{cat} suggest that Cvf (k_2/k_3) is relatively low (compared to Q_2) and product release is not severely rate-limiting. Together this suggests that Q_1 diffusion

dynamics within the binding channel are different to that in Q_2 and likely do not exhibit the “quinone channel blocking” behaviour proposed by (Fedor *et al.*, 2017).

The observed KIE on k_{cat} and apparent K_{sp} for WT complex I catalysing Q_1 is not statistically different to that catalysing Q_{10}, suggesting that the reaction geometry is conserved.

In contrast, the Y144F mutant has a higher observed KIE on k_{cat} and apparent K_{sp} using Q_1 than using Q_{10}, indicating that commitment factors (C_{vf}, C_f) and or the intrinsic isotope effect have changed. This may indicate that the substrates have a different reaction geometry, resulting in a different ΔZPE of the transition state, changing the intrinsic isotope effect.

The analysis of KIE on kinetic parameters using substrates Q_{10}, Q_2, and Q_1 reveals that the rate-limiting step is isoprenoid chain-length and Q-binding geometry dependent, further supporting the view that a proton transfer linked with Q-catalysis is the observed isotopically sensitive step.

Estimation of microscopic rate constants for the complex I-Q_1 reaction.

By inserting parameters k_{cat}, K_{sp}, and $^{D}k_{cat}$, $^{D}K_{sp}$ into equations 3.4 to 3.8 and using scheme 3.1, I estimate the microscopic rate constants of the WT and Y144F complex I variants (using the same methodology as section 3.8.1) for the catalysis of Q_1 (Table 3.4). The turnover time and fractional rate limitation for each step are summarised in Table 3.5. N.B. Apparent k_1, k_{-1}, K_M, and K_d depend on apparent values of substrate Q_1 concentration pools available to complex I. So, they are subject to large errors as the total volume concentration is much lower than the membrane concentration. However, the fitted apparent K_M agrees well with experimentally determined K_M values at pH 7.0, adding confidence to this model.

	WT Q_1	Y144F Q_1
$k_{1\ App}\ mM^{-1}s^{-1}$	27,979.98	6,361.51
$k_{-1\ App}\ s^{-1}$	530.99	160.05
$k_2\ s^{-1}$	922.17	288.57
$k_{-2}\ s^{-1}$	1.00	1.00
$k_3\ s^{-1}$	789.25	542.95
KIE_{Int}	3.30	3.30
Obs $^{D}K_{sp\ App}$	1.84	1.82
Obs $^{D}k_{cat}$	2.06	2.50
C_f	1.74	1.80
C_r	0.00	0.00
C_{vf}	1.17	0.53
$k_{cat}\ s^{-1}$	425.00	188.20
$K_{sp\ App}\ mM^{-1}s^{-1}$	17,120.00	4,092.00
$K_{d\ App}$ (µM)	18.98	8.22
$K_{M\ App}$ (µM)	23.95	46.02

Table 3.4. Scheme 1 kinetic parameters and commitment factors for WT and Y144F catalysing Q_1. Parameters were solved using equations 3.4 to 3.8 using excel solver and the evolution non-linear algorithm. Parameters k_{cat}, Apparent K_{sp}, and their respective observed KIE were constrained to their pH-independent values. Parameters k_1, k_{-1}, k_2, and k_3 were constrained to positive values. The reverse rate constant k_{-2} was constrained to 1, and intrinsic KIE was constrained to 3.3.

The k_{cat} of *Y. lipolytica* WT complex I catalysing Q_1 and Q_{10} is not significantly different. This result is in opposition to that measured by Fedor et al. (Fedor *et al.*, 2017) observed that the k_{cat} for Q_1 catalysis should be similar to Q_2, with both approximately half the k_{cat} for Q_{10}. However, the large observed isotope effects demonstrate that Q_1 clearly has faster substrate and product diffusion dynamics than Q_2, consistent with higher measured k_{cat}. There is little difference found when comparing the microscopic rate constants or fractional rate limitation on WT complex I catalysing Q_1 and Q_{10}, suggesting that the reaction geometry is conserved despite differences in quinone chain lengths.

In the Y144F mutant, k_{cat} for Q_1 is approximately 4.8-fold faster than that for Q_{10}. The increased conformational mobility with Q_1 likely increases the likelihood of adopting a reaction geometry that compensates for the Y144F mutation, increasing k_2. Confoundingly, the k_{cat} of Y144F when using Q_1 is 80 ± 7% that when using Q_2. This discrepancy may be explained by the lack of control for inactive “broken” complex I particles reconstituted within proteoliposomes which are incapable of quinone reduction but can be quantified with a NADH:APAD$^+$ assay for its flavin site activity.

Time	WT Q_1	Y144F Q_1
k_{cat} ms	2.35	5.31
k_2 ms	1.08	3.47
k_3 ms	1.27	1.84
F_a	46%	65%
F_b	54%	35%

Table 3.5. Fractional rate determination for WT and Y144F complex I catalysing Q_1.

Observed KIE on rate increases with Q_1 concentration for Y144F but not WT

Apparent K_{sp} is approximately 4-fold higher in WT than in Y144F, and this is supported by the observation that substrate binding is rate-limiting at low Q_1 concentration in the Y144F mutant. Figure 3.39 shows the substrate concentration dependence of observed KIE for each complex I variant. In the Y144F mutant, observed KIE increases from 1 to the maximum of 2.3 at 40 μM Q_1. In WT, the observed KIE on rate remains constant at ~1.8 even at very low substrate concentration, consistent with that observed in section 3.8.1.

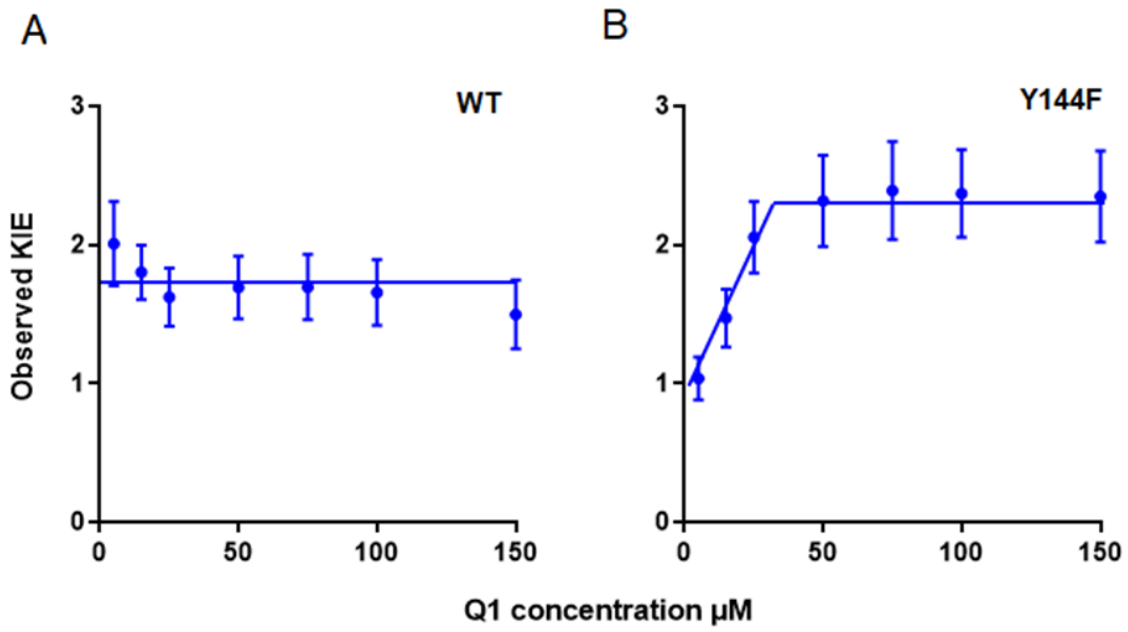

Figure 3.39 The substrate dependence on observed KIE of *Y. lipolytica* WT and Y144F. At each substrate concentration, pH rate profiles are fitted with Equation 1, and the KIE on the fitted Vopt value is plotted. (A) WT enzyme. (B) Y144F mutant. Errors are standard error values calculated using Prism 9.

pH dependence of K_M is dependent on ubiquinone chain length

The pL dependence of apparent K_M is shown in (Figure 3.40) and displays a bell-shaped dependence consistent with that observed with Q_2. The WT enzyme has a lower K_M than the Y144F mutant, which is consistent with higher substrate binding rates in the WT enzyme. Considering that this bell-shaped dependence is observed in both WT and Y144F in both Q_1 and Q_2, this is most likely a chain-length dependent effect independent of specific binding or reaction geometry at the primary Q site. Fedor et al. suggest that transfer along the quinone binding channel is unlikely to take place over a single step but over a complex energy surface with multiple minima and transient binding sites. In particular, the isoprenoid tails of long-chain Q (Q_6-Q_{10}) extend past the hydrophilic "kink region", whereas short-chain Q (Q_1-Q_4) does not. So, longer chain length quinones require fewer re-organization steps leading or trailing the quinone headgroup when binding or dissociating (as isoprenoids are identical) compared to short chain quinones. In the latter case, at every position along the binding channel, water molecules and charged residues must reorganize or change their protonation state respectively to facilitate the movement of the quinone headgroup (Fedor *et al.*, 2017). These effects may cause chain length-dependent changes in the pKas of substrate binding.

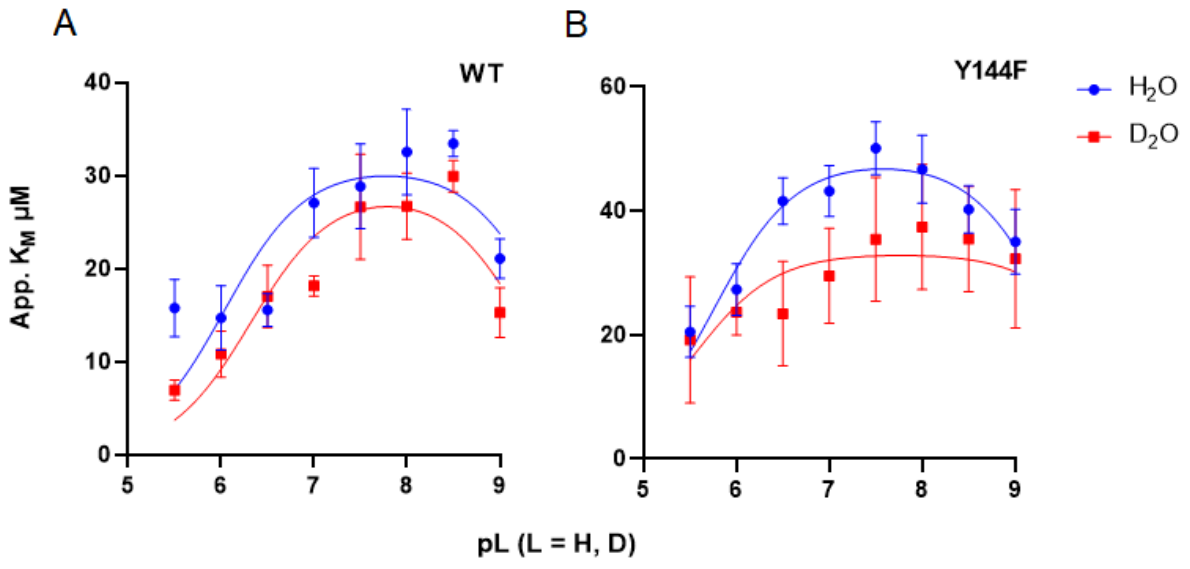

Figure 3.40 pL dependence profiles of K_M of NADH:Q_1 oxidoreduction in proteoliposomes. (A) K_M of the WT enzyme. (B) K_M of the Y144F variant. Errors bars are standard error values calculated using Prism 9.

3.10 Modelling the experimental data sets for the Q-reduction reaction of complex I

3.10.1 Proposed kinetic scheme for pH-dependent rate behavior of complex I

To delineate various pH effects on k_{cat}, K_{sp}, and K_M, a scheme is necessary to capture the distinct steps and equilibria that take place catalytically. Scheme 3.2 describes the proposed kinetic mechanism for complex I and is chosen out of 21 different schemes evaluated (Figure 3.41). Kinetic schemes were evaluated by using the kinetics software Dynafit by Biokin (Kuzmic, 1996). The WT *Y. lipolytica* complex I dataset in proteoliposomes was used to fit [Q] and pH-dependent NADH:AOX oxidoreduction rates to the evaluated kinetic scheme. The kinetic schemes were evaluated by the sum of squares error (SSE), number of kinetic parameters involved, and goodness of fit by comparing simulated and experimental data (see section 3.10.3). Scheme 3.2 was chosen because it has low SSE and contains relatively few parameters to avoid overfitting.

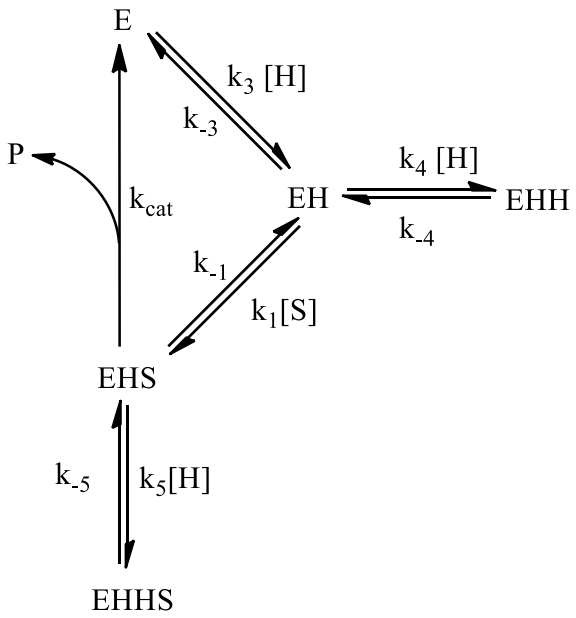

Scheme 3.2 Kinetic reaction scheme used to describe the quinone reduction mechanism of complex I. k_1 and k_{-1} are substrate association and dissociation constants, kcat represents the catalytic conversion and product release step, k_3 and k_{-3} are proton association and dissociation constant for activation, k_4 and k_{-4} are proton association and dissociation constants for competitive inhibition, k_5 and k_{-5} are proton association and dissociation constants for uncompetitive inhibition.

In this scheme, all enzyme forms are expected to be fully reduced because the NADH oxidation reaction has a k_{cat} that is at least an order of magnitude higher than quinone reduction; therefore, within the reaction timescale of quinone reduction, all enzyme forms can be approximated to be in the reduced form. The free enzyme form E reversibly binds to a proton from solution through $k_3^{[H]}$ and k_{-3} (second and first-order rate constant) and becomes the protonated and activated form EH. This can then bind substrate reversibly by $k_1^{[S]}$ and k_{-1} (second and first-order rate constant), where the substrate can be any quinone or be reversibly inhibited by binding a second proton through $k_4^{[H]}$ and k_{-4} (second and first-order rate constant). The substrate-bound enzyme EHS can form and release the product and return to its free enzyme form E through k_{cat} (first-order rate constant) or become reversibly inhibited through $k_5^{[H]}$ and k_{-5} (second and first-order rate constant). Parameters k_{-1}, k_{cat}, and k_{-1} may be combined to form K_M, according to the Briggs-Haldane formulation ($K_M = k_{-1} + k_{cat}/ k_1$). In addition, parameters (k_{-3}/ k_3) are combined to form the equilibrium constant K_3, (k_{-4}/ k_4) to K_4, and (k_{-5}/ k_5) to K_5 to simplify the number of parameters. In this kinetic scheme, a proton is an activator through K_3, a competitive inhibitor through K_4, and an uncompetitive inhibitor through K_5. Note that this mechanism is not a comprehensive definition of the quinone reduction reaction, but it serves as a functional approximation that is explanatory of observed experimental data. Specifically, k_{cat} is not separated into catalytic and product release steps, and additional parameters increase the complexity of the rate equation and exponentially extend the computation time for fitting.

a - 9 params

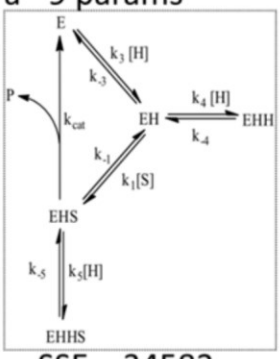

SSE = 34582

b - 9 params

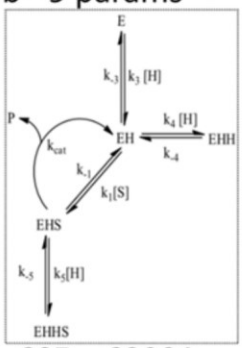

SSE = 68991

c - 7 params

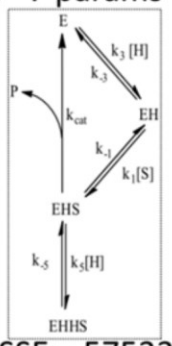

SSE = 57533

d - 7 params

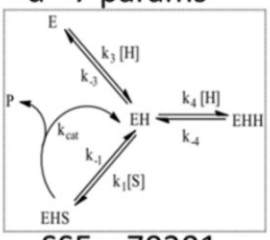

SSE = 70201

f - 9 params

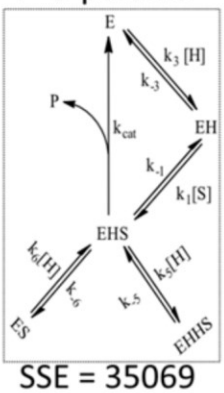

SSE = 35069

e - 7 params

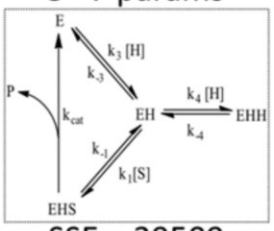

SSE = 39509

d - 7 params

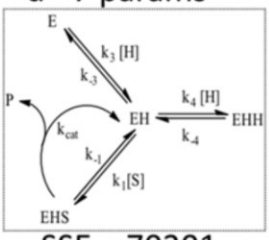

SSE = 70201

e - 7 params

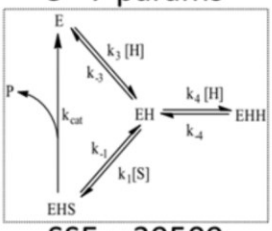

SSE = 39509

g - 11 params

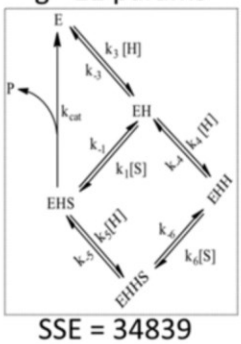

SSE = 34839

h - 15 params

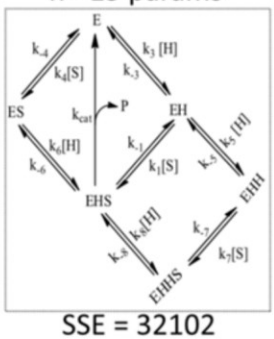

SSE = 32102

i - 11 params

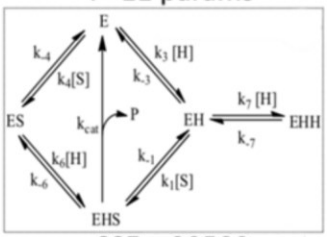

SSE = 39509

j - 11 params

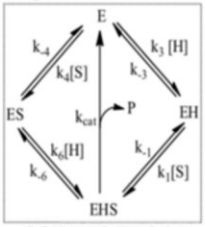

SSE = 251237

k - 11 params

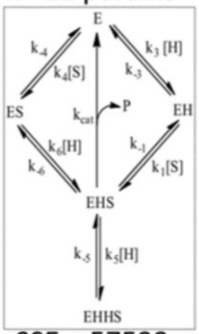

SSE = 57533

l - 13 params

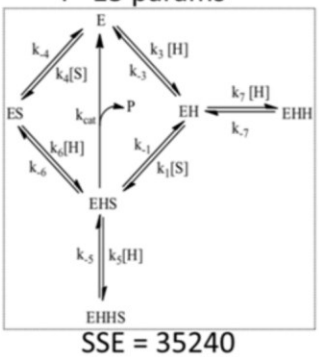

SSE = 35240

m - 9 params

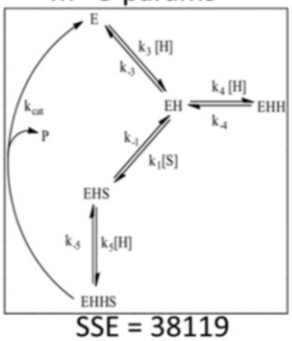

SSE = 38119

n - 9 params

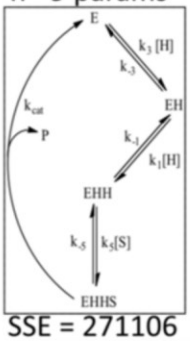

SSE = 271106

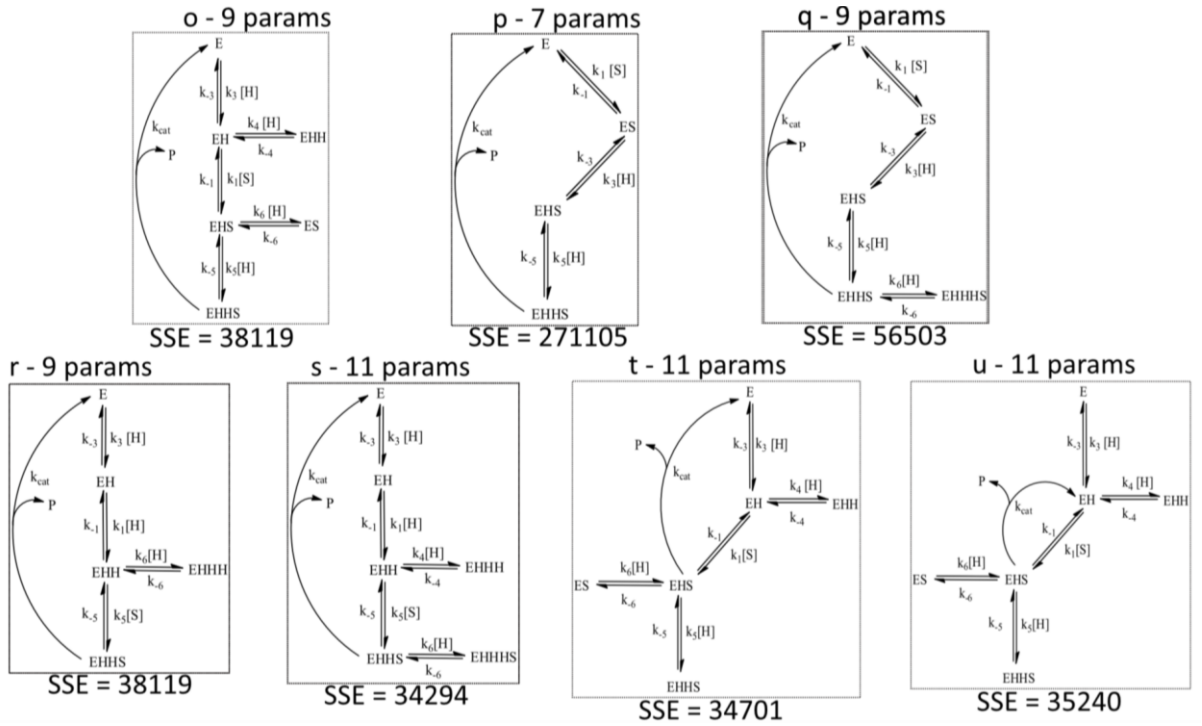

Figure 3.41 The list of kinetic schemes evaluated using Dynafit. Each scheme is labelled with an alphabetical label and the number of parameters above. [Q] and pH-dependent NADH:AOX oxidoreduction rates were fitted with each kinetic scheme using Dynafit, and the resultant output sum of squares error (SEE) is labelled under each scheme. All rate constants were set as variables with an initial value of one. Least-squares fit of experimental data was performed using the trust-region algorithm.

3.10.2 Derivation of the rate equation using the King Altman method

The rate equation for scheme 3.2 was derived using the King-Altman method. The King-Altman method is a schematic method of deriving rate laws for enzyme-catalyzed reactions, which is generally useful for more complicated mechanisms where manual derivation is prone to human error (King *et al.*, 1956; Cornish Bowden, 1977; Sims, 2009). Briefly, for each enzyme species in the reaction scheme, patterns can be drawn as “flux” for its formation (Figure 3.42). Each pattern corresponds to a term in the numerator for the expression of the relative concentration of each enzyme species. This represents the rate constants that govern the rate of formation of this species. The denominator term “Δ” represents the summation of all the “flux” pattern terms for all enzyme species and represents the rate of formation of the total enzyme concentration. A key assumption held by this method is that the reaction follows the steady-state approximation. The steady-state approximation applies here because the reaction is monitored at a stage of the reaction where substrate

concentration exceeds enzyme concentration, and the measured rate is approximately constant over a period of 5 minutes, so the concentration of each enzyme species is at a steady-state (Briggs and Haldane, 1925). The overall rate is then equal to the consumption of the enzyme-substrate complex, $v = k_{cat}[EHS]$, similar to the Michaelis Menten equation.

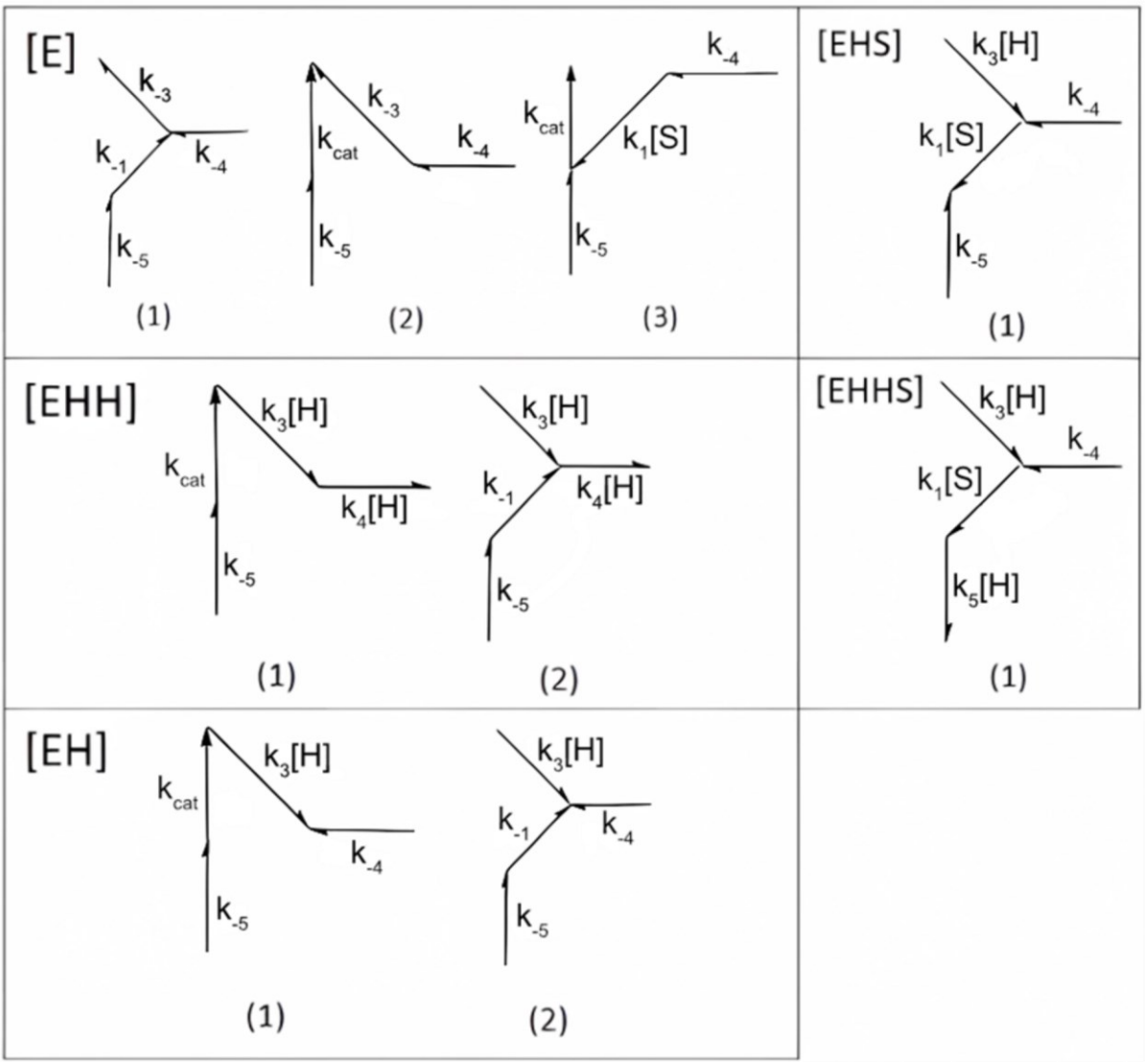

Figure 3.42 The possible patterns that connect the enzyme species E, EH, EHH, EHS, and EHHS. Each pattern represents the number of ways each species can be formed. Each pattern corresponds to a term in the numerator for the expression of the relative concentration of each enzyme species.

Derivation 3.2 – Rate equation for Scheme 3.2 using the King-Altman method:

Create expressions for the relative concentration of each enzyme species

$$\frac{[EHS]}{[E_0]} = \frac{k_1[S]k_3[H]k_{-4}k_{-5}}{\Delta} \quad (1)$$

$$\frac{[E]}{[E_0]} = \frac{k_{cat}k_{-3}k_{-4}k_{-5} + k_1[S\}k_{cat}k_{-4}k_{-5} + k_{-1}k_{-3}k_{-4}k_{-5}}{\Delta} \quad (2)$$

$$\frac{[EH]}{[E_0]} = \frac{k_{cat}k_3[H]k_{-4}k_{-5} + k_3[H]k_{-1}k_{-4}k_{-5}}{\Delta} \quad (3)$$

$$\frac{[EHH]}{[E_0]} = \frac{k_{cat}k_3[H]k_4[H]k_{-5} + k_3[H]k_4[H]k_{-1}k_{-5}}{\Delta} \quad (4)$$

$$\frac{[EHHS]}{[E_0]} = \frac{k_1[S]k_3[H]k_{-4}k_5[H]}{\Delta} \quad (5)$$

$$\Delta = [E_0] = [EHS] + [E] + [EH] + [EHH] + [EHHS] \quad (6)$$

Simplify 1, 2, 3, 4 and 5

$$\frac{[EHS]}{[E_0]} = \frac{k_1[S]k_3[H]k_{-4}k_{-5}}{\Delta} \quad (7)$$

$$\frac{[E]}{[E_0]} = \frac{k_1[S]k_{cat}k_{-4}k_{-5} + (k_{-1} + k_2)k_{-3}k_{-4}k_{-5}}{\Delta} \quad (8)$$

$$\frac{[EH]}{[E_0]} = \frac{(k_{\text{cat}} + k_{-1})k_3[H]k_{-4}k_{-5}}{\Delta} \quad (9)$$

$$\frac{[EHH]}{[E_0]} = \frac{(k_{\text{cat}} + k_{-1})k_3[H]k_4[H]k_{-5}}{\Delta} \quad (10)$$

$$\frac{[EHHS]}{[E_0]} = \frac{k_1[S]k_3[H]k_{-4}k_5[H]}{\Delta} \quad (11)$$

Substitute and simplify.

$K_3 = \frac{k_{-3}}{k_3}$; $K_4 = \frac{k_{-4}}{k_4}$; $K_5 = \frac{k_{-5}}{k_5}$; $K_M = \frac{k_{-1}+k_{cat}}{k_1}$ **or**

$K_{sp} = \frac{k_1 k_2}{k_{-1}+k_{cat}}$

The rate of the overall reaction is determined by the first order rate constant k_{cat} and [EHS]

$$v = k_{cat}[EHS] = \frac{[E_0]k_{cat}[S][H]}{[S]\left(k_{cat}\frac{K3}{k_{-3}} + [H] + \frac{[H]^2}{K_5}\right) + K_M\left(K_3 + [H] + \frac{[H]^2}{K_4}\right)}$$

Equation 3.9

Alternate form using K_{sp}

$$v = k_{cat}[EHS] = \frac{[E_0]k_{cat}K_{sp}K_4K_5[S][H]}{K_5k_{cat}\left(K_4\left(K_3K_{sp}[S] + K_3 + [H]\right) + [H]^2\right) + K_{sp}K_5[S][H]K_4 + K_{sp}K_4[S][H]^2}$$

Equation 3.10

3.10.3 Modelling the NADH:Q reaction: establishing best-fit to the experimental data

The experimental datasets for the NADH:Q_{10}, NADH:Q_1, and NADH:Q_2 reactions were fitted to Equation 3.9 and 3.10 using a computer program developed in MATLAB (Appendix 7.3) to identify 'best fit' parameters. Datapoints are input as a 3-dimensional matrix (pH, substrate, rate) and the model fits to experimental datasets by minimizing the least squares error value (LSQE, the sum of squares difference of calculated rate to the experimental value). Parameters were screened across broad ranges (at least six orders of magnitude) initially to avoid parameters falling into a local minima and iteratively screened by constricting the possibility space to minimize LSQE values. k_{-3} was constrained to 1, as it is interdependent to k_3 as part of parameter K_3. N.B. That several best-fit parameters are identical for multiple datasets, this is because the parameters were screened in logarithmic steps, and so the same values are screened for multiple datasets. This algorithm screens mechanically across a set range of values and is different to how evolutionary algorithms function, which undergo rounds of selection and mutation until a final set of values converge.

To evaluate and allow comparison for the goodness of fit for different datasets, the relative root mean square error (RRMSE) was calculated (Equation 3.11), which is the root mean square error of the dataset normalized to the size of the dataset into a dimensionless unit (0 is perfect fit, and 1 is indistinguishable from noise). This is the preferred metric over calculating the R^2 value because the latter is not valid for non-linear regression models (Spiess and Neumeyer, 2010); an RRMSE of <10% is considered excellent.

$$RRMSE = \sqrt{\frac{\frac{1}{n}\sum_{i=0}^{n}(y_i - \hat{y}_i)^2}{\sum_{i=1}^{n}(\hat{y}_i)^2}} \tag{3.11}$$

Table 3.6 summarizes the best-fit parameters of all proteoliposome datasets measured in this chapter. Parameters K_3, K_4, and K_5 are fitted as pKa values to better compare with experimental pL values. All but one dataset fit satisfactorily below 10% RRMSE, with the exception of Y144F Q_2 in H_2O which fit at 10.1%.

	Best fit value in H_2O								
	WT Q_{10}	D196N Q_{10}	M91I Q_{10}	Y144F Q_{10}	Bovine Q_{10}	WT Q_1	Y144F Q_1	WT Q_2	Y144F Q_2
best_pKa3	11.31	10.14	11.14	9.76	10.58	11.38	11.17	10.90	11.10
best_pKa4	6.62	5.34	6.31	5.45	6.02	3.00	3.00	3.00	3.00
best_pKa5	5.52	4.79	5.97	4.72	5.38	5.86	5.69	5.34	4.59
best_K_{sp} $mM^{-1}s^{-1}$	727.95	96.12	154.77	13.74	188.76	13737.26	4175.32	4954.97	3401.34
best_k_{cat} s^{-1}	417.54	38.57	529.79	38.57	193.06	417.54	188.76	264.48	235.78
best_K_M mM	0.53	0.42	3.63	3.04	0.97	0.030	0.045	0.053	0.068
best_error	20023.10	546.34	9171.72	244.28	2484.42	29205.56	14752.37	6023.66	20148.30
RMSE	18.91	3.12	12.80	2.09	6.66	21.36	15.18	10.37	18.97
RRMSE (%)	4.9%	7.0%	3.7%	7.3%	3.8%	6.4%	8.7%	8.3%	10.1%
	Best fit value in D_2O								
best_pKa3	11.52	10.31	11.28	9.97	10.72	11.59	11.28	10.69	11.17
best_pKa4	6.66	6.62	6.62	5.34	6.86	3.00	3.00	3.00	3.00
best_pKa5	5.90	5.34	6.17	4.34	5.83	5.66	5.38	5.52	5.38
best_K_{sp} $mM^{-1}s^{-1}$	303.95	96.12	75.74	9.61	174.34	8531.59	2807.24	4891.97	3225.34
best_k_{cat} s^{-1}	188.76	16.10	188.76	23.95	121.96	188.76	72.79	239.85	203.89
best_K_M mM	0.62	0.17	2.49	2.49	0.70	0.022	0.026	0.049	0.063
best_error	4509.62	207.07	4287.13	122.95	2086.01	14028.46	2380.28	9372.64	5734.40
RMSE	8.97	1.92	8.75	1.48	6.10	14.81	6.10	12.10	9.47
RRMSE (%)	5.1%	9.7%	5.7%	6.7%	5.2%	7.8%	8.4%	8.5%	6.9%
KIE kcat	2.21	2.39	2.81	1.61	1.58	2.21	2.59	1.10	1.16
KIE Ksp	2.39	1.00	2.04	1.43	1.08	1.61	1.49	1.01	1.05

Table 3.6. Best fit parameters obtained by LSQE minimisation for the pL-dependent rate of NADH:Q reactions in proteoliposomes. The best error represents the minimised LSQE value from the resultant best-fit parameters to the experimental value. K_{sp} and K_M values for Q_1 and Q_2 are apparent values.

The best fit to the data using the optimized parameters is very good and is demonstrated here using the *Y. lipolytica* WT and bovine complex I [Q_{10}] and pH-dependent NADH:AOX oxidoreduction rate datasets. Figure 3.43 compares simulated rates using optimized parameters to experimental data. The curve fits are almost identical, except for at the extremities pH, which is likely due to experimental error and is not a systematic error replicable among the two datasets shown.

Figure 3.44 shows simulated k_{cat}, K_{sp}, and K_M compared to experimental data for *Y. lipolytica* WT and bovine complex I datasets. The simulated pH-dependent k_{cat} and K_{sp} values are very similar to the experimentally determined data points for the *Y. lipolytica* dataset. The simulated K_{sp} for bovine complex I deviates at high pH due to simulated values of K_M being lower than experimental values. Simulated K_M values have the same unidirectional trend present in the experimental data and agree with the exception of extremities of pH. This is also likely due to experimental error, as K_M is generally error-prone at low measured rates, which explains why fitting breaks down at low pH for *Y. lipolytica* and at high pH for bovine complex I.

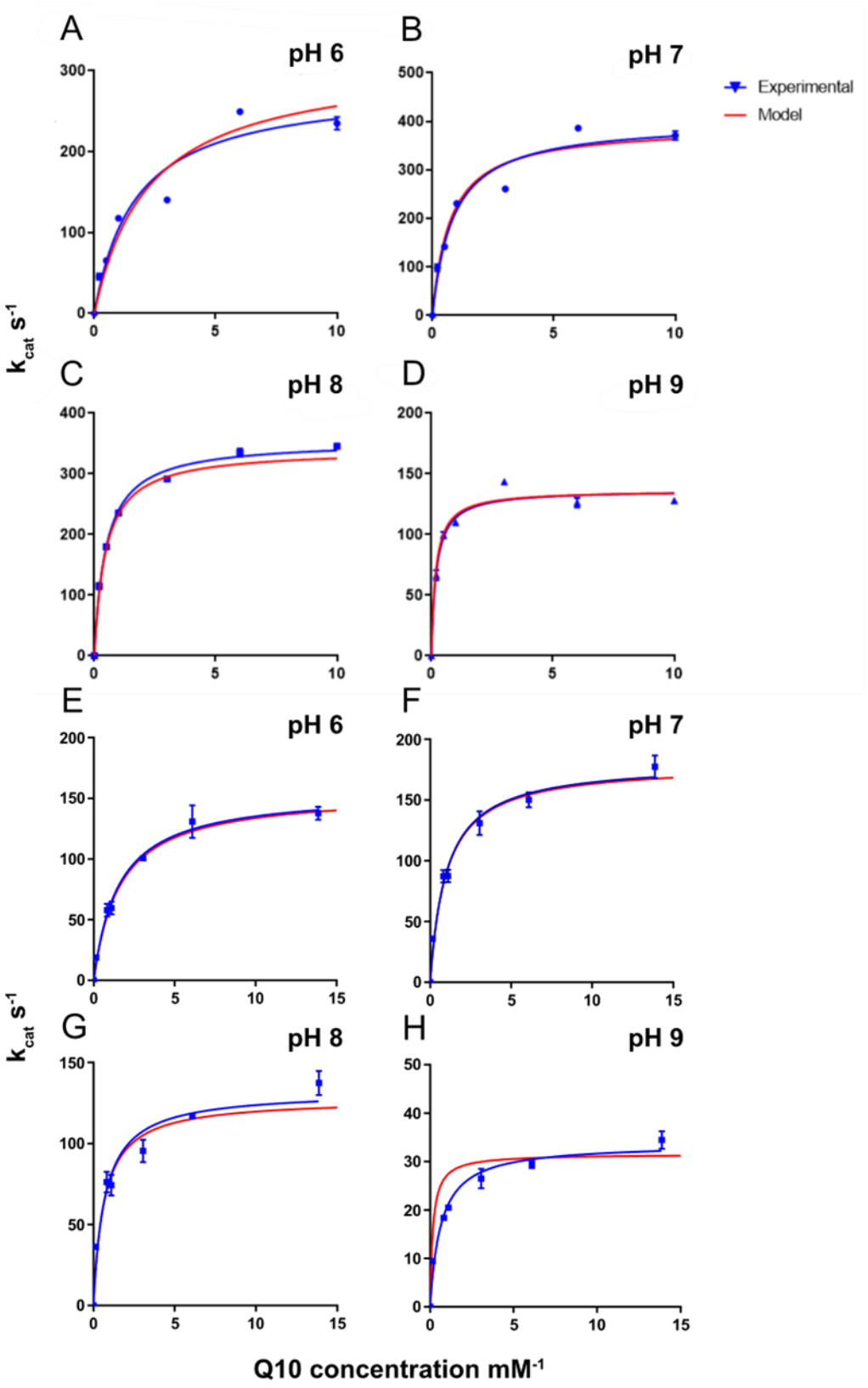

Figure 3.43 Comparison of simulated and experimental K_M curves. Blue symbols represent measured experimental values of the experimental Q_{10} dataset. Red represents datapoints simulated by fitting equation 9 with optimised parameters. (A-D) The Y. lipolytica WT dataset. (E-F) Bovine complex I. (Errors bars are standard errors of the mean (n = 3).

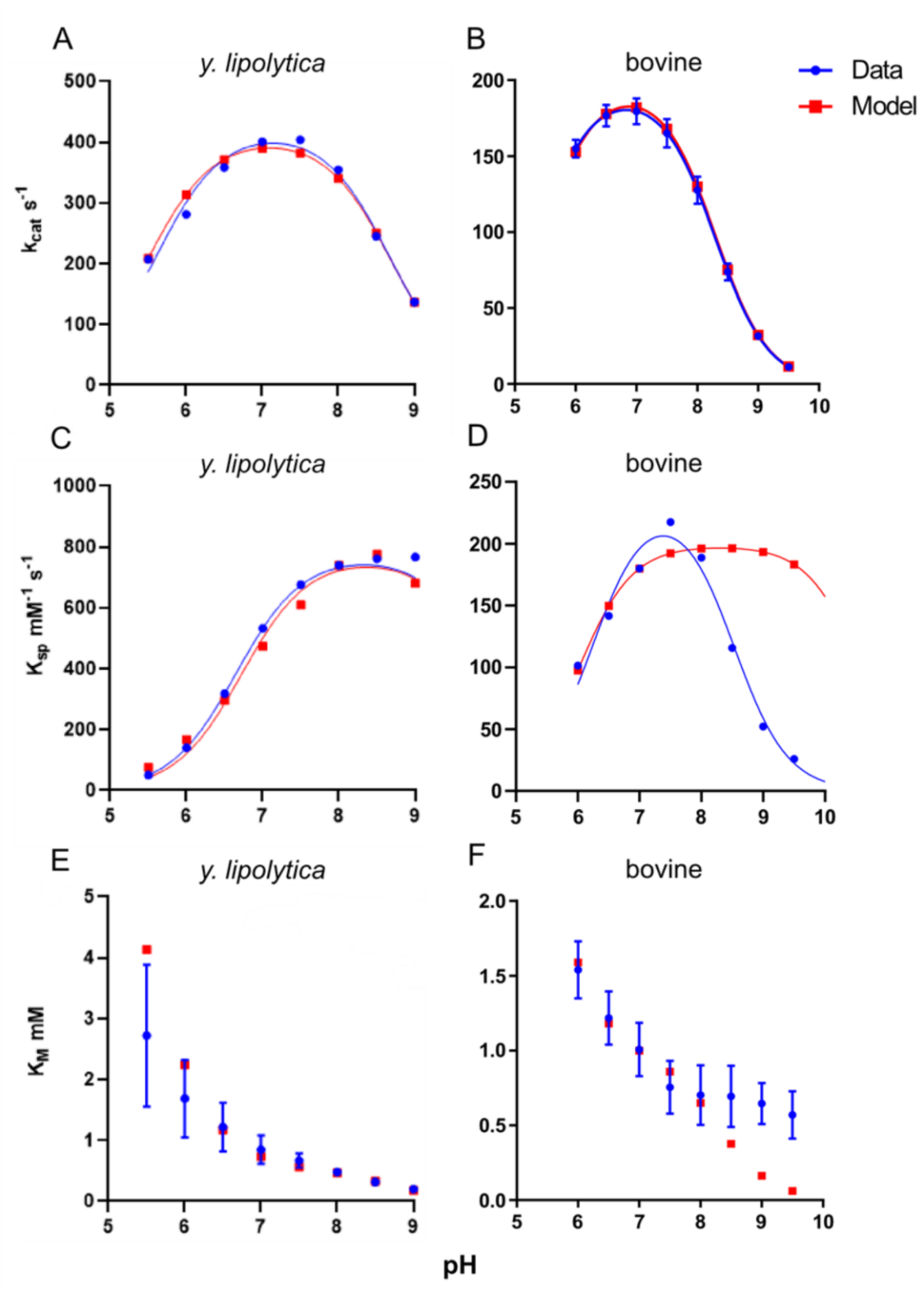

Figure 3.44 Comparison of simulated k_{cat}, K_{sp}, and K_M values and experimental values. Blue symbols represent measured experimental values. Red represents datapoints simulated by fitting equation 9 with optimised parameters. Kinetic parameters are pH dependence of (A-B) k_{cat}, (C-D) K_{sp}. (E-F) K_M, for *Y. lipolytica* and bovine complex I Q_{10} datasets. Errors are calculated as standard error of the mean (n = 3).

3.10.4 Sensitivity analysis

For each parameter, a range of values within which acceptable fits could be generated was estimated by fixing the investigated parameter at a certain value whilst allowing free variation of the other parameters to minimize the LSQE. The acceptable LSQE threshold was determined as the limit of acceptable fit using the relative RMSE method at 10%. And Figure 3.45 shows the variation of LSQE values with a range of pKa values for the *Y. lipolytica* WT Q_{10} dataset, with acceptable values where RRMSE <10% represented as below the dashed lines.

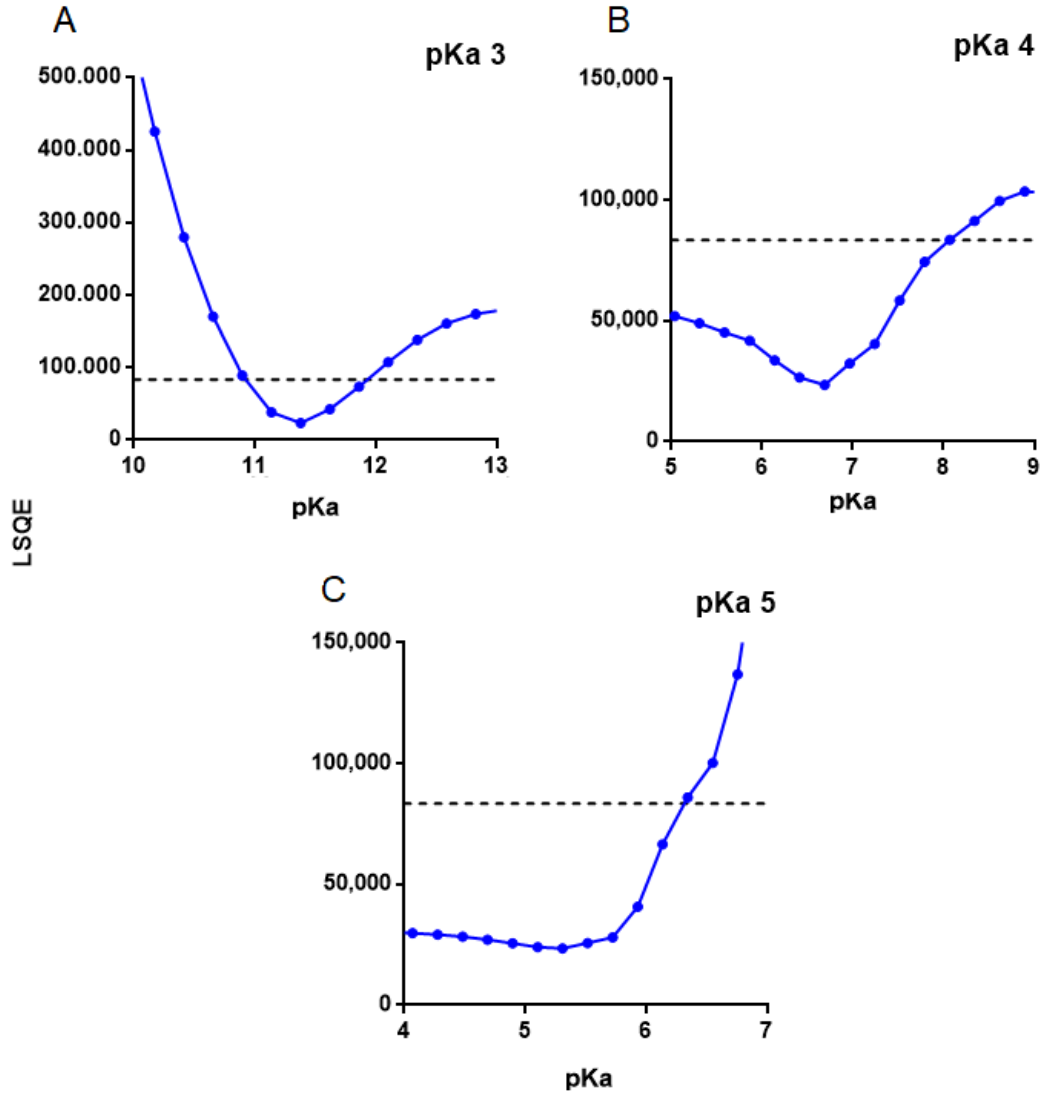

Figure 3.45 LSQE values describing the sensitivity of each best-fit parameter pKa 3, 4 and 5. Values for each parameter value were set, and LSQE values were minimised by screening all other parameters to form a best fit, thus allowing compensatory effects. k_{-3} was constrained to 1. Values below the dashed lines produced fit with the relative RMSE at <10%. For pKa 4 and 5, the trend continued until pKa = 2, the lowest value tested.

The relationship between the pair of parameters k_{cat} and K_{sp} or $K_{sp\ App.}$ is represented using two-dimensional projections, where the two parameters are varied against each other with pKa values fixed at the best-fit values to illustrate their possible parameter combinations. This is illustrated in Figure 3.46, where the Z axis (colours) represents the percentage RRMSE for *Y. lipolytica* WT Q_{10}, Q_2, and Q_1 datasets.

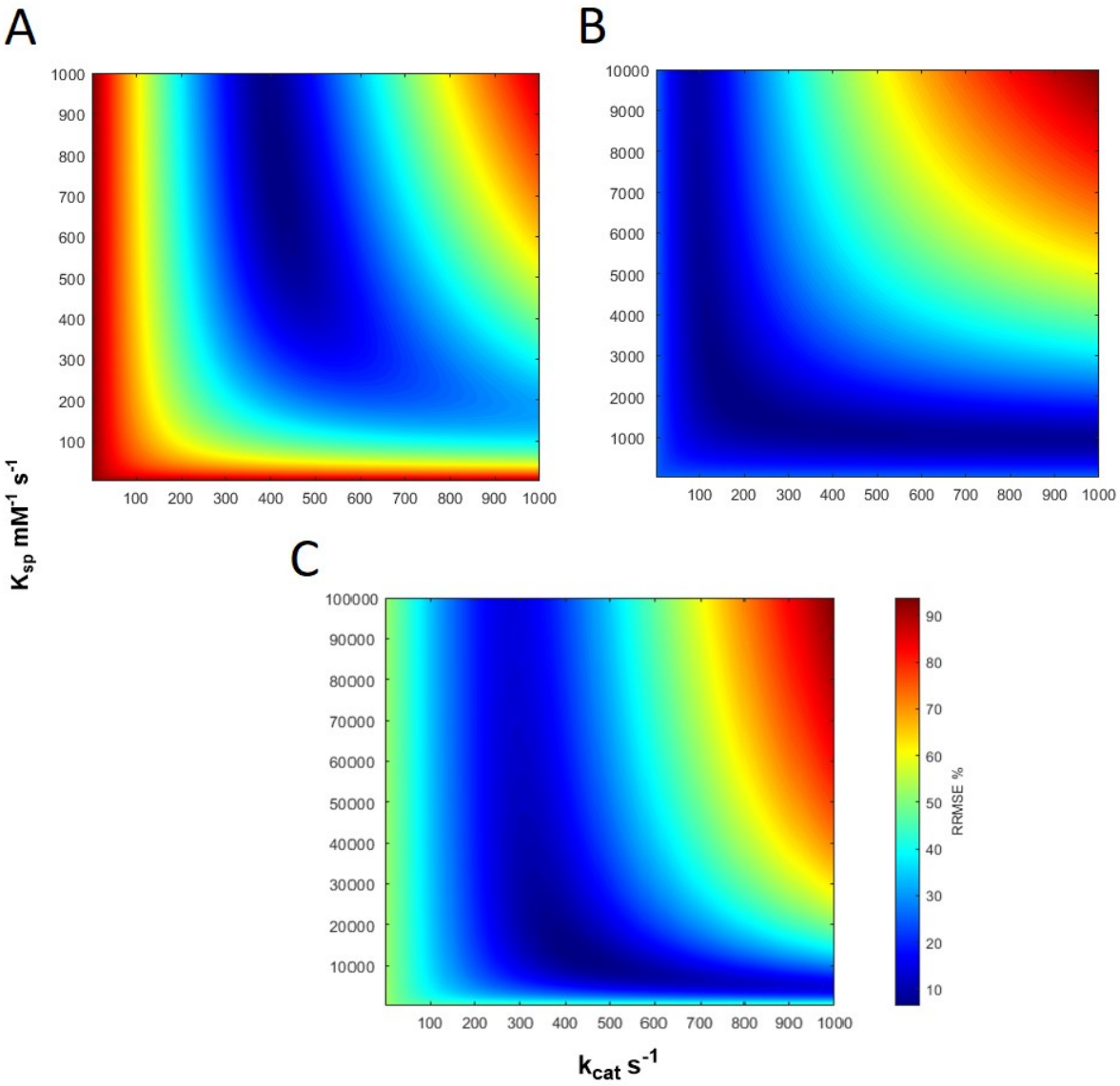

Figure 3.46 Two-dimensional projections used to describe the parameter relationship between k_{cat} and K_{sp} or $K_{sp\ App.}$ for *Y. lipolytica* WT complex I datasets. (A) Q_{10}, (B), Q_2, and (C) Q_1. The parameters K_3, K_4 and K_5 are fixed to each dataset's respective best-fit values. The darker the colour blue within the 2D projection the more favourable the parameter combination.

3.11 pH-dependent activation, competitive, and uncompetitive inhibition causes pH dependence in K_M

Previously, when measuring the pH dependence of K_M for the complex I reaction with Q_{10}, a unidirectional pH dependence was observed on K_M, and for the complex I reaction with Q_1 and Q_2, instead, it is bell-shaped. The use of scheme 3.2 and associated simulation show that the shape of the pH-dependent K_M profile is dependent on pKa 3, pKa 4 and pKa 5 which are the equilibrium constants for pH-dependent activation, competitive and uncompetitive inhibition respectively. In this case, the inhibitor is a proton, and increasing the pKa 4 and pKa 5 values is equivalent to increasing the potency of inhibition. Therefore, increasing pKa4 increases K_M, and increasing pKa5 decreases K_M.

This effect is shown in Figure 3.47, where K_3, K_4, and K_5 are varied and the resultant pH dependence of k_{cat} and K_M are plotted. In this simulation, rates are calculated using the rate equation (Equation 3.10) with enzyme concentration set to 1 and best-fit values of the *Y. lipolytica* WT Q_{10} dataset. pKa 3, pKa 4, and pKa 5 are each varied whilst keeping other parameters constant and compared to experimentally determined data. Decreasing pKa 3 decreases proton activation of complex I, thus lowering V_{max} and K_M. Increasing pKa 4 and pKa 5 both affect the pH dependence of V_{max} by increasing apparent pKa 1 (ascending arm) and increasing pKa 3 increases apparent pKa 2 (descending arm). When varying pKa 4, the pH dependence of K_M changes from unidirectional dependence to a bell-shaped dependence when pKa 4 is below 5. The same is observed when varying pKa 5 but in the opposite direction and K_M is bell-shaped at pKa 5 values above 7. Of note is that below a value of 7, decreasing pKa 4 values cease to affect V_{max} but continue to affect K_M.

The best-fit values for pKa 4 for Q_1 and Q_2 datasets have no distinct minima and fit equally well at a value below 5, which is at least 2 pH units more acidic than the equivalent for Q_{10} datasets. pKa 3 and pKa 5 in contrast, do not shift significantly with substrate chain length. This suggests that pKa 4 is the primary parameter affected by differences in substrate chain length and that the competitive inhibition of substrate binding by protons is chain-length dependent. As of yet, there is no

molecular proposal for this observation, but the “kink region” rich with Glu and Arg residues (Figure 1.9) may offer an avenue for investigation.

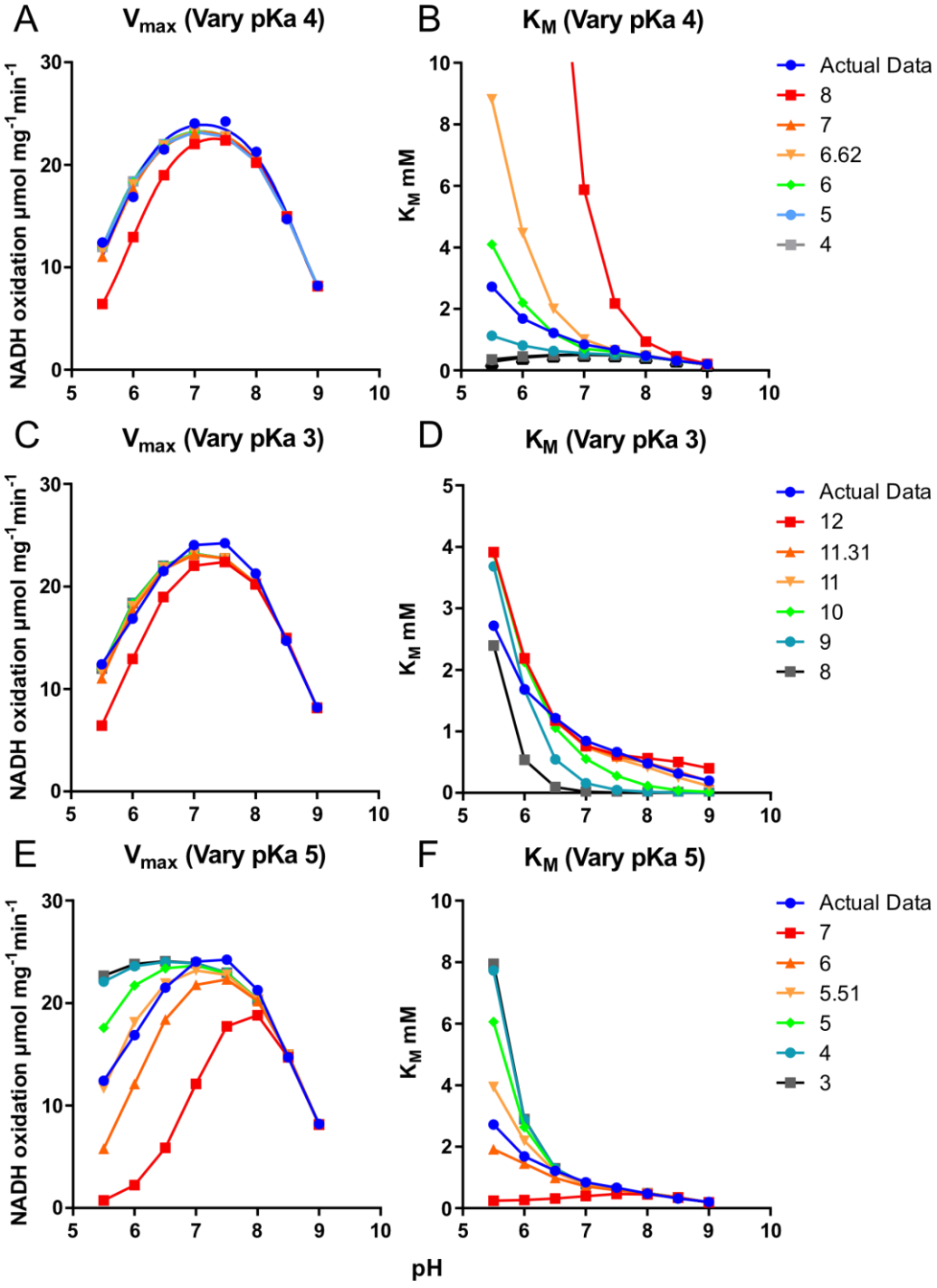

Figure 3.47 Simulated pH-dependent V_{max} and K_M profiles of *Y. lipolytica* WT complex I. NADH:Q_{10} oxidoreduction rates are simulated using the Equation 3.10 with enzyme concentration set to 1, and best-fit values of the *Y. lipolytica* WT Q_{10} dataset. pKa 3, 4, and 5 are each varied whilst keeping other parameters constant. (A) and (B) represent the pH V_{max} and K_M profiles whilst varying pKa 4 respectively. (C) and (D) represent the same whilst varying pK_3, and (E) and (F) whilst varying pKa 5.

3.12 Measuring the proton inventory of mitochondrial complex I

3.12.1 The proton inventory method

A key question in the interpretation of a solvent isotope effect is the number of protons that contribute to the observed isotope effect. This is addressed by carrying out a proton inventory experiment, in which the solvent isotope effect is determined in a range of mixtures of D_2O and H_2O (Venkatasubban and Schowen, 1984; Kohen and Limbach, 2005). This experiment also allows the characterization of the rate-limiting transition state and can be used to characterize the proton donor (see Chapter 4 for an in-depth example) or to characterize the degree of rate-limitation of the proton-transfer step in catalysis (see below).

Proton inventory plots are assessed by their shape, which is fitted to a form of the Kresge-Gross-Butler equation (Equations 3.13 – 3.15). When a single proton is transferred in the transition state, linear proton inventories are obtained. When multiple protonic sites are involved in the rate-limiting transition, the plot becomes "bowl-shaped". In cases where the enzyme is rate-limited by two or more microscopic transition states, the observed isotope effect becomes a weighted average of each state and results in "dome" shape inventory plots (Quinn, 1987).

Figure 3.48 illustrates an example proton inventory plot. The blue line indicates a linear proton inventory, where one proton with an intrinsic isotope effect of 2.3 is solely rate-limiting. The red and purple lines indicate that two and three protons, with an intrinsic isotope effect of 1.5 and 1.3, respectively, are "in flux" in the same transition state. The brown line indicates a scenario where two transition states are equally rate-limiting (each 50% rate-determining), and the first transition state has an intrinsic isotope effect of 3.6, with the second transition state isotopically insensitive. These plots are generated by equations 3.14 and 3.15, described in the next section.

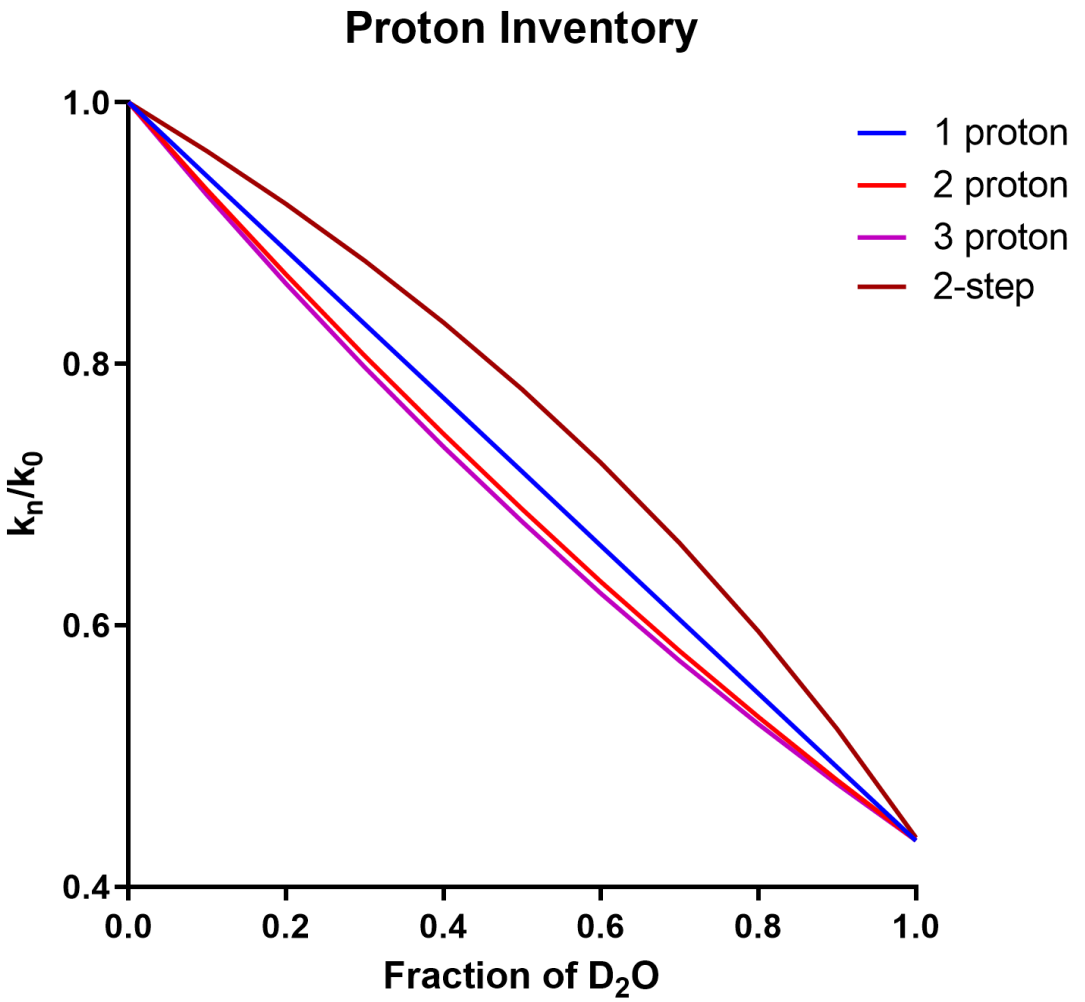

Figure 3.48 A simulated proton inventory plot. Each proton inventory plot has an observed KIE of 2.3, but each has different mechanisms. The blue line (linear) represents a solely rate-limiting transition state with a single proton transferred. The red and purple lines (bowl-shaped) represent a solely rate-limiting transition state with two and three protons involved, respectively. The brown line represents an enzyme rate limited equally by two transition states and gives a “dome” shape. Equations 3.14 and 3.15 are used to generate the plots. The intrinsic isotope effect for the blue line is 2.3, the red line is 1.5, the purple line is 1.3, and the brown line is 3.6 for transition state one and 1 for transition state two.

Note that although the observed kinetic isotope effect is the same for all four plots, the intrinsic isotope effects are different, and the mechanisms are different. Herein lies the utility of the proton inventory method, which allows direct characterization of the isotopically sensitive and rate-limiting transition states. However, as the number of protons involved in the transition state increases, the precision necessary to differentiate this number also increases.

3.12.2 Theoretical basis of solvent isotope effects and the proton inventory method

Scheme 3.3 is a simplified reaction scheme depicting a reaction equilibrium between reactant R-H and product P-H, each of which contains a single proton that can be readily exchanged with a solvent proton/ deuteron.

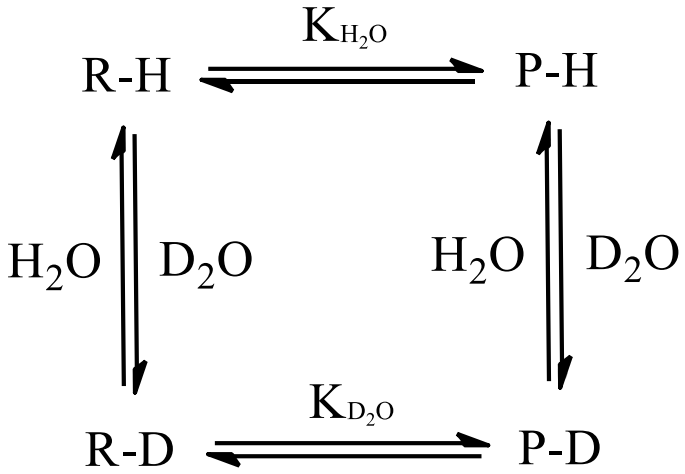

Scheme 3.3. Thermodynamic cycle for equilibrium isotope effects.

The solvent isotope effect on the equilibrium constant is expressed as a ratio of the fractionation factors on the reactant and product states, where n and 1-n are the respective fractions of the solvent D_2O and H_2O (Equation 3.12). These are called fractionation factors as they measure the tendency of a solute site to fractionally contain deuterium, compared to the deuterium fraction of the solvent. Fractionation factors measure the tightness of binding of a particular proton binding site compared to the average O-L site of the solute. A proton binding site with equal proportions of proton and deuteron binding when D_2O represent 50% of the overall solvent has a fractionation factor of 1 and has an equal bond strength to the average solvent molecule. In general, deuterium accumulates where binding is tighter, or the bond strength is higher. So, for a transition state proton bond that is looser than its reactant state, a ϕ of less than 1 is expected, yielding a normal isotope effect. This fractionation factor is affected by pKa values, where the weaker the acid, the higher the fractionation factor. For example, phenol has a reactant fractionation factor of 1.13, compared to carboxylic acids, which yield a value of 0.92 (Jarret and Saunders, 1985). In short, enzymic proton binding sites compete with the solvent for the accumulation of deuterons.

$$\frac{K_{H2O}}{K_{D2O}} = \frac{\phi_R}{\phi_P}; \phi_R = \frac{[R-D]/[R-H]}{n/(1-n)}; \phi_P = \frac{[P-D]/[P-H]}{n/(1-n)}$$

(3.12)

A proton inventory plot is fit to the Kresge-Gross-Butler equation (Equation 3.13 – 3.15), which describes the changes in the fractionation constant of a protic site as it goes from the reactant state to the transition state. k_n represents the measured rate at a specific D_2O fraction, and k_0 represents the rate when the solvent is only H_2O. ϕ^R and ϕ^T represents the fractionation factor at the reactant and transition state respectively. A full derivation of this can be found in appendix 7.2. The Z term in equation 3.13 refers to medium effects, which describes solvation effects on the transition state, which is a kinetic isotope effect that arise based on the difference in solvent interaction in the transition state. These can occur even in situations where no isotopic exchange between the solute and solvent occur. These can occur from three sources: differences in solvation cavity formation, differences in electrostatic and H-bonding interactions between the solute and solvent, and differences in solvent-solvent interactions. This can be ignored as medium effects generally have normal isotope effect contributions and lead to “bowl-shaped” inventories, which is not observed here (see section 3.12.3).

The denominator term can also be dropped if the reactant fractionation factor is approximately 1. Functional groups involved in acid-base and nucleophilic catalysis (e.g., ROH of serine, RCO_2H of aspartic and glutamic acids, N-H bonds of lysine and histidine, and phenol OH of tyrosine) have fractionation factors that are near unity (Jarret and Saunders, 1985). Water (LO^- and L_3O^+) and the R-SL bonds of cysteine have a significantly low reactant fractionation factor of 0.43, 0.69, and 0.55, respectively, and can be the cause of inverse isotope effects or dome-shaped proton inventories (Reactions, Fernandez and Murkin, 2020).

In complex I, the reduction of quinone is tightly coupled and proposed to be carried out by active site Histidine and Tyrosine residues by molecular dynamics simulations (Sharma *et al.*, 2015; Gamiz-Hernandez *et al.*, 2017; Warnau *et al.*, 2018) and the Q-binding channel is expected to be dehydrated upon Q-binding (Kravchuk *et al.*, 2022). Therefore, it is extremely unlikely that water is the proton donor in this reaction and the reactant fractionation factor can be assumed to be unity.

If there are multiple transition state fractionation sites, the observed isotope effect is the sum of each fractionation site's contribution $k_n/\ k_0 = \pi(1 - n + n\phi^T)$. If each protonic site in the transition state has an equal contribution to the isotope effect, this results in equation 3.14.

Equation 3.15 represents a proton inventory where two serial steps contribute to rate determination. Fractional rate limitation fa and fb represents the fractional rate determination of each step and 1/ ϕ_a^T and 1/ ϕ_b^T represent the transition state fractionation factor of the two steps, respectively. The “dome” shape is resultant of the second transition state being isotopically insensitive, and the intrinsic isotope effect of the first transition state is “suppressed” by the second transition state, lowering the observed isotope effect. When the second of the transition states generate even a modest isotope effect, the line becomes indistinguishable from a linear plot.

Measurement of the proton inventory allows the measurement of the intrinsic isotope effect for each complex I variant by fitting it to the correct model. It is worth noting that the same shape proton inventory can be generated using different mechanisms, e.g., bowl-shaped inventories can be generated when one single proton bond is broken, but there is a large, medium effect (where the transition state is well solvated). Dome-shaped inventories are indistinguishable between serial limiting steps (equation 3.15) and the presence of a reactant fractionation factor of < 1 (equation 3.13). Therefore, additional experimental information and prior knowledge is necessary to decide between the possibilities.

$$\frac{k_n}{k_0} = \frac{\pi(1 - n + n\phi^T)}{\pi(1 - n + n\phi^R)} Z_k^n \tag{3.13}$$

$$\frac{k_n}{k_0} = (1 - n + n\phi^T)^x \tag{3.14}$$

$$\frac{1}{kn/k_0} = \frac{fa}{(1-n+n\phi_a^T)} + \frac{fb}{(1-n+n\phi_b^T)}$$

(3.15)

3.12.3 Complex I variants display "domed" proton inventories

The proton inventories of complex I variants were measured as described and are shown in Figure 3.49. Complex I variants were reconstituted into proteoliposomes with 13 mM Q_{10} and assayed in pL 7.5 with a 20:1 mass ratio of added AOX. For proton inventories of complex I using Q_1 as a substrate, 150 µM Q_1 is added in solution assays with no additional AOX. Thus, the measured proton inventory is on k_{cat}. The proton inventory technique requires precision of < 2.8% to distinguish between one and two proton models when the solvent isotope effect is 2 (Venkatasubban andSchowen, 1984). At least 21 technical replicates were performed to achieve this level of precision and, the D_2O fraction was determined in-situ by measuring the water pathlength using the water constant method preinstalled in Molecular Devices plate-readers. This measures the A_{1000}-A_{900} absorbance and discriminates between H_2O and D_2O because the latter has an approximately 100 times lower extinction coefficient at 1000 nm (Bayly, Kartha and Stevens, 1963). The proton inventory of K_{sp} cannot be measured with this level of precision and was not performed. All data points presented in Figure 3.49 are under this threshold.

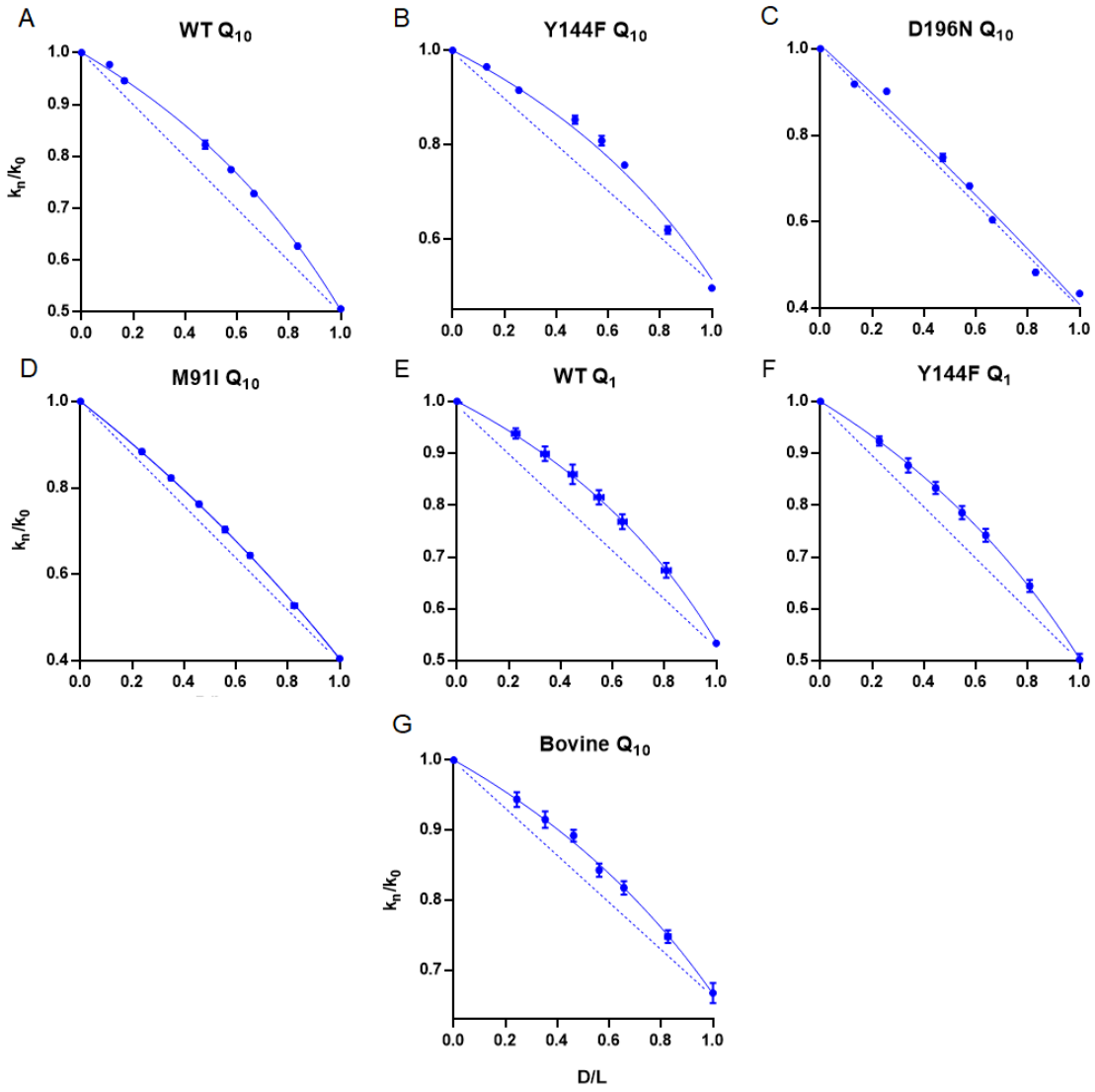

Figure 3.49 Proton inventory of complex I variants. (A) *Y. lipolytica* WT Q_{10}, (B) *Y. lipolytica* Y144F Q_{10}, (C) *Y. lipolytica* D196N Q_{10}, (D) *Y. lipolytica* M91I Q_{10}, (E) *Y. lipolytica* WT Q_1, (F) *Y. lipolytica* Y144F Q_1, (G) Bovine Q_{10}. Solid line indicates the best fit using equation 3.15 and the dashed line acts as a visual guide for a linear proton inventory. Errors are calculated as standard error of the mean (n = 21).

With the exception of D196N, which is indistinguishable from a linear model, all samples show upward curvature in the proton inventory, which rules out that multiple protons are involved in the transition state, as that can only result in a bowl-shaped proton inventory. N.B. The transition state of D196N is also unlikely to involve multiple protons, as the observed isotope effect is no greater than the other variants.

Experimental data is fit to equation 3.15 with ϕ_b^T constrained to 1, and 0.3 was set as the lower limit for ϕ_a^T. This is to reflect that product release has no intrinsic isotope effect and that the upper limit for an expected isotope effect for a single proton

transfer within a solvation catalytic bridge between O, N, and S is 3.3 (ϕ^T of 0.3 to 0.6) (Venkatasubban and Schowen, 1984). The WT and Y144F samples have hit the constrained fractionation factor, but nonetheless, they still fit well by equation 3.15.

As previously explained in section 3.8.1, the isotope effect on k_{cat} and K_{sp} are limited by commitment factors, which are resultant of slow quinone dynamics in the entry and exit of the Q-binding channel. The multiple rate-limiting steps model is consistent with this explanation, whereas the reactant fractionation model requires the assumption that the rate-limiting transition state is strictly rate limiting and has an inverse isotope effect contribution from using hydronium or hydroxide as a proton donor. The presence and use of such species in the Q-reduction mechanism has not been supported. Therefore, the former model has greater mechanistic clarity and is chosen for this analysis. Table 3.7 summarizes the fitted parameters of proton inventory data using equation 3.15.

	WT Q_{10}	Y144F Q_{10}	D196N Q_{10}	M91I Q_{10}	Bovine Q_{10}	WT Q_1	Y144F Q_1
Fa	42%	40%	87%	68%	36%	37%	45%
Fb	58%	60%	13%	32%	64%	63%	54%
φa	0.30	0.30	0.37	0.32	0.42	0.30	0.31
φb	1.00	1.00	1.00	1.00	1.00	1.00	1.00
KIE_{Int}	3.33	3.33	2.68	3.16	2.38	3.33	3.18
KIE_{obs}	1.98	2.02	2.31	2.47	1.50	1.87	1.99
R^2	0.9922	0.9903	0.9866	0.9977	0.9981	0.9997	0.9986

Table 3.7. Summary of parameters from the proton inventory experiment. A lower limit on ϕ_a^T was set to 0.3 and ϕ_{ab}^T was set to one. Fa and Fb represent the fractional rate determination by the solvent-sensitive catalytic step and the solvent-insensitive solvent release step, respectively.

All complex I variants except for bovine and D196N, have an intrinsic isotope effect of greater than 3. Except for D196N and M91I, complex I variants had a greater than 50% rate limitation by the non-isotopically sensitive transition state (Fb). M91I has weakened binding interactions and increases the rate of product release (and k_{cat}) compared to WT. So, a lowered fractional rate limitation on Fb suggests that Fb is likely to be product release. D196N is highly rate-limited by the isotopically sensitive step and has a lower intrinsic isotope effect of 2.68. This suggests that a different proton transfer step is rate-limiting.

3.12.4 Estimating microscopic rate constants using the proton inventory

To quantify the proton inventory output and estimate microscopic rate constants to characterize complex I catalysis, scheme 3.1 and equations 3.4 and 3.5 were expressed in their reciprocal form to yield equations 3.16 and 3.17, respectively. Because the proton inventory of K_{sp} was not measured, k_{-2} is set to 0 to simplify analysis. In doing so, the fractional rate limitation of each microscopic rate constant can be expressed as equation 3.17.

$$\frac{1}{K_{sp}} = \frac{1}{k_1} + \frac{k_{-1}}{k_1 k_2} + \frac{k_{-1}k_{-2}}{k_1 k_2 k_3} \tag{3.16}$$

$$\frac{1}{k_{cat}} = \frac{1}{k_2} + \frac{1}{k_3} + \frac{k_{-2}}{k_2 k_3} \tag{3.17}$$

$$Fa = \frac{k_{cat}}{k_2} \qquad Fb = \frac{k_{cat}}{k_3} \tag{3.18}$$

Microscopic rate constants within k_{cat} may be calculated using Fa and Fb obtained from proton inventory. Equations 3.17 and 3.18 are solved using Excel Solver, and the resulting microscopic rate constants are presented in table 3.8.

Fractional rate determination and microscopic rate constants were estimated in sections 3.8.1 and 3.9.2 using simulations underpinned by measured pL-independent $^{D}k_{cat}$ and $^{D}K_{sp}$ data. With the exception of D196N, which has a different intrinsic isotope effect, the estimated data is and agrees with proton inventory data obtained in this experiment. This shows that the observation and analysis from the two independent methods employed in this chapter, the modelling of ^{D}Ksp and ^{D}kcat and the proton inventory method, are internally consistent.

	WT Q_{10}	Y144F Q_{10}	D196N Q_{10}	M91I Q_{10}	Bovine Q_{10}	WT Q_1	Y144F Q_1
best_k_{cat} s^{-1}	417.54	38.57	38.57	529.79	193.06	417.54	188.76
k_2 s^{-1}	998.90	95.46	44.49	774.31	531.71	1128.19	417.14
k_3 s^{-1}	717.43	64.71	289.53	1677.60	303.13	662.87	347.17
k_{cat} ms	2.39	25.93	25.93	1.89	5.18	2.39	5.30
k_2 ms	1.00	10.48	22.48	1.29	1.88	0.89	2.40
k_3 ms	1.39	15.45	3.45	0.60	3.30	1.51	2.88
Fa	42%	40%	87%	68%	36%	37%	45%
Fb	58%	60%	13%	32%	64%	63%	54%

Table 3.8. Calculated microscopic rate constants for complex I variants catalysing Q_{10} and Q_1. Microscopic rate constants k_2 and k_3 are solved using equations 16 and 17 using excel solver. Fa, Fb, and k_{cat} are constrained to their experimentally determined values.

3.13 Discussion

3.13.1 Implications for the mechanism of mitochondrial complex I

Throughout this chapter, I have attempted to measure the rates of catalysis and product release in mitochondrial complex I. It is important to note that the lens in which these established observations are interpreted (Scheme 3.1) is an extremely simplified framework. In particular, proton pumping steps were not considered in this chapter because there was no change in observed KIE with increased Δp. Other evidence such as the observation that observed KIE is Q concentration, Q-chain length, and Q-binding site mutation dependent, suggests that the rate-limiting step is likely Q-catalysis. Instead, a system in which proton pumping is definitely rate-limiting is investigated in Chapter 4.

Nonetheless, because the rate of reaction within any enzyme is defined by slow steps with the greatest barrier heights, various fast and slow steps in complex I can be grouped into the baskets “catalysis” and “product release”, with each basket containing at least one step that is partially rate-limiting and has a barrier height of between 14-15 kcal mol^{-1} (according to transition state theory, assuming the transmission coefficient is one). The “catalysis” basket contains steps occurring after the oxidation of NADH, and the “product release” basket contains steps occurring after the formation of QH_2 and its release.

The experiments in this thesis are unable to characterize the exact identity of the isotopically sensitive step but impose constraints that i) only one proton is transferred in the transition state, ii) it is approximately 40% rate-limiting, iii) it likely involves a proton stable transition state. As proton tunnelling generally involves KIE > 4, iv) the

transition state barrier must be at least 14 kcal mol^{-1} for the reaction to be in the millisecond timescale. Complex I mutant variants are useful in delineating the different possible rate-limiting steps.

Y144F

Y144F is a first coordination sphere mutation and likely impacts the distribution between “hydrogen bonded” and “stacked” conformation in quinone binding. Ubiquinone binding has multiple conformations. The “stacked” conformation forms π-stacking interactions with His 95 (replaces the hydrogen bond) and is ~5 kcal mol^{-1} less thermodynamically favourable for quinone reduction than the “hydrogen bonded” conformation (Gamiz-Hernandez *et al.*, 2017). Y144F may promote “stacking” interactions by modifying hydrogen bonding geometry. Chung et al. suggest that the Q headgroup has conformational freedom to twist and flip when it is bound in a pre-reactive state and that the Y144F mutant may retain significant activity because the quinone headgroup can find alternative proton-donors (Chung, Wright, *et al.*, 2022). This is consistent with the observation that the Y144F mutant can retain significantly higher activities using Q_1. These results suggest that Q-reduction is rate-limiting, at least in Y144F, with the rate of reaction dependent on the conformational flexibility of quinone. A crucial observation is that the magnitude of the intrinsic isotope effect and shape of the proton inventory remains unchanged compared to WT despite a decrease in k_{cat}. This suggests that the same rate-limiting step occurs in the WT and Y144F variants. Y144F may force unfavourable binding geometry that increases the barrier height for the reduction of ubiquinone without changing the ΔZPE of the proton donor, lowering the rate but not increasing the intrinsic isotope effect. That both WT and Y144F are still 40% rate-limited by Q-reduction suggests that Q-reduction and QH_2 release are strongly coupled, where the rate of Q-reduction directly affects the rate of QH_2 release. This is consistent with previous molecular dynamics simulations showing that the movement of Q along the channel is redox-state dependent, and Q-reduction facilitates Q-headgroup movement away from the primary binding site and into the secondary binding site in the “kink” region, which is a global minimum (Warnau *et al.*, 2018).

D196N

D196 is a second coordination sphere residue and has been proposed to donate a proton to Histidine during Q-reduction and to propagate a signal by “flipping” away from the active site towards the E-channel. The formation of excess negative charge in the region may further lead to protonation of E-channel residues and proton uptake from the N-side bulk solvent in the ND1 subunit (Sharma *et al.*, 2015), which is linked to the coupling of Q-reduction to proton pumping (Kampjut and Sazanov, 2020a; Parey *et al.*, 2021; Kravchuk *et al.*, 2022). Di Luca et al. suggest that the rate for this proton uptake is limited by water chain formation, which has barriers of approximately 8-10 kcal mol^{-1}, placing the overall reaction rate for this step at 100 ns – 1μs (Di Luca, Gamiz-Hernandez and Kaila, 2017). So this step is unlikely to be rate-limiting in the WT enzyme. Sharma et al. suggest that in the equivalent mutation (D329N in *E. coli*), QH^- is formed and MD simulations observe that it rapidly moves ~15 Å away from the active site tyrosine and replaces the functional role of the anionic Asp flip in signal propagation (Sharma *et al.*, 2015). The observed k_{cat} is <10% of the WT enzyme, and the intrinsic isotope effect and proton inventory are different to other complex I variants, suggesting a different proton transfer step is rate-limiting. So, D196N may have an altered and rate-limiting signal propagation mechanism, which may consist of a high barrier for reduction of QH^- by E-channel residues in ND1. Molecular dynamics simulations also suggest that the free energy profile of quinone along the binding channel changes with the protonation state of the Asp-His ion pair (Chung, Wright, *et al.*, 2022). Thus, the D196N mutant may deepen the local minima for the substrate (further down from the primary binding site), leading to the relatively low k_{off} rates estimated in section 3.8.1. Alternatively, the D196N mutation increases the pKa of His 95, by removing the stabilization of its deprotonated form. This basic shift in pKa in His 95 may change the intrinsic isotope effect for its deprotonation in the Q-reduction mechanism.

M91I

M91 is proposed to be central to Q binding and dynamics and has been proposed to bind to the isoprenoid tail of quinone (Angerer *et al.*, 2012) and the quinone headgroup by turnover cryo-EM structures (Parey *et al.*, 2021) and MD simulations (Haapanen, Djurabekova and Sharma, 2019). The M91I mutation seems to

destabilize these interactions and empirically has a higher K_M and K_d (section 3.8.1). Interesting and consistent with the literature (Angerer *et al.*, 2012), this mutation has an approximately 20% higher k_{cat} than WT. Modelled catalytic rate constants and fractional rate limitation suggest that product release is less rate-limiting than WT, which suggests that the weakening of hydrophobic binding interactions may increase the rate of product release. The intrinsic KIE is the same as WT, suggesting that the isotopically sensitive step has the same identity and that the isotopically insensitive step is related to quinone binding or quinol release.

Q-reduction is partially rate limiting

Electron transfer from the FeS chain to quinone is proposed to take place in 90 µs by electrochemical experiments (Verkhovskaya *et al.*, 2008), with subsequent proton transfers to Q^{2-} taking place on pico- to nano-second timescales and semi-quinone formation is transient (Verkhovskaya *et al.*, 2008; Wright *et al.*, 2020). However, in previous simulations, incomplete abstraction of the proton from Histidine was also observed (Sharma *et al.*, 2015). Proton transfer reaction profiles suggest that proton abstraction from His 38 in *T. thermophilus* complex I is ~10 kcal mol^{-1} less exergonic than from Tyr 87 because of transient back-transfer of the proton from QH_2 to His 38 (Sharma *et al.*, 2015). UV difference spectroscopy measurements also observed the accumulation of the QH^- anion, suggesting that it may be mechanistically important and stabilized by the local environment (Nuber *et al.*, 2021). In this study, isotope effects were observed within mutants that interact directly with quinone (Y144F, M91I) which span a k_{cat} from < 10% to >120% of the WT rate yet result in the same intrinsic isotope effect. Additionally, mutation of D196, the residue that directly hydrogen bonds to His 95 resulted in the proton transfer being almost entirely rate limiting. Previous mutagenesis studies mutating His 95 have all resulted in non-functional enzymes, highlighting that this residue is central to any complex I mechanism (Grgic *et al.*, 2004). Thus, my results suggest that proton transfer from His 95 to QH^- is rate-limiting in WT and mutant complex I variants, accounting for an energy barrier of 14-15 kcal mol^{-1} yet to be found in simulation experiments (Kaila, 2021).

Quinol-release is partially rate limiting

The identity of the non-isotopically rate-limiting step is also difficult to interpret. Fedor et al. had previously proposed that product release is not rate-limiting, predicated on the observation that k_{cat} remains approximately unchanged between Q isoprenoid units of 6-10 and that k_{cat}/ K_M increases with isoprenoid length (Fedor *et al.*, 2017). However, k_{cat}/ K_M does not probe product release and instead probes binding only. The dynamics of ubiquinone and ubiquinol are expected to be different based on free energy profile simulations (Warnau *et al.*, 2018), so an isoprenoid chain dependence on substrate binding may be unrelated to the rate of product release. It can also be interpreted that when the isoprenoid chain is long enough to stretch past the "kink region" (> 6), the k_{cat} remains unchanged, suggesting that product release is only chain-length dependent up to a point.

In this study, proton inventory and fitting of $^{D}k_{cat}$ and $^{D}K_{sp}$ suggest that product release is at least partially rate-limiting, with a fractional rate limitation of approximately 60% in *Y. lipolytica* WT complex I. Previous simulations of the free energy profile of Q/ QH_2 along the quinone binding channel in *T. thermophilus* complex I have suggested that Q/ QH_2 may reside in a local minimum ~30 Å away from the N2 cluster (named site 2'), with a free energy barrier of ~6 kcal mol^{-1} towards complete dissociation (Warnau *et al.*, 2018). Warnau et al. have calculated that with diffusion coefficient D at 1/10 of free diffusion and a barrier of only 3 kcal mol^{-1} for the round trip of quinone is already 1 ms, thus rate-limiting in the timescale of complex I catalysis. Gu et al. also observed tight binding of QH_2 at a site (named site 3) near the exit point of the Q channel ~28 Å from the N2 cluster in porcine complex I, which stabilizes QH_2 via hydrogen bonding and π-stacking interactions (Gu *et al.*, 2022), also suggesting that product exit may be rate-limiting. Structural rearrangements/ conformational changes in the Q-binding site that facilitate product exit may also be rate-limiting and coupled to the ubiquinone redox reaction (Parey *et al.*, 2021; Sazanov, 2023). Previous studies have identified conformational changes in the β_1-β_2 loop as linked to Q/ QH_2 movement along the Q-channel. Micro-second MD simulations on the *Y. lipolytica* complex I structure show that Q/ QH_2 populate site 4, ~28 Å from the N2 cluster when the β_1-β_2 loop is in the extended conformation, but populate site 2, ~15 Å from the N2 cluster, when the β_1-β_2 loop is in the retreated

conformation (Lasham *et al.*, 2023). The movement of the β_1-β_2 loop seems to facilitate product release and may be partially rate-limiting.

3.13.2 Conclusions and future directions

Identifying the rate-limiting step is complicated by the lack of prior knowledge of the mechanism of complex I and inconsistent computational modelling. Complex I reliably displays a solvent isotope effect, suggesting that a proton transfer step is rate-limiting. This conclusion is made robust by measuring the KIE of the NADPH:AOX reaction, which is rate-limited by NADPH oxidation and results in no measured KIE. Analysis of Q-dependent NADH:AOX activity in complex I proteoliposomes enabled key observations: that the observed KIE depends on Q concentration, is Q-chain-length dependent, does not vary with Δp, and is affected by binding site mutations. This suggests that the rate-limiting proton transfer step is likely Q-catalysis and that the non-isotopically sensitive rate-limiting step is likely product release.

Proton inventory experiments suggest that complex I is partially rate-limited by a single proton transfer step with an intrinsic KIE of ~3 and approximately 40% and 60% rate-limited by an isotopically sensitive and non-isotopically sensitive step respectively.

Because the intrinsic isotope effect is common across Y144F, M91I, and WT, I propose that the isotopically sensitive step is proton abstraction from His 95, accounting for approximately 40% rate limitation and resulting in an observed KIE of ~2. A non-isotopically sensitive step makes up the other 60% of rate limitation and is accounted for by ubiquinol release, which may be facilitated by the movement of the β_1-β_2 loop.

Further insights into quinone chemistry may be gained by investigating a greater variety of mutations, not only in the primary binding site but also in the secondary binding site. Mutations of conserved Arginine and Aspartate residues in the “kink” region can be produced in the PSST subunit to investigate Q-dynamics along the Q-binding channel, as well as investigate the Q chain-length dependent effect on the pH dependence of K_M. Experimental values of proton and electron transfer rates and the exact KIE of proton transfers in Q reduction may be directly measured using real-time spectroscopy. However, existing studies have thus far only studied NADH

oxidation using stopped-flow spectroscopy (Belevich, Belevich and Verkhovskaya, 2014) due to significant experimental challenges in measuring quinone reduction directly. These challenges include various resting/ deactive states complex I exhibit (Belevich and Verkhovskaya, 2016; Chung, Grba, *et al.*, 2022), as well as the requirement for a membrane system for substrate channeling. However, the development of new stable protein environments such as nanodiscs (Kolata and Efremov, 2021; Chung, Wright, *et al.*, 2022) and a complex I assay system that does not contain a deactive state (Jarman *et al.*, 2021) may allow further experiments in this direction.

4 Investigating the effects of ND4/ Nqo13 subunit mutations on complex I catalysis

4.1 Introduction

The proton pumping domain of complex I is comprised of the antiporter-like subunits (ALS) (ND2/Nqo14, ND4/Nqo13, and ND5/Nqo12) that are homologous to each other and also to subunits of multi-resistance and pH adaptation (Mrp) Na^+/ H^+ antiporters (Efremov and Sazanov, 2011). These subunits are proposed to be responsible for pumping three protons, with the fourth pumped by a putative module located within ND1/ND3/ND4L/ND6 (Nqo8/Nqo7/Nqo11/Nqo10) subunits (Baradaran *et al.*, 2013; Zickermann *et al.*, 2015; Di Luca, Gamiz-Hernandez and Kaila, 2017).

However, despite recent high-resolution structure information of complex I, leading to computationally and structurally led proposals of the proton pumping mechanism, there is yet no clear consensus due to a lack of robust biochemical and biophysical data. Therefore, it is instructive to investigate the matter from the perspective of the proton, using site-directed mutagenesis guided by computational and structural information. This chapter investigates two aspects of catalysis by the antiporter-like subunits using the experimental strategies developed in the preceding chapter. The ND4/ Nqo13 subunit was chosen as a focus of study, as there is a wealth of mechanistic proposals focusing on this subunit (Kampjut and Sazanov, 2020b; Kaila, 2021; Kravchuk *et al.*, 2022; Sazanov, 2023).

4.1.1 A chain of conserved charged residues in the membrane arm of complex I

Each antiporter-like subunit has internal pseudosymmetry and shares a common bundle of 10 transmembrane helical (TMH) bundle segments (TMHs 4 -13). TMH7a/b and TMH12a/b form discontinuous helices broken by short loops in the centre. This feature is commonly used for ion translocation in carrier-type transporters (Screpanti and Hunte, 2007). The ALS and Nqo8/ND1 subunit also contain a chain of highly conserved buried charged residues that span the entire membrane domain, connecting the Q-site and Nqo12/ND5. This chain contains a motif common to each of the ALS, comprised of a lysine-glutamate pair, a central lysine, one or two histidine residues, and a terminal lysine (Nqo12, Nqo14) or glutamate (Nqo13).

A considerable number of site-directed mutagenesis studies performed on *E. coli* complex I have substantiated the importance of these conserved residues (Torres-Bacete *et al.*, 2007, 2009; Euro *et al.*, 2008; Sato *et al.*, 2013). However, most site-directed mutagenesis studies predate detailed structural information and report only on rates of NADH oxidation, so they lack detailed mechanistic interpretation. Although there are no published structures of *P. denitrificans* complex I, there is a high degree of sequence conservation in membrane domain subunits with existing complex I models. Thus, a similar structure and role of key residues in the mechanism is expected. Figure 4.1 shows an overview of the membrane domain of *P. denitrificans* complex I.

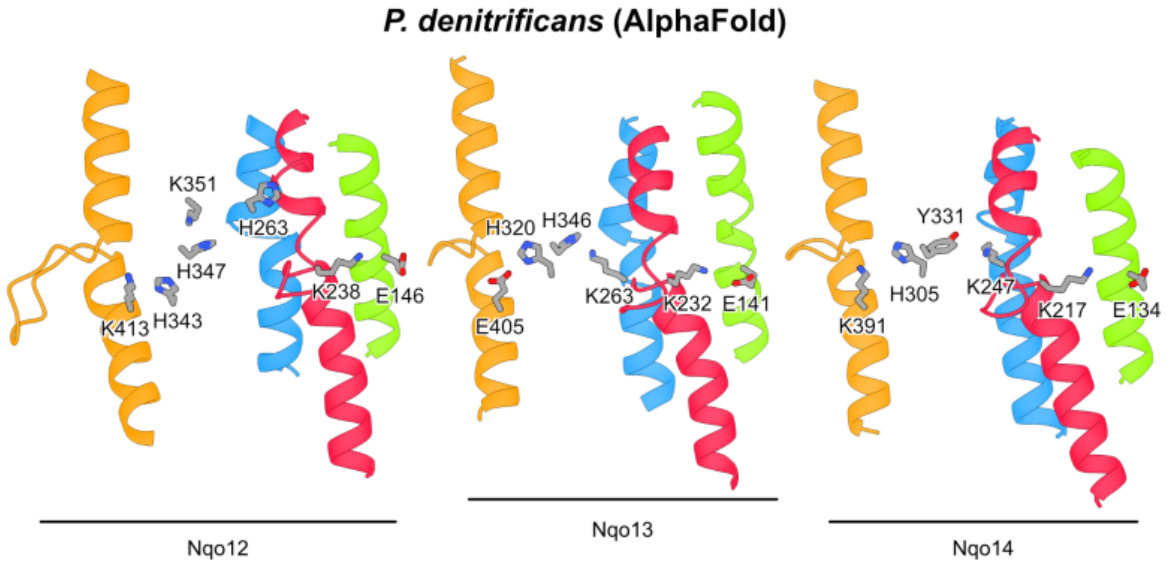

Figure 4.1. Conserved charged residues along the central axis of the membrane domain. The *P. denitrificans* complex I structure is predicted using AlphaFold and shown in cartoon (Jumper *et al.*, 2021). TMHs 5, 7, 8, and 12 are coloured in green, red, blue, and orange, respectively. Key conserved buried charge residues are highlighted in stick. TMH7 and TMH12 are interrupted by substantial loops in the centre of the helix. Figure is adapted from Dr Owen Jarman's thesis (Jarman O, 2022).

Contradicting mechanistic proposals for the role of these conserved residues in complex I have been proposed by computational studies by Kaila et al. (Di Luca, Gamiz-Hernandez and Kaila, 2017; Mühlbauer *et al.*, 2020), Kampjut et al., and Kravchuk et al (Kampjut and Sazanov, 2020b; Kravchuk *et al.*, 2022). Structural representation of the buried conserved charged residues are shown in Figure 4.2. Mechanisms for the function of homologous residues have also been proposed for

Mrp antiporters (Steiner and Sazanov, 2020; Lee *et al.*, 2022) but will not be covered in this thesis.

Kaila's mechanism operates using two elements (Figure 1.13A). The first is the central lysine, the protonation state of which control channel hydration. The second is the lysine-glutamate pair, which controls proton transfer and signal propagation. In the initial state, the glutamate residues located near the middle of TMH5 (E141 in Nqo13) form "closed" intra-subunit ion pairs with an adjacent lysine (K232 in Nqo13) on TMH7. Molecular dynamics simulation studies suggest that these ion pairs are not directly involved in proton transfer but instead transition between "open" and "closed" states. In the "closed" state, the central lysine (K263 in Nqo13) uptakes a proton, and the protonation of this residue is proposed to control N-side half-channel hydration (*vide infra*). Protonation of the central lysine was seen to promote the "closed" state, suggesting that it is a stable state (Di Luca, Gamiz-Hernandez and Kaila, 2017).

However, upon formation of the "open" state, where an inter-subunit ion pair forms between the TMH5 glutamate (E141 in Nqo13) and the terminal lysine/glutamate of TMH12 (K391 in Nqo14) in the preceding subunit, deprotonation of the central lysine occurs and subsequently closes the N-side hydration channel. Notably, despite the difference in positioning of the central lysine (K336) in Nqo12, the same behaviour is observed in MD simulations. Electrostatic repulsion from the TMH7 lysine forces the translocation of a proton from the central lysine to the terminal glutamate (E405 in Nqo13), with water molecules and one or two bridging histidine residues making up the Grotthuss proton transfer network (H346 and H320 in Nqo13). Poisson-Boltzmann simulation suggests that the "open" state decreases the pKa of the central lysine by -5 pH units relative to the closed state, thus facilitating deprotonation (Di Luca, Gamiz-Hernandez and Kaila, 2017). Because the proton is translocated through two disjointed hydration channels, gated through the hydration of the central axis, it creates a rachet mechanism for proton pumping, preventing the backflow of protons. In this mechanism, transduction of released energy from ubiquinone reduction is used to force the opening of "closed" intra-subunit lysine-glutamate pairs, pumping protons in the forward wave. The signal is propagated across the membrane in a wave-like fashion, where protonation of the terminal glutamate/ lysine opens the adjacent lysine/ glutamine pair. After the final proton is

released from Nqo12, a back wave resets each antiporter-like subunit through the relaxation of the “open” lysine/ glutamate pair back to the “closed” position and the opening of the N-side hydration channel (Di Luca, Gamiz-Hernandez and Kaila, 2017).

However, no cryo-EM structures have so far captured any movement of these residues to provide evidence of conformation change needed in this mechanism, including samples described as frozen during turnover (Kampjut and Sazanov, 2020b; Parey *et al.*, 2021; Kravchuk *et al.*, 2022). Furthermore, the distance between the TM7 lysine and TM5 glutamate is approximately ~5.5 Å, which is too far for direct hydrogen bonding, which takes place at distances of 2-3 Å, or salt-bridge formation at 4 Å. Instead, a water molecule bridges this interaction, damping the strength of the interaction. Further, no hydration channels have been observed on the P-side for Nqo13 or Nqo14 (Kampjut and Sazanov, 2020; Parey *et al.*, 2021; Kravchuk *et al.*, 2022); thus, it is unclear whether each putative proton pumping module does indeed pump one proton each.

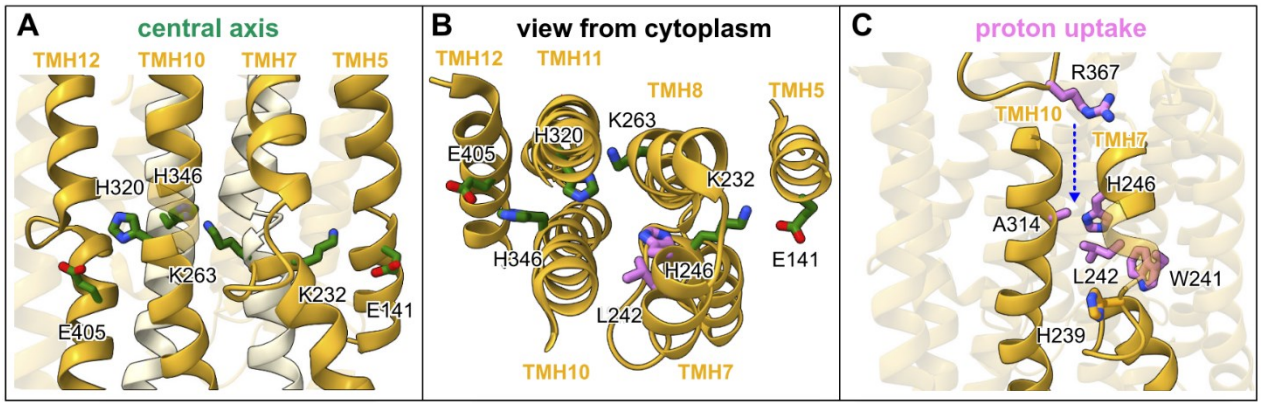

Figure 4.2. Overview of conserved charged residues in mutated in *P. denitrificans* complex I. (A) Conserved residues of the central axis in Nqo13/ND4. (B) Residues in the central axis of Nqo13/ND4 and the conserved residues H246 and L242 in the proposed proton-uptake/hydration channel, viewed from the cytoplasm. (C) Residues involved in the proposed proton-uptake/hydration channel. The conserved Leu-His-Trp triad L242, H349, and W241. Figure is adapted from Jarman et al. (Jarman and Hirst, 2022) and were created using the structure of bovine complex I (PDB: 7QSK).

Sazanov suggests a different proposal for the role of these central axis residues in the proton pumping mechanism, based on reportedly turnover cryo-EM structures (Kampjut and Sazanov, 2020b; Kravchuk *et al.*, 2022) (Figure 1.13B). In the initial

state, the antiporter-like subunits are protonated at the central lysine of TMH8 and the glutamate at TMH5. Sazanov proposes protons only enter complex I from the N side through the Nqo12/ Nqo13 channels, and protons are redistributed along the central axis, which is then disconnected from the Q-site by the Nqo10/ ND6 π-bulge in the de-active state. Unlike Kaila's proposed mechanism, the interaction of the TMH7/ TMH5 lysine-glutamate pair is not central to the proton pumping mechanism. In the initial state, due to the protonation of the TMH5 glutamate, the ion pair is proposed to interact weakly. The terminal lysine/ glutamate at TMH12 is proposed to be deprotonated and has a low pKa value due to the protonation of the TMH5 glutamate. In the active state, the reduction of ubiquinone, with two protons from the active site histidine/ tyrosine pair, initiates proton pumping. The histidine/ tyrosine pair is re-protonated by an aspartate residue from ND1 and the TMH5 glutamate of Nqo14. Thus, it leads to a rearrangement of the protonation pattern via proton hops to adjacent residues: from TMH8 central lysine to TMH7 lysine and from the TMH5 glutamate to TMH12 lysine/ glutamate. This shift in protonation pattern then causes the lysine-glutamate pair to interact strongly. The deprotonation of the TMH8 central lysine as a result of such proton hops leads to de-wetting of the central axis, as observed in molecular dynamics simulations (Di Luca, Gamiz-Hernandez and Kaila, 2017), preventing backflow of protons from the P to N side. The protonation of TMH12 and TMH7 creates a highly energised state, accompanying the active to deactive transition of the ND6 π-bulge to disconnect the membrane arm from the Q-binding site. From this state, the TMH8 central lysine residues of the three ALS subunits and two glutamate residues from the E-channel, a total of 5 protons, would be re-protonated by proton transfers from the hydration channels of Nqo12/ Nqo13. And the ND1 aspartate is re-protonated via the Q-site. From this fully protonated state, with TMH12, TMH8, and TMH7 protonated, a series of events reminiscent of the reverse of the proton transfer steps occur to release protons to the P side: TMH12 to TMH5 (or solvent), TMH7 to TMH8, and TMH8 to TMH12. In total, this step releases 4 protons to the P side from the TMH12 lysine of Nqo12.

In Kaila's mechanism, the charges on the TMH7/ TMH5 lysine glutamate pair do not change throughout the mechanism, and the opening/ closing of this pair promotes proton transfer across the central axis of each antiporter subunit. In stark contrast, in Sazanov's mechanism, these residues instead directly participate in proton transfer

steps. However, there are numerous unanswered questions and inconsistencies with this mechanism. First, the mechanism requires a state in which TM12, 8, and 7 are all protonated in all three antiporter-like subunits. Protonated residues decrease the pKa of adjacent residues. Thus, this highly energised state is likely disfavoured by charge repulsion. Computational simulations will be required to further investigate the plausibility of such a state. Second, in this state, the central lysine is re-protonated; thus, the N-side channel would be open according to molecular dynamic simulations, allowing the backflow of protons from the central axis. While pKas are dependent on the protonation state of the local environment, Sazanov does not explain how the pKa of these residues facilitate the proposed proton transfer steps by using Poisson-Boltzmann pKa calculations or PROPKA calculations (Di Luca, Gamiz-Hernandez and Kaila, 2017; Parey *et al.*, 2021; Hoeser *et al.*, 2022). Third, N-side hydration networks towards the central lysine have been proposed in cryo-EM structures in all three antiporter-like subunits (Parey *et al.*, 2021), questioning the hypothesis that only Nqo12 and Nqo13 have functional proton intakes. Finally, although the hypothesis that all four protons are ejected at the distal end of Nqo12, rather than in separate channels, is based upon the observation that only Nqo12 has a P-side hydration channel in Cryo-EM structures (Kampjut and Sazanov, 2020; Parey *et al.*, 2021; Kravchuk *et al.*, 2022), this mechanism is incompatible with the observation that *Y. lipolytica* complex I can pump protons at a reduced stoichiometry of two, following the loss of Nqo12/ ND5 and Nqo13/ ND4 subunits (Dröse *et al.*, 2011).

Because Nqo13 has a terminal glutamate residue on TMH12 instead of lysine in Nqo12 and Nqo14, Kampjut proposes that there is a charge asymmetry between the antiporter-like subunits, with Nqo13 being out of sync with the other two antiporters, and suggests a two-stroke mechanism (Kampjut and Sazanov, 2020b). However, PROPKA calculations suggest that the pKa at this position is 7.6 in Nqo13 compared to 7.4 in Nqo14 (Hoeser *et al.*, 2022), questioning whether the membrane arm exhibits charge asymmetry and the basis for the proposed two-stroke mechanism.

4.1.2 Gating mechanisms controlling half-channel hydration in Nqo13

N-side hydration water channels have been proposed for each of the three antiporter-like subunits. Water molecules are purported to enter the antiporter-like subunits by a crevice between TMH7b, TM8, and TM10, providing a hydrogen-bonded connectivity (Grotthuss network) between bulk solvent and the conserved charged central lysine on TM8 (Figure 4.2).

Molecular simulations on the *T. thermophilus* structure suggest that this half-channel is gated by the movement of TMH7b on an approximately 0.1 μs timescale, and the association/ dissociation of a backbone hydrogen bond between a histidine-leucine pair (Di Luca, Gamiz-Hernandez and Kaila, 2017). The equivalent leucine residue in Nqo14 is shifted compared to Nqo12 and Nqo13 in a high-resolution Cryo-EM structure of *Y. lipolytica* complex I (Grba and Hirst, 2020), and more water molecules were observed and modelled in the Nqo14 subunit channel. These observations support the proposal that the leucine residue acts as a gating residue and blocks or permits hydration by positionally pointing towards or away from the channel. A conserved Tryptophan at the start of TMH7b also changes position and may be important in positioning the gating residue. Thus, the Leu-His-Trp triad may control access of buried conserved charged residues to bulk water (Grba and Hirst, 2020), and protonation of the central lysine on TMH8 is suggested to stabilise the opening of this channel leading to a stable state (Di Luca, Gamiz-Hernandez and Kaila, 2017). In *P. denitrificans,* the equivalent residues in Nqo13 are L242, H239, and W241. However, mutation of W241 and H239 did not lead to substantial disruption of complex I activity, suggesting that they are not critical in channel opening/ closing dynamics (Jarman and Hirst, 2022).

As part of the half channel, a conserved histidine residue in Nqo13, H246, sits above the Leu-His-Trp triad and is proposed to be a key residue in maintaining the hydration network from the N-side towards the central axis, and mutation of this residue to phenylalanine led to a complete loss of activity in *P. denitrificans* complex I (Di Luca, Gamiz-Hernandez and Kaila, 2017; Kampjut and Sazanov, 2020b; Jarman and Hirst, 2022; Kravchuk *et al.*, 2022).

A different gating mechanism has also been proposed based on a second high-resolution Cryo-EM structure of *Y. lipolytica* complex I (Figure 4.3). Alternative

conformations of a phenylalanine residue in TMH11 in Nqo13 (F343 *in Y. lipolytica*) compared to Nqo14 were suggested to be part of a gating mechanism for channel hydration (Parey *et al.*, 2021), acting in a similar way to the Leu-His-Trp triad. However, mutation of this residue in the homologous enzyme Mrp complex (F341A in MrpD) only reduced the antiporter activity to 64% of wild type, suggesting that it may not be critical for controlling channel hydration (Ito, Morino and Krulwich, 2017; Steiner and Sazanov, 2020).

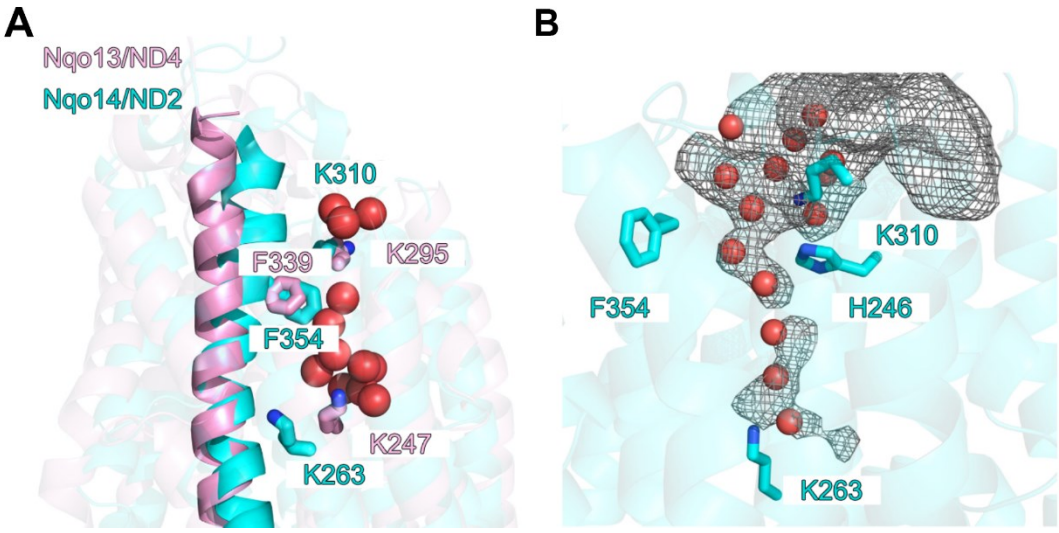

Figure 4.3. Conformational change of the phenylalanine gating residue on TMH11 is proposed to gate the hydration of the N-side half channel. (A) Overlaid structure of Nqo13 (cyan) and Nqo12 (pink) subunits with a conformational change in TMH11, positioning the F354 into the N-side hydration channel and blocking hydration. Waters are modelled from the Nqo14. (B) In-silico modelling of F354 away from the half channel. Mesh shows simulated waters forming a wire to the central lysine on TMH8 (K263). Figure adapted from (Parey *et al.*, 2021). All residues are labelled with equivalent *P. denitrificans* numbering.

4.1.3 Design of complex I variants

Point mutations in the Nqo13 subunit used in this study were made by Dr Owen Jarman using the method described (Jarman and Hirst, 2022). Dr Owen Jarman has produced an extensive mutagenesis library, and the choice of residues used in this work is informed by previous experimental work; residues with full or zero catalytic activity were omitted (Jarman and Hirst, 2022). All mutations were made in the Nqo13 subunit and are single-point mutations.

Mutations were designed to investigate the importance of charge and polarity within the chain of conserved charged central axis residues. To remove the charge and

protonatable group in the conserved lysine and glutamate residues while preserving polarity and size, they were mutated to glutamine (E141Q, K232Q, K263Q, and E405Q), and the functionality of protonation/ deprotonation is investigated during turnover. E405Q did not display any activity and was abandoned for this present study. Two histidine residues proposed to provide a protonation pathway are considered to have equivalent roles, and so each is substituted with a different side chain. One was mutated to glutamine (H346Q) to maintain polarity but affect protonation/ deprotonation. The other (H320L) was mutated to leucine, an aliphatic residue larger than previously investigated alanine mutants, in order to disrupt the establishment of an ordered network of water molecules.

Finally, a set of mutants was produced by Dr Owen Jarman to probe the functions of the N-side hydration channel. Mutations were made to the Leu-His-Trp triad as part of the leucine gating mechanism, which is proposed to control half-channel hydration and allow for proton intake from the N-phase as part of the proton pumping mechanism. The L242A substitution was created to reduce its steric bulk and increase the N-side hydration channel pore size. This may result in an enzyme that has a permanently open or semi-open state. The H239Q and W241F variants were created to perturb their coordination or position with surrounding residues but had no significant effect on complex I activity and were abandoned for this present study. To disrupt the hydration channel, two variants, A314L and H246F, were created. A314 contacts the proposed gating residue L242 and was mutated to A314L, a larger aliphatic residue, in an attempt to permanently close the hydration channel. H246F was created to remove the protonatable group on the histidine proposed to be a crucial link in proton transport (Di Luca, Gamiz-Hernandez and Kaila, 2017; Kampjut and Sazanov, 2020b). However, A314L had no effect on complex I activity, and H246F had no measurable activity, so both variants were abandoned for the purpose of this study. A summary of data collected by Dr Owen Jarman on the discussed mutations is shown in Table 1.

Mutation	Q-reductase activity / % (± S.E.M)		Pumping stoichiometry (± S.D)	RET capable?
	Membranes	Purified		
WT	100 ± 13.4	100 ± 1.2	4.50 ± 0.11	Yes
E141Q	7.3 ± 2.2	11.2 ± 0.8	N.D.	N.D.
K232Q	2.6 ± 1.4	9.3 ± 0.8	N.D.	N.D.
K263Q	17.5 ± 2.6	12.6 ± 2.7	N.D.	N.D.
E405Q	3.8 ± 1.1	7.2 ± 0.9	N.D.	N.D.
H320L	56.7 ± 8.3	44.4 ± 0.9	3.96 ± 0.69	Yes
H346Q	77.9 ± 8.8	49.7 ± 0.6	4.17 ± 0.87	Yes
H239Q	94.9 ± 9.7	58.4 ± 0.9	4.41 ± 0.20	Yes
L242A	10.4 ± 1.5	17.2 ± 0.3	N.D.	N.D.
H246F	2.1 ± 0.3	4.6 ± 0.9	N.D.	N.D.
W241F	95.4 ± 11.0	35.0 ± 0.9	4.11 ± 0.73	Yes
A314L	90.9 ± 13.4	39.6 ± 0.7	4.29 ± 0.33	Yes

Table 4.1. Summary data collected for *P. denitrificans* complex I variants in the Nqo13 subunit by Dr Owen Jarman. Q-reductase activities shown are normalised to NADH:APAD$^+$ activity and is given as a percentage relative to wild type. The complex I stoichiometry and RET capability was also noted. The mutants chosen to be carried forward in this study is coloured in red.

4.1.4 Previous mutagenesis studies in the chosen mutants

E141 & K232, Lys-Glu pair

Various groups have experimented with point mutations in the equivalent residues in Nqo13, primarily in *E. coli* complex I (NDH-1) in membranes. The equivalent glutamate in *E.coli*, E144, has been mutated to A, Q, and D. In all cases, the A and Q mutations abolished dNADH:DQ activity. However, the E144D mutation led to normal rates of complex I Q-reduction activity and proton pumping as measured by ACMA quenching (Torres-Bacete *et al.*, 2007; Euro *et al.*, 2008). These results suggest that this residue plays a key role in catalysis and more likely plays a role in proton transfer rather than controlling channel hydration via “open/close” state changes since the latter would be affected by hydrogen bonding distance and be perturbed by the E144D mutation. A large library of 20 double mutations was then produced, consisting of E144A and a residue within the same TMH to E, in an attempt to replace the glutamate residue and restore proton pumping activity. Only E144A/F140E and E144A/L147E (Figure 4.4) rescued the activities, with oxidoreductase activity of 39-60% and 30-45%, respectively, with proton pumping activity consistent with rates, suggesting normal proton pumping stoichiometry. Both rescue mutations are positionally adjacent to E144, thus suggesting that this residue

needs to be positionally conserved (Torres-Bacete *et al.*, 2009). In the equivalent subunit of the structurally related Mrp complex of Na^+/H^+ antiporter (MrpD), mutation of the equivalent glutamate residue to A or Q also abolished activities (Morino *et al.*, 2010; Steiner and Sazanov, 2020). The equivalent lysine in *E.coli,* K234, has been mutated to A and R; both mutants substantially reduced oxidoreductase activity and proton pumping activity to 10-20% of the WT enzyme. The mutations E141Q and K232Q both resulted in substantially decreased activity in *P. denitrificans* complex I, with oxidoreductase activity at approximately 5-10% and completely abolished, respectively but proton pumping was not measured (Jarman and Hirst, 2022). NanoDSF data indicates that E141Q and K232Q are structurally stable, suggesting rate loss can be mechanistically attributed to the loss of protonatable groups (Jarman and Hirst, 2022).

Mutations of the equivalent residues in Nqo14 had a much milder effect, retaining 53-72% activity of the WT enzyme with mutations to A, C, and D. It was suggested that the mutation is compensated by conserved glutamate in the adjacent Nqo11 subunit, and mutation of both residues reduced activities to 20% of WT (Amarneh and Vik, 2003; Sato *et al.*, 2013).

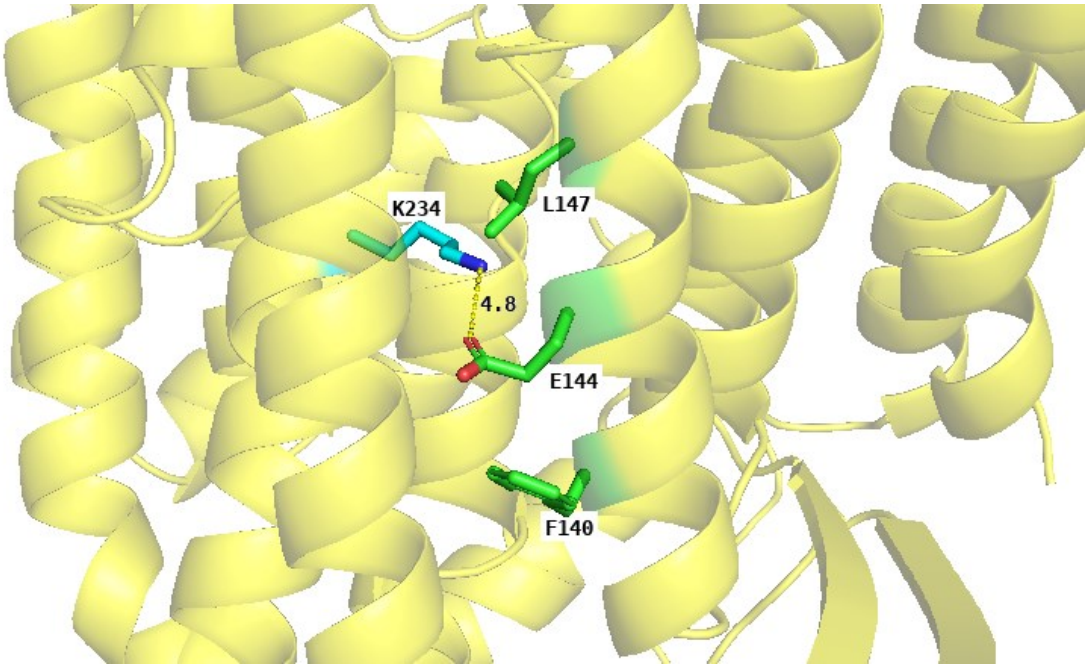

Figure 4.4 Positions of Lys-Glu pair mutations studied in *E. coli* NDH-1. Nqo14 of *E. coli* NDH-1 is shown in yellow cartoon (PDB: 7Z7S) (Kolata and Efremov, 2021). Residues studied are shown in stick. The distance between K234 and E144 is shown as a dashed line and labelled.

K263, central lysine

Mutation of the equivalent residue in *E. coli* complex I to alanine in membranes retained a good proportion of oxidoreductase activity at 35-55% of WT and had an approximately equivalent effect on ACMA quench depth, suggesting that proton pumping stoichiometry remained unchanged (Torres-Bacete *et al.*, 2007; Euro *et al.*, 2008). However, in K263Q *P. denitrificans* complex I, the rate was significantly perturbed, retaining only 5-10% of the WT enzyme, and proton pumping was not measured (Jarman and Hirst, 2022). NanoDSF data indicates the K263Q mutation only had mild perturbation on stability (Jarman and Hirst, 2022).

H320 and H346, central histidines

Mutations of the equivalent residues in *E. coli* complex I, H322 and H348 to alanine retained a good proportion of oxidoreductase and proton pumping activity, studies showing normal activities (Torres-Bacete *et al.*, 2007) and 60-74% of the WT rate, respectively (Mühlbauer *et al.*, 2020). Double mutations had a greater effect on oxidoreductase activity, retaining only 48% of the WT rate (Mühlbauer *et al.*, 2020. The mutations had a greater effect in *P. denitrificans* complex I, in which the H320L and H346Q retained 45-50% of the WT rate, with no change in proton pumping stoichiometry (Jarman and Hirst, 2022). NanoDSF data indicates these histidine mutations had no effect on structural stability (Jarman and Hirst, 2022).

E405, terminal glutamate

Mutation of the equivalent residue in *E.coli* membranes, E407, to alanine substantially decreased activity to 5% of the WT enzyme and retained a low proton pumping activity (Sato *et al.*, 2013). The E407K mutation retained significant activity at 80% of the WT enzyme and supposedly decreased the proton-pumping stoichiometry to 3 (Hoeser *et al.*, 2022). Similar to *E. coli* complex I, mutation of E405Q in *P. denitrificans* complex I completely abolished oxidoreductase activity (Jarman and Hirst, 2022). NanoDSF data indicates this mutation had no effect on structural stability (Jarman and Hirst, 2022).

L242, proton half channel gate

Mutation of this residue to alanine has been performed in *P. denitrificans* and significantly reduced oxidoreductase activity to 5-10% of the WT rate, and proton

pumping was not measured (Jarman and Hirst, 2022). NanoDSF data indicates this mutation had a very mild effect on structural stability (Jarman and Hirst, 2022).

4.2 Aims and strategy

- To investigate the effects of Nqo13 subunit mutations on complex I catalysis from the perspective of the proton by:
- Measuring the effect of mutations on pH dependence of dNADH:O_2 activity;
- Measuring the effect of mutations on the observed isotope effect to probe whether there is a change in the rate-limiting step;
- Measuring the proton inventory to determine the number of protons involved in the rate-limiting step;
- Determine proton pumping competence of mutants using ACMA quench measurements.

4.3 Optimisation of the *Paracoccus denitrificans* sub-bacterial particle system for KIE measurements

4.3.1 Effect of Nqo13 mutations on complex I expression

Sub bacterial particles (SBPs) were prepared for each of the 6 variants, including WT (described in section 2.7). To approximate the expression level of each complex I variant, the dNADH:APAD$^+$ oxidoreduction activities were measured. Nqo13 mutations are not expected to affect transhydrogenase activities performed by the flavin site in complex I, so dNADH:APAD$^+$ rates should be identical given identical amounts of complex I. Figure 4.5 shows the normalised dNADH:APAD$^+$ activities of each variant and that all variants expressed at least 70% of the WT equivalent amount of complex I, with variation likely due to individual batch variation in preparation. This is consistent with that previously observed by Dr Owen Jarman, w saw that variants expressed between 75% to 110% of the WT amount depending on preparation batch (Jarman, 2022).

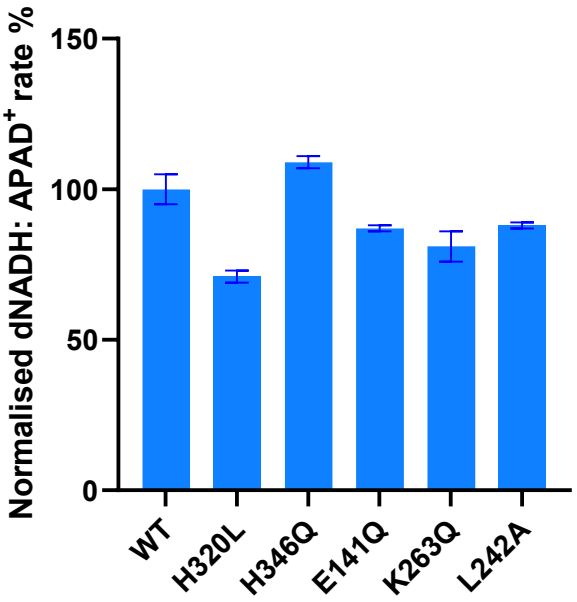

Figure 4.5 Normalised dNADH:APAD⁺ rates of sub-bacterial particles prepared from each *P. denitrificans* variant. 100 µM dNADH was added as the electron donor and 500 µM APAD⁺ as the electron acceptor. 2 µM piericidin A was added to inhibit quinone reduction by complex I. All variants expressed at least 70% of WT. Errors are calculated as standard error of the mean (n = 5).

4.3.2 Ensuring complex I catalysis is rate limiting in the sub-bacterial particle assay system

The alternative oxidase (AOX) from *Trypanosoma brucei* can be used to oxidise the ubiquinol pool to enable steady-state turnover of complex I (Fedor *et al.*, 2017; Wright *et al.*, 2022), so AOX was titrated into SBPs on an mg per mg basis to find the optimum ratio that maximises the rate of complex I turnover and reduces product inhibition. Figure 4.6A shows the rate of dNADH:O_2 oxidoreduction in *P. dentifricans* SBPs with increasing AOX concentration on a µg per µg basis. Antimycin A and potassium cyanide were added to inhibit complex III and IV, respectively, and Gramicidin A was added to uncouple the membranes. Corresponding OD_{600} measurements were taken at the end of the NADH measurement using the endpoint function in the Molecular devices spectra max 384 plate reader to monitor for protein aggregation.

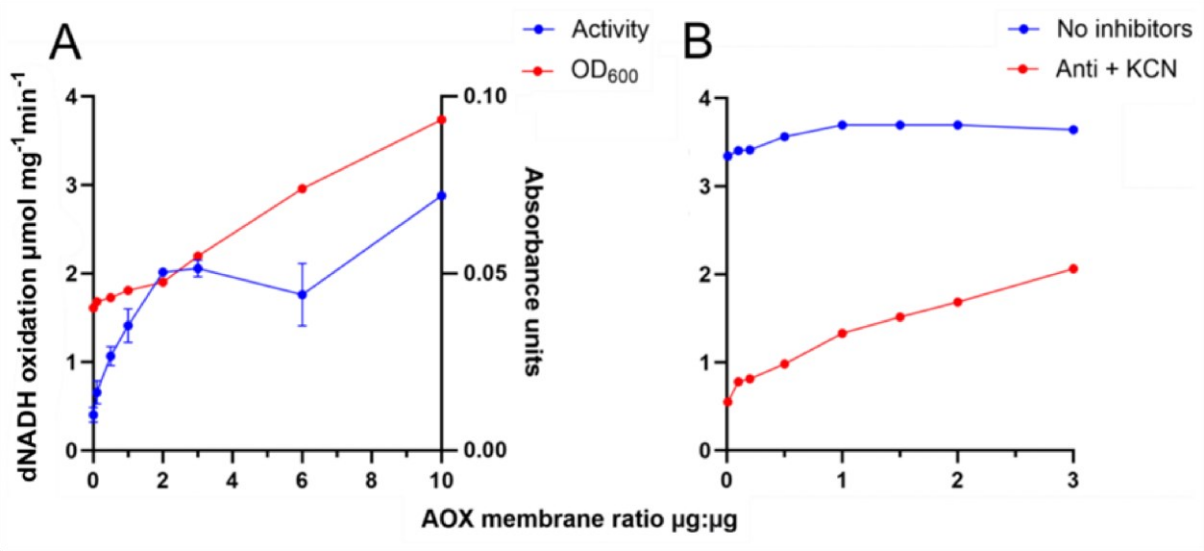

Figure 4.6 dNADH:O_2 oxidoreduction rates with increasing AOX concentration on a µg per µg basis. (A) At an AOX concentration of 2 µg:µg the dNADH oxidation rate plateaus but the corresponding OD_{600} measurement show there is significant aggregation at higher AOX concentrations. 1 µM Antimycin A and 400 µM potassium cyanide were added to inhibit complex III and IV, respectively. 1 µg mL^{-1} Gramicidin A was added to uncouple the membranes. (B) Complex I reaches a maximum rate at 1 µg:µg AOX without inhibition of complex III and IV. With the addition of 1 µM antimycin A and 400 µM cyanide, no AOX amount can allow complex I to reach the maximum rate without significant aggregation. Errors are calculated as standard error of the mean (n = 3).

Significant "cloudiness" of measurement wells was observed at AOX membrane ratios of greater than 2 µg:µg, showing that AOX is aggregating at high concentrations and binds poorly to *P. dentifricans* SBPs. This suggests that AOX may be aggregating before an adequate concentration could be added to ensure the maximum rate of complex I. Figure 4.6B shows the same experiment repeated with and without the addition of antimycin and cyanide. With complex III and IV inhibited by antimycin and cyanide, respectively, complex I rate does not reach the maximum at a concentration of AOX that does not aggregate in the assay. Without inhibition of complex III and IV, the maximum rate of complex I is reached at an AOX to membrane ratio of 1 µg:µg, with 0.5 µg:µg reaching 96% of the maximum rate.

Purified AOX is associated with the detergent n-dodecyl β-D-maltoside (DDM), which disrupts membrane integrity (Fedor and Hirst, 2018). ATP synthesis was measured at increasing AOX concentrations to find the concentration of AOX that could be added without disrupting membrane integrity. ATP synthesis requires the accumulation and

maintenance of a **Δ**p; thus, disruption of membrane coupling also abolishes ATP synthesis. ATP production is monitored using the real-time/ continuous method, and the luminescence readout generated by luciferase/ luciferin is captured by a BMG LABTECH Clariostar plus plate reader. The luminescence response is calibrated to ATP concentration by an addition of a known concentration of ATP to each sample well.

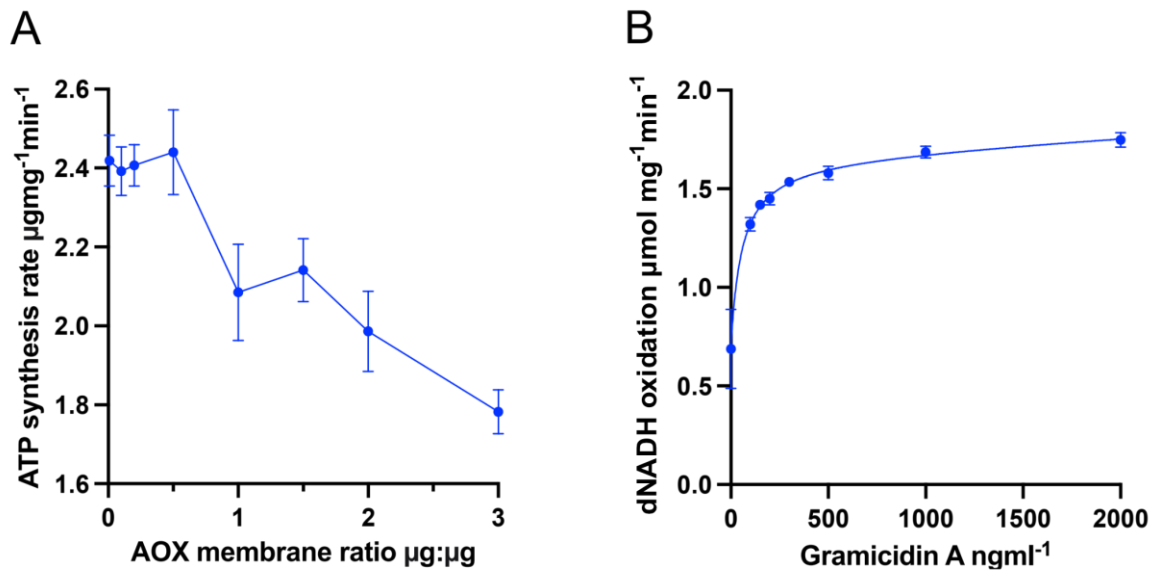

Figure 4.7. *P. dentifricans* SBPs are well coupled and display a respiratory control ratio. (A) ATP synthesis was measured at increasing concentrations of AOX, with disruption to membrane integrity at a mass ratio of greater than 0.5 µg:µg. (B) dNADH:O_2 oxidoreduction rates of SBPs titrated with gramicidin A. 1 µM Antimycin A and 400 µM potassium cyanide were added to inhibit complex III and IV, respectively and 0.5 µg:µg AOX was supplemented to oxidise the ubiquinol pool. No increase in dNADH oxidation rate was observed at a gramicidin A concentration of greater than 1 µg mL^{-1}.

Figure 4.7A shows that at AOX to membrane ratios of greater than 0.5 µg:µg, AOX lowers the rate of ATP synthesis, suggesting that there is a partial compromise of membrane integrity. Considering that a 0.5 µg:µg AOX mass ratio already achieves 96% of the maximum rate, this ratio represents a good compromise between coupling and complex I activity. To measure the respiratory control ratio (RCR), coupled membranes are uncoupled by the protonophore gramicidin A. Figure 4.7B shows the dNADH:O_2 oxidoreduction rates of WT SBPs with increasing gramicidin A. Antimycin and cyanide is added to inhibit complex III and IV. Instead, 0.5 µg:µg mass ratio of AOX is added to oxidise the Q-pool. Maximum uncoupling was achieved with the addition of 1 µg mL^{-1} gramicidin A, suggesting membrane integrity is retained.

In summary, to ensure complex I is rate limiting in *P. denitrificans* SBPs, no antimycin A or cyanide is added, and a 0.5 μg:μg mass ratio of AOX is added to reoxidise ubiquinol along with native complex III and IV. To uncouple the membranes, 1 μg mL^{-1} gramicidin A is added.

4.4 Measuring the pH dependence and kinetic isotope effects of *P. denitrificans* complex I variants in sub bacterial particles

4.4.1 The pH-dependent stability of *P. denitrificans* sub bacterial particles

To assess the pH-dependent stability of the *P. denitrificans* OXPHOS system in sub bacterial particles, I carried out the method described in section 3.4.1 with modifications detailed below. Briefly, SBPs were incubated at the tested pH for 1 hour on ice, and then re-diluted into pH 7.5 before the NADH:O_2 activity was measured. If the SBPs are unstable at a particular pH, the incubation step will denature the complexes, yielding a lower rate compared to pH 7.5. The tested range is between pH 4.5 and 10. Because complex III and IV are necessary for complex I to reach maximum rate, no AOX was added after the incubation step. To differentiate between complex I and NDH2 oxidation, 150 μM dNADH is used as the electron donor.

Figure 4.8 shows that both extremities of pH led to irreversible inactivation of sub bacterial particles, and there is significant irrecoverable activity loss at below pH 5 and above pH 8. However, pH 8.5 still retains 85% activity after 1-hour incubation, and the maximum duration of solution assays is typically 10 minutes. So, to maintain a broad pH coverage, this pH is measured in subsequent assays. Compared to bovine and *Y. lipolytica, P. denitrificans* SBPs prefer acidic conditions with greater pH tolerance below pH 6 but lesser tolerance above pH 8 as compared to bovine membranes. This may reflect differences in complex I pH stability - for example, *P. denitrificans* complex I lack stabilisation by supernumerary subunits - but may also reflect the lack of stability of complex III and IV at high pH.

So, for subsequent kinetic assays, the pH-dependence of complex I activity in SBPs are measured between pH 5 and 8.5, as SBPs are stable over this pH range, at least for the duration of kinetic assays.

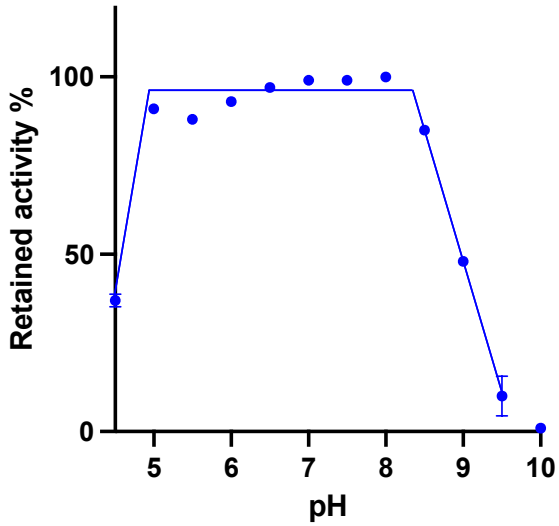

Figure 4.8 Reversibility of pH-inactivation of *P. dentifricans* SBP. dNADH:O_2 oxidoreduction rates were measured after a 1-hour incubation at each corresponding pH on ice and measured after dilution in pH 7.5 buffer. The ratio of activity to the maximum at pH 7 is plotted as the retained activity. Errors are calculated as standard error of the mean (n = 4).

4.4.2 Nqo13 site mutations change the identity of the rate-limiting step

To measure the kinetic isotope effect and pH dependence of complex I in coupled and uncoupled conditions, dNADH:O_2 oxidoreduction activities of *P. denitrificans* SBP variants were measured in H_2O and D_2O buffer in pL 5 to 8.5, with and without the presence of gramicidin. SBPs were supplemented with AOX without the addition of cyanide and/ or antimycin A to allow complex I activity to be rate-limiting. 200 µM dNADH was used to initiate the reaction. The resultant bell-shaped curves (Figure 4.9) are fitted using equation 3.1 to derive pK_a parameters describing the shape of the bell curve and a V_{opt} parameter describing the pL-independent rate of reaction (Tables 4.2 and 4.3).

All complex I variants exhibited V_{opt} rates of 4% and 67% of the WT enzyme (by comparing uncoupled rates measured in H_2O). E141Q and K263Q represent the most deleterious mutations at 4 and 5% of the WT rate respectively. The two histidine mutations, H320L and H346Q, have significant rates of 46% and 67% respectively, consistent with published results (Jarman and Hirst, 2022). L242A retains 20% of WT activity, which is greater than that observed by Jarman et al. (Jarman and Hirst, 2022). All variants displayed bell-shaped pH dependence in H_2O, and with the exception of

L242A, all display pK_a 1 and pK_a 2 values of approximately 5.7 and 8.7. These values are similar to those measured for bovine and *Y. lipolytica* complex I WT and mutant proteoliposomes, suggesting that pH dependence is dependent on the same titrated residues for complex I from different species.

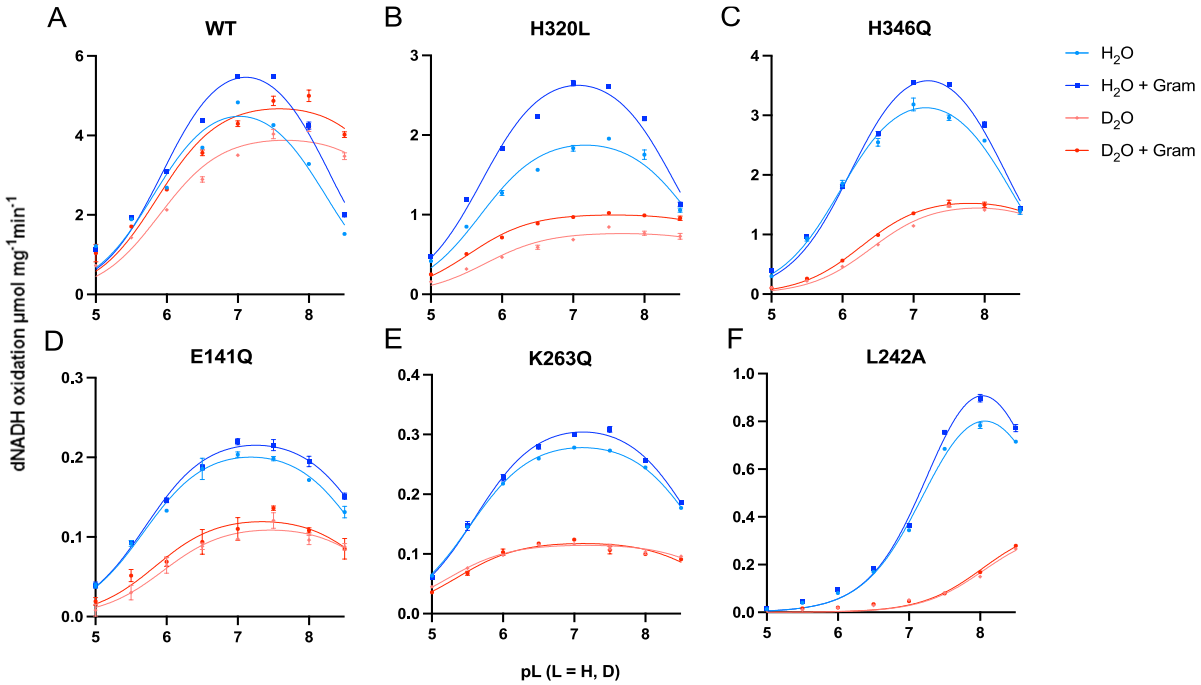

Figure 4.9 pL dependence of dNADH:O_2 oxidoreduction rates in P. denitrificans SBP variants with and without Gramicidin A. pL dependence was measured with SBPs supplemented with 0.5 µg:µg mass ratio of AOX, and membranes were uncoupled with 1 µg mL^{-1} of gramicidin A. (A) WT enzyme. (B) H320L variant. (C) H346Q variant. (D) E141Q variant. (E) K263Q variant. (F) L242A variant.

The L242A variant has a pK_a 1 shifted more basic by approximately 1.5 pH units with an unchanged pKa 2 (making the peak much sharper) - so the pH optimum has shifted from pH 7 (in all other variants) to pH 8. Previously, Jarman et al. measured the dNADH:O_2 rates of each complex I variant in membranes only at pH 7 and, therefore, underestimated the rate of activity of this mutant specifically (Jarman and Hirst, 2022). Consistent with that observed in complex I from bovine and *Y. lipolytica* (Chapter 3), there is a basic shift in pKa values for all variants when SBPs are assayed in D_2O, highlighting the importance of controlling for pH in kinetic isotope effect measurements. In D_2O, due to the pD shift in pKas, pKa 2 is not as reliably fitted as in H_2O; therefore, an artificial constraint was added to fit pKa 2 by fixing the rate of NADH:O_2 oxidation to 0 at pH 10, which is a reasonable assumption considering that there is already a downward

trend at basic pHs. Nonetheless, all variants except for L242A display a bell-shaped pD-dependence, as the rates at pD 8 and 8.5 are lower than the maxima at pD 7.5.

Mutants	V_{opt} H_2O / µmol mg^{-1} min^{-1}	V_{opt} D_2O/ µmol mg^{-1} min^{-1}	V_{opt} H_2O uncoupled / µmol mg^{-1} min^{-1}	$V_{opt}D_2O$ uncoupled / µmol mg^{-1} min^{-1}
WT	5.04 ± 0.40	4.01 ± 0.21	6.21 ± 0.40	4.85 ± 0.27
H320L	2.00 ± 0.09	0.78 ± 0.04	2.86 ± 0.12	1.02 ± 0.02
H346Q	3.53 ± 0.11	1.54 ± 0.06	4.18 ± 0.18	1.61 ± 0.02
E141Q	0.21 ± 0.00	0.12 ± 0.01	0.23 ± 0.00	0.13 ± 0.01
K263Q	0.29 ± 0.00	0.12 ± 0.00	0.32 ± 0.00	0.12 ± 0.00
L242A	1.04 ± 0.07	0.35 ± 0.05	1.26 ± 0.10	0.37 ± 0.05

Table 4.2 Summary of pH and pD-independent NADH:O_2 oxidoreduction rates for complex I variants. Experimental data was fitted using equation 3.1 using GraphPad Prism 9.1. Experimental errors are reported as standard errors of the mean (n = 3).

Mutants	pKa 1 H_2O	pKa 2 H_2O	pKa 1 D_2O	pKa 2 D_2O
WT	5.82 ± 0.13	8.23 ± 0.14	5.90 ± 0.10	9.43 ± 0.40
H320L	5.70 ± 0.09	8.64 ± 0.12	5.77 ± 0.11	9.60 ± 0.50
H346Q	5.98 ± 0.05	8.36 ± 0.05	6.40 ± 0.06	9.40 ± 0.24
E141Q	5.68 ± 0.04	8.69 ± 0.06	5.95 ± 0.09	8.97 ± 0.17
K263Q	5.53 ± 0.01	8.70 ± 0.02	5.22 ± 0.04	9.11 ± 0.09
L242A	7.24 ± 0.07	8.89 ± 0.12	8.05 ± 0.14	ND

Table 4.3 Summary of pKa values of NADH:O_2 oxidoreduction rates for complex I variants. Experimental data was fitted using equation 3.1 using GraphPad Prism 9.1. Experimental errors are reported as standard errors of the mean (n = 3). The uncoupled condition did not change pKas and are not shown.

The observed kinetic isotope effects of SBP variants are summarised in Figure 4.10. WT SBPs exhibit a low KIE of approximately 1.2, similar to that observed in bovine sub-mitochondrial particles, which have a lower KIE compared to proteoliposome samples containing only purified complex I and AOX (section 3.6.2). This is likely a characteristic of the *P. denitrificans* enzyme, as a saturating amount of DQ added did not increase the KIE (data not shown). However, all Nqo13 mutations exhibit a statistically significant increase in KIE ($p = 0.05$) compared to WT, suggesting that the rate-limiting proton transfer step has changed identity and is affected directly by each mutation, and is likely

a proton pumping step. N.B. The presented value of KIE for the L242A variant represents the upper limit, as the pD measurement cut off at pH 8.5 is unable to capture the descending leg without rate loss confounded by denaturation of the enzyme; thus, the V_{opt} value in D_2O may be underestimated from its true value.

Greater reduction of the Q-pool also consistently decreases the respiratory control ratio (RCR), as previously observed in section 3.6.2. RCR is calculated as the ratio of membrane uncoupled and coupled rates. In this case, the RCR has dropped from ~ 2.3 - 2.5, when complex III and IV are inhibited by Antimycin and Cyanide to ~1.1 – 1.2 without inhibitors added, further demonstrating that RCRs are a poor indicator of membrane integrity, but instead represent the FET/ RET equilibria in complex I, influenced by the Q-pool oxidation state.

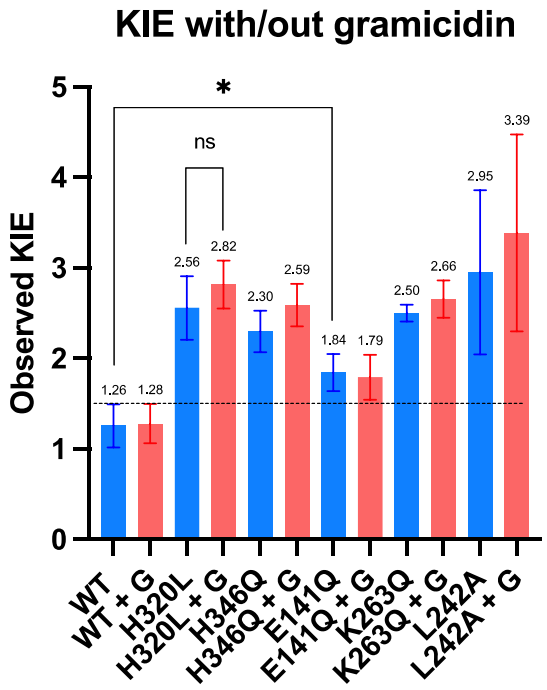

Figure 4.10. Observed KIE of each *P. denitrificans* variant complex I measured in SBPs with and without the addition of gramicidin A. All mutant variants have a statistically significant (p = 0.05) increase in observed KIE compared to the WT enzyme. There is no statistical significance in observed KIE with the addition of gramicidin A for any variant. Error bars represent the 95% confidence interval (n = 3), using a T-score of 2.015 for a one-tailed T-test. The dashed line acts as a visual guide for the upper limit of the WT observed KIE, and all mutant variants have a statistically significant increase in observed KIE. The asterisk denotes that the differences in KIE between the E141Q variant and WT is statistically significant (p = 0.05).

Nqo13 mutants do not statistically significantly increase the observed KIE. In sections 3.6.2 and 3.6.3, the same was observed for bovine SMPs and WT *Y. lipolytica* proteoliposomes. As previously discussed in section 3.6, the RCR effect is resultant of thermodynamic changes in the FET/ RET equilibrium. And an unchanging observed KIE with increased Δp can only be interpreted as the identity of the rate-limiting step remaining the same.

4.5 Measuring the proton inventory of complex I sub bacterial particles

4.5.1 Proton inventories reveal that one proton is rate-limiting in the transition state

To determine the number of protons involved in the transition state, the proton inventory experiment was performed for each mutant. This may also allow differentiation between the rate-limiting steps of mutant variants to reveal specific mechanistic information. An in-depth explanation of the theory of solvent isotope effects and the proton inventory method can be found in section 3.11. Briefly, the proton inventory method requires the measurement of the solvent Isotope effect in a range of mixtures of D_2O and H_2O (Venkatasubban and Schowen, 1984), and the data are fit to a version of the Kresge-Gross-Butler equation (Equation 3.13-3.15). Straight-line proton inventories are consistent with a single proton transfer in the transition state, with no reactant isotope effect contributions. Bowl-shaped proton inventories may be contributed by multiple transition state protons, whereas dome-shaped proton inventories are either caused by serial rate-limiting steps (one of which has no isotope effect) or by reactant contribution to the kinetic isotope effect. Examples of multiple proton transfer catalysis and reactant contribution to KIE are serine proteases and proline elastase respectively. The catalytic transition state of serine proteases involves the concerted transfer of two protons in the solvation catalytic bridge (Blow, 1976; Kraut, 1977). Proline elastase contains active site cysteines which contribute to reactant fractionation, which gives rise to inverse isotope effects (Belasco, Albery and Knowles, 1986).

Grotthuss-capable amino acid side chains (with the exception of arginine and cysteine, with fractionation factors of 1.28 and 0.55 respectively) and water have fractionation factors that are near unity (Jarret and Saunders, 1985). In contrast,

water ions (LO^- and L_3O^+) have low fractionation factors of 0.43 and 0.69 respectively, which have an inverse isotope effect contribution lowering the observed isotope effect from the intrinsic isotope effect.

The proton inventories of complex I variants in *P. denitrificans* SBPs are shown in Figure 4.11. SBPs were supplemented with 0.5 µg:ug AOX and are assayed in pL 7 with the exception of L242A which is assayed at pL 8. The WT variant was not measured because the isotope effect is too low. The proton inventory method requires a precision of <2.8% to distinguish between one and two proton models when the solvent isotope effect is 2 (Venkatasubban and Richard L Schowen, 1984). With the exception of E141Q, where the observed isotope effect is 1.6, all other variants have an observed isotope effect of 2 or greater, and the precision of each data point is less than 2% for all variants. At least 21 technical replicates were measured to increase precision, and the D_2O fraction was measured in situ using the Molecular Devices 384 spectramax plate reader by measuring the pathlength using the water constant function (see section 3.11.3).

The observed isotope effects measured in this experiment are consistent with previously observed values. With the exception of H346Q, the proton inventories of all variants exhibit linear one-proton profiles. Bowl-shaped proton inventory profiles were simulated using equation 3.14 to illustrate this and are included in Figure 4.10. The fractionation factor value was set to make the observed isotope effect between the different profiles. E.g., the two-proton profile and three-proton profiles generated with values that are the square root and cube root respectively of the one-proton value. This is consistent with a single proton transfer in the transition state, with no reactant contribution to the isotope effect (reactant fractionation factor is one). Thus, proton transfer steps are discrete and are not concerted.

The data support the hypothesis that proton pumping steps are primarily rate limiting in *P. denitrificans* Nqo13 mutants, as the proton inventory profiles are different to observed in *Y. lipolytica* mutants or bovine complex I in proteoliposomes, which are dome-shaped and rate limited by multiple rate-limiting steps (section 3.11.3).

The transition state fractionation factor ϕ^T as fitted using equation 3.14, is different for each complex I variant and likely reflects that the identity of the rate-limiting proton transfer step is different for each, as is expected. The proton inventory of H346Q

displays a dome-shaped profile, which can be generated by two different models: reactant contributions to the isotope effect, or multiple rate-limiting steps (proposed for *Y. lipolytica* and bovine complex I). In the case of H346Q, a Zundel-ion was suggested to act as an alternate Grotthuss conductor by computational simulations (Di Luca *et al.*, 2018; Mühlbauer *et al.*, 2020) when central axis histidines are mutated. Thus, the hydronium ion L_3O^+ may be the proton donor in the rate-limiting step, and the dome-shaped profile reflects an inverse isotope effect contribution from the reactant/ proton donor.

Dome-shaped inventories can be caused by multiple microscopic steps with comparable rate-limitation; however, proton pumping is expected to be driven entirely by electrostatic interactions and Grotthuss proton transfers as no conformational changes have been observed for antiporter-like subunits under any condition. Therefore, the most sensible and well-supported interpretation is that the dome-shape is resultant of reactant contributions to the isotope effect, consistent with computational observations (Di Luca *et al.*, 2018; Mühlbauer *et al.*, 2020).

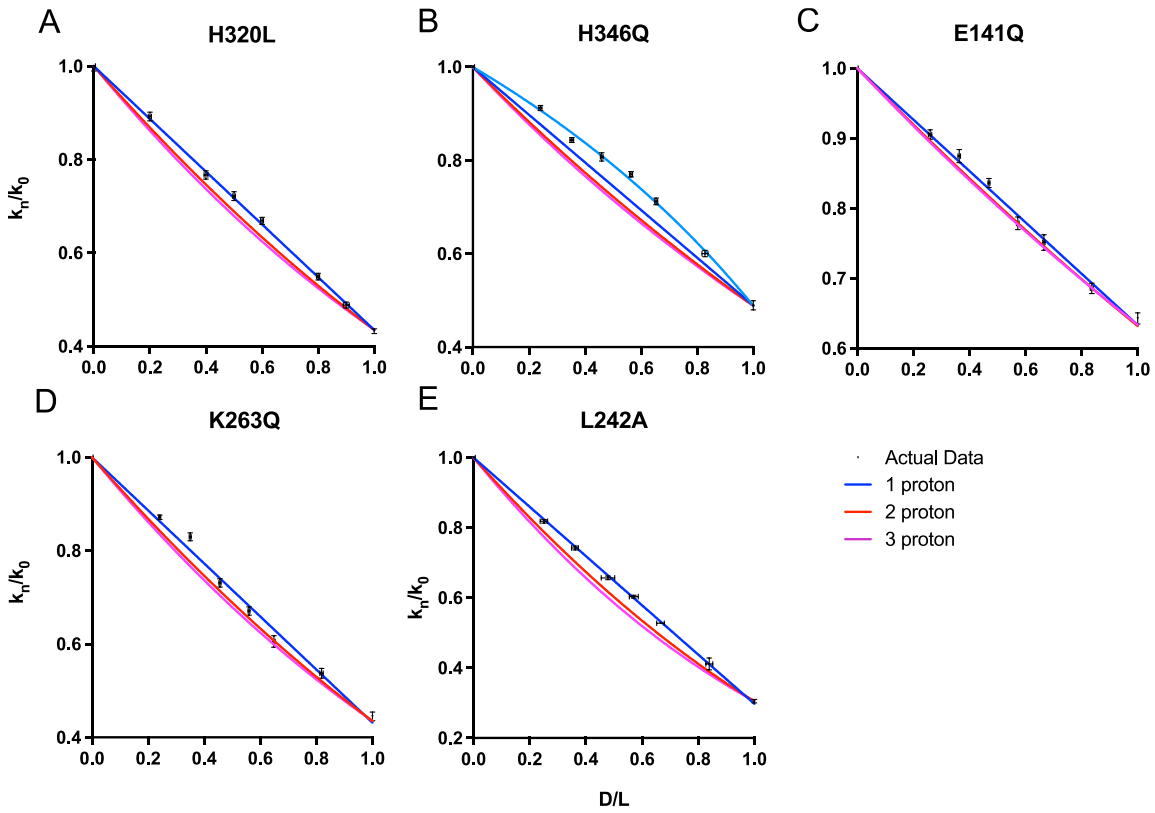

	H320L	H346Q	E141Q	K263Q	L242A
φ^T	0.44	0.34	0.63	0.43	0.30
φ^R		0.70			
KIE_{Int}	2.30	2.94	1.58	2.32	3.35
KIE_{obs}	2.31	2.04	1.56	2.25	3.28
R^2 (one proton)	0.9994	0.9754	0.9955	0.9917	0.9995
R^2 (two proton)	0.9928	0.7152	0.9942	0.9805	0.9918
R^2 (three proton)	0.9887	0.6658	0.9929	0.9694	0.9855
R^2 (reactant proton)		0.9975			

Figure 4.11 Proton inventory of *P. denitrificans* complex I variants in SBPs. The blue line indicates the simulated one proton inventory, the red line two, and the purple line three. Profiles are simulated using the observed isotope effect of the variant and equation 3.14. The light blue line is fitted using equation 3.13. All variants have an error of ≤ 2%. Errors are calculated as standard error of the mean (n = 21). (A) H320L, (B) H346Q, (C) E141Q, (D) K263Q, (E) L242A. The reactant fractionation factor is one for linear profiles and 0.34 for the dome-shaped profile observed in H346Q. ϕ^T and ϕ^R represent the fractionation factor for the transition state and the reactant state, respectively. KIE_{Int} and KIE_{obs} represent the intrinsic and observed KIE, respectively. For each model, an R^2 value is given to assess the quality of fit.

In summary, proton transfer is rate-limiting for all complex I Nqo13 mutants and one-proton is transferred in the rate-limiting transition state. For H346Q, reactant contribution to the observed KIE suggests that a Zundel/ Hydronium ion is the proton donor in the rate-limiting step.

4.6 Determining whether Nqo13 mutants have proton-pumping activity

4.6.1 Determining proton pumping using ACMA quench fluorescence

Stoichiometry measurements have previously been performed on the WT, H320L, and H346Q variants in *P. denitrificans* SBPs and were shown to be 4 (Jarman and Hirst, 2022). However, the same was not performed on the mutant variants E141Q, K263Q, and L242A, as the activity was deemed to be too low to perform stoichiometry experiments.

E141 and K263 are hypothesised to be crucial for proton translocation across the central axis to enable the proton-pumping “signal” to be propagated across the membrane domain. L242 is proposed to act as a gating mechanism to control N-side half-channel hydration. Thus, mutation of all of these residues may lead to uncoupling of proton pumping activity from ubiquinone reduction activity if the signal is unable to be transduced across the membrane (E141Q, K263Q) or there is improper de-wetting of the central axis (L242A). Therefore, it is important to establish whether these mutant variants have proton-pumping activity. To do this, I used the ACMA fluorescence quenching method, which is a qualitative method to assess the proton pumping activity of Nqo13 mutant variants. Upon NADH addition, proton pumping by complex I acidifies the lumen of the SBPs/ proteoliposomes, lowering the fluorescence of the pH-sensitive dye ACMA (9-amino-6-chloro-2-methoxyacridine). Valinomycin, which abolishes Δψ to establish ΔpH in the presence of potassium ions, is added to speed up the acidification process.

ACMA fluorescence quenching has been used extensively to assess proton pumping activities (Dröse, Galkin and Brandt, 2005; Cabrera-Orefice *et al.*, 2018; Hoeser *et al.*, 2022; Wright *et al.*, 2022). A few previous publications have used ACMA fluorescence quenching as a method to quantitatively determine proton pumping stoichiometry (Drose et al. and Hoeser et al.). To accomplish this, an assumption was made that the steady state plateau of ACMA fluorescence quench reflects the pH level where the rate of pumping and leak is equivalent. Hence, the fluorescence level reflects the pump rate. Drose et al. plotted DQA-sensitive activity against normalised ACMA fluorescence quench depth and compared the gradient between the *Y. lipolytica* WT and the deletion strain nb8mΔ and found that the slope has

decreased in the mutant and concluded that the associated stoichiometry has halved. Although Drose et al. have quantified the proton leak, the fluorescence quench of ACMA is also impacted by lipid concentration and lumen size, which changes between each proteoliposome or SBP preparation and has not been quantified or controlled for. Thus, the slope may instead reflect a different systematic factor rather than proton pumping. Hence, the ACMA fluorescence quench experiment provides only a semi-quantitative assessment of proton pumping.

To measure complex I specific proton-pumping, 1 µM antimycin A and 400 µM potassium cyanide were added to inhibit complex III and IV, and 0.5 µg:µg AOX was added to turnover complex I. The ACMA fluorescence quench measurements of each *P. denitrificans* variant in SBPs are shown in Figure 4.12. 500 µM NADH was used to initiate proton pumping (NDH-2 does not pump protons), and 5 µM piericidin A was added for a negative control of complex I turnover. For WT, H320L and H346Q variants, 20 µg mL^{-1} SBPs were used in the experiment. However, 40 µg mL^{-1} SBP was used for L242A and 60 µg mL^{-1} SBPs were used for E141Q and K263Q due to their very low complex I activity. As different amounts of SBPs were added for each variant, this value is considered in analysis of the quench depth (see below).

As control of membrane integrity, proton pumping by complex III and IV was assessed by the addition of 5 mM succinate and 5 µM piericidin A to inhibit complex I turnover. For this control, 20 µg mL^{-1} SBPs were added for all variants. All variants were measured at pH 7.5 regardless of the optimum pH.

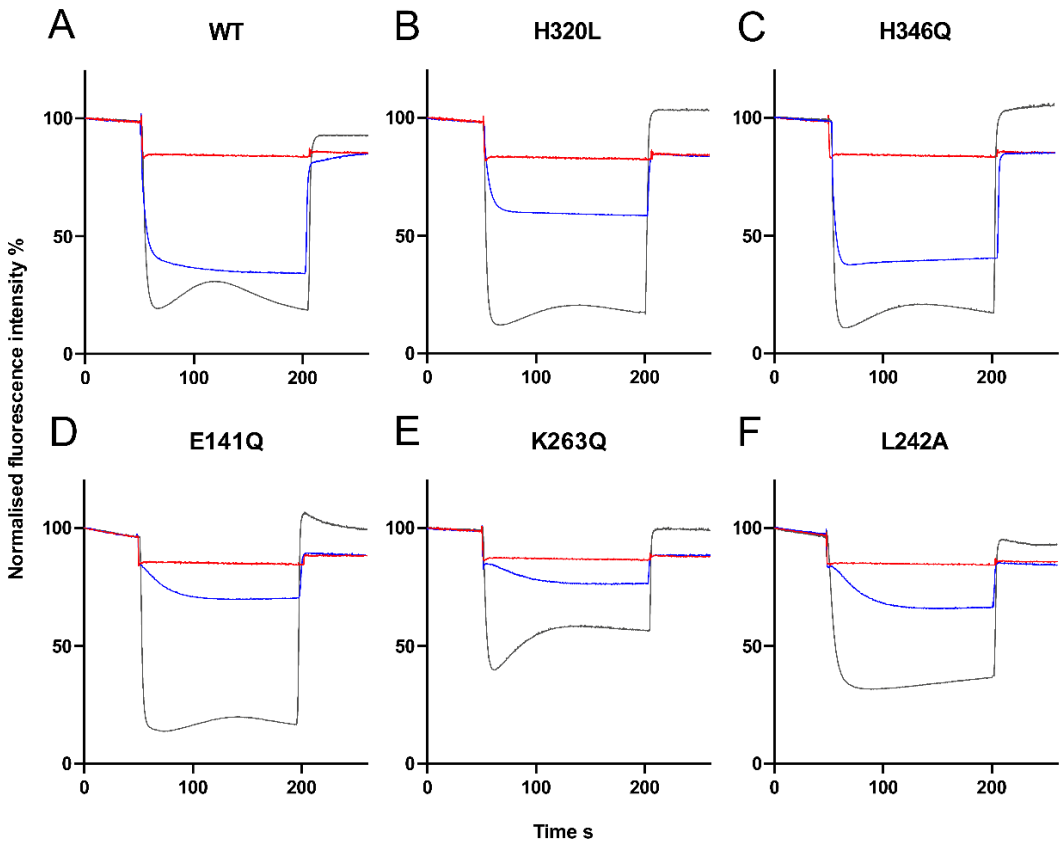

	Normalised ACMA quench depth	Normalised dNADH:O_2 activity
WT	100%	100%
H320L	52%	40%
H346Q	88%	70%
E141Q	13%	4%
K263Q	8%	6%
L242A	19%	20%

Figure 4.11. ACMA fluorescence of *P. denitrificans* complex I variants in SBPs. ACMA fluorescence was measured (excitation at 419 nm, emission at 484 nm) during either (blue) complex I-AOX turnover, which is fully inhibited by the addition of 5 µM Piericidin A, or complex II-III-IV turnover (grey) initiated by the addition of 5 mM succinate. 1 µM Antimycin A and 400 µM KCN were added under complex I-AOX turnover condition, and 5 µM Piericidin A was added under complex II-III-IV turnover conditions. Measurements were performed with constant stirring at 32 °C in a buffer containing 10 mM Tris-SO_4 and 50 mM KCl. 20-60 µg mL^{-1} of SBPs were added to a mixture containing 1 µM ACMA and 0.1 µM Valinomycin. 500 µM NADH was added to initiate the reaction, and 15 µg mL^{-1} of alamethicin was added to dissipate the proton gradient. ACMA fluorescence intensity is normalised to the starting value. ACMA quench depth was measured as the difference in fluorescence intensity with the addition of Alamethicin and is normalised to the WT value and amount of SBPs added to the cuvette. For all variants, the normalised quench depth exceeds the normalised dNADH:O_2 oxidoreduction rate, showing no evidence of reduced proton pumping stoichiometry.

Substantial quenching was observed during complex I-AOX turnover upon the addition of NADH for all variants. Following incubation of piericidin A, the level of ACMA quenching is consistent with only the addition of NADH, showing that all complex I-related ACMA fluorescence quenching is ablated. The maximal quench is also consistent with the activity of the complex I variant, with WT having the greatest fluorescence quenching, followed by H346Q and H320L at similar levels. L242A also displayed ACMA fluorescence quenching. Interestingly, E141Q has a greater quench intensity than K263Q despite lower activities; however, this is likely due to the differences in membrane intactness and as the complex II-III-IV control in K263Q has a lower maximum quench depth. Under the complex II-III-IV turnover, all variants displayed a high level of ACMA quenching, demonstrating that membranes are intact. The addition of alamethicin completely reverses ACMA quenching, demonstrating that the ACMA quench signal is directly caused by ΔpH in the lumen.

Comparing the normalised ACMA quench depth is a simple and semi-quantitative method of assessing proton pumping and has been used previously as standard practice to characterise complex I mutants (Torres-Bacete *et al.*, 2007, 2009; Euro *et al.*, 2008). Here, the ACMA quench depth is defined as the change in fluorescence intensity upon the addition of Alamethicin and is normalised to the WT variant and the amount of SBPs added. The normalised quench depth ranged between 8-88% of WT, which is reflective of the differing activity of each complex I variant. When comparing normalised ACMA quench depth to dNADH:O_2 oxidoreduction rates normalised to WT rates, L242A, K263Q, H320L, and H346Q deviate by less than 1.5 times, and E141Q deviated by greater than 3-fold. However, as all variants showed robust proton pumping activity, and the normalised quench depth is generally greater than the normalised oxidoreduction rate, there is no evidence of decreased proton pumping stoichiometry in the mutants.

4.7 Insights into the proton pumping mechanism of complex I

A summary table of the data compiled for all variants is shown in Table 4.4. The results of these experiments are evaluated against existing proton pumping mechanistic proposals by Sazanov and Kaila et al. (Di Luca, Gamiz-Hernandez and Kaila, 2017; Mühlbauer *et al.*, 2020; Sazanov, 2023).

Mutation	WT	H320L	H346Q	E141Q	K263Q	L242A
Normalised dNADH:O_2 rate	100 ± 8	54.4 ± 2.7	66.7 ± 2	5.1 ± 0.2	7.6 ± 0.2	24.2 ± 2
Normalised ACMA quench depth	100%	52%	88%	13%	8%	19%
pKa changes	No	No	No	No	No	pKa 1 ↑1.5
Observed KIE	1.25 ± 0.119	2.56 ± 0.17	2.30 ± 0.12	1.84 ±0.10	2.50 ± 0.05	2.95 ± 0.45
Proton inventory	1 proton	1 proton	1 proton	1 proton	1 proton	1 proton

Table 4.4. Summary of data collected for all complex I variants. The pH-independent (V_{opt}) value of dNADH:O_2 oxidoreductase activity is normalised to WT rates and dNADH:$APAD^+$ activity. Normalised ACMA quench depth is not normalised to dNADH:$APAD^+$ activity (Figure 4.5). The ACMA quench depth is normalised to WT as a percentage. pKa changes, observed KIE, and the proton inventory are also noted.

4.7.1 Role of conserved histidine residues in the central axis

In Sazanov's mechanism, no explicit reference was made to the role of the two histidine residues (H320 & H346) in Nqo13; however, it is implied that they serve as Grotthuss-capable residues that serve as proton wires for proton translocations between key protonatable residues on TMH8 and TMH12, as bridging residues (Kravchuk *et al.*, 2022). Thus, the proposal is the same as that served by Kaila et al. (Di Luca, Gamiz-Hernandez and Kaila, 2017; Mühlbauer *et al.*, 2020). Mühlbauer et al. performed QM/MM and free energy simulations for the proton transfer between the central lysine (K263) and the terminal glutamate (E405) in the Nqo13 subunit of the *E. coli* complex I molecular structure (PDB: 3RKO (Efremov and Sazanov, 2011)). Free energy simulation of the H322A and H348A mutations (equivalent to H320A and H346A in *P. denitrificans*) in the *E. coli* complex I increased the free energy barrier ΔE for the proton transfer with an overall barrier of 7 kcal mol^{-1} in the WT enzyme to 13.5 kcal mol^{-1} and 14 kcal mol^{-1} for H348A and H322A respectively.

According to transition state theory (see section 3.1.2), the rate of this proton transfer step would decrease by approximately 10^5-fold (to >1000 s^{-1}), causing it to be

significantly rate-limiting. Indeed, experimental results in this present study agree with this proposal, as the NADH:O_2 oxidoreductase activity, when normalised to NADH:APAD$^+$ transhydrogenase activity for H320L and H346Q is 54% and 67% respectively, consistent with the hypothesis that an aliphatic mutation is more deleterious than the polar mutation, and free energy simulations, wherein H322A is creating a greater barrier than H348A. The increase in observed kinetic isotope effect from 1.25 in the WT enzyme to 2.56 and 2.3 for H320L and H346Q respectively, also supports the hypothesis that the rate-limiting step has changed from a step with little isotopic dependence, perhaps ubiquinone binding or product release, to a Grotthuss proton transfer step affected directly by the mutation, likely a proton transfer step between K263 to E405.

The proton inventory for H320L shows a linear profile with a transition state fractionation factor of 0.44 and a reactant fractionation factor of one, suggesting that the proton is transferred from a histidine residue or a water molecule in the transition state. This is in agreement with computational simulations by Muhlbauer et al., which suggest that the proton is likely transferred from H346 to E405 in the rate-limiting transition state, perhaps the deprotonation of the residue by water, followed by proton uptake by E405 (Fig 4.13) (Mühlbauer *et al.*, 2020). The proton inventory for H346Q instead has an upward bulging profile consistent with a reactant fractionation factor of 0.69 and a transition state fractionation factor of 0.34, suggesting that the proton is transferred from a hydronium ion in the transition state. Molecular dynamics simulations suggest that the H348A mutation in *E. coli* complex I contains bridging water molecules in place of the histidine, connecting the central lysine and H322. Thus, proton inventory suggests that in the rate-limiting transition state, the proton is transferred not from the central lysine to H320 but instead from a bridging water molecule, resembling Zundel cation, as suggested in molecular dynamics simulations by Di Luca et al. (Di Luca *et al.*, 2018; Mühlbauer *et al.*, 2020). The intrinsic isotope effect for the proton transfer is 2.3 and 2.9, as measured by the proton inventory method for H320L and H346Q, respectively, which is consistent with a weaker proton bond broken in the transition state of the latter variant. And is likely reflective of tighter binding of reactant proton by H346 (higher pKa) in the transisiton state of the H320L mutant, as compared to by a Zundel cation in the transition state of the H346Q mutant. This also explains why the H320 position

mutation is more deleterious than the H346 position, even when both are mutated to alanine (Mühlbauer *et al.*, 2020).

The transition state fractionation factors of both mutant variants are consistent with Grotthuss proton transfers, which have fraction factors of 0.3-0.6, and the profiles suggest that only a single proton is transferred in the transition state (Venkatasubban and Richard L Schowen, 1984). Thus, the rate-limiting step likely involves discrete proton transfers and not concerted proton transfers. In other words, protons move "one by one" and do not move across multiple sites at the same time. The exact interpretation of this will be discussed in further detail.

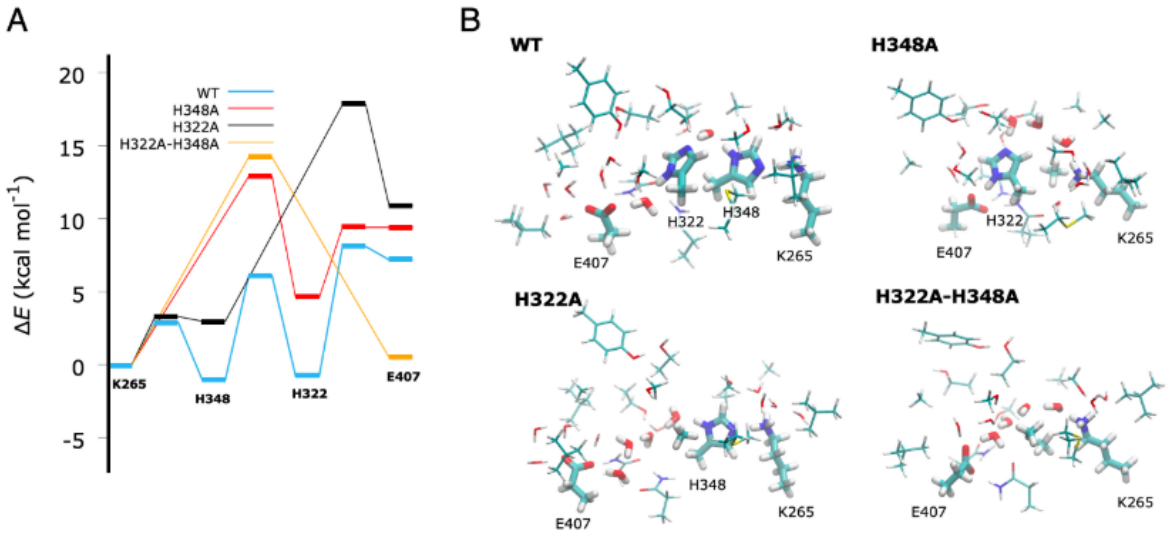

Figure 4.13. Proton transfer barriers in the *E. coli* complex I variants. (A) Free energy simulation of the proton transfer reaction in the WT and H322A, H348A, and H322A/H348A variants. (B) Snapshots of the DFT models of WT and H322A, H348A, and H322A/H348A variants. Figure is adapted from (Mühlbauer *et al.*, 2020). Residues H322 and H348 in *E. coli* are equivalent to H320 and H346 in *P. denitrificans*.

For both H320L and H346Q, there is no evidence of changes in the shape of the pH profile despite a change in the rate-limiting step. According to the molecular dynamic simulations, proton transfer from the central lysine K263 to the terminal glutamate E405 requires hydration of the central axis (Di Luca, Gamiz-Hernandez and Kaila, 2017; Mühlbauer *et al.*, 2020). Since only titratable residues can affect apparent pKa of the enzyme, this suggests that the water molecules compensating for the histidine mutations are not solvent-titratable. This suggests that perhaps central axis

hydration is tightly controlled, and buried waters are not directly connected to bulk solvent.

The ACMA measurement in this study shows a quench depth of 52% and 88% for H320L and H346Q, which is comparable to or higher than the normalised dNADH:O_2 oxidoreduction rate measured. These quench depth values are also consistent with that measured in H322A and H348A mutants in *E. coli* complex I using Oxonol-VI quenching (Mühlbauer *et al.*, 2020). Thus, there is no evidence of a decreased stoichiometry, and it is consistent with the stoichiometry measurements by Jarman et al. showing that histidine mutants pump four protons (Jarman and Hirst, 2022). These observations suggest that the histidine mutations can be compensated by additional waters as Grotthuss bridges and do not affect signal propagation throughout the membrane domain despite a significant decrease in the proton transfer rate across the central axis.

4.7.2 Role of the conserved glutamate residue in the lysine-glutamate pair

A distinct difference between Sazanov and Kaila's proposed proton pumping mechanisms is the hypothesized role of the lysine-glutamate pair (E141 and K232 in Nqo13 of *P. denitrificans*). Kaila proposes that the "opening" and "closing" of the ion-pair play a role in controlling proton transfer from the central lysine to the terminal glutamate in Nqo13 and are not directly involved in proton transfer (Di Luca, Gamiz-Hernandez and Kaila, 2017; Di Luca *et al.*, 2018). Instead, Sazanov proposes that the ion pair are involved directly in proton transfer steps that essentially partition protons across the membrane domain, and little emphasis is placed on the significance of the interaction itself (Kravchuk *et al.*, 2022; Sazanov, 2023). Previous mutagenesis studies of equivalent residues in *E. coli* E144 and K234 residues to a non-protonatable group significantly affected activities, with dNADH:DQ oxidoreductase rates of between 0-20% of WT. However, the E144D mutation led to normal rates of complex I catalysis and proton pumping. Furthermore, double mutations of E144A/F140E and E144A/L147E rescued oxidoreductase activity, with 39-60% and 30-45%, respectively, suggesting that residue needs only to be loosely positionally conserved (Torres-Bacete *et al.*, 2007, 2009; Euro *et al.*, 2008). These findings, alongside the observation in Cryo-EM structures that there is a lack of movement between the Lys-Glu pair across all purported "turnover" complex I structures and the observation that the two residues are not within hydrogen or salt-

bridge bonding distance question the validity of Kaila's hypothesized role for these residues (Kampjut and Sazanov, 2020a; Parey *et al.*, 2021; Kravchuk *et al.*, 2022): the alteration of the distance between the Lys-Glu pair should disable its ability to perform the "opening" and "closing" function in the E144D, E144A/F140E and E144A/L147E mutants. These findings are however not contradictory to Sazanov's hypothesis that protons may be transferred between the TMH7 lysine to the TMH5 glutamate, as water molecules may move position to compensate an altered Grotthuss hydrogen bonding network to rescue proton transfer in mutants.

In the present study, the E141Q mutation yielded a normalized dNAHD:O_2 oxidoreduction rate of 5%, and the K232Q mutant was reported to be completely inactive (Jarman and Hirst, 2022). The observed kinetic isotope effect has also increased from 1.25 to 1.84 in dNADH:O_2 oxidoreductase rate measurements, suggesting that the rate-limiting step has changed to a proton transfer step of unknown identity.

The proton inventory for E141Q shows a linear profile, with a reactant fractionation factor of 1 and a transition state fractionation factor of 0.63, suggesting that the transition state contains a single proton transfer in the trajectory, likely using the Grotthuss mechanism, with the proton donated from a water molecule or a lysine residue. The intrinsic kinetic isotope effect measured at 1.84 is lower than that of all other mutants tested in this study. This suggests that the proton donor has a relatively weakly bound proton. A more acidic residue serves as a good candidate for the proton donor.

The E141Q mutation did not change the shape of the pH profile despite a large decrease in rate. It has been suggested in previous molecular dynamic simulations that the Lys-Glu pair are well solvated by water molecules (Di Luca, Gamiz-Hernandez and Kaila, 2017; Parey *et al.*, 2021). However, the lack of changes in apparent pKa suggests that the residue is not solvent-accessible during the rate-limiting step.

ACMA measurements show a quench depth of 13%, which is higher than the comparable dNADH:O_2 oxidoreduction rate, with discrepancy likely due to measurement error resulting from overall very low rates and other systematic factors. Although this result should not be overinterpreted, there is no evidence of a

decreased proton pumping stoichiometry. Suggesting that the signal propagation is not affected. However, without performing stoichiometry measurements on mutants, which is difficult considering the low rates, a robust conclusion cannot be drawn.

Under this mechanism, the E141Q mutation may also mimic a state in between the "open" and "closed" positions. As the Lys-Glu pair cannot be forced into the "open or closed" position due to the removal of a negative charge, the TMH7 lysine may point closer towards the TMH8 central lysine, permanently lowering its pKa and, therefore, slow the rate of proton uptake by the central lysine (Di Luca, Gamiz-Hernandez and Kaila, 2017). The lowered pKa of K263 is also consistent with being the proton-donor as measured KIE is relatively lower than other mutants. E141Q may also slow down the overall rate by affecting signal propagation across the membrane domain by abrogating the "opening/ closing" mechanism of the Lys-Glu pair. The "opening" of the Lys-Glu pair is proposed to propel proton transfer from the K263 to E405 through electrostatic propulsion. Free energy simulations suggest that this proton transfer is exergonic by 2 kcal mol^{-1} in the "closed" position and endergonic by 5 kcal mol^{-1} in the "open" position, with each energy barrier 4 kcal mol^{-1} and 10 kcal mol^{-1} respectively (Mühlbauer *et al.*, 2020). The combination of differences in activation energy barrier and the energetic favorability of the reaction may explain the large decreases in rate.

As Sazanov's mechanism only requires E141 to act as a conduit for proton transfer, the E141Q water wires may compensate for this role instead, albeit with a significantly higher energy barrier, likely due to "improper tuning" of central axis residue pKas or an altered hydrogen bonding network. Sazanov's mechanism requires the formation of a state where TM12, 8, and 7 sites are all protonated, the three ALS and E-channel containing all the four protons that will be released to the membrane domain. It is noteworthy that in this state, E141 is proposed to be deprotonated, explaining why E141Q does not alter proton pumping stoichiometry. By removing E141Q, proton transfers across this residue are likely to be slowed. Two potential proton transfer steps may be slowed according to Sazanov's mechanism—first, the proton transfer between TMH7 lysine of Nqo13 to the TMH12 lysine of Nqo14. Second, the proton transfer between TMH8 lysine to TMH7 lysine is made unfavourable by the lowering of the pKa of the TMH7 lysine in the E141Q mutant. A proton transfer from a lysine residue made more acidic by the E141Q

mutation is consistent with the relatively small KIE that is observed compared to other mutant variants.

4.7.3 Role of the central lysine

The central lysine on TMH8 in Nqo13, K263 is proposed to be important for proton uptake from the N-side channel in both Kaila and Sazanov's mechanisms and protonation of this residue may control N-side half-channel hydration, according to molecular dynamics simulations (Di Luca, Gamiz-Hernandez and Kaila, 2017; Di Luca *et al.*, 2018). Simulations suggest deprotonation of this residue forces the leucine-histidine gate on the N-side half-channel to close, which is important for de-wetting of the central axis and prevention of proton backflow during proton pumping.

In contrast to the central role of the central lysine in these proposed mechanisms, mutagenesis experiments of this residue in *E. coli* complex I show significant retained activity of 35-55% of WT, with an equivalent effect on ACMA quench depth, suggesting no decrease in stoichiometry (Torres-Bacete *et al.*, 2007; Euro *et al.*, 2008). It is noteworthy that the TMH8 lysine is not positionally conserved across all three antiporter-like subunits only in Nqo14 and Nqo13. Nqo12 instead has the equivalent lysine K351 on TMH10. This shows that the proton network is not conserved across all three antiporter-like subunits and may signal that alternate pathways or hydrogen bonding networks can be established to compensate for mutations.

In the present study, the K263 mutation yielded a normalized dNADH:O_2 oxidoreduction rate of 8%. The observed kinetic isotope effect has increased from 1.25 to 2.50, suggesting that the rate-limiting step has changed to a proton transfer step. The proton inventory for K263Q also shows a linear profile, with a reactant fractionation factor of 1 and a transition state fractionation factor of 0.43. This suggests that the transition state contains a single proton transfer in the trajectory. Despite a significant reduction in activity, the K263Q mutation did not change the shape of the pH profile. Previous molecular dynamics simulations suggest that the central lysine is well-solvated by water molecules upon opening the N-side hydration channel (Di Luca, Gamiz-Hernandez and Kaila, 2017; Parey *et al.*, 2021). However, the lack of changes in apparent pKa suggests that residues determining the rate-limiting step are not solvent-exposed. The ACMA measurement shows a quench

depth of 8%, which is in line with the normalised dNADH:O_2 oxidoreduction rate, in agreement with previous studies that proton pumping stoichiometry is likely not altered (Torres-Bacete *et al.*, 2007; Euro *et al.*, 2008).

Molecular simulations and structural studies show that the central axis residues are well-solvated by water molecules (Di Luca, Gamiz-Hernandez and Kaila, 2017; Grba and Hirst, 2020; Parey *et al.*, 2021); therefore, it is possible that upon N-side hydration opening, histidine H346 uptakes a proton in place of K263 in the K263Q mutant. The magnitude of the observed isotope effect and the shape of the proton inventory curve are comparable to that measured for the H320L mutation, which suggests that the proton transfer in the rate-limiting step may originate from H346.

Under Kaila's mechanism, the central lysine controls N-side half-channel hydration, and the pore is "open" when lysine is protonated and "closed" when it is deprotonated. The K263Q mutation, therefore, mimics the deprotonated lysine and perhaps causes closure of the N-side hydration channel, slowing proton uptake by H346. QM/MM molecular dynamics simulations by Mühlbauer suggest that the translocation of a proton between the central lysine to the terminal glutamate requires hydration of the central axis. In the fully hydrated state, proton transfer occurs in ~2 picoseconds, whereas the proton transfer stalls at the central lysine under dehydrated conditions. Calculated free energy profiles for the proton transfer from the central lysine to terminal glutamate in medium hydration conditions are >20 kcal mol^{-1}, which would slow the reaction timescale into tens of seconds. The data suggest that if K263Q has a dehydrating effect, proton transfer from a protonated H346 to the terminal glutamate E405 is likely to be the rate-determining proton transfer step observed (Mühlbauer *et al.*, 2020).

K263Q may also affect signal propagation. Free energy simulations suggest that the opening of the Lys-Glu pair is hydration state-dependent, with an energy barrier of ~25 kcal mol^{-1}, ~10 kcal mol^{-1}, and ~5 kcal mol^{-1} for the dry, medium, and full hydration states, respectively (Mühlbauer *et al.*, 2020). The dry condition is unrealistic as there are buried ordered water molecules in the central axis (Grba and Hirst, 2020; Parey *et al.*, 2021). Thus, under the medium or full hydration state and a barrier of ≤10 kcal mol^{-1}, the ion-pair opening should not be rate-limited.

While both Kaila and Sazanov's mechanism suggest direct proton transfer by K263, the directionality of subsequent proton transfers differ between the two mechanisms. In Kaila's mechanism, the proton is transferred from the central lysine to the terminal glutamate E405 to be released to the P-side unidirectionally. Whereas in Sazanov's mechanism, K263 can transfer a proton between itself to E405 on TM12 or between itself to K232 on TM7, depending on the stage of proton pumping. Assuming that H346 replaces the function of K263, the Grotthuss transfer distance between H346 and K232 is 20Å as compared to 12Å from K263. H346 and K232 are likely connected by buried water residues in the central axis. However, under more dehydrated conditions in K263Q and the increased distance, this proton transfer is likely to slow. Currently, experimental results are not able to differentiate whether the proton transfer from H346 to E405 or H346 to K232 is the primary rate-limiting proton transfer step. So additional molecular dynamics and free energy simulations will be useful to rationalise current experimental results.

4.7.4 Hypothesized role of the gating leucine in the N-side channel

The leucine residue L242 is proposed to be part of the Leu-His-Trp triad that is important in gating N-side half-channel hydration (Di Luca, Gamiz-Hernandez and Kaila, 2017; Grba and Hirst, 2020). Molecular dynamics simulations suggest that L242 forms a hydrogen bond with the backbone of H239 and controls the N-side channel pore radius through a conformational change of the TM7b helix. This pore "opens" to increase water occupancy when the central lysine K263 is in the protonated state, and vice-versa, resulting in the mean hydration 4 Å around the L242/H239 gate increases from four to eight water molecules during channel opening (Di Luca, Gamiz-Hernandez and Kaila, 2017; Di Luca *et al.*, 2018). Then, H246 uptakes a proton from bulk solvent, and the proton is subsequently transferred to the central lysine K263 at a distance of 10 Å that must be bridged by water molecules. Thus the H246F mutation is lethal, as it completely disrupts this water network and proton transfer (Jarman and Hirst, 2022).

It was proposed that the L242A mutation forces the opening of the N-side hydration half-channel, preventing "de-wetting" and channel cycling (Figure 4.14). It was previously observed that L242A almost completely abolished catalysis (Jarman and Hirst, 2022). This is consistent with the proposal that it is the leucine residue that acts as the primary blocker of hydration, and the pore radius is controlled by

backbone hydrogen bonding. Thus, L242A directly changes the pore radius, whereas the H239Q mutation does not impact backbone hydrogen bonding. Retention of activity for the W241F mutant suggests that this residue is not critical for channel opening/ closing.

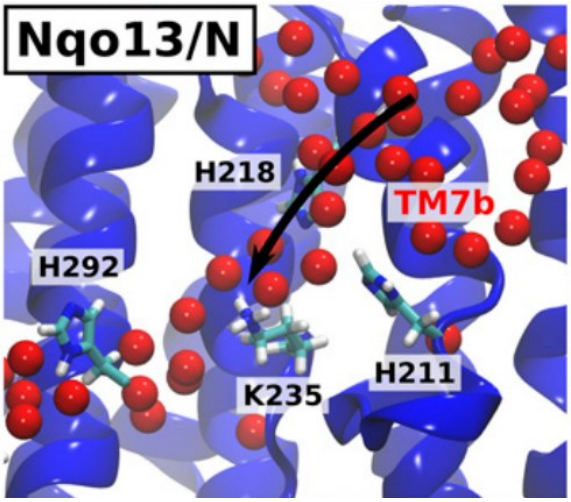

Figure 4.14. The proton transfer pathway into the Nqo13 subunit from the N-side. Water molecules enter between TMH7b, 8, and 10 from the N-side bulk to establish a conduction pathway to the buried residues K235 and H292. The conformational change of TM7b closes this hydration pore. Figure is adapted from (Di Luca, Gamiz-Hernandez and Kaila, 2017) and depicts the T. thermophilus Nqo13 structure. The equivalent residues to H218, K235, and K292 are H239, K263, and H348 in *P. denitrificans* Nqo13.

In this study, the L242A mutation decreased the normalised dNADH:O_2 oxidoreduction rate to 24%, higher than the previously observed value of 5% (Jarman and Hirst, 2022). This is because there is a basic shift in the pH optimum in this mutant, which was not considered in the previous study. Notably, the observed kinetic isotope effect of 3 is the highest measured kinetic isotope effect in all complex I mutants and is at the upper limit expected for a transition state proton transfer involving a solvation catalytic proton bridge (Venkatasubban and Richard L Schowen, 1984). The proton inventory for L242A also shows a linear profile, with a reactant fractionation factor of 1 and a transition state fractionation factor of 0.3. This suggests that the transition state proton transfer involves a one-proton catalytic bridge involving a tightly bound proton in its reactant state. ACMA measurements show a quench depth of 19%, which is comparable to the normalised dNADH:O_2 oxidoreduction rate, showing no evidence for altered proton pumping stoichiometry.

The L242A mutation led to a basic shift in pKa 1 by ~1.5 pH units, with no shift in pKa 2, shifting the pH optimum to pH 8. It is noteworthy that this is the only mutant tested in the thesis thus far that has led to a consistent shift in the pH profile, showing strong evidence that it is affecting a solvent-titratable step during catalysis. To rationalise the residue titrated, this residue must satisfy three characteristics. First, as it is pKa 1 that is shifted, this residue must be deprotonated during catalysis. Second, it must be solvent accessible in L242A so that different pH buffer can affect this residue/ step. Third, the pKa of this residue must be higher in solvent than it is under buried conditions. One standout candidate that satisfies these requirements is K263. Deprotonation of K263 is proposed to be necessary for the closure of the N-side half-channel, which alters the hydrogen bonding network to facilitate proton transfer to the E405 and release to the P-side (Di Luca, Gamiz-Hernandez and Kaila, 2017). Catalytic pH profiles of mutants E141, K263Q, and H346Q do not show pKa shifts, suggesting that the central axis is not solvent accessible. So, the L242A mutation may increase pore radius and allow solvent accessibility to K263 in all states, rendering it titratable during catalysis. The pKa of K263 is expected to be in the region of approximately 6.8 to 8.1, as calculated by Poisson-Boltzmann calculations and Propka calculations, but the side chain of lysine has a solvent pKa 10.6 (Di Luca, Gamiz-Hernandez and Kaila, 2017; Parey *et al.*, 2021; Hoeser *et al.*, 2022). This is consistent with a basic shift upon partial solvation of the residue.

Greater hydration of the central axis of Nqo13 is not expected to affect signal propagation, as the opening of the Lys-Glu gates has a lower energy barrier under well-solvated conditions (Mühlbauer *et al.*, 2020). However, L242A may increase the solvation of K263, removing the buried charge penalty as solvent waters stabilise the positive charge. Increasing the pKa of K263 also increases the proton bond strength, increasing the energy barrier for deprotonation. These factors stabilise the protonation of the central lysine and consequently slow proton transfer steps in both Kaila and Sazanov's proposed mechanisms. Thus, I hypothesize that the rate-limiting step in L242A is the deprotonation of the central lysine. This is consistent with the basic shift in pKa 1, lowered dNADH:O_2 oxidoreduction rates, a proton inventory of one, and a large magnitude of the intrinsic kinetic isotope effect. The intrinsic kinetic isotope effect of 3.3 is larger than other observed mutants and suggests that the donor proton is strongly bound. The basic shift in pKa increases

the force constant for the proton bond in the ground state, which lead to a higher expected kinetic isotope effect by increasing the difference in zero-point energy from isotopic substitution (Cook, 1991).

4.8 Conclusions and future directions

The substantial increase in observed kinetic isotope effect with Nqo13 mutant complex I variants suggests that the identity of the rate-limiting step has changed to a proton transfer step involved during proton pumping. In all mutants but L242A, there is no shift in the catalytic pH profile, suggesting that rate-limiting proton transfer steps takes place between sites that are not solvent accessible. All mutants show that the rate-limiting proton transfer step takes place as discrete proton transfers involving a single proton trajectory in the solvation catalytic bridge and does not involve concerted proton transfers across multiple sites. This implies that the signal is transferred across the membrane domain as a "wave", activating each antiporter subunit in turn. A summary of the proposed rate-limiting proton transfer steps is presented in Table 4.5.

Mutant	Rate limiting proton transfer	Proposed proton donor
H320L	H346 to E405	H346
H346Q	K263 to H320	L_3O^+
E141Q	K263 to H346Q (Or K263 to K232/ K232 to K391^{Nqo14})	K263 (or K391)
K263Q	H346 to E405 (or H346 to K232)	K232 (or H346)
L242A	K263 to E405	K263

Table 4.5. Proposed rate-limiting proton transfer step for each mutant. All steps involve a single proton transfer. Residues use the *P. dentrificans* numbering and refer to subunit Nqo14 unless otherwise specified. Brackets indicate alternate proposal. The proposed proton donor is where the proton is placed when encountering a rate-limiting activation barrier.

Structural studies have identified buried and ordered water residues in the central axis (Grba and Hirst, 2020; Parey *et al.*, 2021). The current data suggest that these waters play a role in proton transfers by providing a hydrogen-bonding network in the Grotthuss mechanism. In particular, there is evidence that in the H346Q mutant, a proton is donated from a Zundel cation rather than a protein residue in the rate-limiting step, in agreement with molecular simulations (Di Luca *et al.*, 2018; Mühlbauer *et al.*, 2020). Mühlbauer's studies also highlight the usefulness of free energy simulations and in-silico mutagenesis in the experimental data for H320L and

H346Q match model predictions, allowing the assignment of the exact proton transfer in the rate-limiting step.

L242A stands out as a unique mutation because it has the highest observed kinetic isotope effect of all mutants tested thus far at 3.3, and it is the only mutant that affected the catalytic pH profile of complex I by causing a 1.5 pH unit basic shift in pKa 1. This suggests that central axis residues are solvent-exposed during the rate-limiting proton transfer and provides compelling evidence that L242 is part of a hydration gating mechanism. To further investigate the hydration gating mechanism, one could create further mutations in the size of this mutant, perhaps to phenylalanine or glycine, or introduce double mutants that rescue or further disrupt activity. For example, L242A/K263E or H may act as a rescue mutation if a basic shift in the pKa of K263 causes a shift in the catalytic pH profile. L242A/K263Q may have compensatory effects, as L242A forces open the hydration channel, whereas K263Q is hypothesized to limit channel opening (Di Luca, Gamiz-Hernandez and Kaila, 2017).

Molecular dynamics experiments previously suggested that the opening and closing of the Lys-Glu pair are important in signal propagation by controlling the deprotonation of the central lysine and, hence, channel hydration (Di Luca, Gamiz-Hernandez and Kaila, 2017). However, the E141Q mutation should trap this pair in Nqo13 into a state that is neither “open” nor “closed”, thus completely disrupting signal propagation across the central axis, possibly decreasing stoichiometry. However, ACMA measurements do not show any evidence of a decrease in stoichiometry for any mutation in this study. Thus, questioning the importance of the Lys-Glu pair in signal propagation. Present data suggest that E141 is more likely to participate in proton transfer directly, akin to Sazanov’s mechanism, rather than act as a passive gating mechanism as in Kaila’s mechanism. However, without more robust stoichiometry measurements using a more quantitative method (Jones *et al.*, 2017; Jarman and Hirst, 2022), decreased stoichiometry and its role in signal propagation cannot be ruled out.

While the Kaila mechanism proposes that protons transfer across the central axis unidirectionally, Sazanov suggests that protons are loaded in the direction towards the Q-site and released in the direction of Nqo12. A limitation of this current study is

the ambiguous interpretation of the effect of the mutants, in particular K263Q and E141Q. The proton inventory method is unable to differentiate between protons transferred from water or amino acid residues that are not arginine or cysteine, and interpretation can only be made in the presence of molecular dynamics, free energy, and pKa simulations, such as those provided by Mühlbauer and Di Luca et al (Di Luca, Gamiz-Hernandez and Kaila, 2017; Di Luca *et al.*, 2018; Mühlbauer *et al.*, 2020). Future studies may be able to clarify the effects of a greater number of central axis mutations using the approach by Mühlbauer et al.

Another method to gain greater clarity in the proton transfer steps during proton pumping, or “mapping the network”, is to increase the number of mutations tested. One can aim to “follow the proton” by mutating conserved charged residues in the central axis along the hypothesized proton transfer network. Mutation of proton transfer residues to cysteine or arginine affects proton transfer rates without removing the proton transfer capability of the residue, which can allow the exact identification of the proton transferred in the rate-limiting step. Cysteine and arginine have reactant fractionation factors that deviate significantly from one (0.55 and 1.28, respectively), decreasing and increasing the observed isotope effect respectively, and changing the shape of the proton inventory to a dome and a bowl shape respectively. This is a painstaking biochemical approach, but this chapter lays the groundwork on how this experiment, along with insights from structural and computational approaches, can be combined to provide much-needed experimental data on the proton pumping mechanism.

5 Investigating a putative conserved ubiquinone re-protonation channel in the NUCM subunit

5.1 Introduction

The complete reduction of ubiquinone by complex I require two protonation events, and it is commonly accepted that the proton donors are likely residues Tyr108^{NDUFS2} and His59^{NDUFS2}, based on a combination of structural and computational studies (Warnau *et al.*, 2018; Kaila, 2021; Parey *et al.*, 2021; Kampjut and Sazanov, 2022; Kravchuk *et al.*, 2022). However, the source of protons for the re-protonation of these two residues is far less clear despite the possibility that it may be of key importance to the mechanism of energy coupling. Computational simulations have shown that the top of the ubiquinone-binding cavity, despite being relatively hydrophobic, can be hydrated (Haapanen and Sharma, 2017; Hoias Teixeira and Menegon Arantes, 2019). Thus, hydration in the cavity may provide a reservoir of protons for the re-protonation of these residues after ubiquinone reduction. Nonetheless, structural, computational, and mutagenesis studies have identified three potential re-protonation pathways. The first pathway, identified by Grba and Hirst (Grba and Hirst, 2020), is comprised of charged residues and ordered water molecules in the NUCM subunit and is the focus of this chapter's investigation. A second pathway, identified by Sazanov and coworkers, suggests a re-protonation route based on the E-channel and ND4L (Kampjut and Sazanov, 2022; Kravchuk *et al.*, 2022). A third pathway, based on residues found to be essential for activity by mutagenesis studies in the supernumerary subunit LYRM6/ NDUFA6 in *Y. lipolytica* structure is identified by Angerer and coworkers (Yoga *et al.*, 2020). The latter two pathways are not the focus of this chapter and are not discussed further.

5.1.1 An evolutionarily conserved hydration pathway in the NUCM subunit

A chain of resolved water molecules (W1-W4) was identified amongst a highly polar channel of Lys, Glu, Asp, Arg, and His residues in the NUCM/ NDUFS2 domain in the high-resolution structure of *Y. lipolytica* (Figure 5.1a). This chain of residues stretches from the ubiquinone binding site directly from H95^{NUCM} towards the matrix and is bridged by the resolved water molecules at distances capable of Grotthuss proton transfer between 2.7 – 3.3 Å (Grba and Hirst, 2020). Strikingly, the channel architecture, key residues (H186, R336, K/R407 and D458) and water molecules are

spatially conserved with that in NiFe hydrogenases as part of an established proton-transfer pathway to the active site (Figure 5.1b) (Fontecilla-camps *et al.*, 2007; Szori-Dorogházi *et al.*, 2012). The R336Q mutation in human complex I has been identified in a patient with Leigh syndrome, a mitochondrial disease associated with complex I dysfunction (Fiedorczuk and Sazanov, 2018).

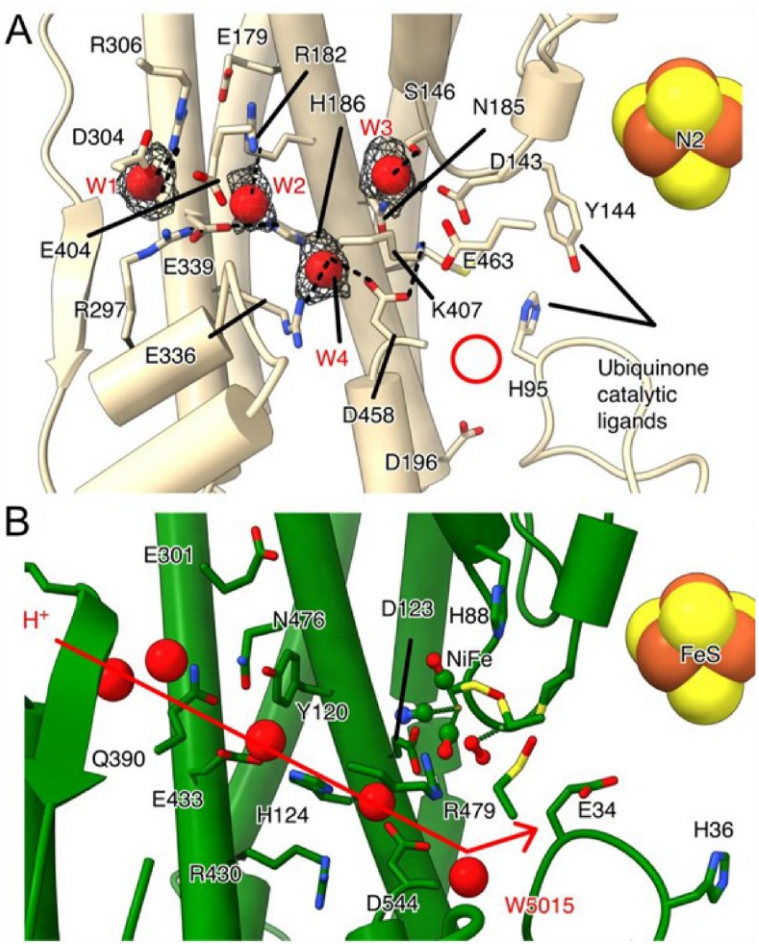

Figure 5.1: Comparison of the proposed conserved proton pathway in *Y. lipolytica* complex I and *Desulfovibrio vulgaris* NiFe hydrogenase. (A) The proposed protonation pathway leads to the ubiquinone reduction site in the NUCM subunit of complex I (PDB: 6YJ4). Dashed lines indicate distances < 3 Å. Water molecules are shown as red spheres. Iron sulphur clusters are shown as orange and yellow spheres. (B) The protonation pathway leading via conserved glutamate to the nickel-iron active site in the large subunit of NiFe hydrogenase (PDB: 1WUI) (Fontecilla-camps *et al.*, 2007; Szori-Dorogházi *et al.*, 2012). W5015 marks a conserved water molecule observed in hydrogenases, and the equivalent position is marked as a red circle in complex I. In complex I, His95 replaces Glu34 in hydrogenases. The flexible NUCM loop where His95 residues clash with the mobile water is depicted by the red circle, though in ubiquinone binding conformations, the water is likely present.

Comparison of the *Y. lipolytica* complex I structure (PDB: 6YJ6) with Hydrogenase from *Desulfovibrio vulgaris* (PDB: 1WUI) (Ogata *et al.*, 2005) reveals overlapping orientations of conserved charged residues and water molecules leading to the catalytic His in complex I (or the catalytic Glu residue in hydrogenase) on the pathway for proton transfer to the NiFe cluster (Dementin *et al.*, 2004). N.B. A conserved water molecule in NiFe hydrogenase between the residues equivalent to NUCM-D458 and H95 in *Y. lipolytica* was not built by Dr. Daniel Grba because of noisy density in the NUCM-*β*1-*β*2-H95 loop. However, an elongated feature that could indicate a mobile water molecule is present in the expected place (Grba and Hirst, 2020).

Mutations of these residues in the membrane-associated hydrogenase of *Thiocapsa roseopersicina* led to decreased hydrogenase activity. The equivalent residues to H124, D123, R279, and E433 (*D. vulgaris* numbering) were mutated (Szori-Dorogházi *et al.*, 2012). H124F/A led to a hydrogenase activity of 6% and 18.2%, respectively, indicating a hydrophobicity penalty consistent with the abrogation of a proton channel. D123L, R479L, and E433L led to a hydrogenase rate of 0%, 0%, and 50% respectively, indicating the presence of a multi-residue proton channel.

The proposed pathway in NiFe hydrogenase supposes that protons enter through residue Lys315 at the protein surface, which is hydrogen bonded to Gln390 through a water dimer. The proton is then expected to travel via the Grotthuss mechanism through residues Glu433, His124, Asp123, and Arg479 to the conserved glu34 residue (Figure 5.2a). Glutamine is not an ionisable residue and is not ordinarily expected to participate in Grotthuss proton transfers, and no explicit explanation was given by Szori-Dorogházi et al. for this discrepancy. However, recent molecular dynamic simulations on the proton transfer pathways of photosystem II in *Thermochromatium tepidum* suggest that amide/imine-tautomerisation of asparagine allows this residue to participate in proton transfers (Sugo and Ishikita, 2023). In the proposed mechanism, the energy barrier for proton transfer from the imidic-asparagine to the hydrogen-bonded serine is provided by the one-electron reduction of ubiquinone, which deprotonates the coordinated serine residue. Taking this into account, I propose a putative mechanism whereby gln390 transfers a proton to the hydrogen-bonded Glu433. First, the hydronium ion donates a proton to Gln390, promoting the formation of the imidic form. Then the reduction of the NiFe cluster

“pulls” protons in the chain forward, deprotonating Glu433, providing the energy to abstract a proton from either the OH-site or the -NH_2 site of Gln390 (Figure 5.2b). The proton transfer pathway proposed by Szori-Dorogházi et al. may indeed be feasible; however, without further QM/MM experiments, the energetic favourability of this mechanism cannot be ascertained.

Multiple putative protonation pathways to the conserved Glu in hydrogenases have been proposed (Fontecilla-camps *et al.*, 2007), but only one of such pathways is conserved in complex I. Also, hydrogenases have much faster turnover rates than complex I (Gutekunst *et al.*, 2018), requiring more rapid re-protonation than complex I, which is likely rate limited by ubiquinone release (see Chapter 3). Hence, the effect of mutations on such a re-protonation pathway may be more limited compared to NiFe hydrogenases.

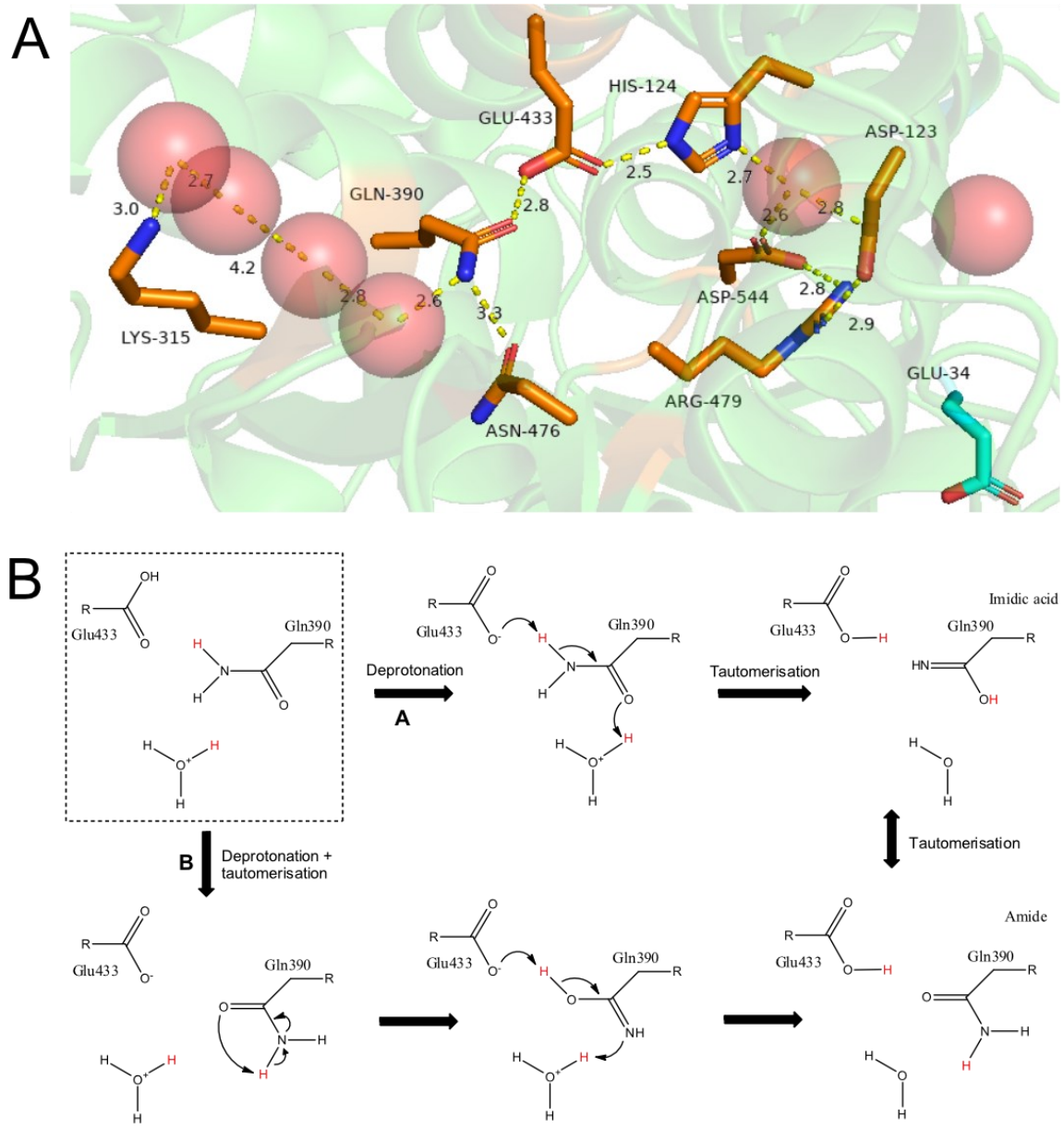

Figure 5.2: Full proton transfer pathway of *Desulfovibrio vulgaris* NiFe hydrogenase and putative proton transfer mechanism. (A) Proposed proton transfer pathway based on the structure of *Desulfovibrio vulgaris* NiFe hydrogenase (PDB: 1WUL). Waters are shown as red spheres. Key residues are shown in stick. Hydrogen bonding is shown as dashed lines and distances are labelled. (B) Two putative proton transfer pathways based on tautomerisation of gln390. Both pathways require an initial deprotonation of Glu433, caused by the reduction of the NiFe centre. In pathway A, the amide -NH_2 faces Glu433 in the initial geometry and tautomerisation results in proton release from the NH_2 side. In pathway B, the first tautomerisation occurs, forming the imidic acid. The amidic acid donates a proton to Glu433 from the -OH side, and the amide is reformed after a proton is abstracted from a hydronium ion. Dashed box indicates the starting position. Transferred protons are indicated in red.

5.2 Aims and strategy

- To further elucidate the proton transfer pathway in NUCM by identifying residues involved using high-resolution complex I structures.
- To create single point mutations using the *Y. lipolytica* model organism.
- To assess the functional effect of these mutations.

5.3 Elucidation of the full re-protonation transfer pathway in the NUCM subunit of complex I

5.3.1 Structural identification of residues involved in proton transfer

Because only four protons were built into NUCM in the aforementioned *Y. lipolytica* complex I structure (PDB: 6YJ4) (Grba and Hirst, 2020), the full Grotthuss proton transfer pathway could not be identified. Therefore, in order to fully elucidate the residues involved in such a proton pathway, the preliminary model for the NDUFS2 subunit of active bovine complex I (eventually published as PDB 7QSK) (Chung, Wright, *et al.*, 2022) was used. This preliminary model has 321 water molecules built, including ordered buried waters and surface waters, allowing the full Grotthuss pathway from the ubiquinone binding site to the matrix to be traced.

First, to identify the Grotthuss protonation pathway, starting from the active site His-59, all Grotthuss capable elements (water molecules, histidine, aspartic and glutamic acid, serine and threonine, tyrosine, lysine, and arginine) within 4 Å were considered. From each such element, the same process is repeated until a pathway towards the matrix is traced. Although a hydrogen bond is 2.7 – 3.3 Å, a larger distance limit of 4 Å is considered to account for potential modelling error and mobility of water molecules. Using Grba's proposed proton channel as a directional starting point, two potential proton transfer pathways containing a long chain of buried ordered waters and charged residues were identified (Figure 5.3). Both pathways lead to the matrix via different entry sites.

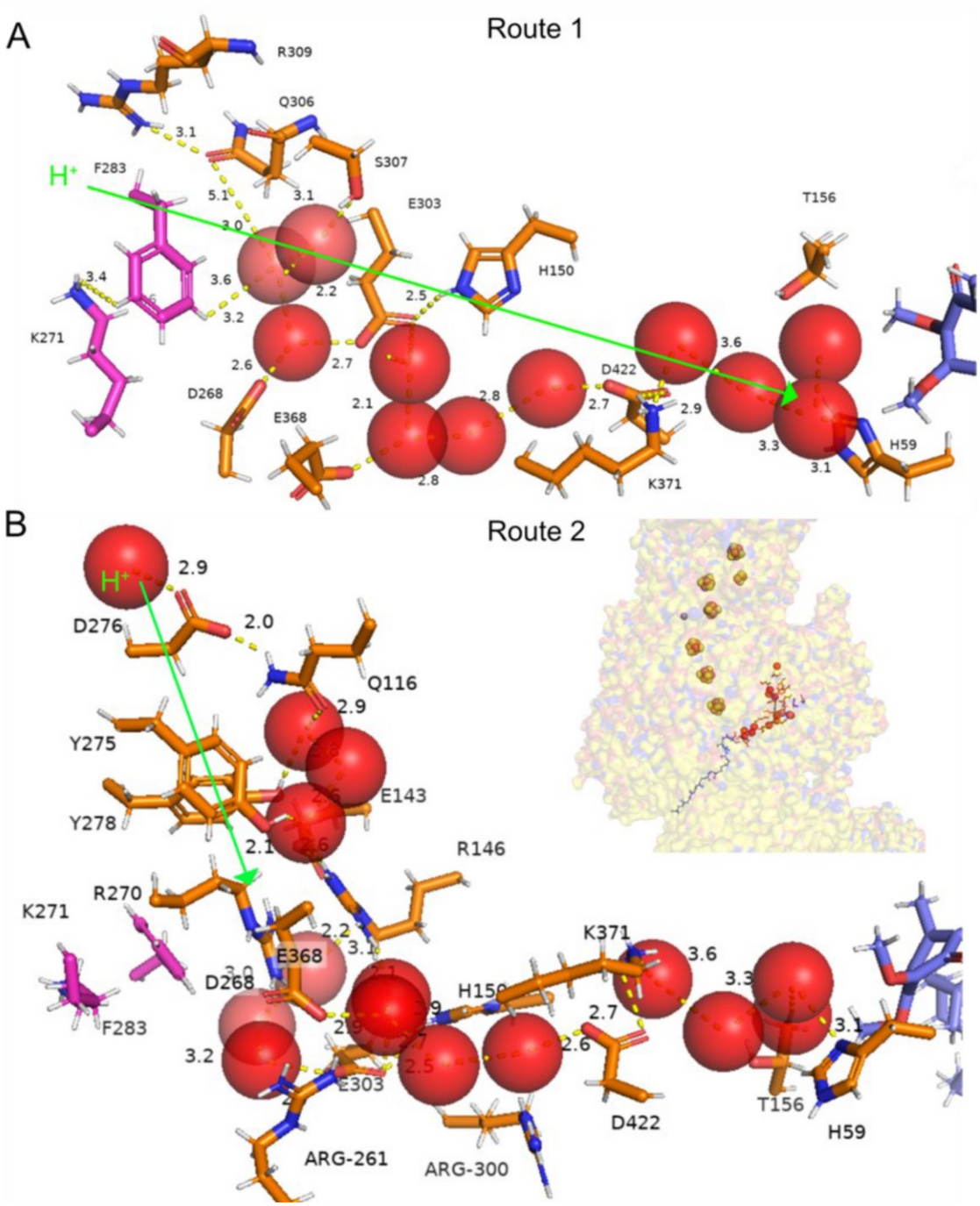

Figure 5.3: Full proton transfer pathways of bovine complex I. (A) Proton transfer pathway conserved with NiFe hydrogenases, named route 1. Protons enter through the conserved residue K271 but is blocked by the conserved F283 (magenta). The remaining route is spatially conserved with NiFe hydrogenase. Waters are displayed as red spheres; hydrogen bonding is indicated by dashed lines, and H-bonding distances are labelled. Key residues are displayed in sticks and labelled. (B) Alternate proton transfer pathway identified only in complex I, named route 2. Protons enter through D276 and pass through Q116 and a trimer of waters into the conserved pathway common to both. Inlay depicts a surface model of complex I, showing that both pathways reach the surface of complex I.

Route 1 is ~30 Å in length and mimics the conserved pathway in NiFe hydrogenases. Protons enter through the spatially conserved K271 (K315 in *Desulfovibrio vulgaris* NiFe hydrogenase) but are blocked by phenylalanine conserved in complex I (F283) or a non-conserved glutamine (Q306) (Figure 5.1A). This suggests that the pathway may be evolutionarily lost in complex I or that proton transfer through this route is mediated by unidentified water molecules or mobile waters.

Route 2 is not identified in NiFe hydrogenase and is ~40 Å in length. Protons enter through Asp276, which is conserved as leucine in *T. thermophilus* and *D. vulgaris* NiFe hydrogenase and histidine in *P. dentrificans*. Then protons are transferred through Gln116, which is conserved within Bovine and *Y. lipolytica* but is replaced by a serine in *T. thermophilus* and *P. dentrificans*. For glutamine to transfer a proton, it requires a push/pull tautomerisation mechanism facilitated by its strong interaction with the adjacent aspartate. Alternatively, the water molecule chelated by Q116 may also be mobile and facilitate proton transfer through that segment.

Both route one and two and the NiFe hydrogenase pathway contain redundancies. For example, H124 in *D. vulgaris* NiFe hydrogenase is essential, whereas a proton can travel through either the equivalent residue H150 in complex I or a triplet of waters chelated by surrounding charged residues. D422 is essential in complex I, but a proton can travel through D544 or D124 (replaced with Asn149 in complex 1) in NiFe hydrogenase (Figure 5.2).

Residues can also have a function purely in chelating water molecules, and such residues are expected to have a lesser effect upon mutation compared to essential residues. Table 5.1 shows a colour-coded list of all residues identified to participate in the two proton transfer pathways. Red denotes essential residues, yellow denotes residues that participate in Grotthuss transfer but redundant pathways are present, and green denotes residues that only chelate water.

To identify whether the residues identified in the bovine complex I structure are conserved across species and NiFe hydrogenase, the protein structure of the NUCM subunits of *Y. lipolytica* complex I (PDB: 6YJ4), *T. thermophilus* complex I (PDB: 4HEA), *P. dentrificans* complex I (AlphaFold structure) were compared (Table 5.1).

B. Taurus	*Y. lipolytica*	*T. Thermophilus*	*P. Dentrificans*	*NiFe hydrogenase*	*Classification*	*Route*	*Mutation*
T156	S192	T135	T136	L131	Pure Water chelator	Both	N/A
D422	D458	D401	D404	D544	Grotthuss	Both	D458L/ N/ F
K371	K407	R350	K353	R479*	Pure Water chelator	Both	K407L
H150	H186	H129	H130	H124*	Grotthuss	Both	H186K/ L/ F
E368	E404	E347	E350	N476	Grotthuss/ water chelator	Both	E404Q
E303	E339	E282	E283	E433*	Grotthuss	Both	E339Q
S307	S343	S286	S287	I437	Grotthuss	Both	S343L
N149	N185	S128	N129	D123*	Grotthuss/ water chelator	Both	N/A
R300^{+}	R336	R279	R336	R430	Pure Water chelator	Both	R336Q
R261	R297	R240	R241	Q390	Pure Water chelator	Both	R297Q
D268	D304	D247	D248	F314	Pure Water chelator	Both	D304N
F283	F319	F262	F263	N/A	NiFe route blocker	Route 1	F319Y
K271	K307	K250	R251	K315	Entry point. Blocked in CxI	Route 1	N/A
R309	R345	K288	L289	E439	Entry point. Blocked in CxI	Route 1	N/A
Q306	Q342	E285	E286	V436	Entry point. Blocked in CxI	Route 1	N/A
E143	E179	E122	E123	N/A	Grotthuss/ water chelator	Route 2	E179Q
R146	R182	R125	R126	N/A	Grotthuss/ water chelator	Route 2	R182Q
R270	R306	R249	R250	N/A	Grotthuss/ water chelator	Route 2	R306Q
Y275	Y311	Y254	Y255	N/A	Pure Water chelator	Route 2	Y311F
Y278	Y314	Y257	Y258	N/A	Grotthuss/ water chelator	Route 2	Y314F
Q116	Q152	L95	H96	N/A	Grotthuss	Route 2	Q152H/ L
D276	D312	S55	E356	N/A	Grotthuss	Route 2	N/A

Table 5.1: A list of residues involved in the putative proton transfer pathways in complex I and NiFe hydrogenase. Residues conserved with the pathways identified with complex I are shown. Red indicates a residue that is essential in the proton transfer pathway. Yellow indicates a residue that performs Grotthuss proton transfer but has redundancy. Green indicates a residue that only acts to chelate water. Red border indicates that residue is conserved across complex I and NiFe hydrogenase. Asterisk indicates the residue was mutated in a previous study. Cross indicates the residue is associated with complex I deficiency in humans.

5.3.2 Computational simulation of pKa using Propka

To assess whether the residues identified are in the pKa ranges capable of Grotthuss proton transfer, pKa values were estimated using Propka 3.1. Propka is a software package that predicts pKa values of ionizable residues. Propka considers whether the residue is surface or buried and sees the protein as an environmental perturbation to the water reference. In order words, the pKa of each ionizable residue is adjusted for by the total effective perturbation contributions from protein groups (Olsson *et al.*, 2011; Søndergaard *et al.*, 2011). Propka is considered "an empirical method" that relies on representing the environment by rules obtained from averaging previous structures and is considered non-rigorous (Olsson *et al.*, 2011). However, Propka has an advantage in ease of use, as well as low computation times compared to more rigorous models that rely on continuum electrostatics or force field approaches, such as Poisson-Boltzmann or molecular dynamics simulations (Olsson *et al.*, 2011). It is worth noting that the pKa values calculated using this method are only an estimate and is used as a guide.

The pKa of ionizable residues involved in proton transfer pathways were calculated using the active and deactive models of the NDUFS2 subunit of bovine complex I (PDB: 7QSK and 7QSM) (Chung, Wright, *et al.*, 2022; Bridges *et al.*, 2023), the deactive model of *Y. lipolytica* complex I (PDB: 6YJ4) (Grba and Hirst, 2020) and the *D. vulgaris* NiFe hydrogenase (PDB: 1WUL) (Ogata *et al.*, 2005). A list of pKa values for these residues is presented in (Table 5.2).

Interestingly, there is a large shift in pKa of several residues (D422, H150, E303, and D268) upon the active/ deactive transition, despite the residues completely overlapping in position in both models. The deactive state pKas of the bovine model also agree with the deactive state *Y. lipolytica* model, supporting the observation that the pKas are state-dependent rather than model-dependent. The pKa of D422 increases from 2.73 in the active state to 4.74 in the deactive state, suggesting that the electrostatic interaction between D422 and K371 may be weaker in the deactive state. The pKa of H150 increases from 2.02 to 4.28 in the deactive transition, which is in the opposite direction to its hydrogen bonding partner E303, where the pKa drops from 4.89 to 1.13 in the deactive transition. This suggests that the deactive to active transition may be involved in facilitating proton transfer along the chain (e.g., from E303 to H150 and from D422 to K371 during the deactive to active transition).

The residues involved in Grotthuss transfer for route 1 (D422, H150, E368, E303, K271) have pKas that are close to neutral in either the active or deactive state. However, route 2 only (E142, R146, R270, Y275) residues have very polarized pKa values that are far from their values in aqueous solution. In particular, R146 is predicted to be essential for this route, and the high pKa value of 18.15 suggests that deprotonating this residue has a high energy barrier and that proton transfer through this channel is likely unfavourable (Salna *et al.*, 2016). Y275, Y278, and R270 have pKa values of 13.91, 16.89 and 14.92 respectively, which also seem to disfavor proton transfer.

The pKas of residues involved in the NiFe hydrogenase proton channel (D544, D123 R479, H124, and E433) show differences to complex I. Strangely, the pKa values of H124 and E433 are very far from solvent pKas, with H124 having a pKa of 1.44 and E433 a pKa of 9.17, suggesting that the histidine is likely deprotonated, and the glutamic acid is protonated. It is possible that the pKa of these residues may change with the redox state of the NiFe cluster (reduced in 1WUL) and that the change in redox state facilitates changes in pKas that promote proton transfer.

B. Taurus			*Y. lipolytica*		*NiFe hydrogenase*	
Residue	pKa (active)	pKa (deactive)	Residue	pKa (deactive)	Residue	pKa (reduced)
D422	2.73	4.74	D458	5.18	D544	6.60
K371	11.84	12.35	K407	12.43	R479	17.47
H150	2.09	4.28	H186	3.57	H124	1.44
E368	6.48	6.70	E404	6.87		
E303	4.89	1.13	E339	1.02	E433	9.17
					D123	4.32
R300	11.07	11.21	R336	11.15	R430	11.40
R261	15.84	16.04	R297	15.15		
D268	1.58	2.77	D304	2.67		
K271	9.83	9.86	K307	10.21	K315	9.92
E143	2.34	2.29	E179	3.30		
R146	18.15	18.30	R182	14.43		
R270	14.92	15.03	R306	16.96		
Y275	13.91	13.89	Y311	13.29		
Y278	16.89	16.61	Y314	17.61		
D276	4.93	4.17	D312	5.02		

Table 5.2: pKa of residues in the identified proton channels as calculated using Propka. Residues with a large active to deactive pKa shift are highlighted with red borders.

5.4 Design of complex I variants

Residues chosen for mutation were identified according to the methods presented above and are summarised in Table 5.1. All mutations were made in the NUCM subunit of the genetically tractable model organism *Y. lipolytica* and are numbered according to the *Y. lipolytica* enzyme.

The residues identified to be important in *D. vulgaris* NiFe hydrogenase are D123, H124, E433, and R479 (*D. vulgaris* numbering). These residues are structurally homologous with residues N185, H186, E339, and K407 in *Y. lipolytica* complex I.

D123 and D544 serve as redundant proton transfer pathways in NiFe hydrogenase, but D123 is replaced with asparagine in complex I and hence is not mutated. Instead, residue D458 is predicted to be essential in complex I and is mutated to asparagine, leucine, and phenylalanine to remove the proton transfer pathway with increasing hydrophobicity. The conserved histidine is mutated into lysine, leucine, and phenylalanine. The lysine mutation is designed as a positive control for Grotthuss proton transfer, and the hydrophobic residues are designed to abrogate the pathway. Residues E339 and K407 are mutated to glutamine and leucine to remove the protonatable group and replicate the previous NiFe hydrogenase mutations.

Along route 1, E404, D304, R336, and R297 are mutated to glutamine to remove the protonatable group but preserve polarity. In particular, R336Q is associated with Leigh's syndrome and is part of this mutation set. S343 is mutated to a leucine to preserve size but remove hydrogen bonding. To remove the redundancy within the proton channel, the double mutants H186L+E404Q and D458N+K407L were created. Residues R345 and Q342 were not mutated as they are not conserved among complex I species.

To assess the role of the phenylalanine that is conserved among complex I but not NiFe hydrogenase, F319 is mutated to tyrosine to add a protonatable group and enable Grotthuss proton transfer whilst preserving its size and hydrophobicity.

For route 2, E179, R182, and R306 are mutated to glutamine to remove the protonatable group but preserve polarity. Y311 and Y314 are mutated to phenylalanine to remove the protonatable group and disrupt the hydration network. Finally, Q152 is mutated to a histidine or a leucine. Q152H is expected to allow

proton transfers to occur at a faster rate by bypassing the amide/imine tautomerism necessary for proton transfer, and the Q152 mutation is expected to disrupt hydrogen bonding in this region, blocking route 2 entirely.

5.5 Creation of complex I variants

The single point mutations outlined above are incorporated into the NUCM subunit of complex I. This is achieved by using a strain of *Y.lipolytica* in which the NUCM subunit has been knocked out and the external alternative NADH dehydrogenase (NDH-2) re-directed to the matrix side of the inner mitochondrial membrane (*Y. lipolytica* GB10 *Δnucm* provided by Brandt and coworkers (Grgic *et al.*, 2004)). The externally directed NDH-2 makes complex I non-essential and therefore allows for the production of deleterious mutations and variants that lead to incompletely assembled complex I. To produce viable complex I that contain the NUCM subunit, a replicative plasmid containing the NUCM gene is transformed into the strain. The NUCM gene with flanking regions was inserted into the pUB26 plasmid (by Dr Ljuban Grgic (Grgic *et al.*, 2004)) with the ClaI and NheI restriction enzymes and then ligating the two fragments together (Figure 5.4). The plasmid contains an autonomous replication sequence (ARS68/CEN) and two antibiotic resistance genes (AmpR & HygR) for selection.

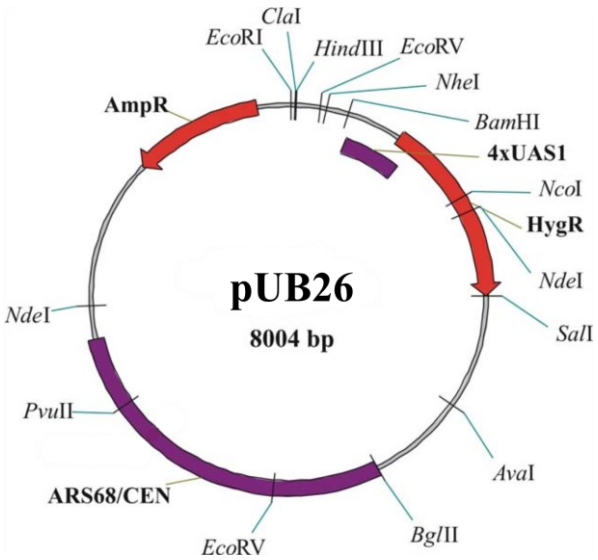

Figure 5.4: Map of the pUB26 shuttle vector. The location of the autonomous replication sequence ARS68/CEN, resistance genes AmpR and HygR, the upstream activation sequence 4xUAS1 and the restriction sites of endonucleases are indicated.

Site-directed mutagenesis of the construct was performed according to the method described by Dr Febin Varghese (Varghese *et al.*, 2015), which uses a method with non-overlapping primers containing the point mutation in the 5' end of the forward primer and a reverse primer fully complementary to the template DNA. The resulting PCR products go through DpnI digestion to remove the plasmid template, and the linear PCR products are ligated together using T4 ligase (see Chapter 2). Subsequently, the circularised plasmid is transformed into *E. coli* (DH5α) and the extracted plasmid is confirmed for the mutation via Sanger sequencing (genewiz) before transformation into competent *Y. lipolytica* cells. For double mutants, the confirmed plasmid is used as template DNA to generate the second mutation. For control experiments throughout this chapter, the parental strain GB10 and the WT strain (where the WT pUB26 is expressed in *Δnucm)* are used and indicated as such. The list of primers used is given in Table 5.3.

Mutation	Primer
D458L For	5' – CATTATTGGTACCATGCTTCTTGTGTTTGG – 3'
D458N For	5' – CATTATTGGTACCATGAATCTTGTGTTTGG – 3'
D458F For	5' – CATTATTGGTACCATGTTCCTTGTGTTTGG – 3'
D458 Rev	5' – GCCACGGCGTCGGGAAG – 3
H186L For	5' – GTGCTCAACCTTCTCATGTCCG – 3'
H186K For	5' – GTGCTCAACAAGCTCATGTCCG – 3'
H186F For	5' – GTGCTCAACTTTCTCATGTCCG – 3'
H186 Rev	5' – TCGGGTGATCTCTCCGAACATG – 3'
K407L For	5' – GAGGCCCCCCTGGGAGAGATG – 3'
K407L Rev	5' – GATGGCGGTGTAGGTCTCTCCG – 3'
E404Q For	5' – CCGCCATCCAGGCCC – 3'
E404Q Rev	5' – TGTAGGTCTCTCCGGGAGGAAC – 3'
E339Q For	5' – CTGATTCGAATGGCCCAGTTCCGACAGTCGCTG – 3'
E339Q Rev	5' – GTATCGGTCGTAACAATCTCCGTTCATGCCGAC – 3'
R336Q For	5' – GATACCTGATTCAAATGGCCGAG – 3'
R336Q Rev	5' – GGTCGTAACAATCTCCGTTCATGC – 3'
D304N For	5' – GATCCGGTATCCCCTTTAACATTCGAAAGAACGCCC – 3'
D304N Rev	5' – CTCGCAGCATGGGGCCGGAAAGAC – 3'
Q152H For	5' – CATGATGACCAACGAGCACGTTTTCTCTCTGGCTG – 3'
Q152L For	5' – CATGATGACCAACGAGCTGGTTTTCTCTCTGGCTG – 3'
Q152 Rev	5' – GACACGTAATCCAGACGATCAAAGTATGGCAGCGCC – 3'
E179Q For	5' – CATGTTCGGACAGATCACCCGAGTGCTCAA C -3'
E179Q Rev	5' – GTTCGGATGTACTTGCCTCGCAGGGG – 3'
R182Q For	5' – GGAGAGATCACCCAGGTGCTCAACCATCTC - 3'
R182Q Rev	5' – GAACATGGTTCGGATGTACTTGCCTCGCAG G - 3'

R297Q For	5’ – GCCCCATGCTGCAGGGATCCGGTA TC - 3’
R297Q Rev	5’ – CGGAAAGACCAAGGTTCAAGGCGTCCTGG – 3’
R306L For	5’ – CCCTTTGACATTCTGAAGAACGCCCCC – 3’
R306L Rev	5’ – GAT ACC GGA TCC TCG CAG CAT GGG G – 3’
S343L For	5’ – CCGAGTTCCGACAGCTGCTGCGAATCATC – 3’
S343L Rev	5’ – CCATTCGAATCAGGTATCGGTCGTAACAATCTCCGTTC – 3’
F319Y For	5’ – GACAAGGTCGACTACGACGTCCCCG – 3’
F319S For	5’ – GACAAGGTCGACTCCGACGTCCCCG – 3’
F319 Rev	5’ – GTA TGC GTC GTA GGG GGC GTT CTT TCG – 3’
Y311F For	5’ – GAAAGAACGCCCCCTTCGACGCATACGAC – 3’
Y311F Rev	5’ – GAATGTCAAAGGGGATACCGGATCCTCGCAG - 3’
Y314F For	5’ – CCCTACGACGCATTCGACAAGGTCGACTTC – 3’
Y314F Rev	5’ – GGCGTTCTTTCGAATGTCAAAGGGGATACCGGATC -3’

Table 5.3: List of primers used to generate complex I variants. The codons that have been altered from the wild-type sequence are highlighted in red.

5.6 Isolation and characterisation of mitochondrial membranes from *Y. lipolytica* complex I variants

Each *Y. lipolytica* variant was cultured in 2xYPD supplemented with 50 μgml^{-1} of Hygromycin B in the method described previously (Bridges *et al.*, 2009). To screen for complex I assembly, each variant was cultured at a small scale in 250 ml flasks, and the resulting cell pellet was prepared into mitochondrial membranes using the Precellys 24 tissue homogenizer, a small-scale high throughput method that allows the mitochondrial membranes of up to 24 variants to be prepared in a single session (see chapter 2).

Blue native polyacrylamide gel electrophoresis (BN-PAGE) can be used to separate and detect high molecular weight protein complexes, such as oxidative phosphorylation complexes (Schägger and von Jagow, 1991). The gels can then be stained using NADH and nitro blue tetrazolium (NBT), where the NBT is reduced to formazan, the chromogenic product by oxidation of NADH catalysed by the flavin site of complex I (Sabar, Balk and Leaver, 2005). As such, the in-gel activity stain can be used to check for the presence of complex I assembly. The BN-PAGE gels staining protocol was previously optimised by Dr. Febin Varghese (Varghese *et al.*, 2015), and the same protocol has been used to visualise the expression and assembly of the 22 complex I mutants alongside the parent GB10 strain serving as positive control (Figure 5.5). In-gel activity staining showed that out of the 23 complex I

mutant variants, only 13 variants expressed and assembled complex I. The double mutant H186L+E404Q did not express or assemble complex I (data not shown).

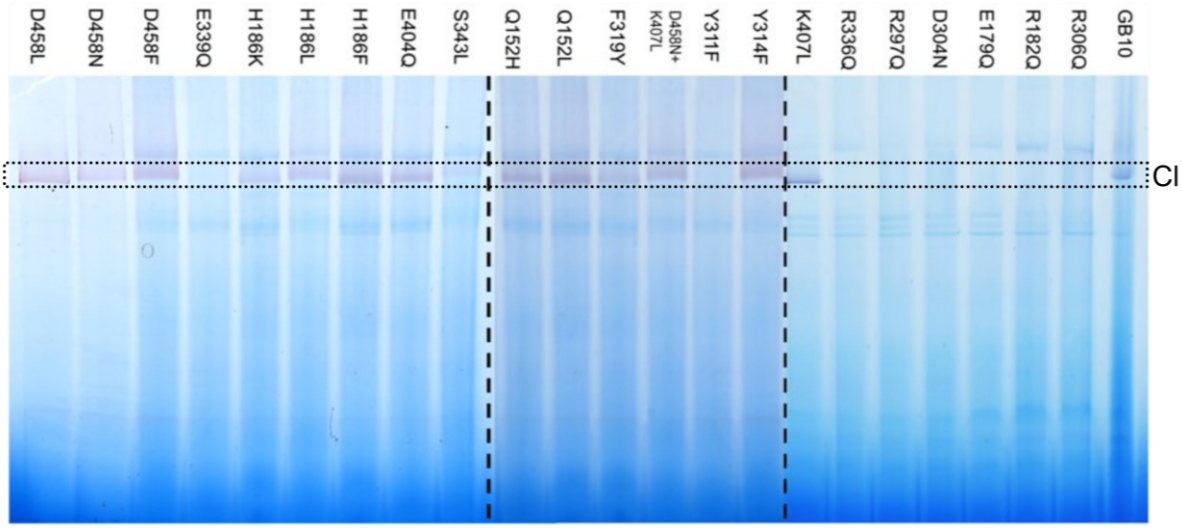

Figure 5.5: BN-PAGE of mitochondrial membranes with in-gel activity staining for complex I. Mitochondrial membranes from 22 complex I mutant variants, alongside the parental strain GB10, were loaded onto the gel. Membranes were solubilised with a 2:1 ratio of DDM to protein, and 40 µg of solubilised proteins were loaded into each well. NADH oxidation by complex I was detected as purple colour using 0.5 mg mL^{-1} NBT and 120 µM NADH. Dashed lines indicate where multiple gels have been combined.

The variants E339Q, S343L, Y311F, R336Q, R297Q, D304N, E179Q, R182Q, and R306Q did not express or assemble complex I. E339 is well conserved between species and is calculated to be an extremely acidic residue (pKa = 1.02) in Propka calculations. Although the glutamine mutation did not affect polarity or size, non-assembly suggests the ionic interaction between E339 and R297 (pKa = 15.15) is potentially structurally important. The same explanation may be applied for E179Q, which removes the strong interaction with R182, and D304N which removes the strong interaction with R306. Furthermore, no arginine mutant successfully assembled complex I, suggesting that these residues provide strong structurally stabilising interactions, as supported by their high pKas and low pKas of interacting acidic residues.

For each variant, the flavin site (dNADH:$APAD^+$) and Q-reductase (dNADH:O_2, dNADH:AOX, dNADH:DQ) activities were measured using the complex I specific substrate dNADH (Matsushita, Ohnishi and Kaback, 1987) (Figure 5.6). For dNADH:O_2 activity measurements, 8 µM of equine heart cytochrome C was

supplemented. For dNADH:AOX activity measurements, a 2:1 mass ratio of AOX was added to reoxidized ubiquinol, and complex III and IV were inhibited with supplementation of antimycin A and KCN, respectively. For dNADH:DQ activity assays, 200 µM of DQ was added. The reductase activities of each complex I variant were normalised to the dNADH:APAD$^+$ activity to correct for complex I concentration in each sample.

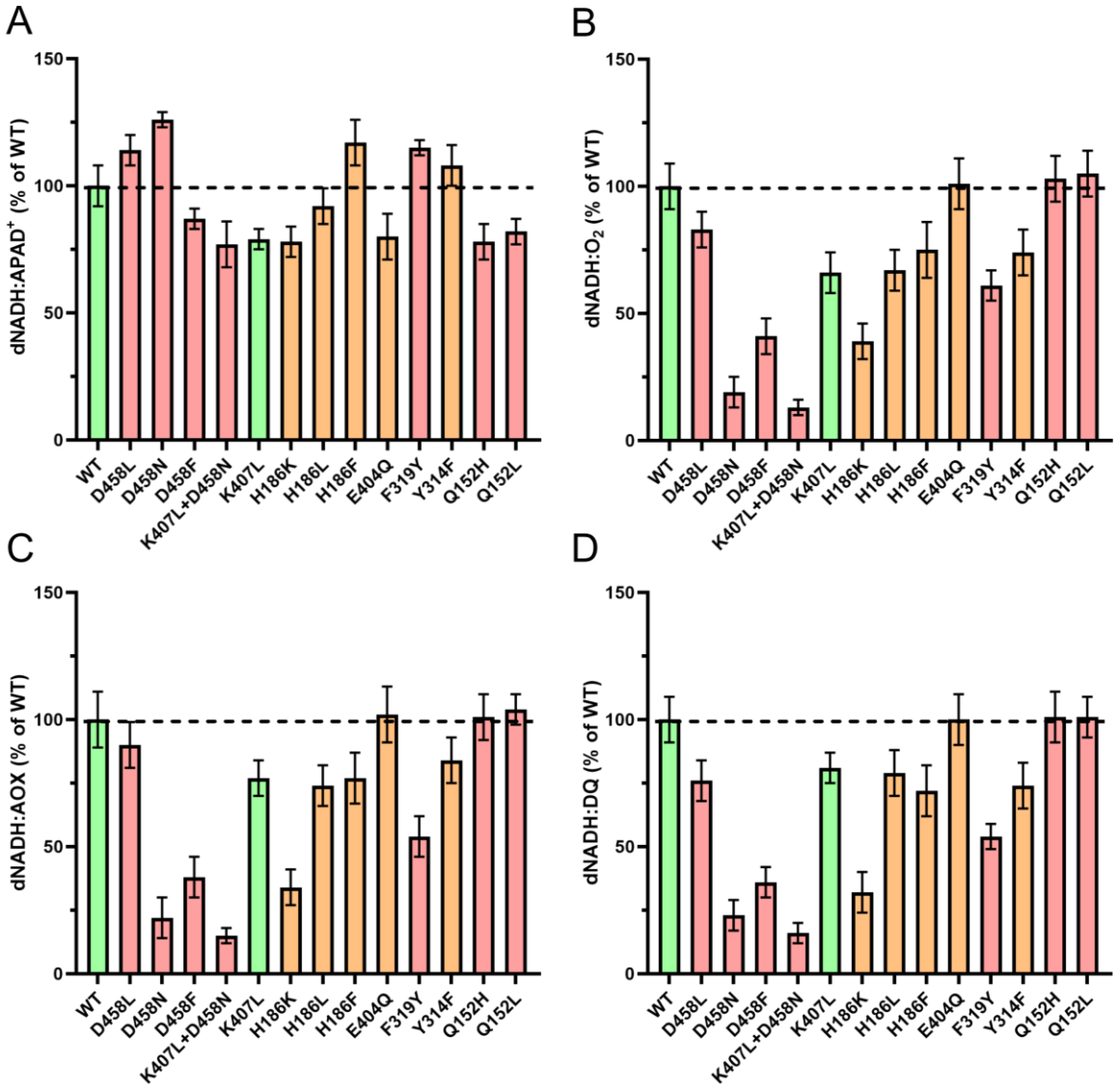

Figure 5.6: Catalytic activities in membranes for wild type and variants. (A) dNADH:APAD$^+$ activities of membranes normalised to WT rate. (B) Normalised dNADH:O_2 activities of membranes. (C) Normalised dNADH:AOX activities of membranes, supplemented with 400 µM KCN and 1 µM Antimycin A. (D) Normalised dNADH:DQ activities of membranes. All Q-reductase activities were normalised to dNADH:APAD$^+$ activities. Error bars represent standard deviations (n = 4). Variants are coloured according to predicted importance to the proton transfer pathway.

All variants had a dNADH:APAD$^+$ activity of more than 75% of WT, and some variants had a greater activity than WT, indicating variance in membrane preparation. Normalised Q-reductase activities measured using dNADH:O_2, dNADH:AOX, and dNADH:DQ showed the same trend, suggesting that complex I turnover was not limited by complex III and IV catalysis.

Q-reductase assays showed that all D458 variants (L, N, F), all H186 variants (K, L, F), K407L, F319Y, and Y314F had reduced activities, whereas variants of Q152 (H, L), E404Q, did not show any loss of activity.

In NiFe hydrogenase, the histidine and aspartate (note D123, not D544) mutations are lethal. Although these mutations did reduce activities in complex I, the order of lethality is inconsistent with the blocking of a proton transfer channel. Contrary to expectations, H186K (~39%) confoundingly had a lower rate than H186L (~67%) and H186F (~75%), as lysine is expected to be Grotthuss capable, and leucine/ phenylalanine are hydrophobic and expected to disrupt such a proton channel. Also, the H186 mutations do not abolish complex I activity unlike the equivalent mutation in NiFe hydrogenase. While this may indicate the differences in proton transfer redundancy between the two enzymes (could not be tested due to H186+E404Q not expressing), the H186F mutation is expected to stop proton transfers through this region by acting as a hydrophobic gate.

The NiFe hydrogenase proton channel can pass protons through D123 (N185 in *Y. lipolytica* complex I) or D544 (D458 in *Y. lipolytica* complex I) (Figure 5.2). As complex I only have one such aspartate; it is considered essential. Therefore, it is confounding that D458L consistently displays a relatively high activity, whereas the more conservative mutation D458N displayed the lowest activity of the mutants in this residue. Furthermore, the activity of the K407L+D458N double mutant (~15%) does not entirely stop activity but merely has the sum of the effects of D458N (~20%) and K407L (~70%) individually, suggesting no cooperative effect between the residues in proton transfer.

The equivalent residue to K407 is R479 in NiFe hydrogenase, of which the mutation to leucine is lethal. However, in complex I, this residue is non-essential and retains a high Q-reductase activity (~70%). R479 is “sandwiched” between D123 and D544 in NiFe hydrogenase and interacts strongly with both aspartates (whereas K407 only

interacts with D458) and may have a structural effect which is not replicated in complex I.

Interestingly, F319Y lowered complex I activity to ~75% of the WT rate, which is unexpected as tyrosine preserves the size of the residue. This residue may affect the Q-reductase rate of complex I by causing uncontrolled protonation of the Q-site. This possibility is further investigated in section 5.7.

Neither Q152 mutations (H, L) had any effect on activities, suggesting that this glutamine likely plays no role at all in proton transfer. Along with the calculated pKas of the residues involved in route 2 (see section 5.3.2), these results suggest that route 2 is highly unlikely to be an active proton transfer route.

5.7 Determining whether the F319Y variant is coupled in complex I proteoliposomes

The F319Y mutation was designed to enable the proton transfer pathway that is conserved within NiFe hydrogenases and displayed ~80% of the WT rate. It is possible that this is the result of uncontrolled protonation of the Q-site through the proposed protonation pathway that led to reduced activity (although it should be expected that Q-reductase activity increases rather than decreases). Uncontrolled re-protonation of the Q-binding site after Q-reduction may lead to loss of charge-mediated signals that couple Q-reduction to proton pumping and may lead to an enzyme that is “short-circuited”.

To test whether this is the case, I used the ACMA fluorescence quenching method to provide a qualitative assessment of proton pumping (for an explanation of the ACMA fluorescence assay, see section 4.6.1). F319Y and WT complex I were purified and reconstituted into proteoliposomes as described in (section 2.22). To measure proton-pumping by complex I, 10 μg:μg AOX was added to turnover complex I and 500 μM NADH was used to initiate proton pumping. For each variant, 1 $\mu g ml^{-1}$ of outward-facing complex I in proteoliposomes were used as the final cuvette concentration. 0.5 μM ACMA and 0.1 μM Valinomycin were added to the buffer mixture (10 mM Tris-SO_4, pH 7.5) to provide the fluorescence signal. To dissipate the proton gradient, 15 $\mu g ml^{-1}$ of alamethicin was added to rupture the lipid membrane. The ACMA fluorescence quench measurements of WT and F319Y are shown in Figure 5.7.

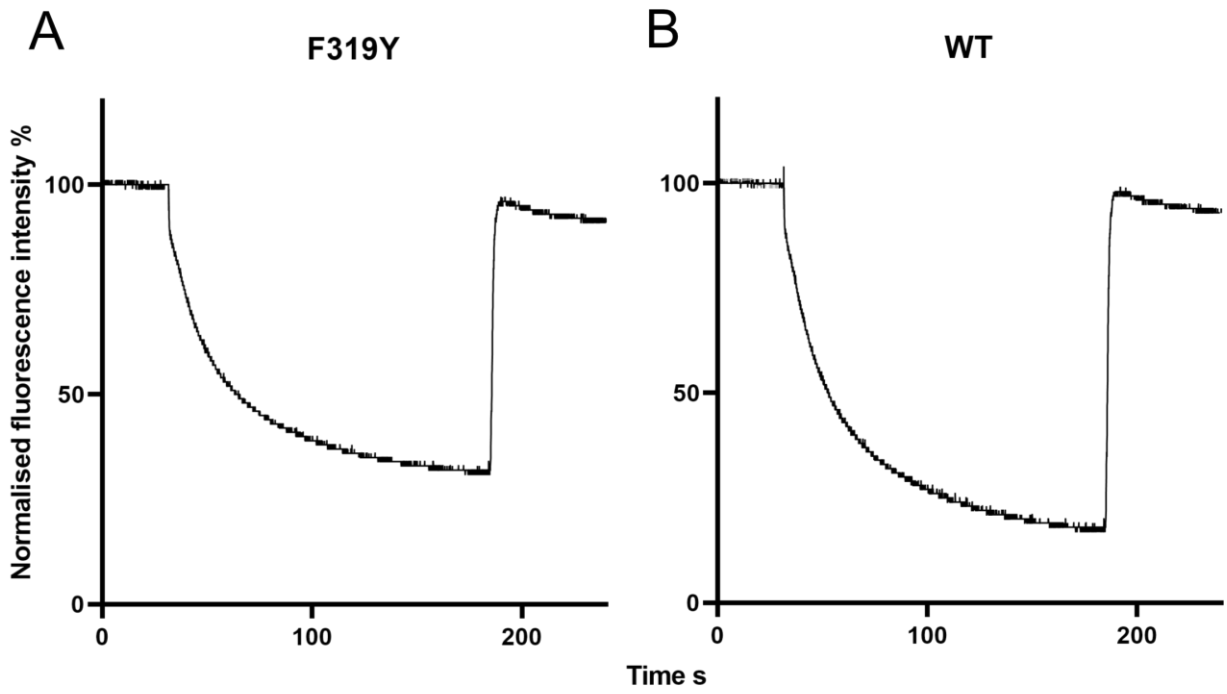

Figure 5.7: ACMA fluorescence of complex I variants in proteoliposomes. ACMA fluorescence was measured (excitation at 419 nm, emission at 484 nm) during complex I-AOX turnover (black). Measurements were performed with constant stirring at 32 °C in a buffer containing 10 mM Tris-SO_4 50 mM KCl. 1 μgml^{-1} of outward-facing complex I in proteoliposomes were added to a mixture containing 0.5 µM ACMA and 0.1 µM Valinomycin. 500 µM NADH was added to initiate the reaction, and 15 μgml^{-1} of alamethicin was added to dissipate the proton gradient. ACMA fluorescence intensity is normalised to the starting value.

Substantial quenching was observed upon the addition of NADH initiating complex I turnover for both the WT and F319Y variant, and the fluorescence quenching was ablated when alamethicin was added, showing that quenching is specific to complex I proteoliposomes. The maximal quench depth is consistent with complex I activity, with the WT enzyme having a greater level of quenching than the F319Y variant.

As both complex I variants displayed high levels of proton pumping, there is no evidence of uncoupling of Q-reductase activity with proton pumping in the F319Y variant. This suggests that the effect of the F319Y mutation on Q-reductase activity is unrelated to that of the coupling pathway expected to be linked to Q-reduction.

5.8 Discussion

An alternative proton transfer pathway in cytoplasmic NiFe hydrogenase was proposed by Szori-Dorogházi et al. on the basis of structural identification, computational analysis, and mutagenesis data (Szori-Dorogházi *et al.*, 2012). However, there are several weaknesses in this proposal. The proton transfer pathway was structurally identified using the *D. vulgaris* NiFe hydrogenase crystal structure (PDB: 1WUL) resolved at 1.5 Å resolution, which was sufficient to resolve ordered water molecules in the structure. However, structural identification of the pathway (Figure 5.2) shows that the proton must pass through Gln-390 in the proton transfer pathway, which is not capable of Grotthuss proton transfer as it lacks a protonatable group. The authors do not address this explicitly but implicitly model the residue in the cationic imidic acid form, suggesting that tautomerisation occurs. However, the computational modelling program used to assign such protonation states, Protonate3D (Labute, 2009), assigns protonation states for each chemical group by minimising the total free energy of the system. This approach does not consider the energy barriers for the proton transfer itself along the reaction coordinate, which is captured in QM/MM models, as demonstrated in the modelling of asparagine-mediated proton transfer in photosystem II (Sugo and Ishikita, 2023). In other words, Protonate3D only considers the “ground state” but not the overall potential energy profile of the proton transfer. Furthermore, the mutants may not specifically affect hydrogenase activity by blocking a proton channel but instead may be structurally important. The variants of NiFe hydrogenase were only characterized using western blots and hydrogenase activities. While western blots show that the protein is expressed and assembled, they are insufficient to demonstrate that the enzyme is completely stable and that the folding is not perturbed. Taken with the above, the deleterious effects of the mutation cannot be easily assigned to the abrogation of a proton transfer channel without additional experimentation on enzyme stability and folding using E.g., nano-DSF and circular dichroism (CD) experiments.

Similar to the proposed NiFe hydrogenase proton transfer pathway, the two putative proton transfer routes identified in bovine complex I were both incomplete from a structural standpoint. Route one had structural conservation with NiFe hydrogenase but was blocked by phenylalanine conserved among complex I or glutamine that is

not conserved among complex I. Whereas route two requires the proton to pass through numerous high pKa arginine residues and requires tautomerisation of the terminal glutamine. Nonetheless, unidentified and mobile water molecules may complete the pathways.

Of the 23 complex I mutant variants created, only 13 variants expressed complex I. None of the aspartate mutants nor the glutamic acid mutants that interact with those aspartates assembled complex I, suggesting that buried arginine and glutamic acid ion pairs have a strong structural role within NUCM. Propka analysis corroborates this as these ion pairs tend to have very polarised pKa values, suggesting strong interaction.

Q-reductase activity assays revealed that mutations of the histidine and aspartate conserved with the putative proton transfer pathway in NiFe hydrogenase, H186 (L,K,F) and D458 (L,N,F) reduced complex I activity. However, the histidine mutation retained a much higher rate of Q-reductase activity than expected for all variants, considering that this mutation is lethal in NiFe hydrogenase (Szori-Dorogházi *et al.*, 2012). D458 mutants had a larger effect; however, neither the histidine nor aspartate mutant variants had an order of lethality consistent with blocking a proton channel. For example, H186K was expected to be a positive control for Grotthuss proton transfer and yet confoundingly had the lowest measured activity of the histidine mutant variants. The same is also true for the D458 variants, in which the D458N had the lowest measured rates despite being the most conserved mutation. Furthermore, the double mutant D458N+K407L displayed measurable activities of ~15%, when structurally, it should block the proton transfer channel completely. F319Y displayed lowered activities and did not affect the coupling between Q-reduction and proton pumping. These observations suggest that this residue does not affect a proton channel but rather may have a structural effect. Q152 mutations (L, H) do not show any effect on complex I activity, suggesting that the proposed tautomerisation mechanism likely does not occur. Together, the activity assay results do not show any evidence of the presence of a proton transfer channel in either route one or route two, and the presence of buried charged residues in NUCM may instead be structurally important for stability or Q-binding.

While a Grotthuss protonation pathway directly leading from the matrix to the Q-binding site would likely be the most efficient pathway to re-protonate the active site proton donors Tyr108^{NDUFS2} and His59^{NDUFS2} out of the proposed pathways outlined in the introduction, buried negative charges that arise upon reduction of ubiquinone are immediately neutralised. While this is energetically favourable, it does not allow for the propagation of energy/ signal across to the membrane domain that is necessary for energy transduction and, ultimately proton pumping. Thus, complex I may evolutionarily shut this proton pathway off to prevent energy loss if, indeed, it is functional in hydrogenases.

5.9 Conclusion and future-directions

At present, there is a lack of consistent structural, computational, and mutagenesis support for the putative proton transfer pathway in both NiFe hydrogenase and the NUCM subunit of complex I. This may be due to the considerable structural redundancy in the Grotthuss proton transfer network in the subunit, which may act less like a “linear pathway” but more as a “canopy/ reservoir” of protons that re-protonate the Q-reduction site, which can “re-charge” its protons upon quinol exit. However, Q-reductase activity assays and BN-PAGE experiments of mutant variants suggest that these residues may instead be structurally important.

The present study is insufficient to indicate the true role of these residues in the NUCM subunit of complex I. In future studies, to assess the stability of these mutant variants, complex I may be purified, and their elution traces compared to the WT to assess stability, and nano-DSF can be used to assess the melting temperature (Tm) of complex I. As the proposed proton transfer pathway is next to the Q-binding site, to assess whether ubiquinone binding is affected by these mutations, K_M measurements can be conducted by measuring complex I activity with increasing ubiquinone concentration or measuring the sensitivity to complex I Q-site inhibitors such as piericidin through an IC50 experiment. In addition, structural simulation studies to characterise solvent penetration into the subunit and molecular dynamics simulations can assess the feasibility of the proton transfer pathways identified in NUCM.

6 Conclusions

Respiratory complex I is mechanistically the least understood enzyme in the mitochondrial electron transfer chain. Although in recent years the emergence of high-resolution structures owing to advances in cryo-EM has led to a proliferation of structurally and computationally derived proposals, there is yet little consensus and a lack of functional validation for such mechanisms. This thesis aims to investigate the mechanism of complex I, specifically the rate-limiting step of complex I through the perspective of the proton, by using a combination of biochemical techniques such as solvent isotope effects, pH effects, enzyme kinetics, and mutagenesis experiments. This creates constraints for existing and future proposals to be tested and provides a blueprint by which such biochemical techniques may be adopted as standard practice for future experiments.

In Chapter 3, the pH-dependent kinetic parameters of complex I variants were determined using the proteoliposome system. First, the experimental set-ups were optimised using the bovine membrane and proteoliposome system, demonstrating that complex I robustly exhibit a solvent kinetic isotope effect, meaning that complex I is at least partially rate-limited by proton transfer steps. This kinetic isotope effect was not dependent on Δp and was expectedly diminished when NADPH was used as a substrate. Then, the effect of ubiquinone-binding site mutants on the rate-limiting step of complex I was investigated using the *Yarrowia lipolytica* model organism. Complex I mutants Y144F, M91I, and D196N of the NUCM/ NDUFS2 subunit were prepared in the proteoliposome system. It was found that for all *Y. lipolytica* mutant variants and bovine complex I, there is a Q concentration dependence on the observed solvent isotope effect, suggesting that Q-binding is rate-limiting at low Q concentrations. The observed kinetic isotope effect was also chain-length dependent, with the complex I reduction of Q_1 and Q_{10}, but not Q_2 demonstrating a kinetic isotope effect. This suggests that when complex I catalyses the reduction of Q_2 product exit is rate-limiting. The pH and Q-dependent rate data of complex I variants were fitted to a rate-equation derived from a kinetic scheme which models the bell-shaped pH dependence in k_{cat}, and the chain-length dependent bi-modal pH-dependence of K_M. The latter has been attributed to differences in the isoprenoid chain interaction with the polar “kink-region” of the Q-binding channel, where short-chain, but not long-chain Q is able to fit past this region

without causing a de-solvation penalty to the residues. Finally, the proton inventory experiment was conducted to investigate the character of the isotopically dependent step. For all variants but D196N, an upward bulging curve was observed, suggesting the presence of multiple rate-limiting steps. The present data suggests that complex I is partially rate-limited by a proton-transfer step and by slow product release. These results are consistent with the observation that observed KIE is Q substrate concentration and Q chain-length dependent, and that the non-isotopically dependent step is affected by Q-binding mutations. An orthogonal approach using equation fitting on the solvent isotope effect of k_{cat}, and k_{cat}/ K_M yielded results consistent with this interpretation, increasing its validity. The residue Y144 is proposed to bind to the Q-headgroup and act as a proton donor upon Q-reduction. The Y144F mutation negatively affected Q-binding, Q-reduction, and product release. However, the intrinsic KIE was the same as that of WT, suggesting that the identity of the rate-limiting proton transfer is the same. The M91 residue was proposed to interact with the first isoprenoid tail of Q. The M91I mutation had an effect on Q-binding and product release, but little effect on Q-reduction. The D196 residue was proposed to donate a proton to H95 during Q-reduction, the mutation of which may increase the pKa of H95. The D196N mutation uniquely made the proton transfer step almost solely rate-limiting, and the intrinsic KIE was different to the other complex I variants. These results suggest that the rate-limiting proton transfer is the deprotonation of H95 upon the reduction of QH^-. Overall, present results suggest that Q-dynamics in the complex I binding channel is rate-limiting in the timescale of complex I turnover and provide functional insight into the Q-reduction mechanism.

In Chapter 4, the role of conserved charged residues in the central axis of the membrane domain was investigated using the *Paracoccus denitrificans* model organism and the sub-bacterial particle assay system (SBP). The Nqo13/ ND4 subunit was chosen for mutation, owing to the wealth of computational studies and mechanistic proposals focusing on this subunit. Five mutant variants in the Nqo13 subunit previously investigated by Dr. Owen Jarman were carried forward for this study: E141Q, H320L, H346Q, K263Q, and L242A. The residues H320 and H346 are hypothesized to be Grotthuss bridging residues between the central lysine K263 and terminal lysine E405. The residue E141 is proposed to form an ion pair with K232 (Lys-Glu pair) at the proximal end of the Nqo13 subunit, which facilitates signal propagation. The central lysine K263 is proposed to control N-side half-channel hydration and facilitate proton

transfer across the central axis. And finally, the L242 residue was proposed to control N-side hydration pore size by conformational changes in the TMH7b helix. All mutations increased the observed KIE significantly as compared to WT, which displayed only a small KIE. Each mutation increased the KIE by different magnitudes, suggesting that in each case a different proton-transfer transition state was rate-limiting. The proton inventory experiment revealed that for all but H346Q, a straight line was observed, suggesting that the proton transfer step was close to solely rate-limiting for complex I turnover. Using the ACMA fluorescence quenching experiment, it was observed that all mutant variants were capable of proton pumping, with no evidence of an altered proton pumping stoichiometry. The combination of analysing the magnitude of the KIE, the shape of the proton inventory, and the pH-dependent activity allowed the presentation/ validation of mechanistic proposals for the rate-limiting step in each mutant. In the H320L mutation, complex I activity is rate-limited by the transfer of a proton from H346 to a water molecule replacing H320 in the proton-transfer pathway to E405. In the H346Q mutation, the deprotonation of a Zundel-ion replacing H346 in the proton transfer pathway from K263 to H320 is rate limiting. For the E141Q mutation, this mutant may mimic an “in-between” state where the Lys-Glu pair is neither open nor closed, making the proton transfer from K263 to E405 less energetically favourable. The K263Q mutation mimics the deprotonated lysine, and may decrease central axis hydration, which affect the opening of the Lys-Glu pair, as well as the proton transfer from H346 to E405. The L242A mutation led to a basic shift in pKa 1 in complex I activity, and the largest observed KIE observed in all mutants. The large shift in pKa gives mechanistic evidence that this mutation increases hydration in the central axis, and may increase the pKa of K263, slowing its deprotonation in the proton transfer to E405. Overall, this Chapter allowed for the evaluation of existing proton pumping mechanisms.

In Chapter 5, the role of a putative re-protonation channel in the Q-reduction site was investigated via site-directed mutagenesis using the *Yarrowia lipolytica* model organism. This proton uptake route is comprised of conserved buried charged residues and is structurally homologous to a proton-uptake route in *Desulfovibrio vulgaris* NiFe hydrogenase. Analysing the bovine complex I cryo-EM structures, two putative Grotthuss proton-transfer routes were identified that span the Q-reduction site histidine to the edge of the NUCM subunit, named routes one and two. Essential to route one

involves the Grotthuss-competent residues (*Y. lipolytica* numbering) D458, K407, H186, E404, E339, and S343. Essential to route two involves the residues E179, R182, R306, Y311, and Y314 in addition to route one residues. However, access to the mitochondrial matrix in route one was blocked by F319 and Q342, and blocked by Q152 in route two, requiring structural rearrangement, tautomerisation, or mobile waters to transfer protons from the mitochondrial matrix to the Q-reduction site. Computational analysis of residue pKa using the software Propka revealed that the pKa of residues along route one are close to neutral and displayed a pKa shift upon the active/ deactive transition. However, route two involves multiple high pKa (>13) arginine and tyrosine residues, disfavouring proton transfers. A total of twenty-three complex I mutations were created in the NUCM subunit by expressing NUCM on the pUB26 plasmid in a GB10 Δnucm deletion strain of *Yarrowia lipolytica.* Mitochondrial membranes were prepared for each mutant using a high-throughput small-scale preparation and analysed using BN-PAGE. Of the mutant variants, only thirteen expressed complex I, with variants E339Q, S343L, Y311F, R336Q, R297Q, D304N, E179Q, R182Q, and R306Q not expressing or assembling complex I. These residues have highly polarised pKa values as analysed by Propka, suggesting that the strongly interacting Glu-Arg ion pairs serve a structural function in NUCM assembly. Of the intact complexes I, D458 (L, N, F), K407L, H186 (K, L, F), E404Q, F319Y, Y214F, Q152 (H, L), and the double mutant K407L+D458N all expressed complex I to >75% of the WT, as measured by the dNADH:APAD$^+$ oxidoreduction solution assay. However, no variant managed to completely abolish complex I activity, with the double mutant K407L+D458N yielding a rate of 15% in the dNADH: AOX assay, and mutants of essential residues yielding relatively high rates of between 20-80% of the WT rate, remarkably different to the behaviour observed in *Desulfovibrio vulgaris* NiFe hydrogenase thus providing no evidence for the presence of a proton-transfer pathway in NUCM. Mutation of the phenylalanine blocker residue F319Y did not uncouple complex I, as measured by the ACMA fluorescence quench experiment, providing no evidence that it serves to regulate a proton-transfer route. Overall, the combination of mutagenesis, structural, and computational analysis suggest that these conserved buried charged residues likely do not play a part in a proton-uptake pathway but may instead serve a structural function.

7 Bibliography

Abdrakhmanova, A. *et al.* (2004) 'Subunit composition of mitochondrial complex I from the yeast Yarrowia lipolytica.', *Biochimica et biophysica acta*, 1658(1–2), pp. 148–156. doi: 10.1016/j.bbabio.2004.04.019.

Abrahams, J. P. *et al.* (1994) 'Structure at 2.8 A resolution of F1-ATPase from bovine heart mitochondria.', *Nature*, 370(6491), pp. 621–628. doi: 10.1038/370621a0.

Agip, A. N. A. *et al.* (2019) 'Mammalian Respiratory Complex i Through the Lens of Cryo-EM', *Annual Review of Biophysics*, 48, pp. 165–184. doi: 10.1146/annurev-biophys-052118-115704.

Amarneh, B. and Vik, S. B. (2003) 'Mutagenesis of subunit N of the Escherichia coli Complex I. Identification of the initiation codon and the sensitivity of mutants to decylubiquinone', *Biochemistry*, 42(17), pp. 4800–4808. doi: 10.1021/bi0340346.

Angerer, H. *et al.* (2012) 'Tracing the tail of ubiquinone in mitochondrial complex i', *Biochimica et Biophysica Acta - Bioenergetics*, 1817(10), pp. 1776–1784. doi: 10.1016/j.bbabio.2012.03.021.

Anraku, Y. and Gennis, R. B. (1987) 'The aerobic respiratory chain of Escherichia coli', *Trends in Biochemical Sciences*, 12, pp. 262–266. doi: https://doi.org/10.1016/0968-0004(87)90131-9.

Baker, S. C. *et al.* (1998) 'Molecular genetics of the genus Paracoccus: metabolically versatile bacteria with bioenergetic flexibility.', *Microbiology and molecular biology reviews : MMBR*, 62(4), pp. 1046–1078. doi: 10.1128/MMBR.62.4.1046-1078.1998.

Baradaran, R. *et al.* (2013) 'Crystal structure of the entire respiratory complex i', *Nature*, 494(7438), pp. 443–448. doi: 10.1038/nature11871.

Barbara Schowen, K. and Schowen, R. L. (1982) *Solvent Isotope Effects on Enzyme Systems*, *Methods in Enzymology*. doi: 10.1016/S0076-6879(82)87031-6.

Barker, C. D., Reda, T. and Hirst, J. (2007) 'The flavoprotein subcomplex of complex I (NADH:ubiquinone oxidoreductase) from bovine heart mitochondria: insights into the mechanisms of NADH oxidation and NAD+ reduction from protein film voltammetry.', *Biochemistry*, 46(11), pp. 3454–3464. doi: 10.1021/bi061988y.

Bayly, J. G., Kartha, V. B. and Stevens, W. H. (1963) 'The absorption spectra of liquid phase H2O, HDO and D2O from 0·7 μm to 10 μm', *Infrared Physics*, 3(4), pp. 211–222. doi: 10.1016/0020-0891(63)90026-5.

Belasco, J. G., Albery, W. J. and Knowles, J. R. (1986) 'Energetics of proline racemase: Double fractionation experiment, a test for concertedness and for transition-state dominance', *Biochemistry*, 25(9), pp. 2552–2558. doi: 10.1021/bi00357a040.

Belevich, G. *et al.* (2011) 'Probing the mechanistic role of the long α-helix in subunit L of respiratory Complex I from Escherichia coli by site-directed mutagenesis', *Molecular Microbiology*, 82(5), pp. 1086–1095. doi: https://doi.org/10.1111/j.1365-2958.2011.07883.x.

Belevich, N., Belevich, G. and Verkhovskaya, M. (2014) 'Real-time optical studies of respiratory Complex I turnover', *Biochimica et Biophysica Acta - Bioenergetics*, 1837(12), pp. 1973–1980. doi: 10.1016/j.bbabio.2014.09.010.

Belevich, N. and Verkhovskaya, M. (2016) 'Resting state of respiratory Complex I from Escherichia coli', *FEBS Letters*, 590(Iii), pp. 1570–1575. doi: 10.1002/1873-3468.12199.

Beltrán, J. L. and Franco, R. (2019) 'The meaning of the Michaelis-Menten constant : K_M describes a Solving a Michaelis-Menten paradox Keywords Cell metabolism', *bioRxiv*, pp. 1–16 bioRxiv 608232; doi: https://doi.org/10.1101/608232.

Bendall, D. S. and Bonner, W. D. (1971) 'Cyanide-insensitive Respiration in Plant Mitochondria', *Plant Physiology*, 47(2), pp. 236–245. doi: 10.1104/pp.47.2.236.

Berndtsson, J. *et al.* (2020) 'Respiratory supercomplexes enhance electron transport by decreasing cytochrome c diffusion distance', *EMBO reports*, 21(12), p. e51015. doi: https://doi.org/10.15252/embr.202051015.

Berrisford, J. M. and Sazanov, L. A. (2009) 'Structural basis for the mechanism of respiratory complex I.', *The Journal of biological chemistry*, 284(43), pp. 29773–29783. doi: 10.1074/jbc.M109.032144.

Bianchi, C. *et al.* (2004) 'The mitochondrial respiratory chain is partially organized in a supercomplex assembly: kinetic evidence using flux control analysis.', *The Journal of biological chemistry*, 279(35), pp. 36562–36569. doi: 10.1074/jbc.M405135200.

Biner, O. *et al.* (2020) 'Bottom-Up Construction of a Minimal System for Cellular Respiration and Energy Regeneration', *ACS Synthetic Biology*, 9(6), pp. 1450–1459. doi: 10.1021/acssynbio.0c00110.

Birrell, J. A. and Hirst, J. (2013) 'Investigation of NADH binding, hydride transfer, and NAD+ dissociation during NADH oxidation by mitochondrial complex i using modified nicotinamide nucleotides', *Biochemistry*, 52(23), pp. 4048–4055. doi: 10.1021/bi3016873.

Birrell, J. A., Yakovlev, G. and Hirst, J. (2009) 'Reactions of the flavin mononucleotide in complex I: A combined mechanism describes NADH oxidation coupled to the reduction of APAD+, ferricyanide, or molecular oxygen', *Biochemistry*, 48(50), pp. 12005–12013. doi: 10.1021/bi901706w.

Blaza, J. N. *et al.* (2014) 'Kinetic evidence against partitioning of the ubiquinone pool and the catalytic relevance of respiratory-chain supercomplexes.', *Proceedings of the National Academy of Sciences of the United States of America*, 111(44), pp. 15735–15740. doi: 10.1073/pnas.1413855111.

Blaza, J. N., Vinothkumar, K. R. and Hirst, J. (2018) 'Structure of the Deactive State of Mammalian Respiratory Complex I.', *Structure (London, England : 1993)*, 26(2), pp. 312-319.e3. doi: 10.1016/j.str.2017.12.014.

Blow, D. M. (1976) 'Structure and Mechanism of Chymotrypsin', *Accounts of Chemical Research*, 9(4), pp. 145–152. doi: 10.1021/ar50100a004.

Bridges, H. R. *et al.* (2009) 'The respiratory complexes I from the mitochondria of two Pichia species.', *The Biochemical journal*, 422(1), pp. 151–159. doi: 10.1042/BJ20090492.

Bridges, H. R. *et al.* (2014) 'Effects of metformin and other biguanides on oxidative phosphorylation in mitochondria', *Biochemical Journal*, 462(3), pp. 475–487. doi: 10.1042/BJ20140620.

Bridges, H. R. *et al.* (2020) 'Structure of inhibitor-bound mammalian complex I', *Nature Communications*, 11(1), pp. 1–11. doi: 10.1038/s41467-020-18950-3.

Bridges, H. R. *et al.* (2023) 'Structural basis of mammalian respiratory complex I inhibition by medicinal biguanides.', *Science (New York, N.Y.)*, 379(6630), pp. 351–357. doi: 10.1126/science.ade3332.

Bridges, H. R., Bill, E. and Hirst, J. (2012) 'Mössbauer spectroscopy on respiratory complex I: the iron-sulfur cluster ensemble in the NADH-reduced enzyme is partially oxidized.', *Biochemistry*, 51(1), pp. 149–158. doi: 10.1021/bi201644x.

Briggs, G. E. and Haldane, J. B. S. (1925) 'A Note on the Kinetics of Enzyme Action', *Biochemical Journal*, 19(2), pp. 338–339. doi: 10.1042/bj0190338.

Burnell, J. N., John, P. and Whatley, F. R. (1975) 'The reversibility of active sulphate transport in membrane vesicles of Paracoccus denitrificans.', *The Biochemical journal*, 150(3), pp. 527–536. doi: 10.1042/bj1500527.

Cabrera-Orefice, A. *et al.* (2018) 'Locking loop movement in the ubiquinone pocket of complex I disengages the proton pumps', *Nature Communications*, 9(1). doi: 10.1038/s41467-018-06955-y.

Cavalier-Smith, T. (2006) 'Origin of mitochondria by intracellular enslavement of a photosynthetic purple bacterium.', *Proceedings. Biological sciences*, 273(1596), pp. 1943–1952. doi: 10.1098/rspb.2006.3531.

Cecchini, G. (2003) 'Function and Structure of Complex II of the Respiratory Chain', *Annual Review of Biochemistry*, 72(1), pp. 77–109. doi: 10.1146/annurev.biochem.72.121801.161700.

Chance, B. and Hollunger, G. (1960) 'Energy-Linked Reduction of Mitochondrial Pyridine Nucleotide', *nature*, 185, pp. 666–672.

Chomyn, A. *et al.* (1986) 'URF6, Last Unidentified Reading Frame of Human mtDNA, Codes for an NADH Dehydrogenase Subunit', *Science*, 234(4776), pp. 614–618. doi: 10.1126/science.3764430.

Chouchani, E. T. *et al.* (2014) 'Ischaemic accumulation of succinate controls reperfusion injury through mitochondrial ROS.', *Nature*, 515(7527), pp. 431–435. doi: 10.1038/nature13909.

Chouchani, E. T. *et al.* (2016) 'A Unifying Mechanism for Mitochondrial Superoxide Production during Ischemia-Reperfusion Injury.', *Cell metabolism*, 23(2), pp. 254–263. doi: 10.1016/j.cmet.2015.12.009.

Chung, I. *et al.* (2021) 'Cork-in-bottle mechanism of inhibitor binding to mammalian complex I', *Science Advances*, 7(20). doi: 10.1126/sciadv.abg4000.

Chung, I., Wright, J. J., *et al.* (2022) 'Cryo-EM structures define ubiquinone-10 binding to mitochondrial complex I and conformational transitions accompanying Q-site occupancy', *Nature Communications*, 13(1), pp. 1–13. doi: 10.1038/s41467-022-30506-1.

Chung, I., Grba, D. N., *et al.* (2022) 'Making the leap from structure to mechanism: are the open states of mammalian complex I identified by cryoEM resting states or catalytic intermediates?', *Current Opinion in Structural Biology*, 77, p. 102447. doi: 10.1016/j.sbi.2022.102447.

Cleland, W. (1959) 'Steady State Kinetics', 1st edition, The enzymes, Academic press

Cook, P. F. (1991) *Enzyme mechanism from isotope effects*. Crc Press.

Cornish Bowden, A. (1977) 'An automatic method for deriving steady state rate equations', *Biochemical Journal*, 165(1), pp. 55–59. doi: 10.1042/bj1650055.

Crofts, A. R. (2004) 'The Q-cycle - A Personal Perspective.', *Photosynthesis research*, 80(1–3), pp. 223–243. doi: 10.1023/B:PRES.0000030444.52579.10.

Cross, R. L. (2000) 'The rotary binding change mechanism of ATP synthases', *Biochimica et Biophysica Acta (BBA) - Bioenergetics*, 1458(2), pp. 270–275. doi: https://doi.org/10.1016/S0005-2728(00)00079-7.

Dementin, S. *et al.* (2004) 'A glutamate is the essential proton transfer gate during the catalytic cycle of the [NiFe] hydrogenase.', *The Journal of biological chemistry*, 279(11), pp. 10508–10513. doi: 10.1074/jbc.M312716200.

Dickson, V. K. *et al.* (2006) 'On the structure of the stator of the mitochondrial ATP synthase.', *The*

EMBO journal, 25(12), pp. 2911–2918. doi: 10.1038/sj.emboj.7601177.

Djafarzadeh, R. *et al.* (2000) 'Biophysical and structural characterization of proton-translocating NADH-dehydrogenase (complex I) from the strictly aerobic yeast Yarrowia lipolytica', *Biochimica et Biophysica Acta - Bioenergetics*, 1459(1), pp. 230–238. doi: 10.1016/S0005-2728(00)00154-7.

Dröse, S. *et al.* (2011) 'Functional dissection of the proton pumping modules of mitochondrial complex I', *PLoS Biology*, 9(8). doi: 10.1371/journal.pbio.1001128.

Dröse, S., Galkin, A. and Brandt, U. (2005) 'Proton pumping by complex I (NADH:ubiquinone oxidoreductase) from Yarrowia lipolytica reconstituted into proteoliposomes', *Biochimica et Biophysica Acta - Bioenergetics*, 1710(2–3), pp. 87–95. doi: 10.1016/j.bbabio.2005.10.001.

Dröse, S., Stepanova, A. and Galkin, A. (2016) 'Ischemic A/D transition of mitochondrial complex I and its role in ROS generation.', *Biochimica et biophysica acta*, 1857(7), pp. 946–957. doi: 10.1016/j.bbabio.2015.12.013.

Efremov, R. G. and Sazanov, L. A. (2011) 'Structure of the membrane domain of respiratory complex i', *Nature*, 476(7361), pp. 414–421. doi: 10.1038/nature10330.

Esser, C. *et al.* (2004) 'A Genome Phylogeny for Mitochondria Among α-Proteobacteria and a Predominantly Eubacterial Ancestry of Yeast Nuclear Genes', *Molecular Biology and Evolution*, 21(9), pp. 1643–1660. doi: 10.1093/molbev/msh160.

Euro, L. *et al.* (2008) 'Conserved lysine residues of the membrane subunit NuoM are involved in energy conversion by the proton-pumping NADH:ubiquinone oxidoreductase (Complex I)', *Biochimica et Biophysica Acta - Bioenergetics*, 1777(9), pp. 1166–1172. doi: 10.1016/j.bbabio.2008.06.001.

Fassone, E. and Rahman, S. (2012) 'Complex I deficiency: clinical features, biochemistry and molecular genetics.', *Journal of medical genetics*, 49(9), pp. 578–590. doi: 10.1136/jmedgenet-2012-101159.

Fearnley, I. M. and Walker, J. E. (1992) 'Conservation of sequences of subunits of mitochondrial complex I and their relationships with other proteins.', *Biochimica et biophysica acta*, 1140(2), pp. 105–134. doi: 10.1016/0005-2728(92)90001-i.

Fedor, J. G. *et al.* (2017) 'Correlating kinetic and structural data on ubiquinone binding and reduction by respiratory complex I', *Proceedings of the National Academy of Sciences of the United States of America*, 114(48), pp. 12737–12742. doi: 10.1073/pnas.1714074114.

Fedor, J. G. and Hirst, J. (2018) 'Mitochondrial Supercomplexes Do Not Enhance Catalysis by Quinone Channeling', *Cell Metabolism*, 28(3), pp. 525-531.e4. doi: 10.1016/j.cmet.2018.05.024.

Fernández-Agüera, M. C. *et al.* (2015) 'Oxygen Sensing by Arterial Chemoreceptors Depends on Mitochondrial Complex I Signaling.', *Cell metabolism*, 22(5), pp. 825–837. doi: 10.1016/j.cmet.2015.09.004.

Fiedorczuk, K. and Sazanov, L. A. (2018) 'Mammalian Mitochondrial Complex I Structure and Disease-Causing Mutations.', *Trends in cell biology*, 28(10), pp. 835–867. doi: 10.1016/j.tcb.2018.06.006.

Fontecilla-camps, J. C. *et al.* (2007) 'Structure / Function Relationships of [NiFe] - and [FeFe] - Hydrogenases'. Chemical Reviews 2007 107 (10), pp. 4273-4303 doi: 10.1021/cr050195z

Forcé, R. K. and Carr, J. D. (1974) 'Temperaure-Dependent Response of the Glass Electrode in Deuterium Oxide', *Analytical Chemistry*, 46(13), pp. 2049–2052. doi: 10.1021/ac60349a020.

Frey, T. G. and Mannella, C. A. (2000) 'The internal structure of mitochondria', *Trends in Biochemical*

Sciences, 25(7), pp. 319–324. doi: https://doi.org/10.1016/S0968-0004(00)01609-1.

Galkin, A. *et al.* (2008) 'Identification of the mitochondrial ND3 subunit as a structural component involved in the active/deactive enzyme transition of respiratory complex I.', *The Journal of biological chemistry*, 283(30), pp. 20907–20913. doi: 10.1074/jbc.M803190200.

Galkin, A. (2019) 'Brain Ischemia/Reperfusion Injury and Mitochondrial Complex I Damage.', *Biochemistry. Biokhimiia*, 84(11), pp. 1411–1423. doi: 10.1134/S0006297919110154.

Galkin, A. and Moncada, S. (2017) 'Modulation of the conformational state of mitochondrial complex I as a target for therapeutic intervention.', *Interface focus*, 7(2), p. 20160104. doi: 10.1098/rsfs.2016.0104.

Galkin, A. S., Grivennikova, V. G. and Vinogradov, A. D. (1999) '→H+/2ē stoichiometry in NADH-quinone reductase reactions catalyzed by bovine heart submitochondrial particles', *FEBS Letters*, 451(2), pp. 157–161. doi: 10.1016/S0014-5793(99)00575-X.

Gamiz-Hernandez, A. P. *et al.* (2017) 'Terminal Electron-Proton Transfer Dynamics in the Quinone Reduction of Respiratory Complex i', *Journal of the American Chemical Society*, 139(45), pp. 16282–16288. doi: 10.1021/jacs.7b08486.

de Gier, J. W. *et al.* (1994) 'The terminal oxidases of Paracoccus denitrificans.', *Molecular microbiology*, 13(2), pp. 183–196. doi: 10.1111/j.1365-2958.1994.tb00414.x.

Gledhill, J. R. *et al.* (2007) 'Mechanism of inhibition of bovine F1-ATPase by resveratrol and related polyphenols.', *Proceedings of the National Academy of Sciences of the United States of America*, 104(34), pp. 13632–13637. doi: 10.1073/pnas.0706290104.

Good, N. E. *et al.* (1966) 'Hydrogen Ion Buffers for Biological Research', (2), pp. 467–477. Biochemistry. 1966 Feb;5(2):467-77. doi: 10.1021/bi00866a011. PMID: 5942950.

Grba, D. N. and Hirst, J. (2020) 'Mitochondrial complex I structure reveals ordered water molecules for catalysis and proton translocation', *Nature Structural and Molecular Biology*, 27(10), pp. 892–900. doi: 10.1038/s41594-020-0473-x.

Grgic, L. *et al.* (2004) 'Functional significance of conserved histidines and arginines in the 49-kDa subunit of mitochondrial complex I', *Journal of Biological Chemistry*. doi: 10.1074/jbc.M313180200.

Grover, G. J. *et al.* (2004) 'Excessive ATP hydrolysis in ischemic myocardium by mitochondrial F1F0-ATPase: effect of selective pharmacological inhibition of mitochondrial ATPase hydrolase activity.', *American journal of physiology. Heart and circulatory physiology*, 287(4), pp. H1747-55. doi: 10.1152/ajpheart.01019.2003.

Gu, J. *et al.* (2022) 'The coupling mechanism of mammalian mitochondrial complex I', *Nature Structural and Molecular Biology*, 29(2), pp. 172–182. doi: 10.1038/s41594-022-00722-w.

Guo, R. *et al.* (2017) 'Architecture of Human Mitochondrial Respiratory Megacomplex I(2)III(2)IV(2).', *Cell*, 170(6), pp. 1247-1257.e12. doi: 10.1016/j.cell.2017.07.050.

Gutekunst, K. *et al.* (2018) 'In-vivo turnover frequency of the cyanobacterial NiFe-hydrogenase during photohydrogen production outperforms in-vitro systems.', *Scientific reports*, 8(1), p. 6083. doi: 10.1038/s41598-018-24430-y.

Gutiérrez-Fernández, J. *et al.* (2020) 'Key role of quinone in the mechanism of respiratory complex I', *Nature Communications*, 11(1), pp. 1–17. doi: 10.1038/s41467-020-17957-0.

Haapanen, O., Djurabekova, A. and Sharma, V. (2019) 'Role of second quinone binding site in proton pumping by respiratory complex I', *Frontiers in Chemistry*, 7(APR), pp. 1–14. doi: 10.3389/fchem.2019.00221.

Haapanen, O. and Sharma, V. (2017) 'Role of water and protein dynamics in proton pumping by respiratory complex I', *Scientific Reports*, 7(1), pp. 1–12. doi: 10.1038/s41598-017-07930-1.

Hanahan, D. (1983) 'Studies on transformation of Escherichia coli with plasmids.', *Journal of molecular biology*, 166(4), pp. 557–580. doi: 10.1016/s0022-2836(83)80284-8.

Hardy, R. C. and Cottington, R. L. (1949) 'Viscosity of deuterium oxide and water in the range 5 to 125 C', *Journal of Research of the National Bureau of Standards*, 42(6), p. 573. doi: 10.6028/jres.042.049.

Herzig, S. *et al.* (2012) 'Identification and functional expression of the mitochondrial pyruvate carrier.', *Science (New York, N.Y.)*, 337(6090), pp. 93–96. doi: 10.1126/science.1218530.

Hirst, J. *et al.* (2003) 'The nuclear encoded subunits of complex I from bovine heart mitochondria.', *Biochimica et biophysica acta*, 1604(3), pp. 135–150. doi: 10.1016/s0005-2728(03)00059-8.

Hirst, J. (2011) 'Why does mitochondrial complex I have so many subunits?', *The Biochemical journal*, 437(2), pp. e1-3. doi: 10.1042/BJ20110918.

Hirst, J. (2013) 'Mitochondrial complex i', *Annual Review of Biochemistry*, 82, pp. 551–575. doi: 10.1146/annurev-biochem-070511-103700.

Hirst, J. and Roessler, M. M. (2016) 'Energy conversion, redox catalysis and generation of reactive oxygen species by respiratory complex i', *Biochimica et Biophysica Acta - Bioenergetics*, 1857(7), pp. 872–883. doi: 10.1016/j.bbabio.2015.12.009.

Hoeser, F. *et al.* (2022) 'Respiratory complex I with charge symmetry in the membrane arm pumps protons', *Proceedings of the National Academy of Sciences of the United States of America*, 119(27), pp. 1–10. doi: 10.1073/pnas.2123090119.

Hoias Teixeira, M. and Menegon Arantes, G. (2019) 'Balanced internal hydration discriminates substrate binding to respiratory complex I', *Biochimica et Biophysica Acta - Bioenergetics*, 1860(7), pp. 541–548. doi: 10.1016/j.bbabio.2019.05.004.

Holmström, K. M. and Finkel, T. (2014) 'Cellular mechanisms and physiological consequences of redox-dependent signalling.', *Nature reviews. Molecular cell biology*, 15(6), pp. 411–421. doi: 10.1038/nrm3801.

Hu, S. *et al.* (2019) 'Comparative kinetic isotope effects on first- And second-order rate constants of soybean lipoxygenase variants uncover a substrate-binding network', *Journal of Biological Chemistry*, 294(48), pp. 18069–18076. doi: 10.1074/jbc.RA119.010826.

Huang, C. S., Kopacz, S. J. and Lee, C. P. (1983) 'Mechanistic differences in the energy-linked fluorescence decreases of 9-aminoacridine dyes associated with bovine heart submitochondrial membranes.', *Biochimica et biophysica acta*, 722(1), pp. 107–115. doi: 10.1016/0005-2728(83)90163-9.

Hyland, L. J., Tomaszek, T. A. J. and Meek, T. D. (1991) 'Human immunodeficiency virus-1 protease. 2. Use of pH rate studies and solvent kinetic isotope effects to elucidate details of chemical mechanism.', *Biochemistry*, 30(34), pp. 8454–8463. doi: 10.1021/bi00098a024.

Ino, T., Nishioka, T. and Miyoshi, H. (2003) 'Characterization of inhibitor binding sites of mitochondrial complex I using fluorescent inhibitor.', *Biochimica et biophysica acta*, 1605(1–3), pp. 15–20. doi: 10.1016/s0005-2728(03)00060-4.

Ito, M., Morino, M. and Krulwich, T. A. (2017) 'Mrp antiporters have important roles in diverse bacteria and archaea', *Frontiers in Microbiology*, 8(NOV), pp. 1–12. doi: 10.3389/fmicb.2017.02325.

Iverson, T. M. (2013) 'Catalytic mechanisms of complex II enzymes: A structural perspective', *Biochimica et Biophysica Acta (BBA) - Bioenergetics*, 1827(5), pp. 648–657. doi: https://doi.org/10.1016/j.bbabio.2012.09.008.

Iwata, S. *et al.* (1995) 'Structure at 2.8 A resolution of cytochrome c oxidase from Paracoccus denitrificans.', *Nature*, 376(6542), pp. 660–669. doi: 10.1038/376660a0.

Iwata, S. *et al.* (1998) 'Complete structure of the 11-subunit bovine mitochondrial cytochrome bc1 complex.', *Science (New York, N.Y.)*, 281(5373), pp. 64–71. doi: 10.1126/science.281.5373.64.

Jarman, O. (2022) 'Paracoccus denitrificans as a model system for studying the mechanism of respiratory complex I'. doi: 10.17863/CAM.85812.

Jarman, O. D. *et al.* (2021) 'Paracoccus denitrificans: a genetically tractable model system for studying respiratory complex I.', *Scientific reports*, 11(1), p. 10143. doi: 10.1038/s41598-021-89575-9.

Jarman, O. D. and Hirst, J. (2022) 'Membrane-domain mutations in respiratory complex I impede catalysis but do not uncouple proton pumping from ubiquinone reduction', *PNAS Nexus*, 1(5), pp. 1–12. doi: 10.1093/pnasnexus/pgac276.

Jarret, R. M. and Saunders, M. (1985) 'A new method for obtaining isotopic fractionation data at multiple sites in rapidly exchanging systems', *Journal of the American Chemical Society*, 107(9), pp. 2648–2654. doi: 10.1021/ja00295a017.

Jault, J. M. *et al.* (1995) 'The alpha 3 beta 3 gamma complex of the F1-ATPase from thermophilic Bacillus PS3 containing the alpha D261N substitution fails to dissociate inhibitory MgADP from a catalytic site when ATP binds to noncatalytic sites.', *Biochemistry*, 34(50), pp. 16412–16418. doi: 10.1021/bi00050a023.

Johnson, K. A. (2019) 'New standards for collecting and fitting steady state kinetic data', *Beilstein Journal of Organic Chemistry*, 15, pp. 16–29. doi: 10.3762/bjoc.15.2.

Jones, A. J. Y. *et al.* (2016) 'A Self-Assembled Respiratory Chain that Catalyzes NADH Oxidation by Ubiquinone-10 Cycling between ComplexI and the Alternative Oxidase', *Angewandte Chemie - International Edition*, 55(2), pp. 728–731. doi: 10.1002/anie.201507332.

Jones, A. J. Y. *et al.* (2017) 'Respiratory complex i in bos taurus and paracoccus denitrificans pumps four protons across the membrane for every NADH oxidized', *Journal of Biological Chemistry*, 292(12), pp. 4987–4995. doi: 10.1074/jbc.M116.771899.

Jumper, J. *et al.* (2021) 'Highly accurate protein structure prediction with AlphaFold', *Nature*, 596(7873), pp. 583–589. doi: 10.1038/s41586-021-03819-2.

Kaila, V. R. I. (2021) 'Resolving Chemical Dynamics in Biological Energy Conversion: Long-Range Proton-Coupled Electron Transfer in Respiratory Complex I', *Accounts of Chemical Research*, 54(24), pp. 4462–4473. doi: 10.1021/acs.accounts.1c00524.

Kamiya, K. *et al.* (2007) 'Possible mechanism of proton transfer through peptide groups in the H-pathway of the bovine cytochrome c oxidase.', *Journal of the American Chemical Society*, 129(31), pp. 9663–9673. doi: 10.1021/ja070464y.

Kampjut, D. and Sazanov, L. A. (2020a) 'The coupling mechanism of mammalian respiratory complex I', *Science*, 370(6516), pp. 1–35. doi: 10.1126/SCIENCE.ABC4209.

Kampjut, D. and Sazanov, L. A. (2020b) 'The coupling mechanism of mammalian respiratory complex I', *Science*, 370(6516). doi: 10.1126/SCIENCE.ABC4209.

Kampjut, D. and Sazanov, L. A. (2022) 'Structure of respiratory complex I – An emerging blueprint for the mechanism', *Current Opinion in Structural Biology*, 74, p. 102350. doi: 10.1016/j.sbi.2022.102350.

Kao, M. C. *et al.* (2005) 'Characterization of the membrane domain subunit NuoK (ND4L) of the NADH-quinone oxidoreductase from Escherichia coli', *Biochemistry*, 44(27), pp. 9545–9554. doi: 10.1021/bi050708w.

Kashani-Poor, N. *et al.* (2001) 'Efficient large scale purification of his-tagged proton translocating NADH:ubiquinone oxidoreductase (complex I) from the strictly aerobic yeast Yarrowia lipolytica', *Biochimica et Biophysica Acta - Bioenergetics*, 1504(2–3), pp. 363–370. doi: 10.1016/S0005-2728(00)00266-8.

Kato-Yamada, Y. *et al.* (1999) 'Epsilon subunit, an endogenous inhibitor of bacterial F(1)-ATPase, also inhibits F(0)F(1)-ATPase.', *The Journal of biological chemistry*, 274(48), pp. 33991–33994. doi: 10.1074/jbc.274.48.33991.

Kerscher, S. *et al.* (2002) 'Yarrowia lipolytica, a yeast genetic system to study mitochondrial complex I', *Biochimica et Biophysica Acta - Bioenergetics*, 1555(1–3), pp. 83–91. doi: 10.1016/S0005-2728(02)00259-1.

Kerscher, S. J. (2000) 'Diversity and origin of alternative NADH:ubiquinone oxidoreductases', *Biochimica et Biophysica Acta - Bioenergetics*, 1459(2–3), pp. 274–283. doi: 10.1016/S0005-2728(00)00162-6.

Kessler, R. J. and Fanestil, D. D. (1986) 'Interference by lipids in the determination of protein using bicinchoninic acid', *Analytical Biochemistry*, 159(1), pp. 138–142. doi: 10.1016/0003-2697(86)90318-0.

Kim, H. J. *et al.* (2012) 'Structure, function, and assembly of heme centers in mitochondrial respiratory complexes.', *Biochimica et biophysica acta*, 1823(9), pp. 1604–1616. doi: 10.1016/j.bbamcr.2012.04.008.

King, B. E. L. *et al.* (1956) 'Deriving the rate laws for enzyme- catalyzed reactions', *J Am Chemical Society*. 60 (10), 1375-1378. doi: 10.1021/j150544a010

Klusch, N. *et al.* (2021) 'A ferredoxin bridge connects the two arms of plant mitochondrial complex I.', *The Plant cell*, 33(6), pp. 2072–2091. doi: 10.1093/plcell/koab092.

Kohen, A. and Limbach, H.-H. (2005) *Isotope effects in chemistry and biology*. cRc Press.

Kolata, P. and Efremov, R. G. (2021) 'Structure of escherichia coli respiratory complex i reconstituted into lipid nanodiscs reveals an uncoupled conformation', *eLife*, 10, pp. 1–32. doi: 10.7554/eLife.68710.

Konstantinov, A. A. *et al.* (1997) 'The roles of the two proton input channels in cytochrome c oxidase from Rhodobacter sphaeroides probed by the effects of site-directed mutations on time-resolved electrogenic intraprotein proton transfer.', *Proceedings of the National Academy of Sciences of the United States of America*, 94(17), pp. 9085–9090. doi: 10.1073/pnas.94.17.9085.

Kotlyar, A. B., Albracht, S. P. J. and van Spanning, R. J. M. (1998) 'Comparison of energization of complex I in membrane particles from Paracoccus denitrificans and bovine heart mitochondria', *Biochimica et Biophysica Acta (BBA) - Bioenergetics*, 1365(1), pp. 53–59. doi: https://doi.org/10.1016/S0005-2728(98)00042-5.

Kotlyar, A. B. and Vinogradov, A. D. (1990) 'Slow active/inactive transition of the mitochondrial

NADH-ubiquinone reductase.', *Biochimica et biophysica acta*, 1019(2), pp. 151–158. doi: 10.1016/0005-2728(90)90137-s.

Kraut, J. (1977) 'Serine proteases: structure and mechanism of catalysis.', *Annual review of biochemistry*, 46, pp. 331–358. doi: 10.1146/annurev.bi.46.070177.001555.

Kravchuk, V. *et al.* (2022) 'A universal coupling mechanism of respiratory complex I', *Nature*, 609(7928), pp. 808–814. doi: 10.1038/s41586-022-05199-7.

Kreevoy, M. M. and Liang, T. M. (1980) 'Structures and Isotopic Fractionation Factors of Complexes, A1HA2-', *Journal of the American Chemical Society*, 102(10), pp. 3315–3322. doi: 10.1021/ja00530a002.

Kühlbrandt, W. (2015) 'Structure and function of mitochondrial membrane protein complexes', *BMC Biology*, 13(1), p. 89. doi: 10.1186/s12915-015-0201-x.

Kühlbrandt, W. (2019) 'Structure and Mechanisms of F-Type ATP Synthases.', *Annual review of biochemistry*, 88, pp. 515–549. doi: 10.1146/annurev-biochem-013118-110903.

Kunji, E. R. S. (2004) 'The role and structure of mitochondrial carriers', *FEBS Letters*, 564(3), pp. 239–244. doi: 10.1016/S0014-5793(04)00242-X.

Kussmaul, L. and Hirst, J. (2006) 'The mechanism of superoxide production by NADH:ubiquinone oxidoreductase (complex I) from bovine heart mitochondria', *Proceedings of the National Academy of Sciences of the United States of America*, 103(20), pp. 7607–7612. doi: 10.1073/pnas.0510977103.

Kuzmic, P. (1996) 'Program DYNAFIT for the analysis of enzyme kinetic data: application to HIV proteinase.', *Analytical biochemistry*, 237(2), pp. 260–273. doi: 10.1006/abio.1996.0238.

Labute, P. (2009) 'Protonate3D: Assignment of ionization states and hydrogen coordinates to macromolecular structures', *Proteins: Structure, Function and Bioinformatics*, 75(1), pp. 187–205. doi: 10.1002/prot.22234.

Laemmli, U. K. (1970) 'Cleavage of structural proteins during the assembly of the head of bacteriophage T4.', *Nature*, 227(5259), pp. 680–685. doi: 10.1038/227680a0.

Laidler, K. J. and King, M. C. (1983) 'Development of transition-state theory', *The Journal of Physical Chemistry*, 87(15), pp. 2657–2664. doi: 10.1021/j100238a002.

Lasham, J. *et al.* (2023) 'Tunnel dynamics of quinone derivatives and its coupling to protein conformational rearrangements in respiratory complex I', *Biochimica et Biophysica Acta - Bioenergetics*, 1864(2), p. 148951. doi: 10.1016/j.bbabio.2022.148951.

Lee, S. *et al.* (2011) 'Mitochondrial H2O2 generated from electron transport chain complex I stimulates muscle differentiation.', *Cell research*, 21(5), pp. 817–834. doi: 10.1038/cr.2011.55.

Lee, Y. *et al.* (2022) 'Ion transfer mechanisms in Mrp-type antiporters from high resolution cryoEM and molecular dynamics simulations', *Nature communications*, 13(1), p. 6091. doi: 10.1038/s41467-022-33640-y.

Letts, J. A., Fiedorczuk, K. and Sazanov, L. A. (2016) 'The architecture of respiratory supercomplexes.', *Nature*, 537(7622), pp. 644–648. doi: 10.1038/nature19774.

Lin, P.-C., Puhar, A. and Steuber, J. (2008) 'NADH oxidation drives respiratory Na+ transport in mitochondria from Yarrowia lipolytica.', *Archives of microbiology*, 190(4), pp. 471–480. doi: 10.1007/s00203-008-0395-1.

Di Luca, A. *et al.* (2018) 'How inter-subunit contacts in the membrane domain of complex I affect

proton transfer energetics', *Biochimica et Biophysica Acta - Bioenergetics*, 1859(9), pp. 734–741. doi: 10.1016/j.bbabio.2018.06.001.

Di Luca, A., Gamiz-Hernandez, A. P. and Kaila, V. R. I. (2017) 'Symmetry-related proton transfer pathways in respiratory complex I', *Proceedings of the National Academy of Sciences of the United States of America*, 114(31), pp. E6314–E6321. doi: 10.1073/pnas.1706278114.

LURIA, S. E., ADAMS, J. N. and TING, R. C. (1960) 'Transduction of lactose-utilizing ability among strains of E. coli and S. dysenteriae and the properties of the transducing phage particles.', *Virology*, 12, pp. 348–390. doi: 10.1016/0042-6822(60)90161-6.

Magnitsky, S. *et al.* (2002) 'EPR characterization of ubisemiquinones and iron-sulfur cluster N2, central components of the energy coupling in the NADH-ubiquinone oxidoreductase (complex I) in situ.', *Journal of bioenergetics and biomembranes*, 34(3), pp. 193–208. doi: 10.1023/a:1016083419979.

Maldonado, M. *et al.* (2020) 'Atomic structure of a mitochondrial complex I intermediate from vascular plants', *eLife*. Edited by D. M. Kramer et al., 9, p. e56664. doi: 10.7554/eLife.56664.

Mannella, C. A. (1992) 'The "ins" and "outs" of mitochondrial membrane channels.', *Trends in biochemical sciences*, 17(8), pp. 315–320. doi: 10.1016/0968-0004(92)90444-e.

Mannella, C. A. (2006) 'The relevance of mitochondrial membrane topology to mitochondrial function.', *Biochimica et biophysica acta*, 1762(2), pp. 140–147. doi: 10.1016/j.bbadis.2005.07.001.

Mannella, C. A., Lederer, W. J. and Jafri, M. S. (2013) 'The connection between inner membrane topology and mitochondrial function.', *Journal of molecular and cellular cardiology*, 62, pp. 51–57. doi: 10.1016/j.yjmcc.2013.05.001.

Margulis, L. (1970) 'Origin of eukaryotic cells: evidence and research implications for a theory of the origin and evolution of microbial, plant, and animal cells on the Precambrian earth', *New Haven, Yale University Press.*

Marino, P. (2018) 'Studies on assembly and genetic variation of mitochondrial respiratory complex I', https://doi.org/10.17863/CAM.36634

Martin S King (2010) 'Structural and functional studies of mitochondrial complex I', *Thesis*, pp. 1–292. Available at: papers2://publication/uuid/C82D0FC9-84EB-4504-B252-1FDB6963C7A9.

Matsushita, K., Ohnishi, T. and Kaback, H. R. (1987) 'NADH-Ubiquinone Oxidoreductases of the Escherichia coli Aerobic Respiratory Chain', *Biochemistry*, 26(24), pp. 7732–7737. doi: 10.1021/bi00398a029.

Mazat, J.-P., Devin, A. and Ransac, S. (2020) 'Modelling mitochondrial ROS production by the respiratory chain.', *Cellular and molecular life sciences : CMLS*, 77(3), pp. 455–465. doi: 10.1007/s00018-019-03381-1.

Milenkovic, D. *et al.* (2017) 'The Enigma of the Respiratory Chain Supercomplex.', *Cell metabolism*, 25(4), pp. 765–776. doi: 10.1016/j.cmet.2017.03.009.

Mileykovskaya, E. and Dowhan, W. (2009) 'Cardiolipin membrane domains in prokaryotes and eukaryotes.', *Biochimica et biophysica acta*, 1788(10), pp. 2084–2091. doi: 10.1016/j.bbamem.2009.04.003.

Milgrom, Y. M. and Cross, R. L. (1993) 'Nucleotide binding sites on beef heart mitochondrial F1-ATPase. Cooperative interactions between sites and specificity of noncatalytic sites.', *The Journal of biological chemistry*, 268(31), pp. 23179–23185.

Mimaki, M. *et al.* (2012) 'Understanding mitochondrial complex I assembly in health and disease.', *Biochimica et biophysica acta*, 1817(6), pp. 851–862. doi: 10.1016/j.bbabio.2011.08.010.

Morales-Rios, E. *et al.* (2015) 'Structure of ATP synthase from Paracoccus denitrificans determined by X-ray crystallography at 4.0 Å resolution.', *Proceedings of the National Academy of Sciences of the United States of America*, 112(43), pp. 13231–13236. doi: 10.1073/pnas.1517542112.

Morino, M. *et al.* (2010) 'Single site mutations in the hetero-oligomeric Mrp antiporter from alkaliphilic Bacillus pseudofirmus OF4 that affect Na+/H+ antiport activity, sodium exclusion, individual Mrp protein levels, or Mrp complex formation', *Journal of Biological Chemistry*, 285(40), pp. 30942–30950. doi: 10.1074/jbc.M110.118661.

Moser, C. C. *et al.* (2006) 'Electron tunneling chains of mitochondria', *Biochimica et Biophysica Acta (BBA) - Bioenergetics*, 1757(9), pp. 1096–1109. doi: https://doi.org/10.1016/j.bbabio.2006.04.015.

Mühlbauer, M. E. *et al.* (2020) 'Water-Gated Proton Transfer Dynamics in Respiratory Complex i', *Journal of the American Chemical Society*, 142(32), pp. 13718–13728. doi: 10.1021/jacs.0c02789.

Nakamaru-Ogiso, E. *et al.* (2010) 'The membrane subunit NuoL(ND5) is involved in the indirect proton pumping mechanism of Escherichia coli complex I', *Journal of Biological Chemistry*, 285(50), pp. 39070–39078. doi: 10.1074/jbc.M110.157826.

Narayanan, M. *et al.* (2015) 'Semiquinone intermediates are involved in the energy coupling mechanism of E. coli complex I.', *Biochimica et biophysica acta*, 1847(8), pp. 681–689. doi: 10.1016/j.bbabio.2015.04.004.

Niatsetskaya, Z. V *et al.* (2012) 'The oxygen free radicals originating from mitochondrial complex I contribute to oxidative brain injury following hypoxia-ischemia in neonatal mice.', *The Journal of neuroscience : the official journal of the Society for Neuroscience*, 32(9), pp. 3235–3244. doi: 10.1523/JNEUROSCI.6303-11.2012.

Nicholls, D. G. (2013) *Bioenergetics*. Academic press. pp. 1-419. doi: 10.1016/C2010-0-64902-9

Nihei, C. *et al.* (2003) 'Purification of active recombinant trypanosome alternative oxidase', *FEBS Letters*, 538(1–3), pp. 35–40. doi: 10.1016/S0014-5793(03)00120-0.

Northrop, D. B. (1975) 'Steady-State Analysis of Kinetic Isotope Effects in Enzymic Reactions', *Biochemistry*, 14(12), pp. 2644–2651. doi: 10.1021/bi00683a013.

Northrop, D. B. (1998) 'On the meaning of Km and V/K in enzyme kinetics', *Journal of Chemical Education*, 75(9), pp. 1153–1157. doi: 10.1021/ed075p1153.

Nuber, F. *et al.* (2021) 'A Quinol Anion as Catalytic Intermediate Coupling Proton Translocation With Electron Transfer in E. coli Respiratory Complex I', *Frontiers in Chemistry*, 9(May), pp. 1–11. doi: 10.3389/fchem.2021.672969.

Ogata, H. *et al.* (2005) 'Activation process of [NiFe] hydrogenase elucidated by high-resolution X-ray analyses: conversion of the ready to the unready state.', *Structure (London, England : 1993)*, 13(11), pp. 1635–1642. doi: 10.1016/j.str.2005.07.018.

Olsson, M. H. M. *et al.* (2011) 'PROPKA3: Consistent treatment of internal and surface residues in empirical p K a predictions', *Journal of Chemical Theory and Computation*, 7(2), pp. 525–537. doi: 10.1021/ct100578z.

Oyedotun, K. S., Sit, C. S. and Lemire, B. D. (2007) 'The Saccharomyces cerevisiae succinate dehydrogenase does not require heme for ubiquinone reduction.', *Biochimica et biophysica acta*, 1767(12), pp. 1436–1445. doi: 10.1016/j.bbabio.2007.09.008.

Padavannil, A. *et al.* (2021) 'The Mysterious Multitude: Structural Perspective on the Accessory Subunits of Respiratory Complex I.', *Frontiers in molecular biosciences*, 8, p. 798353. doi: 10.3389/fmolb.2021.798353.

Page, C. C. *et al.* (1999) 'Natural engineering principles of electron tunnelling in biological oxidation-reduction.', *Nature*, 402(6757), pp. 47–52. doi: 10.1038/46972.

Parey, K. *et al.* (2021) 'High-resolution structure and dynamics of mitochondrial complex I-Insights into the proton pumping mechanism', *Science Advances*, 7(46), pp. 1–13. doi: 10.1126/sciadv.abj3221.

Peter Mitchell (1961) 'Coupling of Phosphorylation to Electron and Hydrogen Transfer by a Chemi-Osmotic type of Mechanism', *Nature*, 191, pp. 144–148.

Pfitzner, U. *et al.* (2000) 'Tracing the D-pathway in reconstituted site-directed mutants of cytochrome c oxidase from Paracoccus denitrificans.', *Biochemistry*, 39(23), pp. 6756–6762. doi: 10.1021/bi992235x.

Plesner, I. W. (1986) 'The apparent Km is a misleading kinetic indicator.', *The Biochemical journal*, 239(1), pp. 175–178. doi: 10.1042/bj2390175.

Powell, S. G. and Batt, R. J. (2008) 'Appendix A: Guide to Solver', *Modeling for Insight*, pp. 445–450. doi: 10.1002/9780470387207.app1.

Pryde, K. R. and Hirst, J. (2011) 'Superoxide is produced by the reduced flavin in mitochondrial complex I: A single, unified mechanism that applies during both forward and reverse electron transfer', *Journal of Biological Chemistry*, 286(20), pp. 18056–18065. doi: 10.1074/jbc.M110.186841.

Pudney, C. R. *et al.* (2013) 'Enzymatic single-molecule kinetic isotope effects.', *Journal of the American Chemical Society*, 135(10), pp. 3855–3864. doi: 10.1021/ja309286r.

Quinn, D. M. (1987) 'Acetylcholinesterase: Structure', pp. 955–979. Chemical Reviews 1987 87 (5), 955-979 doi: 10.1021/cr00081a005

Quinn, D. M. and Sutton, L. D. (1991) *Theoretical basis and mechanistic utility of solvent isotope effects*. CRC Press Boca Raton, FL.

Reactions, E., Fernandez, P. L. and Murkin, A. S. (2020) 'Inverse Solvent Isotope E ff ects in Enzyme-Catalyzed Reactions', Molecules. 2020 Apr 21;25(8):1933. doi: 10.3390/molecules25081933. PMID: 32326332; PMCID: PMC7221790.

Rich, P. R. and Maréchal, A. (2013) 'Functions of the hydrophilic channels in protonmotive cytochrome c oxidase.', *Journal of the Royal Society, Interface*, 10(86), p. 20130183. doi: 10.1098/rsif.2013.0183.

Robb, E. L. *et al.* (2018) 'Control of mitochondrial superoxide production by reverse electron transport at complex I.', *The Journal of biological chemistry*, 293(25), pp. 9869–9879. doi: 10.1074/jbc.RA118.003647.

Röpke, M. *et al.* (2020) 'Functional Water Wires Catalyze Long-Range Proton Pumping in the Mammalian Respiratory Complex i', *Journal of the American Chemical Society*, 142(52), pp. 21758–21766. doi: 10.1021/jacs.0c09209.

Ruprecht, J. J. and Kunji, E. R. S. (2020) 'The SLC25 Mitochondrial Carrier Family: Structure and Mechanism.', *Trends in biochemical sciences*, 45(3), pp. 244–258. doi: 10.1016/j.tibs.2019.11.001.

Sabar, M., Balk, J. and Leaver, C. J. (2005) 'Histochemical staining and quantification of plant mitochondrial respiratory chain complexes using blue-native polyacrylamide gel electrophoresis', *Plant Journal*, 44(5), pp. 893–901. doi: 10.1111/j.1365-313X.2005.02577.x.

Salna, B. *et al.* (2016) 'Wide-dynamic-range kinetic investigations of deep proton tunnelling in proteins', *Nature Chemistry*, 8(9), pp. 874–880. doi: 10.1038/nchem.2527.

Sarewicz, M. *et al.* (2021) 'Catalytic Reactions and Energy Conservation in the Cytochrome bc(1) and b(6)f Complexes of Energy-Transducing Membranes.', *Chemical reviews*, 121(4), pp. 2020–2108. doi: 10.1021/acs.chemrev.0c00712.

Sato, M. *et al.* (2013) 'Energy transducing roles of antiporter-like subunits in Escherichia coli NDH-1 with main focus on subunit NuoN (ND2)', *Journal of Biological Chemistry*, 288(34), pp. 24705–24716. doi: 10.1074/jbc.M113.482968.

Sazanov, L. A. (2023) 'From the "black box'' to 'domino effect'' mechanism: what have we learned from the structures of respiratory complex I'"', *Biochemical Journal*, 480(5), pp. 319–333. doi: 10.1042/bcj20210285.

Sazanov, L. A. and Hinchliffe, P. (2006) 'Structure of the hydrophilic domain of respiratory complex I from Thermus thermophilus.', *Science (New York, N.Y.)*, 311(5766), pp. 1430–1436. doi: 10.1126/science.1123809.

Schägger, H. and von Jagow, G. (1991) 'Blue native electrophoresis for isolation of membrane protein complexes in enzymatically active form.', *Analytical biochemistry*, 199(2), pp. 223–231. doi: 10.1016/0003-2697(91)90094-a.

Schimpf, J. *et al.* (2022) 'Structure of the peripheral arm of a minimalistic respiratory complex I.', *Structure (London, England : 1993)*, 30(1), pp. 80-94.e4. doi: 10.1016/j.str.2021.09.005.

Screpanti, E. and Hunte, C. (2007) 'Discontinuous membrane helices in transport proteins and their correlation with function', *Journal of Structural Biology*, 159(2 SPEC. ISS.), pp. 261–267. doi: 10.1016/j.jsb.2007.01.011.

Sharma, V. *et al.* (2015) 'Redox-induced activation of the proton pump in the respiratory complex i', *Proceedings of the National Academy of Sciences of the United States of America*, 112(37), pp. 11571–11576. doi: 10.1073/pnas.1503761112.

Sheely, M. L. (1932) 'Glycerol Viscosity Tables', *Industrial and Engineering Chemistry*, 24(9), pp. 1060–1064. doi: 10.1021/ie50273a022.

Shimokata, K. *et al.* (2007) 'The proton pumping pathway of bovine heart cytochrome *c* oxidase', *Proceedings of the National Academy of Sciences*, 104(10), pp. 4200–4205. doi: 10.1073/pnas.0611627104.

Sims, P. A. (2009) 'An "aufbau" approach to understanding how the King-Altman method of deriving rate equations for enzyme-catalyzed reactions works', *Journal of Chemical Education*, 86(3), pp. 385–389. doi: 10.1021/ed086p385.

Smith, A. L. (1967) '[13] Preparation, properties, and conditions for assay of mitochondria: Slaughterhouse material, small-scale', in *Oxidation and Phosphorylation*. Academic Press (Methods in Enzymology), pp. 81–86. doi: https://doi.org/10.1016/0076-6879(67)10016-5.

Smith, P. K. *et al.* (1985) 'Measurement of protein using bicinchoninic acid.', *Analytical biochemistry*, 150(1), pp. 76–85. doi: 10.1016/0003-2697(85)90442-7.

Søndergaard, C. R. *et al.* (2011) 'Improved treatment of ligands and coupling effects in empirical calculation and rationalization of p K a values', *Journal of Chemical Theory and Computation*, 7(7), pp. 2284–2295. doi: 10.1021/ct200133y.

Soufari, H. *et al.* (2020) 'Specific features and assembly of the plant mitochondrial complex I revealed by cryo-EM.', *Nature communications*, 11(1), p. 5195. doi: 10.1038/s41467-020-18814-w.

Van Spanning, R. J. M. *et al.* (1995) 'Regulation of oxidative phosphorylation: The flexible respiratory network ofParacoccus denitrificans', *Journal of Bioenergetics and Biomembranes*, 27(5), pp. 499–512. doi: 10.1007/BF02110190.

Spiess, A. N. and Neumeyer, N. (2010) 'An evaluation of R2as an inadequate measure for nonlinear models in pharmacological and biochemical research: A Monte Carlo approach', *BMC Pharmacology*, 10, pp. 1–11. doi: 10.1186/1471-2210-10-6.

Spikes, T. E., Montgomery, M. G. and Walker, J. E. (2020) 'Structure of the dimeric ATP synthase from bovine mitochondria', *Proceedings of the National Academy of Sciences*, 117(38), pp. 23519–23526. doi: 10.1073/pnas.2013998117.

Steimle, S. *et al.* (2012) 'Asp563 of the horizontal helix of subunit NuoL is involved in proton translocation by the respiratory complex I.', *FEBS letters*, 586(6), pp. 699–704. doi: 10.1016/j.febslet.2012.01.056.

Steiner, J. and Sazanov, L. (2020) 'Structure and mechanism of the MRP complex, an ancient cation/proton antiporter', *eLife*, 9, pp. 1–42. doi: 10.7554/eLife.59407.

Stroh, A. *et al.* (2004) 'Assembly of respiratory complexes I, III, and IV into NADH oxidase supercomplex stabilizes complex I in Paracoccus denitrificans.', *The Journal of biological chemistry*, 279(6), pp. 5000–5007. doi: 10.1074/jbc.M309505200.

Sugo, Y. and Ishikita, H. (2023) 'Mechanism of Asparagine-Mediated Proton Transfer in Photosynthetic Reaction Centers', *Biochemistry*, 62(10), pp. 1544–1552. doi: 10.1021/acs.biochem.3c00013.

Sun, F. *et al.* (2005) 'Crystal structure of mitochondrial respiratory membrane protein Complex II', *Cell*, 121(7), pp. 1043–1057. doi: 10.1016/j.cell.2005.05.025.

Symersky, J. *et al.* (2012) 'Structure of the c(10) ring of the yeast mitochondrial ATP synthase in the open conformation.', *Nature structural & molecular biology*, 19(5), pp. 485–91, S1. doi: 10.1038/nsmb.2284.

Szori-Dorogházi, E. *et al.* (2012) 'Analyses of the large subunit histidine-rich motif expose an alternative proton transfer pathway in [NiFe] hydrogenases.', *PloS one*, 7(4). doi: 10.1371/journal.pone.0034666.

Taanman, J. W. (1999) 'The mitochondrial genome: structure, transcription, translation and replication.', *Biochimica et biophysica acta*, 1410(2), pp. 103–123. doi: 10.1016/s0005-2728(98)00161-3.

Tocilescu, M. A., Zickermann, V., *et al.* (2010) 'Quinone binding and reduction by respiratory complex I', *Biochimica et Biophysica Acta - Bioenergetics*, 1797(12), pp. 1883–1890. doi: 10.1016/j.bbabio.2010.05.009.

Tocilescu, M. A., Fendel, U., *et al.* (2010) 'The role of a conserved tyrosine in the 49-kDa subunit of complex I for ubiquinone binding and reduction', *Biochimica et Biophysica Acta - Bioenergetics*, 1797(6–7), pp. 625–632. doi: 10.1016/j.bbabio.2010.01.029.

Torres-Bacete, J. *et al.* (2007) 'Characterization of the NuoM (ND4) subunit in Escherichia coli NDH-1: Conserved charged residues essential for energy-coupled activities', *Journal of Biological Chemistry*, 282(51), pp. 36914–36922. doi: 10.1074/jbc.M707855200.

Torres-Bacete, J. *et al.* (2009) 'Features of subunit NuoM (ND4) in Escherichia coli NDH-1. Topology and implication of conserved GLU144 for coupling site 1', *Journal of Biological Chemistry*, 284(48), pp. 33062–33069. doi: 10.1074/jbc.M109.059154.

Uno, S. *et al.* (2020) 'Oversized ubiquinones as molecular probes for structural dynamics of the ubiquinone reaction site in mitochondrial respiratory complex I', *Journal of Biological Chemistry*, 295(8), pp. 2449–2463. doi: https://doi.org/10.1074/jbc.RA119.012347.

Varghese, F. *et al.* (2015) 'Characterization of clinically identified mutations in NDUFV1, the flavin-binding subunit of respiratory complex I, using a yeast model system', *Human Molecular Genetics*, 24(22), pp. 6350–6360. doi: 10.1093/hmg/ddv344.

Venkatasubban, K. S. and Schowen, Richard L (1984) 'The Proton Inventory Technique', *Critical Reviews in Biochemistry*, 17(1), pp. 1–44. doi: 10.3109/10409238409110268. PMID: 6094099.

Venkatasubban, K. S. and Schowen, R L (1984) 'The proton inventory technique.', *CRC critical reviews in biochemistry*, 17(1), pp. 1–44. doi: 10.3109/10409238409110268.

Verkhovskaya, M. L. *et al.* (2008) 'Real-time electron transfer in respiratory complex I', *Proceedings of the National Academy of Sciences of the United States of America*, 105(10), pp. 3763–3767. doi: 10.1073/pnas.0711249105.

Verkhovskaya, M. and Wikström, M. (2014) 'Oxidoreduction properties of bound ubiquinone in Complex i from Escherichia coli', *Biochimica et Biophysica Acta - Bioenergetics*, 1837(2), pp. 246–250. doi: 10.1016/j.bbabio.2013.11.001.

Verkhovsky, M., Bloch, D. A. and Verkhovskaya, M. (2012) 'Tightly-bound ubiquinone in the Escherichia coli respiratory complex I.', *Biochimica et biophysica acta*, 1817(9), pp. 1550–1556. doi: 10.1016/j.bbabio.2012.04.013.

Vinogradov, A. D. (1998) 'Catalytic properties of the mitochondrial NADH-ubiquinone oxidoreductase (complex I) and the pseudo-reversible active/inactive enzyme transition.', *Biochimica et biophysica acta*, 1364(2), pp. 169–185. doi: 10.1016/s0005-2728(98)00026-7.

de Vries, G. E. *et al.* (1989) 'Isolation and characterization of Paracoccus denitrificans mutants with increased conjugation frequencies and pleiotropic loss of a (nGATCn) DNA-modifying property', *Archives of Microbiology*, 152(1), pp. 52–57. doi: 10.1007/BF00447011.

De Vries, S. *et al.* (2015) 'Electron tunneling rates in respiratory complex I are tuned for efficient energy conversion', *Angewandte Chemie - International Edition*, 54(9), pp. 2844–2848. doi: 10.1002/anie.201410967.

Walker, J. E. (2013) 'The ATP synthase: the understood, the uncertain and the unknown.', *Biochemical Society transactions*, 41(1), pp. 1–16. doi: 10.1042/BST20110773.

Walker, J. E., Skehel, J. M. and Buchanan, S. K. (1995) 'Structural analysis of NADH: ubiquinone oxidoreductase from bovine heart mitochondria.', *Methods in enzymology*, 260, pp. 14–34. doi: 10.1016/0076-6879(95)60127-9.

Warnau, J. *et al.* (2018) 'Redox-coupled quinone dynamics in the respiratory complex I', *Proceedings of the National Academy of Sciences of the United States of America*, 115(36), pp. E8413–E8420. doi: 10.1073/pnas.1805468115.

Watt, I. N. *et al.* (2010) 'Bioenergetic cost of making an adenosine triphosphate molecule in animal mitochondria.', *Proceedings of the National Academy of Sciences of the United States of America*, 107(39), pp. 16823–16827. doi: 10.1073/pnas.1011099107.

Weiss, H. *et al.* (1991) 'The respiratory-chain NADH dehydrogenase (complex I) of mitochondria.', *European journal of biochemistry*, 197(3), pp. 563–576. doi: 10.1111/j.1432-1033.1991.tb15945.x.

Wikström, M. and Verkhovsky, M. I. (2006) 'Towards the mechanism of proton pumping by the haem-copper oxidases.', *Biochimica et biophysica acta*, 1757(8), pp. 1047–1051. doi: 10.1016/j.bbabio.2006.01.010.

Wright, J. J. *et al.* (2020) 'Using a chimeric respiratory chain and EPR spectroscopy to determine the origin of semiquinone species previously assigned to mitochondrial complex i', *BMC Biology*, 18(1), pp. 1–13. doi: 10.1186/s12915-020-00768-6.

Wright, J. J. *et al.* (2022) 'Reverse Electron Transfer by Respiratory Complex I Catalyzed in a Modular Proteoliposome System', *Journal of the American Chemical Society*, 144(15), pp. 6791–6801. doi: 10.1021/jacs.2c00274.

Xia, D. *et al.* (2013) 'Structural analysis of cytochrome bc1 complexes: implications to the mechanism of function.', *Biochimica et biophysica acta*, 1827(11–12), pp. 1278–1294. doi: 10.1016/j.bbabio.2012.11.008.

Xu, F. (2021) 'Comparison of the Kinetic Parameters of Alternative Oxidases From Trypanosoma brucei and Arabidopsis thaliana—A Tale of Two Cavities', *Frontiers in Plant Science*, 12(October). doi: 10.3389/fpls.2021.744218.

Yagi, T. *et al.* (1998) 'Procaryotic complex I (NDH-1), an overview.', *Biochimica et biophysica acta*, 1364(2), pp. 125–133. doi: 10.1016/s0005-2728(98)00023-1.

Yakovlev, G. and Hirst, J. (2007) 'Transhydrogenation reactions catalyzed by mitochondrial NADH-ubiquinone oxidoreductase (complex I)', *Biochemistry*, 46(49), pp. 14250–14258. doi: 10.1021/bi7017915.

Yano, H. *et al.* (2005) 'Distinct functional units of the Golgi complex in Drosophila cells.', *Proceedings of the National Academy of Sciences of the United States of America*, 102(38), pp. 13467–13472. doi: 10.1073/pnas.0506681102.

Yin, Z. *et al.* (2021) 'Structural basis for a complex I mutation that blocks pathological ROS production', *Nature Communications*, 12(1), pp. 1–12. doi: 10.1038/s41467-021-20942-w.

Yip, C. *et al.* (2011) 'Evolution of respiratory complex I: "supernumerary" subunits are present in the alpha-proteobacterial enzyme.', *The Journal of biological chemistry*, 286(7), pp. 5023–5033. doi: 10.1074/jbc.M110.194993.

Yoga, E. G. *et al.* (2020) 'Essential role of accessory subunit LYRM6 in the mechanism of mitochondrial complex I', *Nature Communications*, pp. 1–8. doi: 10.1038/s41467-020-19778-7.

Yoon, S. and Harris, M. E. (2021) 'Beyond the Plateau: PL Dependence of Proton Inventories as a Tool for Studying Ribozyme and Ribonuclease Catalysis', *Biochemistry*, 60(37), pp. 2810–2823. doi: 10.1021/acs.biochem.1c00489.

Yu, C.-A. *et al.* (2008) 'Domain conformational switch of the iron-sulfur protein in cytochrome bc1 complex is induced by the electron transfer from cytochrome bL to bH.', *Biochimica et biophysica acta*, 1777(7–8), pp. 1038–1043. doi: 10.1016/j.bbabio.2008.03.033.

Yu, H. *et al.* (2018) 'Structure of an Ancient Respiratory System', *Cell*, 173(7), pp. 1636-1649.e16. doi: 10.1016/j.cell.2018.03.071.

Yu, H. *et al.* (2020) 'Structure of the respiratory MBS complex reveals iron-sulfur cluster catalyzed sulfane sulfur reduction in ancient life', *Nature Communications*, 11(1), pp. 1–13. doi: 10.1038/s41467-020-19697-7.

Zeth, K. and Thein, M. (2010) 'Porins in prokaryotes and eukaryotes: common themes and variations.', *The Biochemical journal*, 431(1), pp. 13–22. doi: 10.1042/BJ20100371.

Zhou, L. *et al.* (2022) 'Structures of Tetrahymena's respiratory chain reveal the diversity of eukaryotic core metabolism.', *Science (New York, N.Y.)*, 376(6595), pp. 831–839. doi: 10.1126/science.abn7747.

Zhu, J. *et al.* (2010) 'Decoupling mutations in the D-channel of the aa(3)-type cytochrome c oxidase from Rhodobacter sphaeroides suggest that a continuous hydrogen-bonded chain of waters is essential for proton pumping.', *Biochemistry*, 49(21), pp. 4476–4482. doi: 10.1021/bi100344x.

Zhu, J., Vinothkumar, K. R. and Hirst, J. (2016) 'Structure of mammalian respiratory complex i', *Nature*, 536(7616), pp. 354–358. doi: 10.1038/nature19095.

Zhu, S. and Vik, S. B. (2015) 'Constraining the Lateral Helix of Respiratory Complex I by Cross-linking Does Not Impair Enzyme Activity or Proton Translocation.', *The Journal of biological chemistry*, 290(34), pp. 20761–20773. doi: 10.1074/jbc.M115.660381.

Zickermann, V. *et al.* (2015) 'Mechanistic insight from the crystal structure of mitochondrial complex I', *Science*, 347(6217), pp. 44–49. doi: 10.1126/science.1259859.

8 Appendix

8.1 Effect of salt concentration on bovine mitochondrial membrane NADH oxidation rate

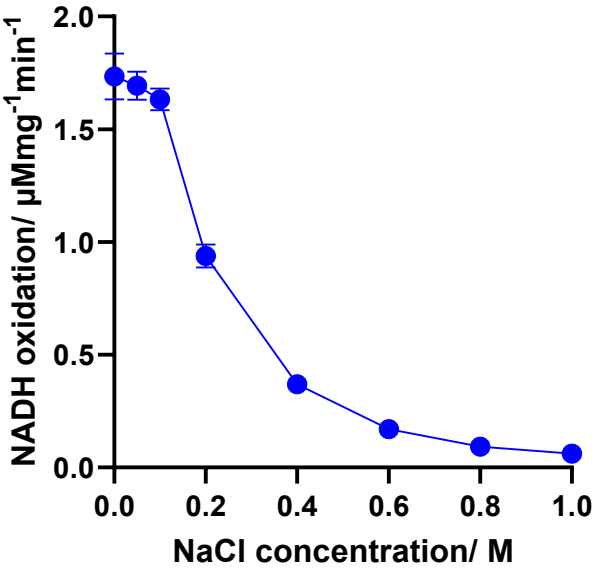

Figure 7.1: Titration of NaCl concentration against the NADH oxidation rate of bovine mitochondrial membranes. Titration was carried out at pH 7.5 at 32 °C. NaCl concentration does not affect the NADH oxidation rate of bovine mitochondrial membranes until more than 200 mM NaCl was added.

8.2 Derivation of the Kresge-Gross-Butler equation

First consider the Eyring equation and the rate equation.

$$K^{\ddagger} = \frac{k_B T}{h\nu} e^{\frac{-\Delta G^{\ddagger}}{RT}};\ k = k^{\ddagger} K^{\ddagger} \quad (1)$$

Consider that two protonic sites are titrated in the transition state equilibria $K^{\ddagger}$ between reactant R protons, and transition state T protons. k_0 denotes when the solvent is free of D_2O:

$$k_0 = k^{\ddagger} \frac{[TH_1H_2]}{[RH_1H_2]} e^{\frac{-\Delta G^{t_0}}{RT}} \quad (2)$$

Should there be a fraction of D_2O, the two protonic sites may each exchange against deuteron. k_n denotes the rate at n fraction of D_2O in the solvent.

$$k_n = k \neq \frac{k_B T}{h} \frac{[TH_1H_2]+[TD_1H_2]+[TH_1D_2]+[TD_1D_2]}{[RH_1H_2]+[RD_1H_2]+[RH_1D_2]+[RD_1D_2]} e^{\frac{-\Delta G^{tn}}{RT}} \quad (3)$$

The proton inventory is measured at multiple fraction of D_2O and compared against the rate in solvent free of D_2O. Divide k_n by k_0.

$$\frac{k_n}{k_0} = \frac{1 + \frac{[TD_1H_2]}{[TH_1H_2]} + \frac{[TH_1D_2]}{[TH_1H_2]} + \frac{[TD_1D_2]}{[TH_1H_2]}}{1 + \frac{[RD_1H_2]}{[RH_1H_2]} + \frac{[RH_1D_2]}{[RH_1H_2]} + \frac{[RD_1D_2]}{[RH_1H_2]}} \cdot \frac{e^{\frac{-\Delta G^{tn}}{RT}}}{e^{\frac{-\Delta G^{t_0}}{RT}}} \quad (4)$$

Fractionation factors ϕ^R and ϕ^T are derived using scheme 3.1. As n increases, more sites are saturated with D.

$$\frac{[RD_1D_2]}{[RH_1H_2]} = \frac{\phi_1^R \phi_1^R n^2}{(1-n)^2} \; ; \; \frac{[TD_1D_2]}{[TH_1H_2]} = \frac{\phi_1^T \phi_1^T n^2}{(1-n)^2} \quad (5)$$

The medium effect Z monitors solvation effects and is given as the ratio of the activation energy difference based on the interaction of the solvent with the transition state:

$$Z_k^n = \frac{e^{\frac{-\Delta G^{tn}}{RT}}}{e^{\frac{-\Delta G^{t_0}}{RT}}} \quad (6)$$

Simplifying equation 4 with 5 and 6 derives:

$$\frac{k_0}{k_n} = \frac{(1-n+n\phi_1^R)(1-n+n\phi_2^R)}{(1-n+n\phi_1^T)(1-n+n\phi_2^T)} Z_k^n \quad (7)$$

This further simplifies the Kresge-Gross-Butler equation to.

$$\frac{k_n}{k_0} = \frac{\pi(1-n+n\phi^T)}{\pi(1-n+n\phi^R)} Z_{n,k}^{-1} \quad (8)$$

8.3 Script used for fitting the rate equation in MATLAB

```
function A

error = zeros(1,length(Rate));
totalerror = [0];
besterror = 9e9;
calcrate = [1];

%nested loops
        for K3 = logspace(-15,-8,30)
            for K4 = logspace(-10,-2,30)
                for K5 = logspace(-8,-2,30)
                    for Km = logspace(-3,3,30)
                        for kcat = logspace(-2,5,30)
                            for k3r = 1
                                for i = 1:length(Rate)

                                    n1 = kcat;
                                    d1 = K3*Km;
                                    d2 = kcat*(K3/k3r);
                                    d3 = Km;
                                    d4 = (1/K4)*Km;
                                    d5 = 1;
                                    d6 = (1/K5);

                                    N = n1*S(i)*H(i);
                                    D = d1 + d2*S(i) + d3*H(i) + d4*H(i)*H(i) + d5*S(i)*H(i) + d6*S(i)*H(i)*H(i);

                                calcrate = N/D;
                                error(i) = (calcrate - Rate(i))^2;

                                while i == length(Rate)
                                      i = 1;
                                      loop = loop + 1;
                                      totalerror = sum(error);

                                    if totalerror < besterror
                                        BestK3 = K3;
                                        BestK4 = K4;
                                        BestK5 = K5;
                                        Bestk3r = k3r;
                                        BestKm = Km;
                                        Bestkcat = kcat;

                                      besterror = totalerror;
                                    end
                                end
                                    while i <= length(Rate)
                                          i = i + 1;
```

Figure 7.3: MATLAB script used for parameter fitting of rate equation 3.9.